Sound source contributions for the prediction of vehicle pass-by noise

by

Michael E Braun

A Doctoral Thesis

Submitted in partial fulfilment
of the requirements for the award of

Doctor of Philosophy
of
Loughborough University

20th November 2014

Dedication

Dedicated to my father with whom I would have loved to discuss any topic related to mechanical engineering.

Acknowledgements

This thesis has been made possible through the financial support provided by the Department of Aeronautical and Automotive Engineering at Loughborough University for which I am very grateful.

First of all I would like to thank my supervisor, Dr Stephen J Walsh, for his valuable support and his patience throughout the duration of my research project at Loughborough University. Many thanks to Dr Keith Peat, joint supervisor at the beginning of my project, and Dr Jane L Horner, who took over joint supervision responsibilities when Keith retired. Their advice and support is greatly appreciated.

I would like to thank Dr Dan J O'Boy for the many discussions and advice about the tyre cavity noise subject. I am grateful to Dr Chris Harvey and Mr Shuo Dai for the introduction to the Digital Image Correlation technology and their support in the preparation as well as in the operation of the testing equipment. Thanks to Mr Dan Clouth for his assistance on the shell noise experiments. The manufacturing of the test rigs and the preparation of various sensors would not have been possible without the help of Grenville Cunningham, Dave Roche, Pradip Karia and Martin Cramp. Many thanks to Dr Binoy Sobnack and Ms Karen Oppong-Banahene for proof-reading my thesis.

To all my friends in the UK who made my stay here a lot more enjoyable and who provided me with a diverse range of experiences through all their different cultural origins, I say a big thank you. This includes the students of Harry French hall of residence as well as its warden team with Binoy and family, Andrew and Wangari, Karen, Quang Bob. Special thanks go to Dr Ramin Rahmani, Dr George Koronias and Dr Yannis Karayannis for their help and support regarding work related topics or life in general. Finally, I want to express my deepest gratitude to my mother and my late grandmother for their never ending support and advice.

Abstract

Current European legislation aims to limit vehicle noise emissions since many people are exposed to road traffic noise in urban areas. Vehicle pass-by noise is measured according to the international standard ISO 362 in Europe. More recent investigations of urban traffic have led to the proposal of a revised ISO 362 which includes a constant-speed test in addition to the traditional accelerated test in order to determine the pass-by noise value. In order to meet the legal pass-by noise requirements, vehicle manufacturers and suppliers must analyse and quantify vehicle noise source characteristics during the development phase of the vehicle. In addition, predictive tools need to be available for the estimation of the final pass-by noise value.

This thesis aims to contribute to the understanding of vehicle pass-by noise and of the characteristics of the vehicle noise sources contributing to pass-by noise. This is supported through an extensive literature review in which current pass-by noise prediction methods are reviewed as well. Furthermore, three vehicle noise sources are replicated experimentally under laboratory conditions. This involves an orifice noise source, represented by a specially designed loudspeaker on a moving trolley, shell noise, represented by a metal cylinder structure, and tyre cavity and sidewall noise, represented by an annular membrane mounted on a tyre-like structure. The experimentally determined directivity characteristics of the acoustically excited noise sources are utilised in the pass-by noise prediction method. The predictive results are validated against experimental measurements of the three vehicle-like noise sources made within an anechoic chamber.

Keywords: Vehicle noise source characteristics; vehicle pass-by noise test; pass-by noise prediction; engine noise; exhaust noise; tyre/road noise.

Contents

List of Figures

List of Tables

Copyright Acknowledgements

Fig. 1.1 is reprinted from 'BS ISO 362-1:2007 Measurement of noise emitted by accelerating road vehicles. Engineering method. M and N categories.'. © British Standards Institution (BSI www.bsigroup.com). With kind permission of British Standards Institution.

Figs. 2.3, 2.8 and 2.11 are reprinted from 'Biermann J-W. Geruschverhalten von Kraftfahrzeugen (Noise characteristics of vehicles) Lecture notes'. With kind of permission of Prof Biermann.

Figs. 2.4, 2.5 and 2.6 are reprinted from 'VDI-Richtlinien 2563. Geräuschanteile von Straßenfahrzeugen - Meßtechnische Erfassung und Bewertung (Guideline of the Association of German Engineers (VDI): Noise components of vehicles; measurement and assessment). Düsseldorf: Verein Deutscher Ingenieure; 1990'. With kind permission of Verein Deutscher Ingenieure.

Figs. 2.7 and 2.20 are reprinted from 'Alt N, Wolff K, Eisele G, Pichot F. Fahrzeugaussengeräuschsimulation (Vehicle exterior noise simulation). Automobiltechnische Zeitschrift 2006; 108:832-36'. With kind permission of Dr Alt.

Fig. 2.9 is reprinted from 'Bosch Kraftfahrtechnisches Taschenbuch (Bosch - Automotive Handbook). 25th ed. Wiesbaden: Vieweg+Teubner; 2004'. With kind permission of Robert Bosch GmbH.

Fig. 2.10 is reprinted from 'Arndt R, Fliesser W, Rein D, Fankhauser C. Analysis of pass-by noise using Nearfield Acoustic Holography'. Copyright Virtual Vehicle Research Center. With kind permission of DEGA e.V. (German Acoustical Society) and Mr Arndt.

Figs. 2.12, 2.13, 2.21, 2.22, 2.23 and 2.24 are reprinted with permission from 'Park S-H, Kim Y-H. Visualization of pass-by noise by means of moving frame acoustic holography. J Acoust Soc Am, vol. 110 p. 2326 – 39 (2001)'. Copyright 2001, Acoustical Society of America. With kind permission of Prof Kim.

Fig. 2.14 is reprinted from 'Zeller P. Handbuch Fahrzeugakustik (Handbook Vehicle Acoustic). Vieweg + Teubner Verlag; 2009'. With kind permission of Springer Science and Business Media.

Fig. 2.15 is reprinted from 'Davies P, Holland K. I.C. engine intake and exhaust noise assessment. J Sound Vibr 1999; 223:425-44'. With kind permission of

Elesevier Ltd.

Figs. 2.16, 2.17 and 2.18 are reprinted from 'Alfredson R, Davies P. The radiation of sound from an engine exhaust. J Sound Vibr 1970; 13:389-408'. With kind permission of Elsevier Ltd.

Fig. 2.19 is reprinted from 'Sandberg U, Ejsmont JA. Tyre/road noise reference book. Kisa (Sweden): Informex; 2002'. With kind permission of Informex HB.

Figs. 2.25, 2.26 and 2.27 are reprinted from 'Sakata T, Morimura H, Ide H. Effects on tire cavity resonance on vehicle road noise. Tire Science and Technology, 18(2):68-79, 1990'. With kind permission of Dr Taheri, President of The Tire Society.

Figs. 2.28 and 2.29 are reprinted from 'Kim GJ, Holland KR, Lalor N. Identification of the airborne component of tyre-induced vehicle interior noise. Applied Acoustics, 51(2):141-156, 1997'. With kind permission of Elesevier Ltd.

Figs. 2.30, 2.31 and 2.32 are reprinted from 'Kim BS, Kim GJ, Lee TK. The identification of tyre induced vehicle interior noise. Applied Acoustics, 68:133-156, 2007'. With kind permission of Elesevier Ltd.

Eq. 3.1 is reproduced from 'BS EN 61672-1:2013 Electroacoustics. Sound level meters. Specifications.'. © British Standards Institution (BSI www.bsigroup.com). With kind permission of British Standards Institutions.

Nomenclature

Roman Symbols

A	variable within the Green's Function
a	acceleration
B	variable within the Green's Function
c	wave propagation speed, speed of sound
$\mathrm{d}r$	infinitesimal displacement in radial direction
d_s	travelled distance of a (sound) source
$\mathrm{d}z$	infinitesimal deflection in z direction
E	modulus of elasticity
f	frequency
$f_{0/1}$	functions
$f_{0,c,n}$	calculated eigenfrequency of the nth mode
$f_{0,m,n}$	measured eigenfrequency of the nth mode
f_n	resonance frequency of the nth mode of a duct
f_{nm}	eigenfrequency of the (n, m) mode
$F_{(z)}$	force in z direction
G	Green's Function
$g_{0/1}$	functions
h	wall thickness of a membrane
i	order of the cavity resonance

k	wavenumber
k_{nm}	wavenumber of the (n, m) mode
$L_{A\tau}$	frequency-weighted and time-weighted sound pressure level
l_{cp}	length of the contact patch or the deformed region of the tyre cavity
l	length of the duct, length of the tyre cavity
m	mass, or mode number
m	ratio of the deformed cross-section area to the undeformed cross-section area of the tyre cavity
n	revolution, or mode number
p	sound pressure
p_0	reference sound pressure
p^2_{interp}	interpolated squared sound pressure
p_A	A-weighted instantaneous sound pressure
p_r	predicted pass-by sound pressure
p_s	measured sound pressure of the noise source in the directivity measurements
r	radius, radial direction or coordinate
r_D	distance between noise source reference point and microphone in the directivity measurements
R_i	inner radius
R_o	outer radius
r_s	instantaneous distance between source and receiver
$r_{s,pass}$	shortest distance between the reference point on the noise source and the microphone in the pass-by noise test
s	distance, displacement
T	tension
t	time

$T_{1/2}$	tension in the membrane in the principal stress directions
$\overline{T}_{1/2}$	average value of the principal tensions T_1 or T_2
$\overline{T}$	average value of the averaged principal tensions $\overline{T}_{1/2}$
v	velocity
v_s	velocity of a (sound) source
x	Cartesian coordinate, horizontal direction
y	Cartesian coordinate, vertical direction
Z	variable within the Green's Function
z	coordinate in orthogonal direction to the membrane plane, field variable
$\ddot{z}$	acceleration in z direction

Greek Symbols

α	deflection angle of a membrane in the vertical-circular z-$r\varphi$ plane
Δl	end correction in duct acoustics
$\mathrm{d}\varphi$	infinitesimal displacement in tangential direction
η	integration variable for tangential direction
ε	strain
$\varepsilon_{r\varphi}$	shear strain in the r-φ plane
$\varepsilon_{rr/\varphi\varphi}$	strain in radial or tangential direction
$\varepsilon_{xx/yy}$	strain in horizontal or vertical direction
ε_{xy}	shear strain in the x-y plane
ε_{zz}	strain in orthogonal direction
$\hat{\mu}$	mass per unit area
μ	roots
ν	Poisson's number
ω_{nm}	natural frequency of the nm mode

φ_0	polar angle for the location of the principal planes
ρ	density per unit volume, density of air
$\sigma_{r/\varphi}$	normal stress in either radial or tangential direction
$\sigma_{1/2}$	principal stress in either direction 1 or 2
$\sigma_{r\varphi}$	shear stress in the r-φ plane
$\sigma_{rr/\varphi\varphi}$	normal stress in radial or tangential direction
τ	integration variable for time, time constant
θ	angle specifying the directivity sound pressure, instantaneous angle between the direction of motion of a noise source and the instantaneous distance vector in the pass-by noise test
φ	polar angle, tangential or circumferential direction or coordinate
ϑ	deflection angle of a membrane in the vertical-radial z-r plane, polar angle
ξ	integration variable for radial direction or time

Subscripts

i	interpolation index denoting circumferential direction
j	interpolation index denoting radial direction
m	subscript index, zero of the Bessel function
n	subscript index, order of the Bessel function

Acronyms

AMM	Annular Membrane Model
BEM	Boundary Element Method
DIC	Digital Image Correlation
FEM	Finite Element Method
FIR	Finite Impulse Response
FMBEM	Fast Multipole Boundary Element Method

FRF	Frequency Response Function
IBEM	Indirect Boundary Element Method
MFAH	Moving Frame Acoustic Holography
FMM	Fast Multipole Method
NAH	Nearfield Acoustic Holography
1D CFD	Computational Fluid Dynamics
ONS	Orifice Noise Source
RMS	Root mean square
RN	Rolling or background noise of the pass-by noise test rig
SNS	Shell noise source
SPB	Statistical Pass-By
TSR	Tyre Sidewall Replica

Chapter 1

Introduction

Road traffic noise represents a main contributor to environmental noise, which represents a burden to the exposed population resulting in annoyance, sleep disturbance or cardiovascular disease [29]. Road traffic noise is aimed to be limited in order to increase health and life quality. In the European Union, legislation intends to reduce and limit vehicle exterior noise [18]. Vehicle exterior noise emission is quantified in terms of idle noise and pass-by noise with the latter being considered to represent an approximation to typical urban driving behaviour. The international standard ISO 362 [10] represents a guideline for the measurement and calculation of the pass-by noise level for every vehicle class. In the vehicle homologation process, it must be verified that the vehicle pass-by noise level is in conformity with current regulations. A selection of current pass-by noise limits of different vehicle categories are presented in Table 1.1.

The vehicle pass-by noise test and limits were first introduced in the 1970s. Since then, vehicle pass-by noise limits have been gradually reduced for all vehicle classes in the European Union. For example, the noise emission of a passenger vehicle was decreased from 82 dB(A) in 1970 to 74 dB(A) in 1996, which corresponds to a reduction of 84%. Figuratively, the noise emission of a vehicle at 82 dB(A) is equivalent to the noise emission of six vehicles at 74 dB(A), which can be seen as a success in terms of noise reduction. Vehicles are the sources of traffic noise, the reduction of the contributions of the sources should have resulted in decreased traffic noise. However, road traffic noise in urban areas was not as significantly reduced as the pass-by noise limits [11]. Recent criticism on the current pass-by noise test procedure concludes that it does not simulate the typical vehicle noise characteristics under urban traffic conditions appropriately [11]. The current wide-open throttle test procedure is dominated by powertrain noise, which is rarely observed in urban traffic, and, thus, masking or suppressing tyre/road noise [11]. However, tyre/road noise can represent a substantial noise source under urban traffic conditions. In addition, the technical developments in vehicle

propulsion and transmission technology are unaccounted for. Therefore, a revised test procedure was devised, which is assumed to reflect urban driving behaviour more realistically. The implementation of the revised method and the further reduction of pass-by noise limits are currently being discussed. This will result in an increased challenge in the vehicle development process for manufacturers and suppliers.

Vehicle category	Pass-by noise limit [dB(A)]
Passenger vehicle	74
Commercial vehicle ($< 2\,\mathrm{t}$)	76
Lorry ($> 3.5\,\mathrm{t}$)	
engine power $< 75\,\mathrm{kW}$	77
$75\,\mathrm{kW} \leq$ engine power $< 150\,\mathrm{kW}$	78
engine power $\geq 150\,\mathrm{kW}$	80

Table 1.1: Exemplarily selected pass-by noise limit values of standard vehicles [18]

This thesis aims to contribute to the understanding and prediction of vehicle pass-by noise. For the understanding of the pass-by noise test procedure, the current and the revised test methods are presented in the following section. This is then followed by the thesis structure and objectives.

1.1 The standardised ISO 362 vehicle pass-by noise test procedure

The international standard ISO 362 [10] from 1998 is the guideline for the implementation of the vehicle pass-by noise test. Its intention is to reflect the noise emission of a vehicle in an urban traffic environment. The test facility, illustrated in Fig. 1.1, consists of a planar 20 m by 20 m acceleration area with a reference line CC' across its centre representing the driving direction of the vehicle. The surface of the acceleration area and the driving lane 10 m prior and after the acceleration area are covered with a tarmac according to the requirements of the standard ISO 10844 [9] in order to ensure equally equipped test facilities. This shall provide repeatable and comparable readings under the same conditions for any test facility. There shall be no large reflecting objects within a radius of 50 m. Two microphones are located midway in the acceleration area at a distance of 7.5 m away from the reference line and at a height of 1.2 m. The microphones are positioned horizontal and perpendicular to the line CC'. The space between the vehicle and the microphone shall be free of any reflecting objects in order to not affect the acoustic field.

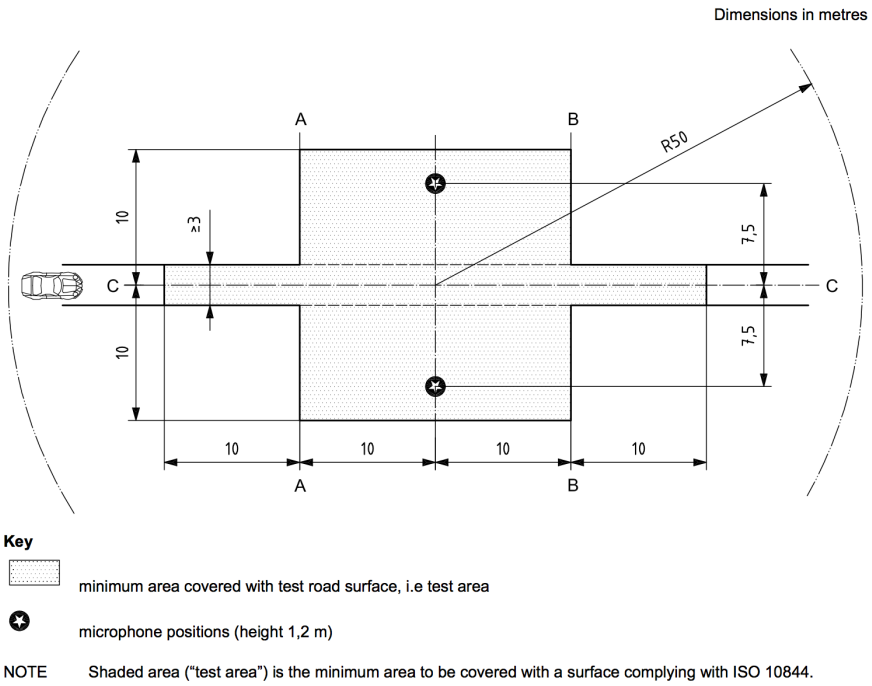

Figure 1.1: Pass-by noise test site [11] (© British Standards Institution (BSI www.bsigroup.com). Extract reproduced with permission. Source: BS ISO 362-1:2007 Measurement of noise emitted by accelerating road vehicles. Engineering method. M and N categories.).

The sound pressure measurement system used for the recording shall meet the requirements of Class 1 instruments according to the standard IEC $61672-1$ [13]. For the recording, the time weighting 'F' (Fast) and the frequency A-weighting shall be used. Quantities like engine speed, vehicle road speed or meteorological data (temperature, wind speed, barometric pressure, relative humidity) shall be measured as well, using devices with a low tolerance rate. During the test, meteorological data have to be within certain tolerance ranges and shall be monitored. High wind speeds and rain prevent the test. For example, it is required that the ambient air temperature is within $5\,°C$ to $40\,°C$ and that the wind speed is less than $5\,m/s$. The background noise level is to be checked before and after the pass-by noise test. It shall be at least $10\,dB$ below the A-weighted pass-by sound pressure level.

A vehicle according to the specifications from the vehicle manufacturer is provided for the test. The test track shall be dry during the measurement. In case of a passenger car, the vehicle is driven on the reference line CC' approaching the acceleration area at a constant speed of $50\,k.p.h$ in the current test procedure according to Ref. [10]. The accelerator control is fully engaged when the front of the vehicle reaches the line AA' of the acceleration area, and it is fully disengaged when the rear of the vehicle leaves the area at the line BB'. The maximum A-

weighted pass-by noise level is recorded by the two microphones. For the majority of passenger cars with manual transmissions, the pass-by is driven in second and third gear. Four consecutive runs are carried out for each gear. The recorded pass-by noise levels on each side of the vehicle are required to be within a range of 2 dB(A), then they are averaged for each side and each gear. The highest averaged values of the second and third gear are averaged again resulting in the pass-by noise level. The accelerated pass-by is also the core of the pass-by noise determination of other vehicle classes. The only decision criterion of the pass-by noise test is the maximum A-weighted sound pressure level; sound quality is not of an issue.

Despite the decreasing pass-by noise limits over the previous decades, the core test procedure has remained unchanged. It is a common criticism that the test procedure does not reflect nowadays typical urban traffic conditions. Due to the full acceleration, the test is dominated by powertrain noise masking tyre/road noise [11]. However, urban traffic noise is not dominated by full accelerating vehicles, thus, the standard test has been revised in order to devise a test procedure, which reflects nowadays urban driving behaviour more realistically. After comprehensive observations of traffic noise in Europe, Asia and the United States, a test method is proposed combining the maximum noise levels of an accelerated and a constant-speed pass-by on the same test facility. Usually two gears are selected according to the acceleration capability of the tested vehicle. In the acceleration pass-by, the speed of 50 k.p.h. shall be reached when the front of the vehicle reaches the line between the two microphones. In the constant-speed test, the vehicle is driven at 50 k.p.h. The maximum A-weighted sound pressure level shall be measured on both sides of the vehicle for four consecutive runs in each gear. The readings of consecutive runs have to be within 2 dB(A). This measurement sequence is repeated for the accelerated and the constant-speed pass-by. The recordings of the accelerated and the constant-speed pass-by are averaged for each side and each gear. The higher value of each side is used for the calculation of the pass-by noise level L_{urban}. From the traffic noise observations, a formula for the calculation of the pass-by noise level L_{urban} was statistically derived, which takes the measured sound pressure of the accelerated and constant-speed tests and engine power into account. This pass-by noise level represents the noise emission of a partial accelerated vehicle under urban traffic conditions.

Between 2008 and 2010, a comparison database was established containing pass-by noise levels obtained according to both versions of the standard. On average, the pass-by noise level of a passenger car according to ISO 362:1998 is 72 dB(A), which is 2 dB(A) higher than the noise level of the suggested new test method [22].

Currently, the implementation of the new test method and the adapted noise

limits are still being discussed. Practically this means that the Council Directive 70/157/EEC [18] and its amendments from the past decades will be repealed. It is proposed to implement the new pass-by noise limits for the European Union in three phases with a limit of 68 dB(A) for a passenger vehicle to be reached five years after the publication of the pass-by noise limits [19]. Considering the current wish for a reduction of vehicle exterior noise, it has to be considered that in the future hybrid and electrical vehicles may change the acoustical perception of traffic noise. Such vehicles emit much less noise, of an unfamiliar characteristic, which may cause difficulties, especially for blind people. It may be decided that these vehicles have to emit a minimum noise level in order to raise their acoustical identification potential [19, 14]. However, it is expected that this minimum noise level will still be much lower than the current pass-by noise limits.

1.2 Thesis structure

Prior to market launch, a new vehicle is tested in order to certify its compliance with current pass-by noise legislation. During the vehicle development process, manufacturers and suppliers are required to ensure that this compliance is achieved. Hence, it is important that vehicle engineers have access to predictive tools at the design stage. Complete vehicle prototypes are usually only available at a later stage in the development process. Thus, a predictive method which indicates the pass-by noise contribution of a single vehicle noise source can be beneficial and applicable in the early stages of the vehicle development process. The change of the test procedure as well as the intention to reduce vehicle pass-by noise limits impose another challenge on manufacturers and suppliers.

In this thesis, a method for the prediction of pass-by noise contributions of vehicle noise sources is presented. It is envisaged that the proposed prediction method feeds into the requirements and the range of application of the ISO 362 pass-by noise test.

Comprehensive knowledge about the pass-by noise characteristics and the effective vehicle noise source in a pass-by driving manoeuvre is essential, which is reviewed from the literature in Chapter 2. This comprises the analysis of pass-by noise level in the time and frequency domain as well as the ranking of vehicle noise sources. The characteristics of the four major vehicle noise sources, which are the engine, the exhaust and the intake system as well as the tyre/road combination, in the pass-by noise test are analysed. Then, existing pass-by noise prediction methods are reviewed. This includes numerical methods as well as experimental methods, like the indoor simulation of pass-by noise on a chassis dynamometer in a semi-anechoic chamber or the pass-by noise prediction through experimental

quantification of individual noise source strengths and airborne transfer paths. It is also reported about the identification of the tyre sidewall noise source, which radiates sound due to the excitation from the tyre cavity modes.

Numerical simulations of the pass-by noise test do not achieve the same accuracy as experimental methods. Therefore, an experimental pass-by noise prediction method is proposed in this thesis, which makes use of the available experimental facilities and test equipment. In the centre of the prediction method, presented in Section 3.1, is the horizontal directivity characteristic of a single noise source, which is defined as the sound pressure readings at discrete intervals on a horizontal circle around the noise source. The sound pressure recordings are time-weighted and frequency-weighted, in compliance with the standard ISO 362. Obtaining the horizontal directivity characteristic supports the analysis of the sound radiation pattern of the noise source. The directivity sound pressure serves as a quantification of the noise source strength. For the pass-by noise prediction, the inverse square law is applied in order to combine the directivity sound pressure and the instantaneous distance between noise source on the test track and pass-by microphone. Thus, the pass-by noise level versus distance is obtained as a result. In order to validate the proposed pass-by noise prediction method, a pass-by noise test rig is developed, which is presented in Section 3.2 in order to replicate a pass-by noise test situation of a vehicle-like noise source on a laboratory scale and under laboratory conditions. The test rig consists of a moving trolley on a static test track with various sensors available in order to determine position and speed of the trolley. Thus, experimental measurements made within an anechoic chamber are then compared to the prediction of the pass-by noise characteristic of the moving orifice source.

Three noise sources are selected from the discussion in Chapter 2 with which the proposed prediction method is tested. The noise sources represent an orifice noise source (ONS), a shell noise source (SNS) and a tyre cavity and sidewall noise source. Orifice and shell noise sources on the vehicle are identified as significant contributors to the pass-by noise of the accelerated test scenario, which is dominated by powertrain noise. Tyre/road noise is a dominant noise source in urban traffic, which is taken into account in the proposed constant-speed pass-by noise test. The contribution of a tyre sidewall, excited by tyre cavity resonances, to vehicle pass-by noise has not been investigated previously. These three vehicle noise sources are replicated and presented in Sections 4.1, 5.1 and 6.1.

The directivity sound pressure characteristics are quantified experimentally within an anechoic chamber in Sections 4.2, 5.2 and 6.5.5 in order to analyse their noise radiation characteristics and to provide this data for the prediction method. From the measured data, it can also be estimated how close the noise source

replicas are to reality. For the tyre cavity and sidewall noise source, a more in-depth analysis is carried out including the measurement of the cavity resonances (Section 6.2), the experimental estimation of the tension in the annular membrane (Section 6.4), which replicates the tyre sidewall, as well as the sound radiation in close proximity to the annular membrane (Section 6.5.2), which shall confirm that the membrane replicates the mode shape of the cavity. The annular membrane in Section 6.3 estimates the tension in the annular membrane which is required to match resonances of the annular membrane and the cavity, which replicates the real excitation mechanism.

Applying the proposed pass-by noise prediction method, the measured directivity sound pressure data of each noise source is combined with the instantaneous distance between the pass-by noise microphone and the noise source in the inverse square law, resulting in an pass-by noise estimate for each of the three noise sources in Sections 4.3, 5.3 and 6.6. In order to validate the pass-by noise prediction method, direct and reciprocal pass-by noise measurements are conducted with the noise source replicas under laboratory conditions. These validation data sets are then compared to the predicted pass-by noise.

Chapter 2

Literature review

2.1 The characteristics of vehicle pass-by noise in the ISO 362 test

After the regulation and legislation of vehicle pass-by noise were introduced in Chapter 1, this section identifies the general characteristics of vehicle pass-by noise. Therefore, the analysis of recordings of vehicle pass-by noise levels from the accelerated test of ISO 362:1998 are presented in Sections 2.1.1 to 2.1.3. The information and data, which is found in the literature, differs in terms of quality. The underlying reasons can be variations in the measurement environment, measurement or processing errors, vehicles of different type and age, or different types of measurement equipment. Furthermore recently developed measurement systems and equipment may provide the more accurate recordings. In addition, pass-by noise limits have been reduced several times in the past. Time history and frequency spectra of pass-by noise tests are utilised for the analysis in Sections 2.1.1 and 2.1.2. The contribution of noise sources to the vehicle overall pass-by noise as well as noise source ranking is given in Section 2.1.3.

2.1.1 Pass-by noise versus distance

Figs. 2.1 and 2.2 [80] present recordings of the left-hand and right-hand side pass-by microphones of a passenger vehicle in the second and third gear. The vehicle approaches the entry to the acceleration area, at $-10\,\mathrm{m}$, with constant speed. Hence, the sound pressure level appears to be similar to a single sound source approaching a receiver from a far distance, which results in an almost linear increase of the sound pressure level with distance. The sound pressure level of the second gear has a steeper gradient than the sound pressure level of the third gear test upon the activation of the accelerator at $-10\,\mathrm{m}$. This may

be due to the abrupt change in engine load and rapid increase in engine speed, which is associated with greater pressure pulses from the engine and intake system and a greater amount of air taken into the intake system. This would be clearly identifiable in the pass-by noise data in case of a vehicle with the engine mounted on the vehicle front. The speed difference for the second gear is about 16 k.p.h. and for the third gear, it is approximately 12 k.p.h. Large differences in speed in the vehicle pass-by noise test indicate a higher-powered engine in general. Since the acceleration in third gear is less than in second gear, the sound pressure gradient in third gear is less steep. Assuming that the interference effects between coherent sound sources are negligible, it is assumed that the noise from the exhaust orifice and the tyres contribute most to the maximum pass-by noise level at +5 m since this value occurs after the vehicle has passed the microphone position at 0 m. The relatively short distance between the pass-by microphone and the noise sources reduces the effect of attenuation through distance. Furthermore, the sound radiation angle between the noise source and the receiver and a non-obscured transfer path lead to higher sound pressure levels. In this track position, the engine noise is screened by the vehicle body and is attenuated by the distance. After the peak level, at +5 m, the sound pressure level is decreasing as in the case of a sound source leaving a receiver. According to the inverse square law for a stationary source, the sound pressure is inversely proportional to the distance between sound source and receiver. However, the pass-by noise measurement data do not show this characteristic as the source is moving. Tyre/road noise is considered to be a major contributor in the velocity range of the vehicle pass-by noise test. However, two effects may decrease its contribution: (1) the angle between the longitudinal tyre axis and the pass-by microphone, which lessens the horn effect when the receiver is off-axis from the rolling direction; and (2) the attenuation with distance. Coast-by experiments have shown that tyre/road noise gradually increases until the vehicle passes the pass-by microphones, then it decreases with increasing distance between the vehicle and the microphone [76]. Thus, it is assumed that tyre/road noise also contributes to the overall pass-by noise level change with distance shown in Figs. 2.1 and 2.2. The measurement variability in the repetition of pass-by runs shown in Figs. 2.1 and 2.2 may occur due to the non-linearities caused by the programming characteristics of the vehicle engine control unit.

Fig. 2.3 [6] presents the recorded pass-by noise level of a medium class vehicle in second and third gear. The microphone is positioned on the left-hand side of the vehicle. The vehicle starts accelerating at the 0 m mark and stops accelerating at the 24 m mark, hence, the vehicle length is 4 m. The change of sound pressure level is similar to the previous diagrams with the sound pressure level gradient being

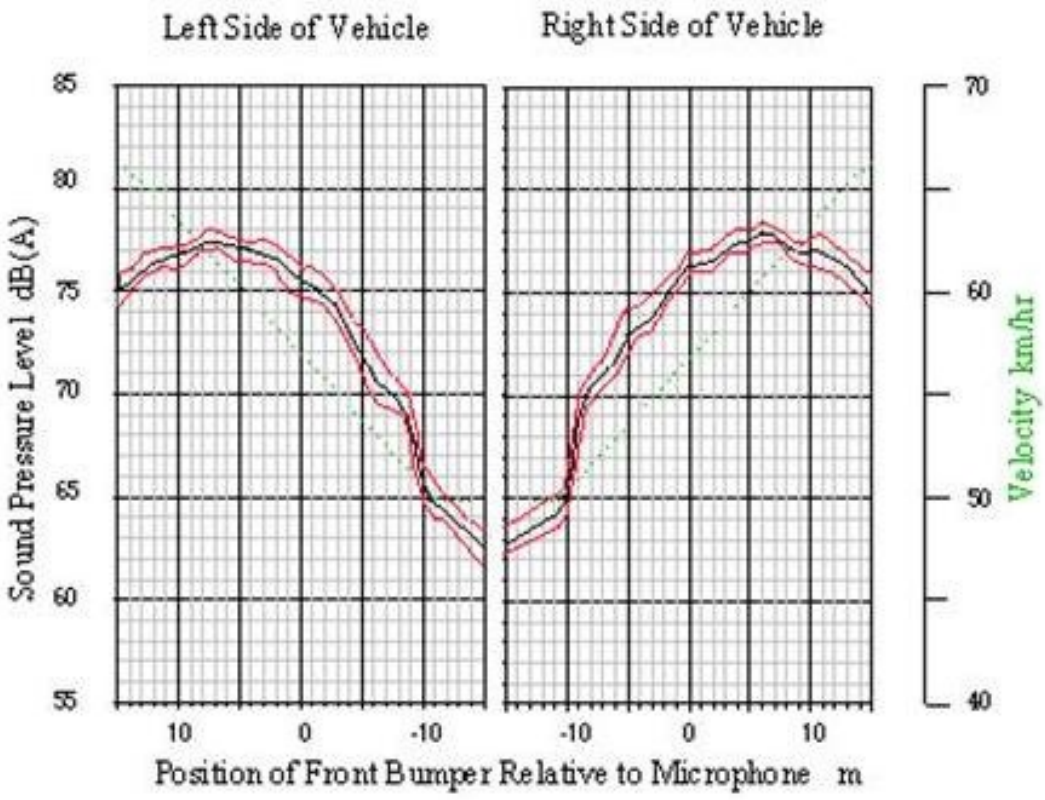

Figure 2.1: Pass-by noise recording in second gear according to ISO 362 [80].

steeper for the second gear test at the very beginning of the acceleration area. This is probably related to the engine or the intake system, since they are closest to the microphone for the approaching vehicle. In third gear, the increase of sound pressure level with distance is more linear in the first half of the acceleration area. Around the 10 m mark, i.e. between 8.5 m and 12.5 m, when the engine passes the microphone, the noise level is almost constant. It is assumed that the engine is the dominant noise source in this test area. However, the radiation characteristic of the exhaust orifice noise becomes dominant shortly afterwards. For both gears, the exhaust system noise seems to be the most dominant contribution at around 17 m. Here, the exhaust orifice is actually at the 13 m mark and, thus, closer to the microphone than the engine or intake system and it is without the screening effects from the vehicle body. Towards the end of the test track, the noise level decreases with increasing distance between the vehicle and the microphone. It can be derived from the Figs. 2.1 to 2.3 that the contribution of each of the four major noise sources depends upon vehicle speed or engine speed, respectively, as well as the vehicle position on the test track, i.e. the distance between the microphone and the noise source, as well as the orientation of the major radiation direction of the noise source to the microphone.

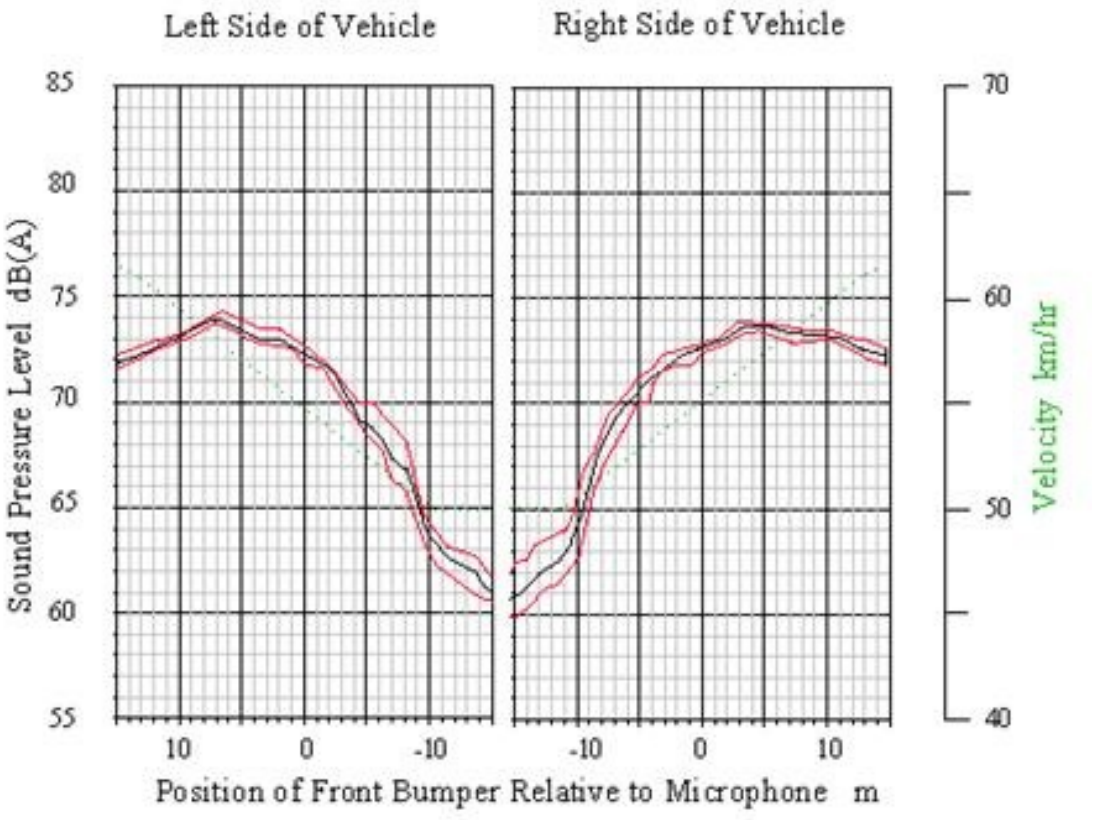

Figure 2.2: Pass-by noise recording in third gear according to ISO 362 [80].

2.1.2 Pass-by noise frequency content

Fig. 2.4 [88] presents a typical recording of an A-weighted pass-by noise level of the left-hand and right-hand side microphones against the position of the front of a passenger vehicle. A scatter band frames the curve of sound pressure level. The vehicle speed is also plotted. The diagram originates from the year 1990, which means that different pass-by noise limitations were effective in comparison to 2012. However, the characteristic is similar to Figs. 2.1 and 2.2. From the experimental data in Fig. 2.4, the A-weighted pass-by noise octave levels from 125 Hz to 8 kHz are determined and shown in Figs. 2.5 and 2.6, respectively. The differences in the pass-by noise level in Fig. 2.5 are due to the interferences between the coherent noise sources of the engine, the intake system and the exhaust system, or the effect of direct and reflected sound waves [88]. The maximum contribution can be found in the frequency range between 500 Hz to 2 kHz. Analysis of the pass-by noise frequency content assists in the understanding of noise source characteristics. However, detailed testing of each major noise source itself is required in order to identify and reduce critical pass-by noise contributions.

Fig. 2.7 [3] presents three colour map diagrams of different pass-by noise test carried out with a compact class vehicle. The evolution of the spectral content

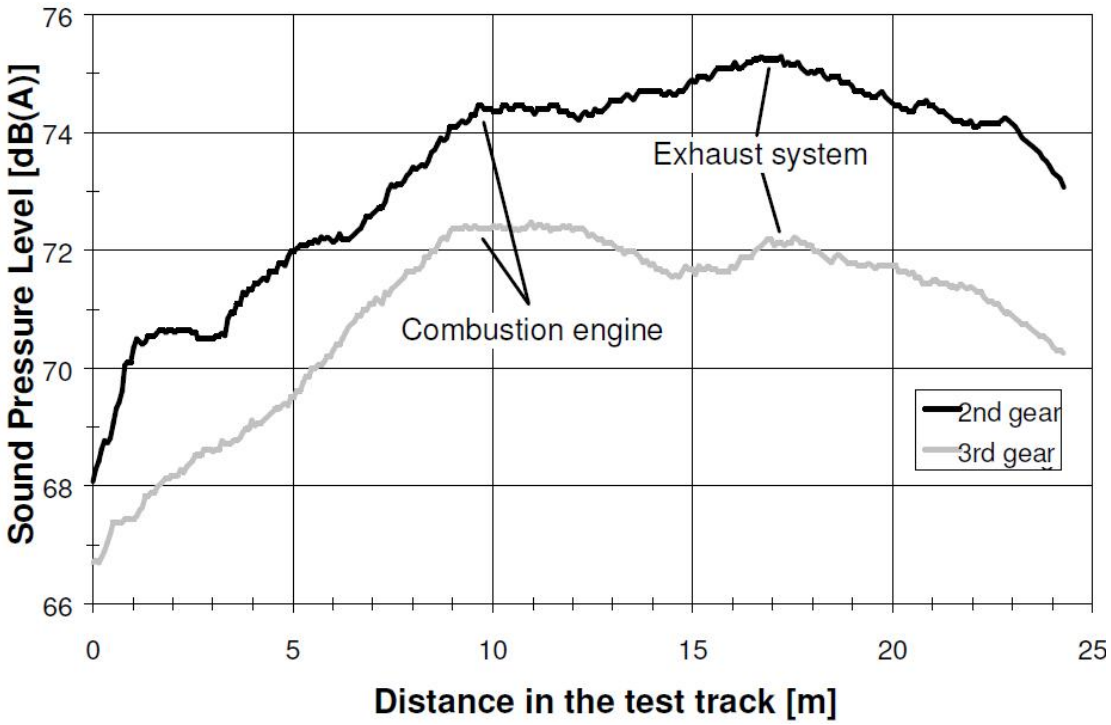

Figure 2.3: Pass-by noise recording of the left-hand side microphone in second and third gear of a medium class vehicle according to ISO 362 [6] (reprinted from Biermann J-W. Geräuschverhalten von Kraftfahrzeugen (Noise characteristics of vehicles). Lecture notes. With kind permission of Prof Biermann.).

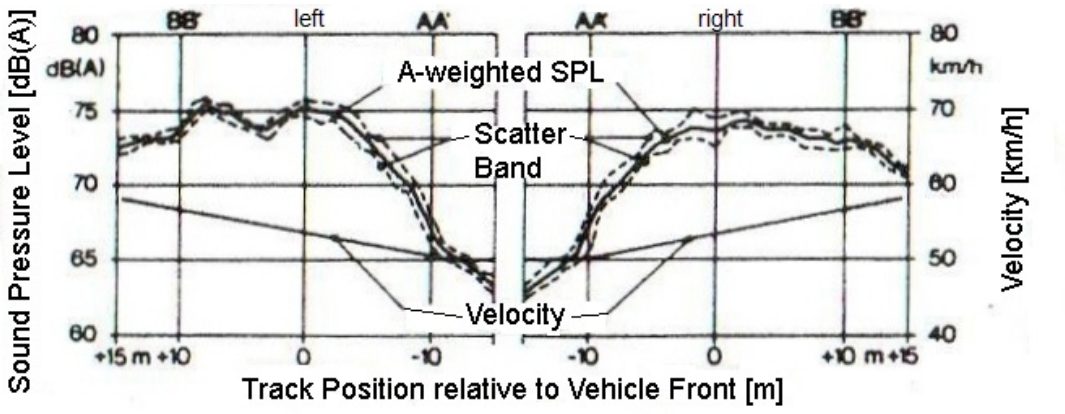

Figure 2.4: A-weighted pass-by noise level of the left-hand (left) and right-hand (right) side of the vehicle [88] (reprinted from VDI-Richtlinien 2563. Geräuschanteile von Straßenfahrzeugen - Meßtechnische Erfassung und Bewertung (Guideline of the Association of German Engineers (VDI): Noise components of vehicles; measurement and assessment). Düsseldorf: Verein Deutscher Ingenieure; 1990. With kind permission of Verein Deutscher Ingenieure.).

with time is visualised and indicates individual noise source characteristics and contributions. The plot on the left-hand side, Fig. 2.7a, is the result of a vehicle pass-by noise test with the engine being switched off and slick tyres in use, thus, only the wind noise is measured. In the middle diagram, Fig. 2.7b, the vehicle is

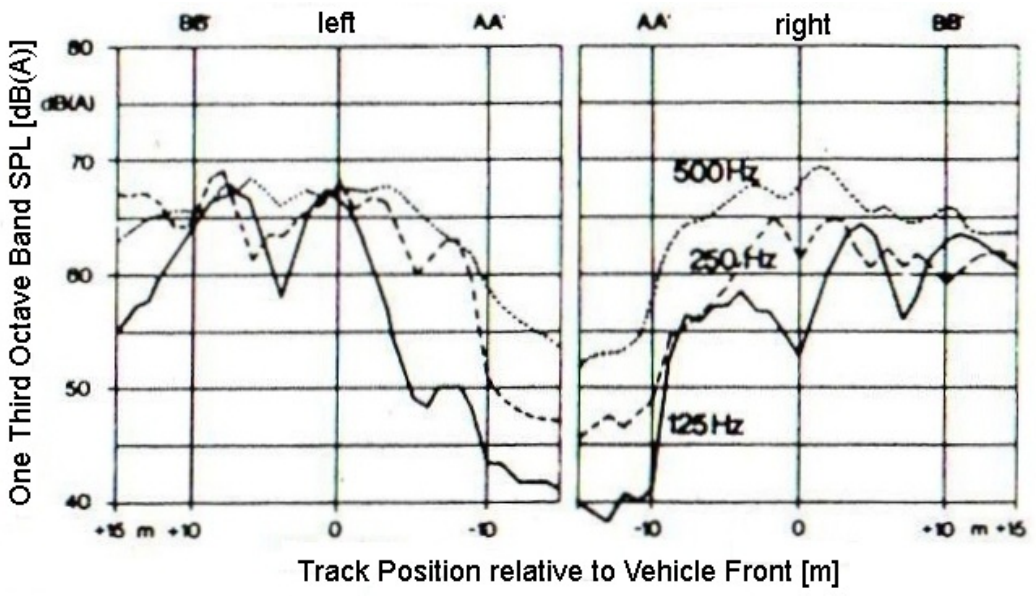

Figure 2.5: A-weighted pass-by noise octave band levels from 125 Hz to 500 Hz [88] (reprinted from VDI-Richtlinien 2563. Geräuschanteile von Straßenfahrzeugen - Meßtechnische Erfassung und Bewertung (Guideline of the Association of German Engineers (VDI): Noise components of vehicles; measurement and assessment). Düsseldorf: Verein Deutscher Ingenieure; 1990. With kind permission of Verein Deutscher Ingenieure.).

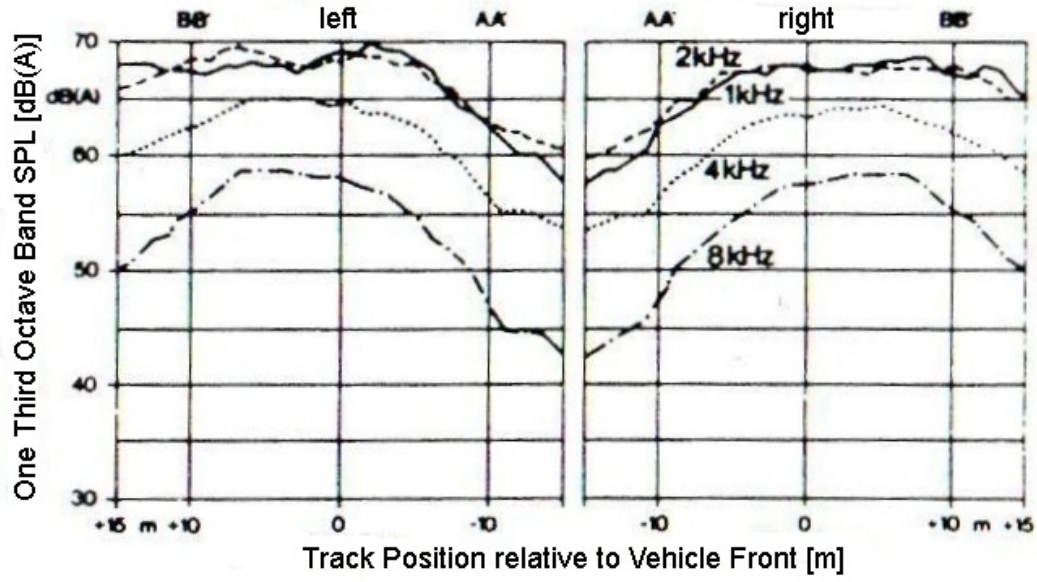

Figure 2.6: A-weighted pass-by noise octave band levels from 1 kHz to 8 kHz [88] (reprinted from VDI-Richtlinien 2563. Geräuschanteile von Straßenfahrzeugen - Meßtechnische Erfassung und Bewertung (Guideline of the Association of German Engineers (VDI): Noise components of vehicles; measurement and assessment). Düsseldorf: Verein Deutscher Ingenieure; 1990. With kind permission of Verein Deutscher Ingenieure.).

equipped with regular tyres, but the engine still remains switched off during the pass-by resulting in a combination of wind and tyre/road noise. There is no specific resonance frequency, but the increased amplitudes in the frequency range between 500 Hz and 2 kHz are caused by tyre/road noise [3]. It appears to have random noise characteristic. The right-hand side diagram, Fig. 2.7c, demonstrates the sound pressure frequency spectrum during the regular ISO 362 test. In comparison to the middle diagram, Fig. 2.7 b, even higher amplitude components are shown between 500 Hz and 2 kHz, which may be due to the increasing vehicle speed or tyre rotational speed, respectively. Furthermore, higher sound pressure levels can be identified in the high frequency range, $>$ 2 kHz. The frequency range below 500 Hz is dominated by the engine orders, which consist of the noise contributions of the engine, intake and exhaust system [3]. Typical firing or engine orders have their origin in the periodic combustion process of the engine. Due to the aspiration of air and blow-out of exhaust gas, high sound pressure levels at the frequency of the firing orders occur also at the intake and exhaust system. The exhaust orifice noise contributes significantly to overall vehicle pass-by noise, especially in the frequency range dominated by the firing orders [90]. Depending upon the vehicle position, the contribution of each noise source varies. The exhaust orifice noise is dominant when the vehicle has passed the microphone position. When the vehicle approaches the microphone, exhaust orifice noise is shielded by the vehicle body. The situation is similar for engine and intake system radiated noise when the vehicle is in the second half of the acceleration area. Since only information about the current measurement time is given in Fig. 2.7, it is not possible to relate any of the sound pressure spectra directly to the vehicle position on the test track, which would have given a better understanding of the local radiation characteristic of noise sources.

Similar conclusions are obtained from the analysis of ISO 362 pass-by noise tests in Refs. [67, 36]. It is concluded that the vehicle noise sources are significantly influenced by engine speed. In general, it appears that the higher the vehicle or engine speed the higher is the radiated sound. Therefore, the highest sound emission occurs at the highest engine speed. However, the highest engine speed is reached at the end of the acceleration area when the distance between the vehicle noise sources and the microphone is greater. In this case, the radiated sound is attenuated through distance, and the recorded sound pressure at the microphone location is less than sound pressure closer to the source. Consequently, the pass-by noise level is dependent on the sound radiation of the noise sources and the distance between the noise sources and the microphone. Thus, the highest pass-by noise level occurs when the combination of sound radiation and distance are most favourable. Furthermore, the shielding of the noise source and the angle

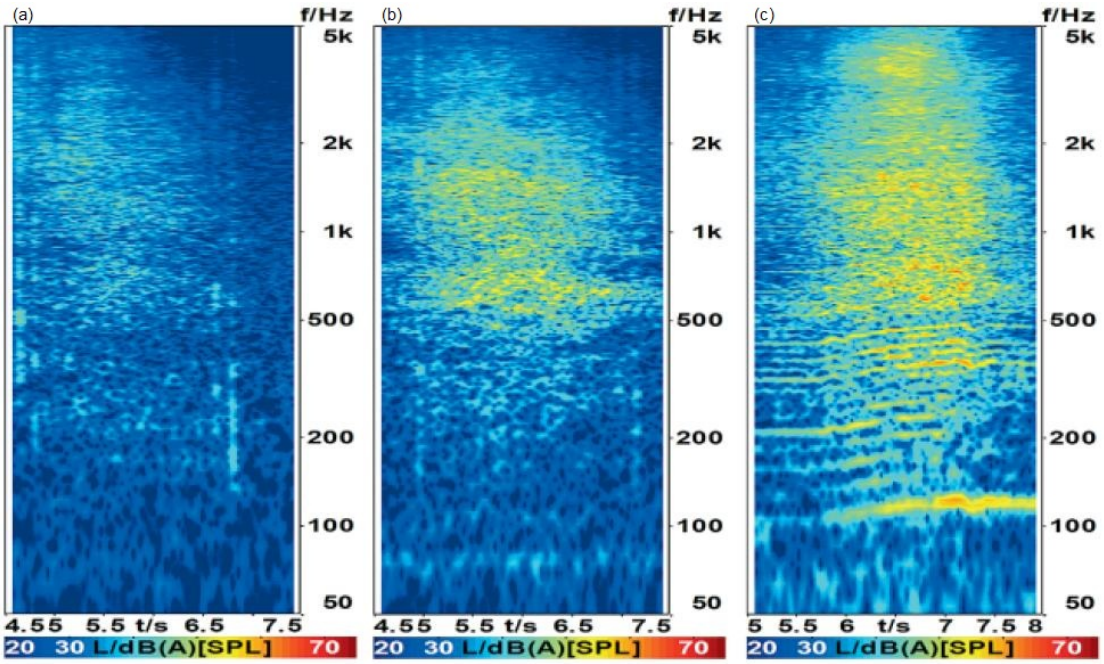

Figure 2.7: Colourmap plots of different pass-by noise tests: (a) engine switched off and slick tyres; (b) engine switched off with standard tyres; (c) ISO 362 test [3] (reprinted from Alt N, Wolff K, Eisele G, Pichot F. Fahrzeugaussengeräuschsimulation (Vehicle exterior noise simulation). Automobiltechnische Zeitschrift 2006; 108:832 – 36. With kind permission of Dr Alt.).

between sound radiation direction of the noise source and the receiver microphone is decisive for the detection of the noise source emission quantity at the receiver position

2.1.3 Ranking of vehicle noise sources

Noise isolated vehicles are designed for the identification of noise source characteristics and for the determination of noise source rankings. Different types of noise isolated vehicles have been developed which has been reported in Refs. [6, 4, 7, 57]. In general, the windowing or shielding technique is applied on the vehicle in order to isolate the major noise sources. Usually, the engine is encapsulated with absorption material according to Refs. [6, 7, 5]. The intake and exhaust system noise is attenuated by mufflers with high volumes, which are attached to their orifices [6, 7, 5]. The tyres are either encapsulated with absorption material to minimise their sound radiation [6] or replaced with slick tyres [5]. Each noise source is unmasked in turn, and the pass-by noise levels of each source are recorded [6, 5, 43]. In addition, the pass-by noise of the completely unshielded vehicle is measured in order to determine the overall pass-by noise level and, then, to analyse the relative contribution of each noise source. Such a vehicle could also be applied in indoor

pass-by noise experiments. A guideline for the application of shielding techniques on a vehicle is given in Ref. [43].

The relative contributions of the noise sources to the overall pass-by noise level vary in Fig. 2.8, which is determined experimentally with a noise isolated vehicle of the medium class in second gear. The engine noise level contributes most to the overall pass-by noise level. It increases approximately linearly until the vehicle front is 1 m away from the microphone line. Then, the sound pressure level remains almost constant, until it starts decreasing when the front of the vehicle is at the 16 m mark. Tyre/road noise is the second largest contributor. Its noise level increases until the front of the vehicle reaches the 13 m mark, it then decreases. The different inclinations of the tyre/road noise level of the approaching and receding vehicle indicate different noise radiation characteristics from the front and the rear tyre/road combinations. The maximum tyre/road noise level occurs when the rear axle is approximately in line with the microphones, which is probably due to a simultaneous contribution of the front and the rear tyres. Since the gradient of the tyre/road noise level of the receding vehicle is not as steep as of the approaching vehicle, the sound radiation of the tyres at the rear axle must be higher than at the front axle. Exhaust orifice noise has a very low impact when the vehicle is in the first half of the test track. After passing the microphone position, the noise level increases significantly until the vehicle leaves the test track area, since the noise can radiate freely from the tailpipe to the microphone.

Experiments are conducted on a high performance sports vehicle in Ref. [5], in which the noise sources are unmasked in turn, thus, showing the dominance of intake noise in the first half of the test track. In the second half of the test track, the exhaust system is the dominant noise source. Therefore, it appears that the relative contributions of the intake and the exhaust system are interchanged for the first and second half of the test track. Engine and transmission noise are of minor importance. If pass-by noise has to be reduced, measures should be implemented on the most dominant noise sources first [5, 34]. Experiments with a noise isolated sporting saloon vehicle show that the relative noise levels of each noise source depend upon the position of the vehicle on the test track. At the beginning of the test track, the intake system noise is dominant on the right-hand side microphone. The powertrain noise is highest in the middle of the test track, when the distance of the vehicle to the microphone is the shortest. At the end of the test track, the exhaust orifice noise is dominant on the left-hand side microphone [5]. Presumably, the intake orifice is installed on the right-hand side of the vehicle, the exhaust orifice is on the left-hand side. The overall pass-by noise level in third gear is much lower than in second gear, because the relative contributions of the engine, the intake and the exhaust system noise are less. This

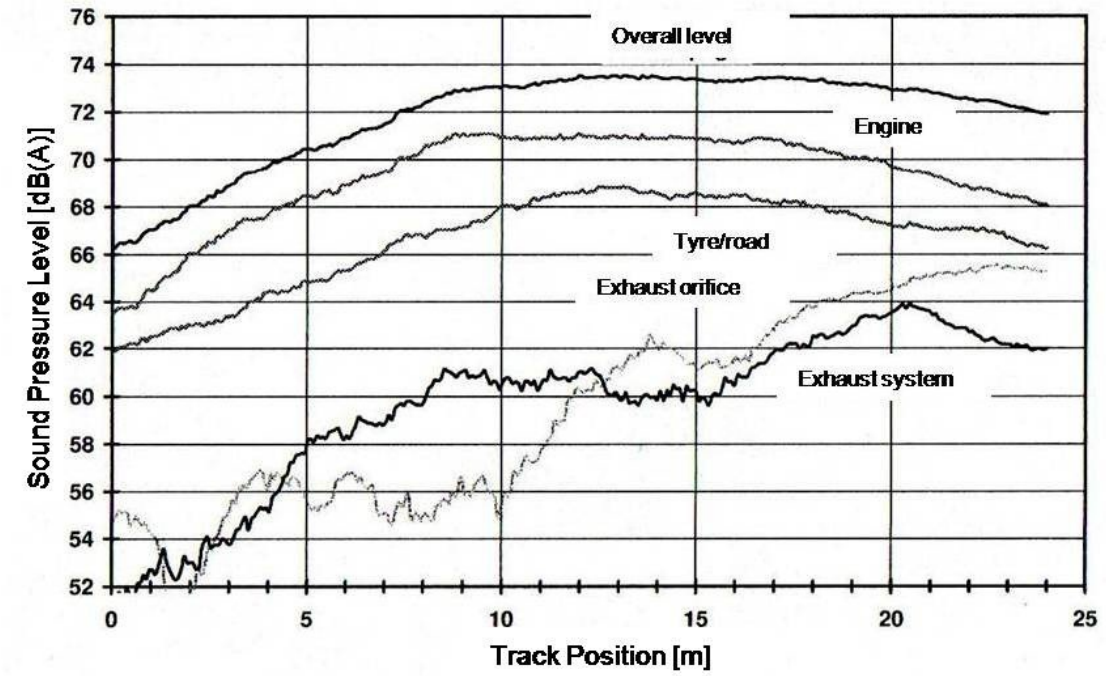

Figure 2.8: Individual noise source contributions to the overall pass-by noise level [6] (reprinted from Biermann J-W. Geräuschverhalten von Kraftfahrzeugen (Noise characteristics of vehicles). Lecture notes. With kind permission of Prof Biermann.).

results in a relatively higher contribution from the tyre/road system in comparison to the other noise sources [5].

A different noise source ranking for the vehicle pass-by noise test can be found in other references. Fig. 2.9 [38] presents a ranking of the noise sources with the highest contributions to pass-by noise in the following order: tyres, exhaust system, intake system and engine. It can be assumed that each vehicle type has its specific design characteristics which leads to a different order in the rankings across different vehicle types. Information about the method with which the results are achieved are not given in Ref. [38]. However, it is assumed that the noise levels in Fig. 2.9 are determined in conjunction with ISO 362. Both Figs. 2.8 and 2.9 provide a reasonable qualitative idea of relative noise source contributions and ranking. After establishing a noise source ranking, it is important to analyse the spectral content of each noise source in order to gain full understanding and, hence, to be capable to reduce pass-by noise [5].

Nearfield Acoustic Holography (NAH) is applied to create Fig. 2.10, which illustrates the distribution of the sound pressure level in the 1000 Hz one-third octave band. Since a stationary signal is required to carry out NAH, the four-wheel-drive vehicle is set up on a chassis dynamometer in a semi-anechoic chamber and driven at a constant speed of 56 k.p.h., which was found to be the condition

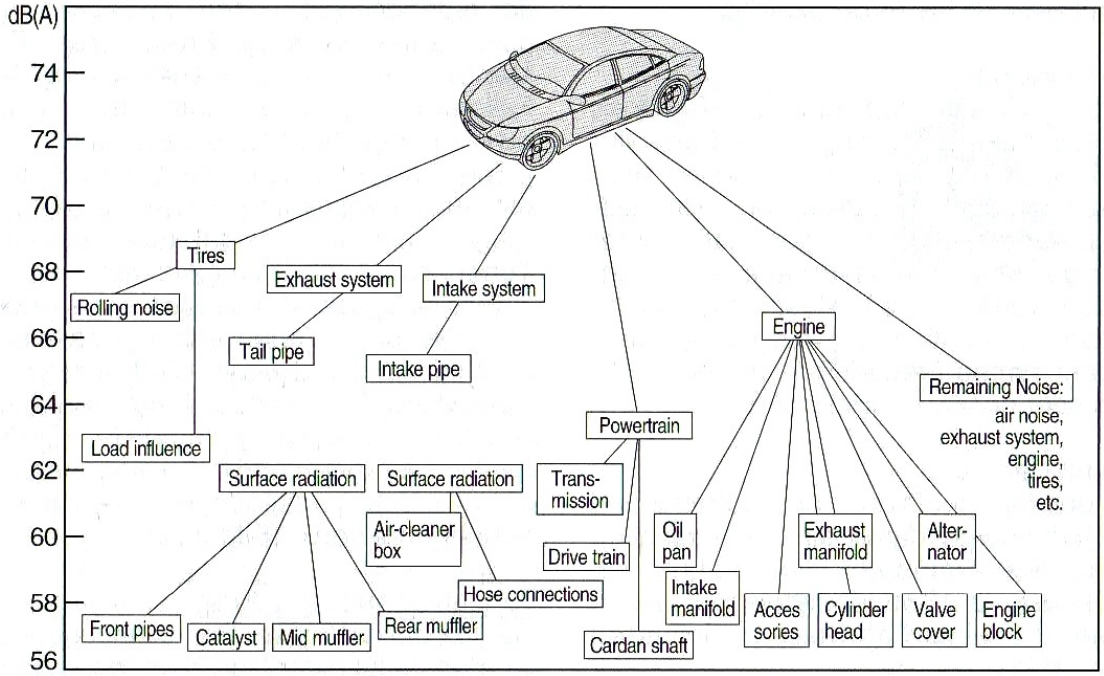

Figure 2.9: Noise source ranking for a vehicle during the pass-by noise test [38] (reprinted from Bosch - Kraftfahrtechnisches Taschenbuch (Automotive Handbook). 25th ed. Wiesbaden: Vieweg+Teubner; 2004. With kind permission of Robert Bosch GmbH).

with the highest noise emission [4]. A microphone array measures sound pressure at a distance of approximately 0.2 m from the side of the vehicle. The measurement plane is subdivided into several noise source areas, which can be ranked according to their highest noise emission [4]. Sound radiation is clearly visible at the exhaust tailpipe and around the tyres. The area between the front and the rear axle shows high sound radiation as well, which is related to the exhaust system [4]. However, it has to be considered that sound radiation due to the horn effect of the tyres can increase the noise level in that area as well. Presumably, the engine and the gearbox also contribute to the sound pressure level around the front tyre, since the sound radiation is less in the area of the rear tyre. NAH seems to be a valuable technique in order to visualise sound radiation during the pass-by noise test. Although no ISO-approved test track surface is used (only the chassis dynamometer), a pass-by noise level is calculated for the ISO 362 microphone position, which only deviates 0.2 dB from the measured pass-by noise level on the test track [4].

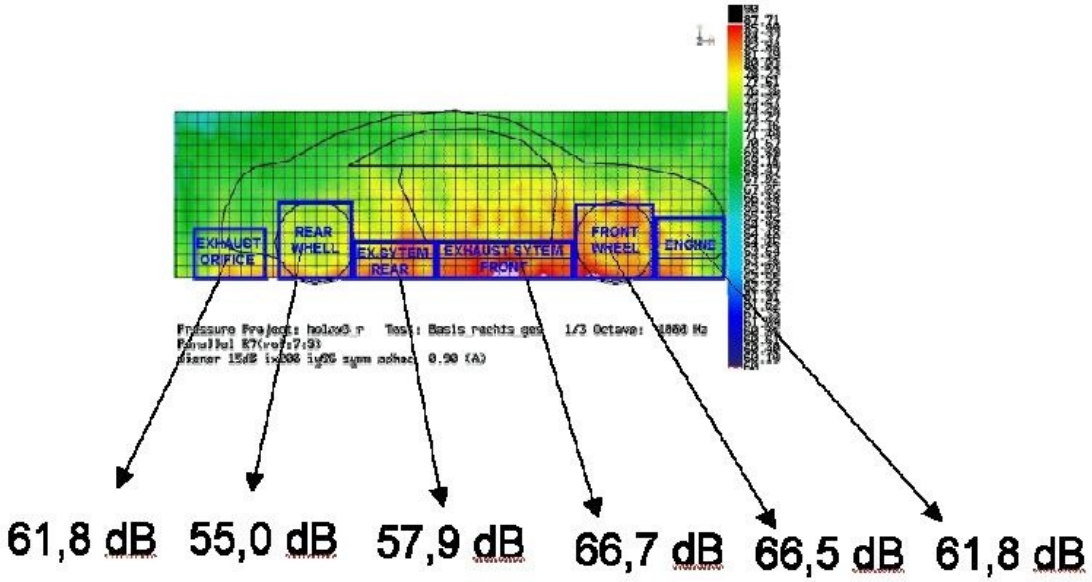

Figure 2.10: Analysis of a stationary indoor pass-by noise test by means of Nearfield Acoustic Holography [4] (reprinted from Arndt R, Fliesser W, Rein D, Fankhauser C. Analysis of pass-by noise using Nearfield Acoustic Holography. Copyright Virtual Vehicle Research Center. With kind permission of DEGA e.V. (German Acoustical Society) and Mr Arndt.).

2.2 Vehicle noise source characteristics and their influence on pass-by noise

Details about each of the major noise sources including the engine, intake system, exhaust system and tyre/road system are given in this section. Their stand-alone characteristics are described as well as the noise emission from each noise source within the vehicle system in the ISO 362 pass-by noise test.

2.2.1 Engine

Diesel engines usually emit higher noise levels than petrol engines at the same engine speeds [6], which is caused by the higher in-cylinder pressure excitations [68]. The higher the engine speed, the higher are the noise emissions. At its highest rotational speed, the petrol engine reaches the same noise level as that of Diesel engines[6]. Radiated engine noise depends on the in-cylinder pressure characteristics during the combustion process as well as the mechanically and flow induced noise[68]. The noise from the bottom of the engine can contribute significantly to the overall noise radiation[67].

An engine noise map is presented in Fig. 2.11 [6] in which the radiated sound pressure level of an engine is plotted versus torque and rotational speed. In general, sound pressure level increases with rising engine speed. Sound pressure level

increases with rising torque only at low engine speeds and remains relatively constant at higher engine speed. An accelerated pass-by in second gear covers an engine speed range between 3000 r.p.m. and 4500 r.p.m., and between 2000 r.p.m. and 3000 r.p.m. in third gear [67]. Considering the range of engine speeds in the pass-by noise test, it is possible to estimate the radiated sound pressure levels from the engine during the pass-by noise test. However, differences in radiation on each side of the engine as well as the attenuation properties of the vehicle body have to be taken into account.

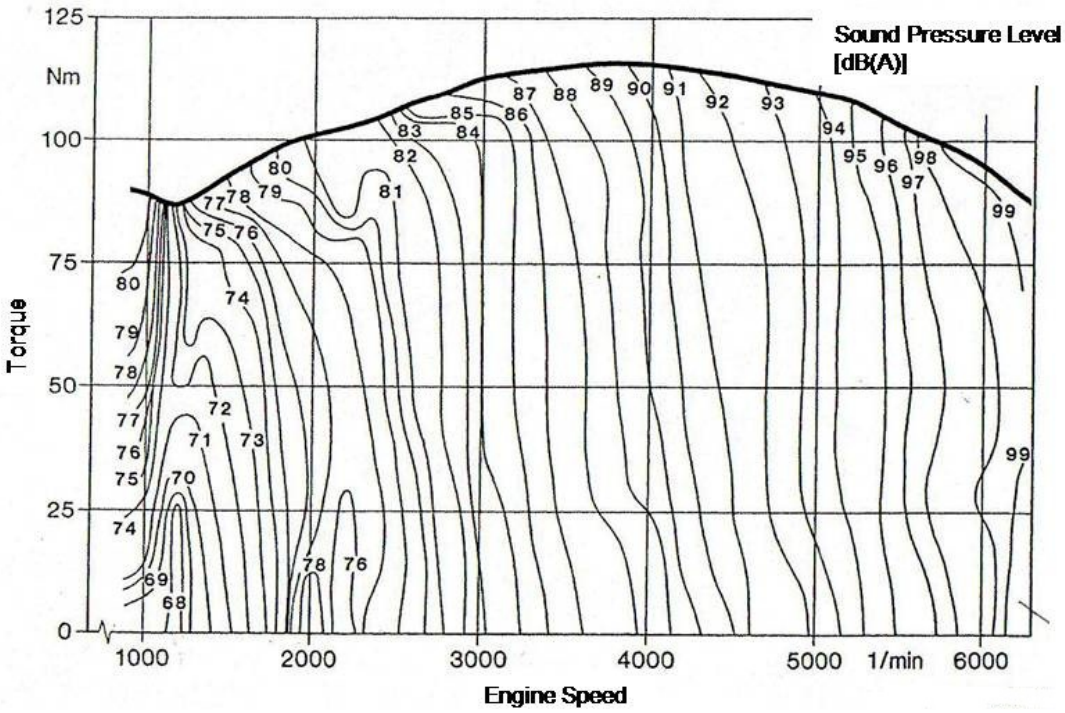

Figure 2.11: Engine noise map of sound pressure level versus torque and rotational speed [6] (reprinted from Biermann J-W. Geräuschverhalten von Kraftfahrzeugen (Noise characteristics of vehicles). Lecture notes. With kind permission of Prof Biermann.).

Figs. 2.12 and 2.13 [65] illustrate the noise emission of an engine mounted on the front of the vehicle, which visualises the sound radiation of the engine in the pass-by noise test. Both figures are the result of the application of moving frame acoustic holography (MFAH) on a pass-by noise test under ISO 362 conditions. Therefore, a microphone array is positioned very close to the passing vehicle midway on the test track. The measurement duration is less than half a second, since this method requires a quasi-stationary condition, i.e. the vehicle speed is assumed to be constant and frequency changes are neglected. The sound pressure distribution in the measurement plane for the second (120 Hz) and third (180 Hz) harmonic of the firing frequency, respectively, are shown in Figs. 2.12 and 2.13. All noise sources besides the engine are noise isolated. The sound from

the engine radiates from underneath the vehicle into the environment. It can be assumed that the vehicle body causes reflections and diffractions. It also shields the directly radiated engine noise from the engine compartment, since there is no visible sound radiation from the vehicle body region in Figs. 2.12 and 2.13. Moving source beamforming appears to be a suitable tool for the visualisation of noise emissions of moving vehicles as well [37]. However, detailed work about the application for the analysis of pass-by noise source characteristics has not been published.

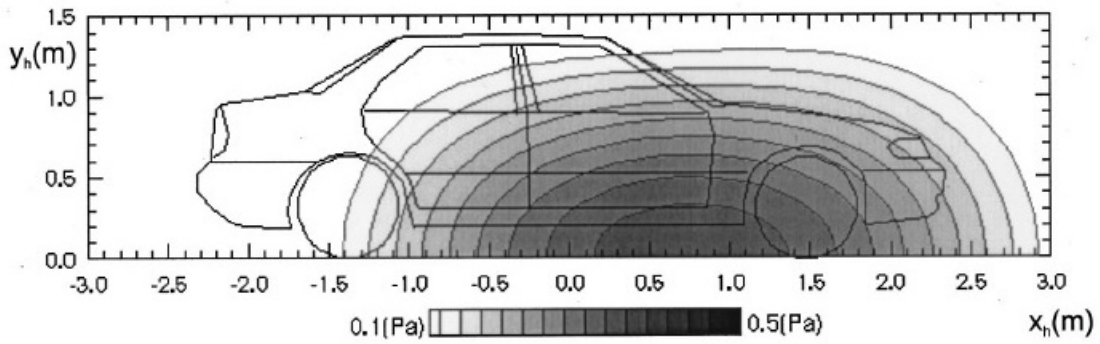

Figure 2.12: Engine noise distribution on measurement plane at 120 Hz [65] (reprinted with permission from Park S-H, Kim Y-H. Visualization of pass-by noise by means of moving frame acoustic holography. J Acoust Soc Am, vol. 110 p. 2326 – 39 (2001). Copyright 2001, Acoustical Society of America. With kind permission of Prof Kim.).

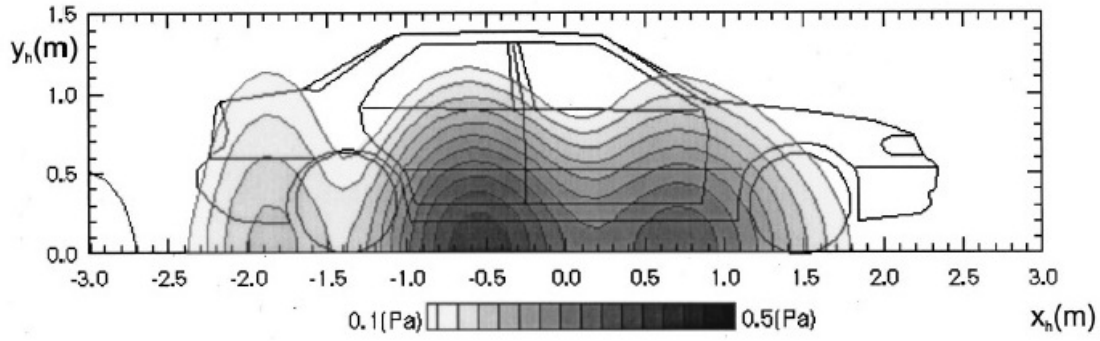

Figure 2.13: Engine noise distribution on measurement plane at 180 Hz [65] (reprinted with permission from Park S-H, Kim Y-H. Visualization of pass-by noise by means of moving frame acoustic holography. J Acoust Soc Am, vol. 110 p. 2326 – 39 (2001). Copyright 2001, Acoustical Society of America. With kind permission of Prof Kim.).

2.2.2 Intake and exhaust system noise

The intake and exhaust systems represent noise sources of similar characteristics, which contribute significantly to vehicle exterior noise. A brief historical overview

is given in Ref. [43]. Until the 1960s, the dominant noise source for vehicle exterior noise was exhaust tailpipe noise. Due to noise limiting legislation and the introduction of large volume mufflers, noise levels were reduced in the following years. This unmasked intake system noise, which was the most significant noise source at full load from around 1980 onwards. Port fuel injection technology and the application of plastic intake manifold, instead of steel, in combination with silencing elements have lowered intake system noise. Today, the overall noise of the intake and exhaust system is on a similar level in comparison to the engine and tyre/road noise. However, intake and exhaust system noise contributes significantly, if the engine runs under high load [89]. Sports cars present an exception with the exhaust system noise being up to 20 dB higher than the intake system noise under full load conditions, which is to sharpen the subjective perception of the vehicle [90]. Nonetheless, these noise emissions have to comply with current legislations.

Intake and exhaust system noise can be subdivided in primary and secondary noise sources [43]. Primary noise sources are pressure pulses, which are caused by the opening and closing events of the engine valves. The pressure pulses advance through the intake and exhaust system to the orifices, where they radiate as noise into the environment. Since the valve motion is related to the engine combustion rate and engine speed, intake and exhaust system noise occurs at the engine firing frequency and its multiples depending on the specific design [89]. The mass flow moving inside the intake and exhaust system is considered to be the secondary noise source. The so-called flow noise is caused by turbulence and vortices of the high speed mass flow around sharp edges, small bends and free jets [89]. The opinions about its characteristic are different. In Ref. [89], flow noise is described as of a broadband character between 1 kHz and 3 kHz. In contrast, it is described as of a rather tonal character with low and high frequency components in Ref. [43].

Shell noise can be seen as another noise source, but it hardly contributes to pass-by noise nowadays. Large plane surfaces, for example, the air filter box, manifolds, and mufflers, are likely to radiate shell noise, which can be caused by the pressure pulses and the flow noise as well as the vibrations from the engine and powertrain. Countermeasures are to increase the stiffness of the structure with ribbing, pressed muffler shells, or two layers of thin sheet-steel walls in order to shift the eigenfrequency of a particular structure above the main excitation frequency [89]. According to Ref. [67], the exhaust muffler surface can contribute occasionally to pass-by noise.

Both, intake and exhaust systems can be tuned to either attenuate or emphasise specific frequency content. The radiated noise at the orifices is dependent

upon the acoustic properties of the ducts, and the reactive and resistive mufflers. Uneven pipe lengths from different cylinder banks and uneven firing sequences result in the generation of half engine orders. Reactive mufflers are expansion chambers, quarter-wave and Helmholtz resonators. They initiate reflections of the moving pressure wave in order to change its phase and, thus, use phase cancellation as an attenuation measure [89]. It is assumed that the compressor housing of a turbocharger acts like a reactive silencer element being able to reduce intake noise [43]. Ref. [90] reports that high turbulence in the compressor attenuates predominantly the sound pressure amplitudes of the engine orders. However, the compressor and the turbine are also noise sources. Stall on the blades causes broadband noise at $1-4\,\mathrm{kHz}$; imbalance of the turbocharger shaft and pressure pulses within the turbocharger creates tonal noise, which is known as whining noise; the rotational noise of the compressor and turbine blades occurs between $4-14\,\mathrm{kHz}$ due to pressure differences on the intake and exhaust side, and is known as whistling' noise [90, 69]. The generated noise is radiated from the turbocharger housing or transmitted to the adjacent parts of the intake and exhaust systems. Additional reactive measures may be necessary, for example, an air intercooler can function as a broadband attenuator [90]. Resistive mufflers filled with absorption material like fibreglass or mineral wool decrease the wave amplitudes through absorption. They are predominantly applied in the exhaust system to lower broadband noise; in general, they are more effective in the high frequency range [89]. The air filter box of the intake system can be designed as a resistive muffler. The acoustic performance of resistive mufflers increases with the adequate absorber density. This should not result in higher weight, which is not desired in terms of costs and fuel consumption. It is usually attempted to avoid any measure resulting in higher back-pressure in the exhaust system, since this leads to reduced engine power. A reduction of flow noise can be achieved by decreasing the flow velocity which can be realised through the application of large diameter pipes instead of small diameter pipes, and by the avoidance of sharp edges and bends, which, thus, provides smoother flow conditions [89].

The frequency spectrum of intake orifice features the excitation of primary and secondary noise sources, as shown in Fig. 2.14 [90]. High sound pressure levels due to the engine orders can be identified as well as flow noise, which affects almost the whole engine speed range. It appears that a broad frequency band above 400 Hz is excited by flow noise, with frequency ranges around 450 Hz, 600 Hz and 820 Hz having the highest amplitudes.

The noise characteristic or perceived sound quality of the exhaust system affects the recognition of a vehicle by customers [89]. Therefore, target values are agreed very early in the development process of a vehicle. Additionally, exterior

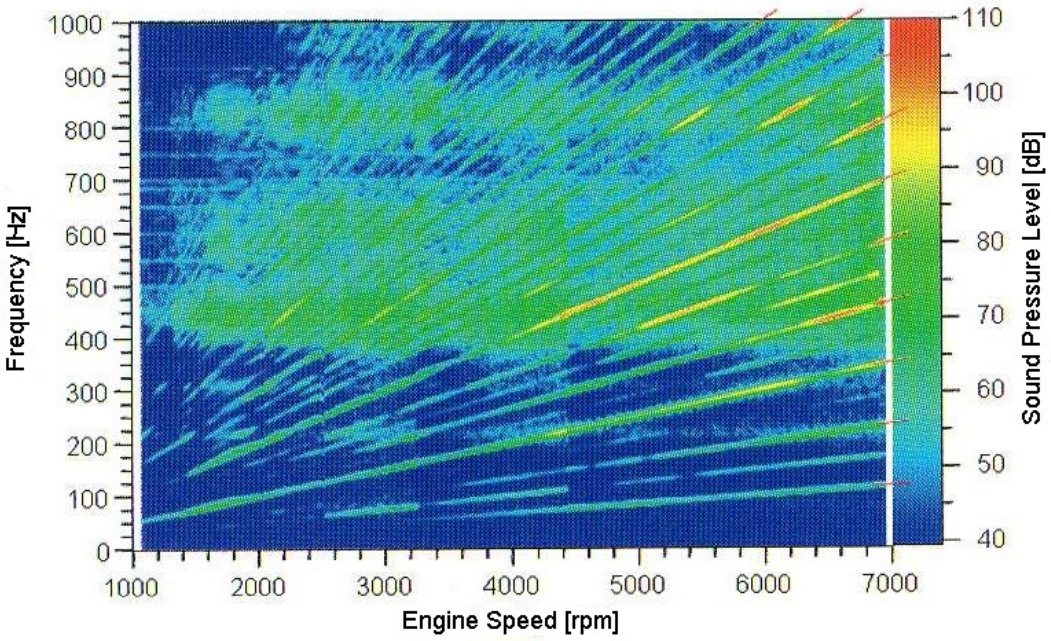

Figure 2.14: Sound pressure level of intake orifice noise versus engine speed and frequency [90] (reprinted from Zeller P. Handbuch Fahrzeugakustik (Handbook Vehicle Acoustic). Vieweg + Teubner Verlag; 2009. With kind permission of Springer Science and Business Media.).

noise regulations regarding idle and pass-by noise have to be adhered to, which can potentially counteract with powertrain performance requirements[89]. In contrast to the intake system, the flow in the exhaust system is considered to be much more influential due to the higher flow speed [43]. In addition, temperature gradients are much higher, and back-pressure has a greater impact on engine performance than wave motion in the manifold[43]. Flow noise is normally amplified in the complex structure of a silencer [20].

Typical exhaust tailpipe noise emissions are shown in the waterfall plot of Fig. 2.15a. The second engine order dominates up to about 3500 r.p.m. as it can be seen in the diagram with the unweighted Decibel scale. Flow-induced noise can be detected at higher engine speeds over a broad frequency range. According to Ref. [45], flow noise has a decisive influence on the overall sound pressure level of the exhaust orifice. Considering the engine speed range from approximately 3000 r.p.m. to 4500 r.p.m. in second gear [67], flow noise can contribute significantly to the pass-by noise level.

The results of a one-dimensional Computational Fluid Dynamics (1D CFD) simulation, which is valid for frequencies below 1 kHz [45], shows good agreement regarding engine orders between the measured and simulated data. However, flow noise is not taken into account, which represents a weakness of the simulation.

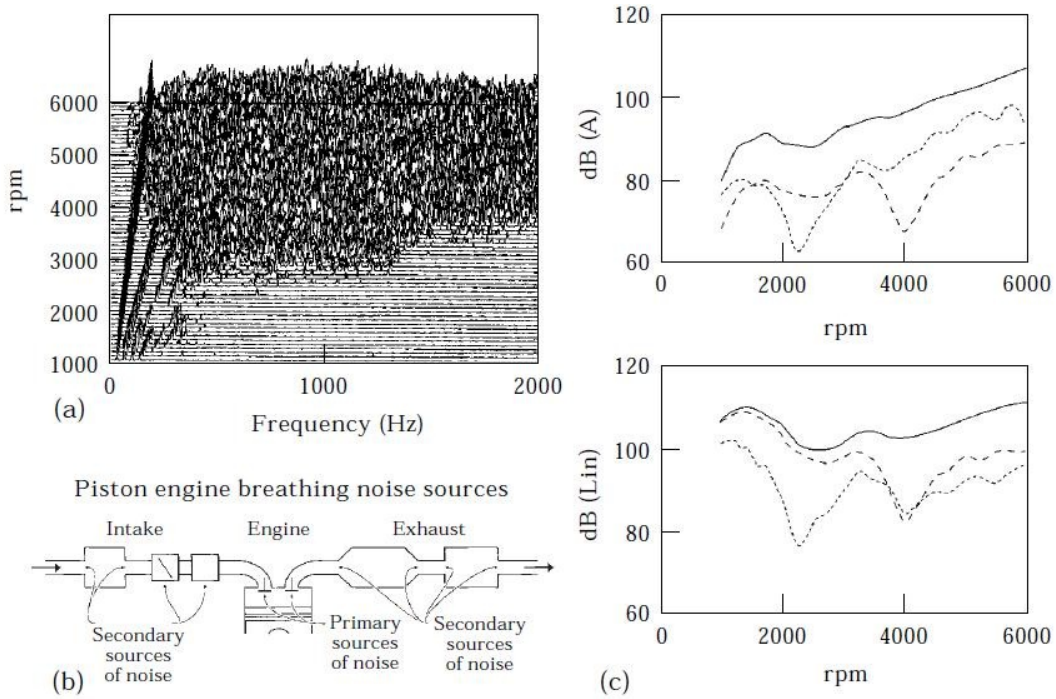

Figure 2.15: Exhaust tailpipe emissions from a 4-cylinder 4-stroke engine: (a) Campbell diagram; (b) system schematic; c) A-weighted and unweighted dB spectra measured at 0.25 m and 45° from the orifice (—overall; ——2nd order; . . . 4th order) [21] (reprinted from Davies P, Holland K. I.C. engine intake and exhaust noise assessment. J Sound Vibr 1999; 223:425 – 44. With kind permission of Elesevier Ltd.).

Current commercial software products offer a method to estimate the sound power level caused by flow noise at the exhaust orifice [35]. The applied flow noise model uses atmosheric pressure, exhaust gas temperature and velocity at the exit as well as the pipe diameter of the exhaust orifice [35]. The model needs to be calibrated and cannot calculate flow noise at specific frequencies [35]. If 1D CFD simulation is to be used for pass-by noise prediction, flow noise, reflections from the vehicle and ground, as well as the instantaneous distance between the source and receiver will also need to be considered.

To determine the measurement results shown in Figs. 2.16 to 2.18, an engine is set up in a sound-proofed chamber and the exhaust pipes are led outside [2]. The exhaust orifice is about 3 m away from the wall and 1.8 m above ground [2], which means that sound is radiated into relatively free space and reflections are negligible. Fig. 2.16 shows that the sound pressure levels at the exhaust orifice are higher under full load condition than under the no load condition. The sound pressure levels in the low to mid-engine speed range are reduced significantly through the application of A-weighting. In the high engine speed range, the difference between linear and A-weighted sound pressure levels remains rather constant.

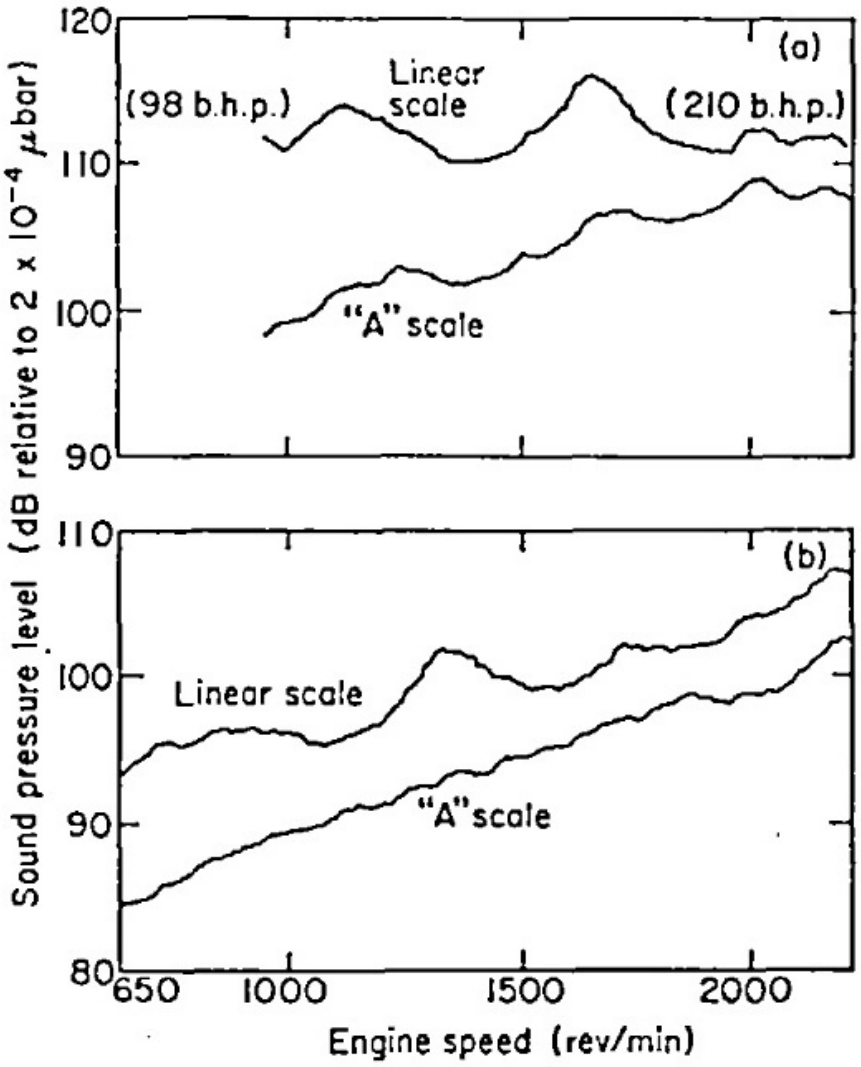

Figure 2.16: Variation of exhaust noise with engine speed: (a) full load; (b) no load [2] (reprinted from Alfredson R, Davies P. The radiation of sound from an engine exhaust. J Sound Vibr 1970; 13:389−408. With kind permission of Elsevier Ltd.).

Fig. 2.17 presents a typical frequency spectrum of exhaust noise at 1880 r.p.m.. The high sound pressure levels in the frequency range up to 1000 Hz dominate the noise spectrum. High sound pressure amplitudes can be identified at discrete frequency components, which are multiples of the firing frequency. This shows that exhaust noise in the low frequency range is mainly caused by the combustion cycle of the engine, and the contribution from flow noise is marginal in this case [2].

The radiated sound characteristics of an exhaust tailpipe are measured and presented in two scenarios in Fig. 2.18 [2]: Fig. 2.18a illustrates the sound pressure level on ±135° circular arc around the orifice at 0.9 m distance and Fig. 2.18b along a radial path at an angle of 45° to the tailpipe. The relative change in sound

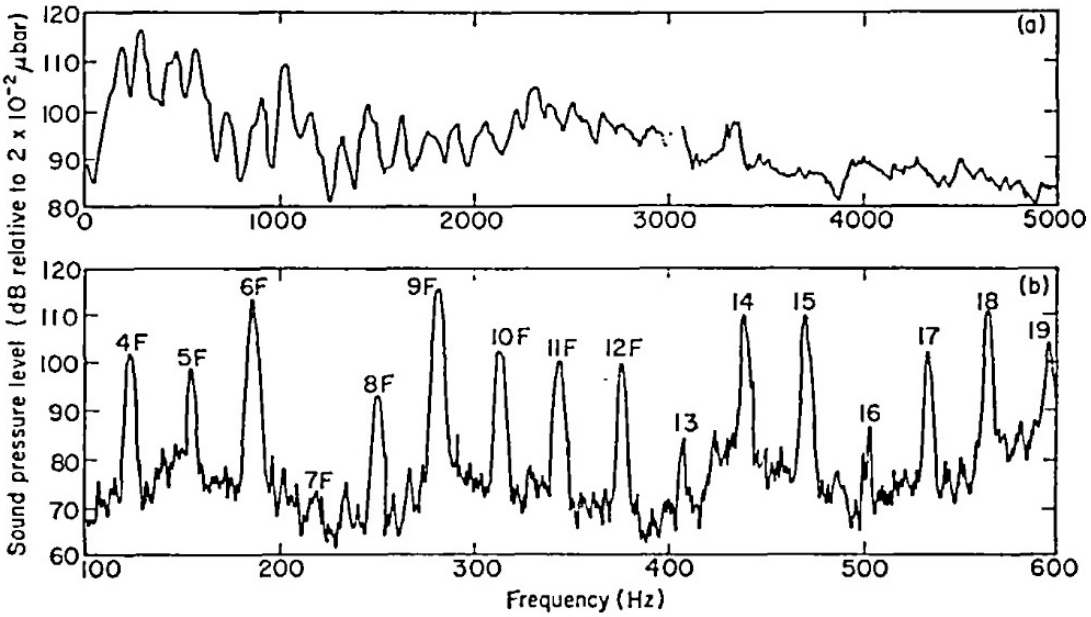

Figure 2.17: Typical frequency spectrum of exhaust noise measured at 1880 r.p.m. and 0.9 m from the outlet: (a) $0 - 5000$ Hz; (b) $100 - 600$ Hz [2] (reprinted from Alfredson R, Davies P. The radiation of sound from an engine exhaust. J Sound Vibr 1970; 13:389 – 408. With kind permission of Elsevier Ltd.).

pressure level is plotted against angular position (Fig. 2.18a) or distance from the outlet (Fig. 2.18b) for two non-dimensional frequencies, ka, where k is the wave number and a is the pipe radius. In circular ducts, higher-order modes are cut-off for values of $ka < 1.84$ [63]. The two ka values of 0.15 and 0.7 are well below this limit and, hence, it is assumed that plane wave propagation occurs in the duct and that the influence of higher-order modes is assumed negligible. In Fig. 2.18a, the sound pressure level varies significantly depending upon the angle on the arc. For $ka = 0.15$, the relative sound pressure level has a rather smooth characteristic. However, its amplitudes are higher in front of the tailpipe, i.e. 0°, and decrease towards the larger angles. Sound pressure increases again after the +90° mark. For −90° to −135°, the sound pressure level is approximately constant. For the non-dimensional frequency $ka = 0.7$, the relative sound pressure level has rather small amplitude fluctuations in the region ±25°. In the region +25° to +135°, high amplitude fluctuations up to 6 dB occur, whereas the relative sound pressure level remains approximately constant in the region −90° to −135°. Different characteristics between +90° and +135° and −90° to −135° can be identified in both ka plots. Certain level variations exist, but for the thorough analysis of the directivity pattern of exhaust orifice noise more measurement data are required from several distances around the orifice. In Ref. [2], a spherically diverging sound wave from the orifice is assumed. In Fig. 2.18b, the trace of radiated sound pressure is in conformity with the inverse square law of acoustics. Although

fluctuations appear again for the $ka = 0.7$ plot, the trend follows the theoretical decline of sound pressure. The fluctuations in relative sound pressure level are higher for $ka = 0.7$ in both measurement scenarios. These fluctuations may be caused by turbulent activity in the exhaust gas flow. The effect of evanescent modes at the end of the exhaust may become noticeable for $ka = 0.7$ causing increased sound pressure fluctuations.

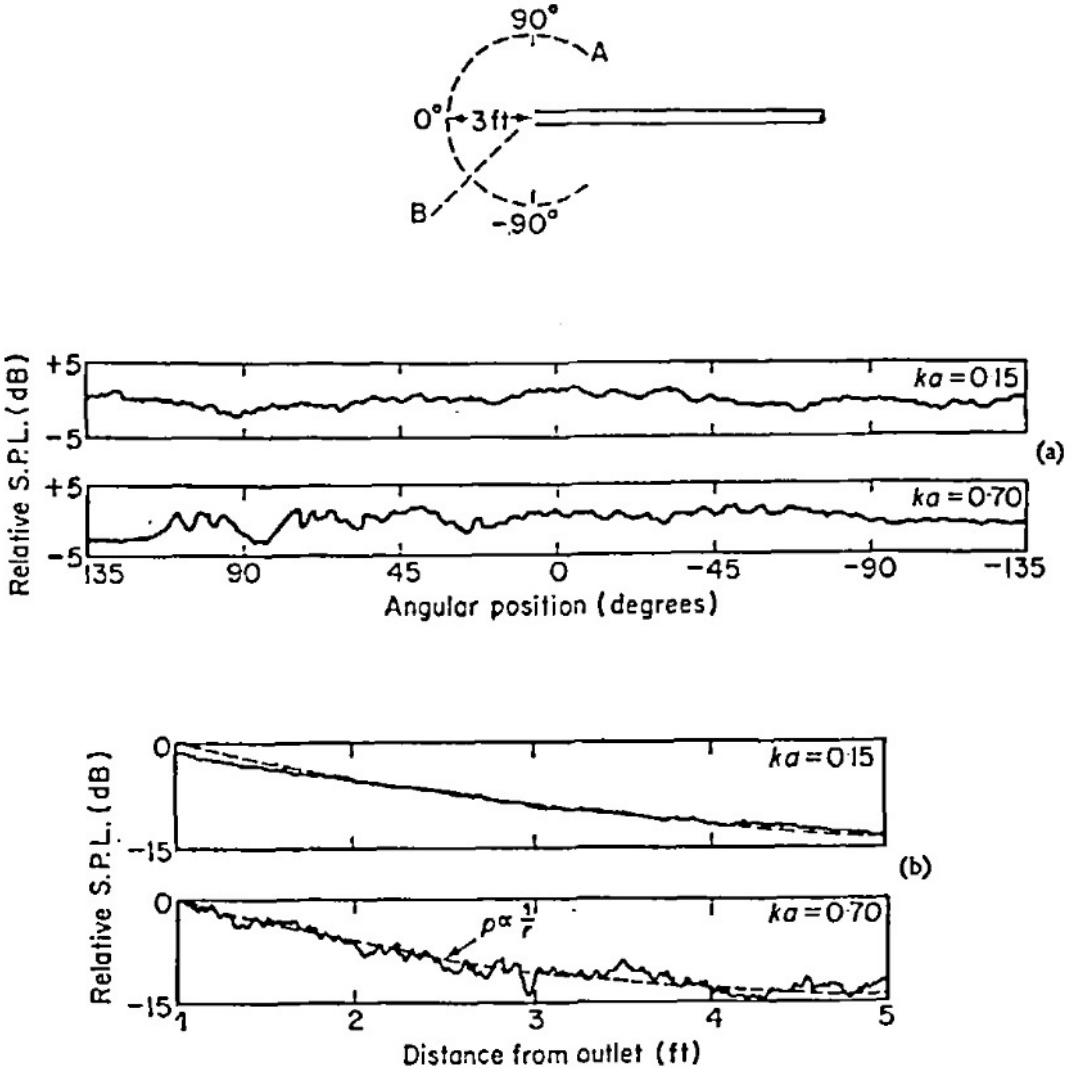

Figure 2.18: Radiated sound characteristics of an exhaust orifice: (a) directivity patterns along circular path A; (b) relation of sound pressure level to distance along radial path B [2] (reprinted from Alfredson R, Davies P. The radiation of sound from an engine exhaust. J Sound Vibr 1970; 13:389 − 408. With kind permission of Elsevier Ltd.).

It can be summarised that exhaust orifice noise is dependent on engine speed, load and the design of the exhaust system, since the exhaust system consists of several noise sources itself when gas flows through its pipes with different size of cross sections, as shown in Fig. 2.15. Exhaust orifice noise appears to radiate

sound in a spherical direction according to the inverse square law. The frequency range of interest is up to approximately 1 kHz.

Noise from the exhaust tailpipe orifice is one of the main contributors to overall pass-by noise. The exhaust orifice noise or jet noise is caused through the mixing of ambient air and exhaust gas flowing out of the exhaust orifice with high velocity [1]. The exhaust gas jet consists of the potential core region and the turbulent mixing region of the exhaust gas and ambient air. High frequency noise with a high sound pressure level is generated by small vortices; larger vortices cause lower frequency noise with a lower sound pressure level. The frequency spectrum of jet noise is characterised by a broad-band random noise. The exhaust jet flows of two different types of silencers are analysed in Ref. [1]. The shape of the jet flow and its velocity profile are influenced by the structure of the tailpipe, for example, sintered or solid metal [1]. The velocity profile of a sintered metal tube is not as wide as of a conventional exhaust tube due to the different friction properties between the gas and the pipe wall as well as the gas permeability including a heat loss through the sintered metal tube [1]. The width of the jet flow depends upon the engine speed, for example, the higher is the engine speed the wider is the jet flow [1]. It is assumed that a smaller jet width provides a smaller turbulent mixing region and, thus, a reduced noise radiation.

The flow pattern downstream of a pipe orifice and its related noise is experimentally investigated in Ref. [25]. In the experiment, compressed air is released into a pipe simulating the exhaust system. Schlieren pictures show a high pressure wave leaving the orifice, which can develop into a shock wave depending upon the speed of the exhaust valve. In order to analyse the far field, sound pressure measurements are conducted at a 1 m distance from the pipe orifice at angles of 15°, 30°, 45° and 60° to the extended pipe axis. For different low to high exhaust valve speeds, the highest sound pressure amplitude occurs at 30° followed by the angles of 15°, 45° and 60°, respectively.

Source models for the prediction of exhaust orifice noise in the vehicle pass-by noise test are developed in Ref. [33]. Based on experiments, two source models are implemented to cover exhaust discharge noise. The first point source model is located at the exhaust orifice and covers the pulsation noise component up to 500 Hz, i.e. pressure pulsations originating from the opening and closing of the exhaust valves. The second point source model is located at 2.5 times the orifice diameter downstream of the exhaust orifice and covers the jet noise component over 500 Hz. The predicted values show a good agreement with measured values for the departing vehicle, when the transfer path between the exhaust orifice and the pass-by microphone is not shielded by the vehicle body. When the vehicle approaches the pass-by microphone, deviations occur, which may be due to an

insufficient description of the noise source directivity, or the neglect of diffraction and reflection of sound from the vehicle body and the ground surface in the model.

2.2.3 Tyre/road noise

Tyre/road noise has not been reduced as much as powertrain and exhaust system noise over the recent decades [88]. Thus, it remains a significant contributor to overall pass-by noise. The generation mechanisms for tyre/road noise are complex but can roughly be divided into structure-borne and air-borne related mechanisms. Impact mechanisms, for example, the impact of the road surface pattern on the tyre surface, and adhesion mechanisms, for example the stick/slip effect between the tyre tread element and the road surface, are assumed to generate structure-borne noise. Air displacement mechanisms, for example, the pumping effect of air in pockets between the tyre tread and the road surface, are responsible for air-borne noise. The contribution of each mechanism to overall tyre/road noise varies depending upon the tyre type and size, the road and pavement construction and the vehicle operating condition [76]. Although the entire tyre radiates sound, the influence of the road structure must not be neglected. Tyre/road noise is a result of the interaction between the tyre and the road. The sources which mainly contribute to the overall A-weighted noise level are located close to the tyre contact patch at or in the vicinity of the leading and trailing edges and at the sidewall [76]. Amplification mechanisms like the horn effect, the effect of acoustical and mechanical impedances, and the different tyre resonances of structural and acoustical kind have an influence on the transfer of radiated tyre/road noise to a receiver [76]. The horn effect is considered to be the most influential among these mechanisms, and, thus, can have a decisive contribution to the pass-by noise level.

In Refs. [76, 55] the horn effect is analysed using two different experimental arrangements consisting of (1) a single tyre resting on the ground, and (2) the tyre being mounted on a vehicle. The geometrical boundary of the acoustical horn is defined by the leading or trailing edge of the tyre and the road surface. It is suspected that the acoustic impedance in the 'horn' and the ambient acoustic impedance correspond well and, thus, provide favourable conditions for the amplification of sound radiation [76]. In the experiment, a single tyre rests on the ground and a loudspeaker is positioned at 1 m distance to the tyre in line with the tyre plane. Conducting reciprocity measurements, an amplification of up to 23 dB is measured with a microphone at a distance of 10 mm off the contact patch edge of the tyre and the road is detected [55]. It is concluded that the horn effect is greatest at the location closest to the contact patch edge. The influence of the horn effect can be identified in the frequency range from $1 - 5$ kHz with a max-

imum amplification between $2-3\,\mathrm{kHz}$. The analysis of the angular properties of the horn effect shows that the sound radiation decreases when the receiver moved from the in-line plane of the tyre to a position perpendicular to the tyre plane. A coast-by situation of the tyre is simulated with the receiver position at 7.5 m distance and 1.2 m height to the centre of the tyre, which changes the angular acoustic properties [55]. The interaction between distance attenuation and horn effect leads to a maximum amplification between the angles of 45° and 75° off the tyre plane in the frequency range around 1000 Hz. This can have a high influence on pass-by noise, since the pass-by noise level is determined using frequency A-weighting. The horn effect of a tyre mounted on a vehicle is investigated using the previous measurement arrangement [55]. The overall amplification due to the horn effect at the receiver position is higher than without the vehicle body. Maximum amplification occurs again at angles between 45° and 75°. In particular, the low frequency range, less than 400 Hz, shows a significant increase. Sound reflections from the vehicle body and the ground contribute to the horn effect in a manner which does not occur in the single tyre experiments. The amplification differs by only 2 dB for angles between 45° and 90°. However, the amplification in the tyre plane is lower, which might be related to the screening effect of the vehicle body. It is concluded that a shorter distance between the noise source and the receiver in conjunction with the angles at which the influence of the screening effects of the vehicle body is the smallest provide the most favourable conditions for the highest contributions to vehicle pass-by noise [55].

Tyre/road noise radiation is not omni-directional because a certain directivity exists. The directivity pattern can be divided into horizontal and vertical directivity. Fig. 2.19 [76] represents an example of the horizontal directivity of tyre/road noise. The third-octave band frequency spectra of a standard tyre, which is tested on a dynamometer outer drum with a special replication of a road surface, is shown. The sound radiation of frequencies up to 1000 Hz occurs predominantly at the front of the tyre (0° or 360°) whereas higher frequencies ($1.5-8\,\mathrm{kHz}$) radiate mainly towards the rear (180°). In general, sound radiation at the front of the tyre is slightly higher than at the rear. The sound radiation in the lateral direction is rather small in comparison to the forward and aft directions. The sound radiation in the vertical direction is especially affected by the vehicle body. An indication about vertical directivity is given in Ref. [62]. Measurements are conducted on a public road with an average vehicle speed of 90 k.p.h. Sound pressure is recorded on the side of and above the road. The results indicate a constant level of sound radiation between the road and a vertical angle of 45°. The sound radiation declines by approximately 3 dB for higher vertical angles until it reaches a constant level for the vertical angle right above the vehicle, which is due to the screening

effect of the vehicle body. Both the horizontal and vertical directivity of tyre/road noise will have an influence on pass-by noise.

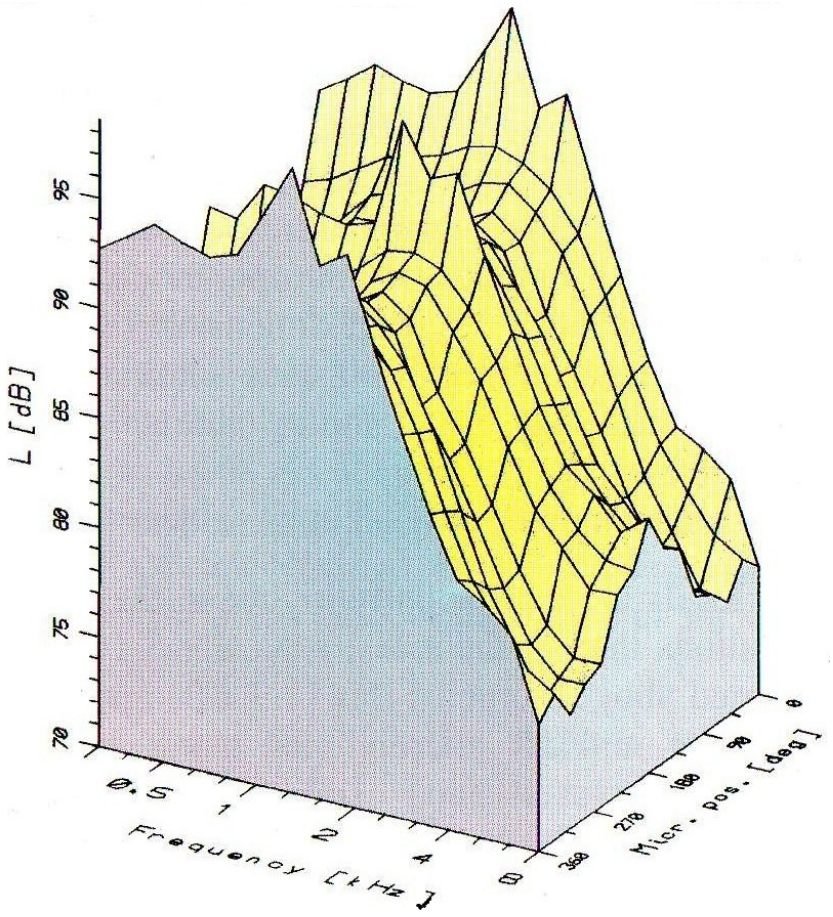

Figure 2.19: Horizontal directivity of the tyre/road noise of a single tyre measured on a dynamometer drum at a radius of approximately 0.4 m around the tyre [76] (reprinted from Sandberg U, Ejsmont JA. Tyre/road noise reference book. Kisa (Sweden): Informex; 2002. With kind permission of Informex HB.).

Due to the acceleration process in the vehicle pass-by noise test, the drive wheels experience high acceleration, torque and slip. Furthermore, a weight displacement towards the drive axle results in higher vertical loads on the drive wheels. The sound intensity level of a tyre/road system rises with increasing acceleration [76]. Increasing torque results in higher tyre/road noise at 30 k.p.h. [78]. Trailer measurements of a summer tyre on an asphalt concrete road show an increase in sound pressure level of about 20 dB(A) at a speed of 50 k.p.h., if the slip increases up to 10% [76]. The noise level remains constant for higher slip values [76]. A study [47] about the influence of vertical load on tyre/road noise finds increasing sound pressure levels for vertical loads up to 3000 N in the velocity range of $50 - 70$ k.p.h. For higher loads up to 5000 N, the sound pressure levels decrease slightly. However, an exception is the sound pressure level for 5000 N at 50 k.p.h., which is the maximum sound pressure level for that particular speed

value.

Vehicle deceleration can be used instead of acceleration in order to reproduce the contribution of torque to tyre/road noise. It is noted in Ref. [76] that there is no difference in the noise level for an accelerated or a braked tyre. It is reported in Ref. [3] that a decelerating vehicle is used to measure tyre/road noise of different tyre types. Fig. 2.20 [3] displays the measured sound pressure level in the form of waterfall plots from a wide summer tyre, a regular summer tyre and a slick tyre. Since the tyres are mounted on the vehicle, the measurements take also into account the influence of the vehicle body on the tyre/road noise radiation. Measurements are conducted with the engine being switched off and the vehicle being braked. Therefore, the preset deceleration corresponds to the negative value of the acceleration used during the actual ISO 362 test in order to reproduce analogous torque condition for the tyre/road noise measurement. The frequency range of 200−1000 Hz is dominant for the wide summer tyre, whereas the dominant frequency range for the regular summer tyre is $500 - 1000$ Hz. The radiated noise level of the slick tyre is much lower and there is no dominant frequency. It is concluded that the wider is the tyre the higher are the noise levels and the larger is the excited frequency band.

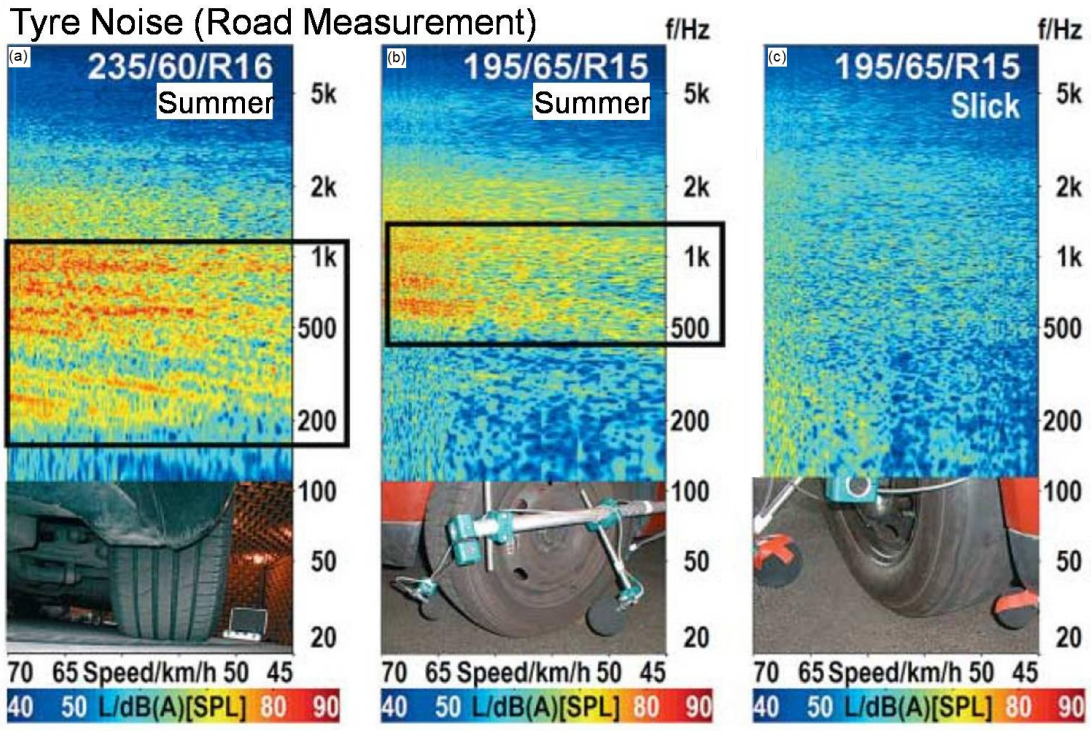

Figure 2.20: Waterfall plots of tyre/road noise measured on the road with different tyre types: (a) wide summer tyre; (b) regular summer tyre; (c) slick tyre [3] (reprinted from Alt N, Wolff K, Eisele G, Pichot F. Fahrzeugaussengeräuschsimulation (Vehicle exterior noise simulation). Automobiltechnische Zeitschrift 2006; 108:832-36. With kind permission of Dr Alt.).

Cruise-by noise measurements are conducted for passenger vehicles travelling at constant speed over a speed range from $40 - 100$ k.p.h. according to the Statistical Pass-By (SPB) method in Ref. [76]. The results show a linear relation between the measured sound pressure level and the vehicle speed on a logarithmic scale. The noise level varies from $69 - 78$ dB(A) over a speed range from $50 - 70$ k.p.h. The SPB method measures the noise of single vehicles on regular roads at constant speeds. A regression line visualises the relation of noise and speed. The exact tyre type or vehicle type is unknown, but vehicles are classified in different categories. The noise level for heavy vehicles is higher than that for passenger vehicles. The noise-speed relation is not entirely linear for the lower speed range. The SPB method is conducted on public roads, where the road surface structure and material is different to the standardised pass-by noise test track. However, it provides an indication of pass-by noise level values which would be expected in the pass-by noise test.

The Moving Frame Acoustic Holography (MFAH) method is applied in order to analyse tyre/road noise radiation under different pass-by conditions [65]. Figs. 2.21 to 2.23 display the effect of different driving conditions: accelerating condition according to ISO 362 (Fig. 2.21); constant speed condition (Fig. 2.22); coast-down condition (Fig. 2.23). A vehicle with reduced noise radiation and special tread pattern tyres on the measurement side is used, while smooth tyres are installed on the opposite side. The special tread pattern tyre is designed to radiate sound in a narrow frequency band around 500 ± 5 Hz at a vehicle speed of 55 k.p.h. It is not known, if the front or rear axle is driven. Figs. 2.21 to 2.23 present the sound pressure distribution in the measurement plane which is parallel to the side of the vehicle. When the vehicle passes the microphone array, sound pressure is recorded for less than 0.5 s. During this short period of time, vehicle speed is assumed to be constant and frequency changes are neglected in order to apply MFAH. The frequencies analysed in Figs. 2.21 to 2.23 cover a similar frequency range. A source is located at the rear of the front tyre and its location remains almost unchanged regardless of the driving state. Viewing all driving conditions, it can be seen that the sound source location at the rear of the rear tyre moves towards the tyre contact patch when the propulsion force is smaller. The noise source amplitudes vary due to the driving condition. Noise sources are approximately equal in strength for the front and the rear axle in the accelerating condition. For the constant speed condition, the noise source at the front tyre is dominant. For the coast-down condition, the noise source at the rear axle shows the highest amplitudes. It is concluded that tyre/road noise depends on the driving state, which includes force transfer in the tyre contact patch, tyre vibrations, oscillating air cavities, etc. Furthermore, an area of high sound pressure can be identified

between the front and rear axle for the driving state of constant velocity. This is due to interference effects between sound radiation from the front and rear tyre [65].

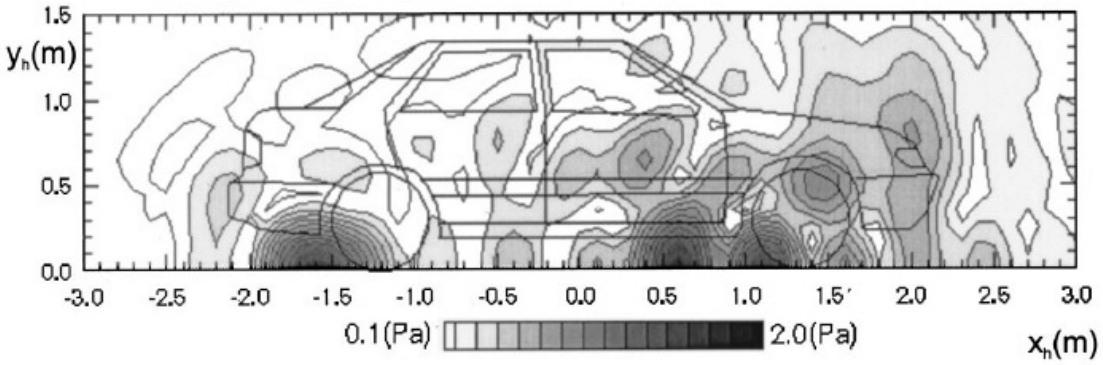

Figure 2.21: Tyre/road noise distribution on a measurement plane at 474 Hz under accelerating condition according to ISO 362 [65] (reprinted with permission from Park S-H, Kim Y-H. Visualization of pass-by noise by means of moving frame acoustic holography. J Acoust Soc Am, vol. 110 p. 2326 – 39 (2001). Copyright 2001, Acoustical Society of America. With kind permission of Prof Kim.).

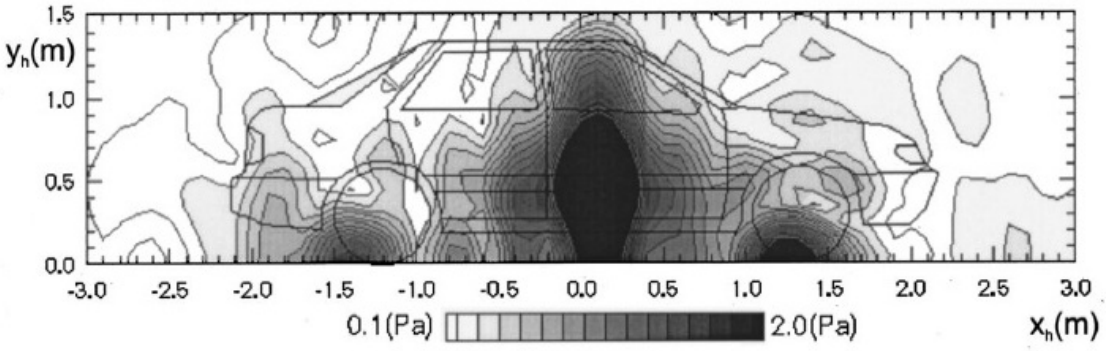

Figure 2.22: Tyre/road noise distribution on a measurement plane at 500 Hz during constant velocity of 55 k.p.h. [65] (reprinted with permission from Park S-H, Kim Y-H. Visualization of pass-by noise by means of moving frame acoustic holography. J Acoust Soc Am, vol. 110 p. 2326 – 39 (2001). Copyright 2001, Acoustical Society of America. With kind permission of Prof Kim.).

The propagation of noise in the far field is visualised using sound intensity measurement data in a plane 0.5 m above the ground in Fig. 2.24 [65]. The noise sources identified in Figs. 2.21 to 2.23 can be found at the origin of the abscissa in Fig. 2.24. The sound intensity into the far field is illustrated up to the z-coordinate value 7.5 m in Fig. 2.24b-d. Sound spreads out from the noise sources in different directions away from the vehicle. The noise level decays along the abscissa and at 7.5 m distance, the noise level is reduced significantly compared with the measurement surface at z = 0. In the accelerating condition, higher intensity levels occur

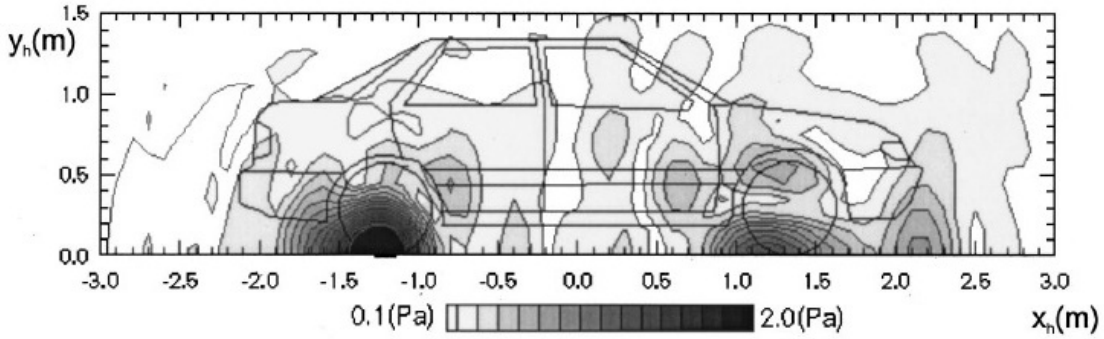

Figure 2.23: Tyre/road noise distribution on a measurement plane at 486 Hz under coast-down condition from 55 k.p.h. [65] (reprinted with permission from Park S-H, Kim Y-H. Visualization of pass-by noise by means of moving frame acoustic holography. J Acoust Soc Am, vol. 110 p. 2326 – 39 (2001). Copyright 2001, Acoustical Society of America. With kind permission of Prof Kim.).

than in the constant-speed and coast-down conditions. The constant-speed condition is heavily influenced by the interference effect between the radiated sound from the front and rear tyres, which creates a strong directivity pattern between the axles pointing away from the vehicle. In the accelerating and coasting-down condition, the directivity points not only away from the side of the vehicle but also towards and away from the driving direction with increasing z-coordinates. All three driving conditions are important for the analysis of vehicle pass-by noise. The accelerating and constant speed conditions are both implemented in the revised version of ISO 362 from 2007. The coast-down condition is often used to determine the contribution of tyre/road noise to the overall pass-by noise levels.

2.3 Existing methods for the prediction of vehicle pass-by noise

Different objectives can be accomplished through the application of predictive methods for the vehicle pass-by noise test. The basic objective is the prediction of the maximum A-weighted sound pressure level as an indication of whether the ISO 362 pass-by noise test can be passed. However, a more in-depth analysis of the evolution of exterior noise may be desirable. Certain methods allow contribution analysis of the vehicle noise sources enabling identification of critical noise sources. Predicted pass-by noise can be analysed against track position or evaluated in the frequency domain at discrete positions on the test track. Distinctive features of the methods are experimental or numerical, indoor or outdoor, complete vehicle test or system based tests. Predictive methods can combine one or more of these features.

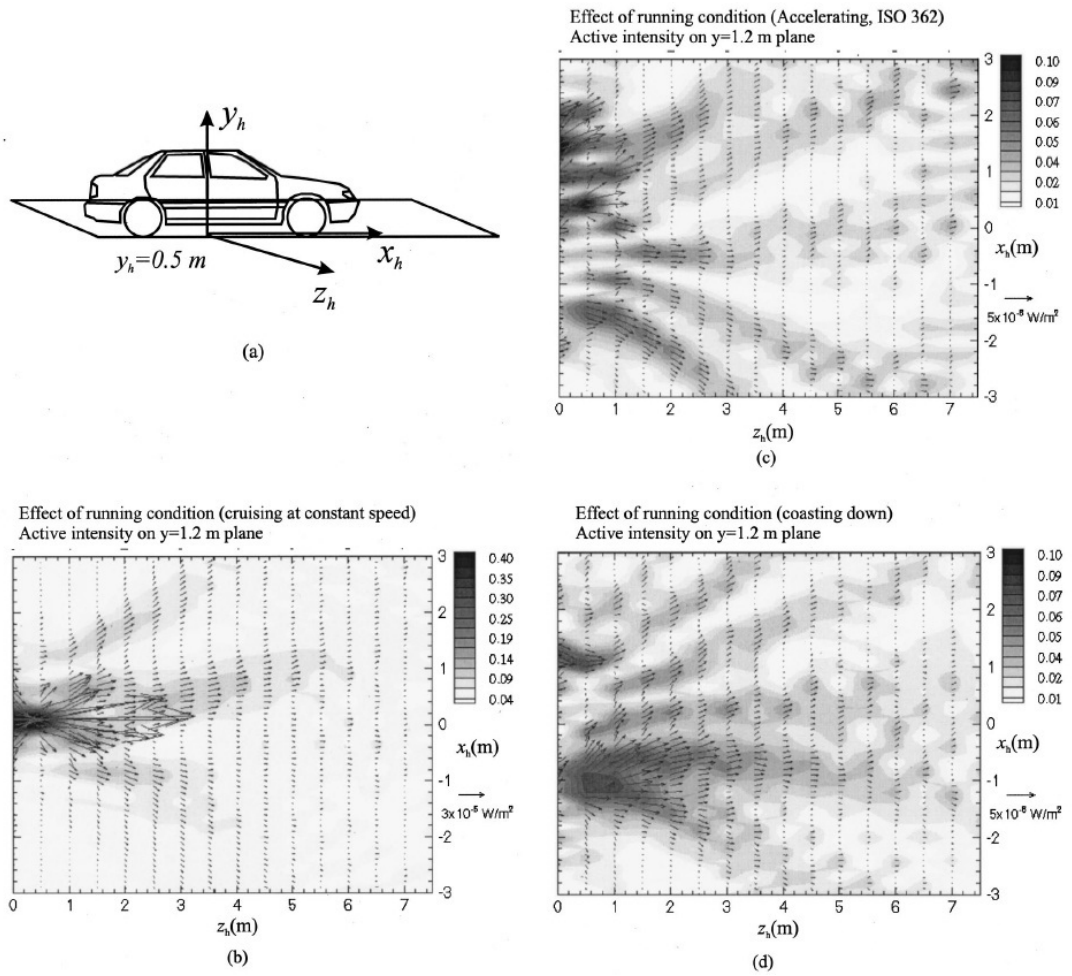

Figure 2.24: Illustration of noise propagation in the far field by means of sound intensity: (a) schematic of the measurement plane 0.5 m above ground level; (b) result of constant speed test; (c) result of acceleration test (ISO 362); (d) result of coast-down test [65] (reprinted with permission from Park S-H, Kim Y-H. Visualization of pass-by noise by means of moving frame acoustic holography. J Acoust Soc Am, vol. 110 p. 2326 – 39 (2001). Copyright 2001, Acoustical Society of America. With kind permission of Prof Kim.).

The indoor simulation of the pass-by noise test with microphone line arrays aims at providing similar test conditions without any environmental restrictions. The experimental determination of the strength of the major exterior noise sources and their corresponding airborne transfer functions gives details about each source contribution to the overall pass-by noise. This can be achieved on indoor or outdoor test facilities. Numerical techniques intend to replicate the real pass-by noise virtually, thus, reducing the number of physical prototypes in the vehicle development process. The following sub-sections contain a detailed overview about these techniques.

2.3.1 Indoor simulation of pass-by noise with microphone arrays

Large semi-anechoic chambers with chassis dynamometers provide an alternative test environment for pass-by noise experiments. For any indoor simulation of pass-by noise, it is generally advisable to provide similar test conditions as are required in the standard ISO 362. This decreases systematic measurement errors and approximates the experimental result of the real pass-by noise test more accurately.

A vehicle is positioned centrally on a chassis dynamometer within a semi-anechoic chamber, which provides approximately free-field conditions over a reflective plane. A large room provides enough space to cover the square between the lines of AA' and BB' as given in ISO 362. Microphones are arranged in a line array on both sides of the vehicle at a distance of 7.5 m to its centre line and at a height of 1.2 m. The spacing between microphones is either constant, for example 1 m, or varying with smaller spacing where the highest noise levels are expected [36, 24]. The number of microphones depends on the spacing and size of the chamber, for example 15 microphones per side are used in Ref. [36] and 19 microphones per side in Ref. [24]. The speed and load conditions of the real pass-by test are simulated by means of the chassis dynamometer enabling acceleration or constant-speed driving conditions, while sound pressure is recorded by the microphones. The indoor simulation can be run fully automatically and is well controlled, which provides a good experimental repeatability, which cannot always be achieved by a driver in road tests [36, 24, 72]. Since the vehicle and microphones are stationary, an inverse approach has to be applied in order to estimate the pass-by noise level against track position from the sound pressure recordings of each microphone [36]. Basically, the microphones in the front of the vehicle determine the pass-by noise when the vehicle enters the test track, while the microphones behind the vehicle determine pass-by noise when the vehicle leaves the test track. Estimates of the vehicle speed are obtained from a combination of chassis dynamometer and engine speed measurements in order to determine the theoretical vehicle position on the test track [36]. The microphone signals are selected in agreement with the vehicle's position, the data is interpolated between adjacent microphones and then connected in series. The transitions between adjacent microphone signals are smoothed to avoid leaps and discontinuities in the overall signal. Coherent and incoherent parts of the signal are treated with different algorithms [36, 27]. Finally, a filter is utilised to account for the Doppler frequency shift of a moving noise source [36]. The resulting signal is an estimate of a time-dependent pass-by noise signal [36, 72], which can also be utilised in jury

listening tests for subjective evaluation and psychoacoustic analyses [36].

In cases where large semi-anechoic chambers are not available, the indoor simulation of the pass-by noise test can be carried out in smaller rooms, if certain correction measures are applied. The microphone line array has to be positioned in the acoustic far-field of the vehicle, but the distance between the microphone line array and the vehicle centre line can be less than 7.5 m. A correction based on the inverse square law is applied to estimate the sound pressure at 7.5 m [36, 72]. The necessary assumption for this procedure is that the radiated noise originates from a single point, which is denoted the acoustic centre. It is assumed to be located on the ground within vehicle dimensions and may be dependent on frequency and driving condition [36, 72]. This implies that the acoustic centre is not a fixed location but can be moved during the pass-by simulation to improve the correction procedure. The acoustic centre is determined by the highest sound pressure reading of the sideline microphones, which cover the vehicle length. Vehicles with front engine tend to have the acoustic centre in the middle of the vehicle, since the exhaust orifice noise is a major noise contributor in addition to the engine noise. The acoustic centre moves to the rear of the vehicle for a rear mounted engine [36]. The length of certain test rooms may be too small making it impossible to cover the measurement angle with the microphone line array. The measurement angle is the maximum angle between the vehicle entering the test track and the ISO 362 pass-by microphone. In the indoor test facility, the microphones can be positioned outside the line array in order to cover the whole angle area [36]. The acoustic centre can be rated as an idealisation, since it cannot represent the origin of the sound radiation of all vehicle noise sources. Nevertheless, the systematic error resulting from the utilisation of the small room is reduced by the correction procedure [36].

The accurate replication of tyre/road noise on the drum of the chassis dynamometer is related to the replication material and its surface structure; the drum curvature appears to be of less influence [75]. The non-driven tyres are usually blocked, if only one chassis dynamometer is available. Hence, the contribution to rolling noise of these tyres is neglected. Slick tyres are utilised in order to record only the propulsion system noise of a vehicle in the semi-anechoic chamber [27]. Tyre/road noise, which is measured with a noise isolated vehicle, and the propulsion noise can be summed for pass-by noise estimation [27]. The comparison of indoor simulated pass-by noise and real pass-by noise against test track position, measured on slicks in second gear, shows an agreement within 1 dB(A) for the overall pass-by noise level, which confirms the high accuracy of the indoor test facility. The sound pressure levels of the corresponding one third octave spectra of the indoor simulation show higher values in the high frequency range above

2 kHz, which is due to different absorption characteristics of the ground of the indoor test facility [27].

The indoor simulation of pass-by noise also supports the identification of the interaction of low frequency coherent noise sources. The engine, the intake and the exhaust systems belong to the group of coherent noise sources, since their noise emission mainly originates from the periodic pressure pulses of the intake and exhaust valves [90]. The noise of the intake and exhaust orifices is dominated by strong correlating engine order noise [90]. This results in a complicated directivity pattern [71]. For the correct calculation of the overall sound pressure level of a number of coherent noise sources, the phase information between the sound pressure signals from each noise source have to be considered. In this frequency range, the acoustic wavelength is of the order of the vehicle length and approximately half the distance between the vehicle and the pass-by noise microphone. A distinctive interference pattern can be identified in the radiated sound field in Refs. [71, 90]. Thus, the phase relation between the signals has a significant influence on the location of the maximum and minimum sound pressure amplitudes [71]. It is mentioned in Ref. [90] that the influence of interference, either constructive or destructive, is less in real situations due to the presence of many excitation frequencies and the contributions of uncorrelated noise signals.

The interference effect from low frequency coherent noise sources on the measured pass-by noise level in the ISO 362 test is reported in Refs. [81, 34]. An example shows that two distinct peaks occur in the 100 Hz 1/3 octave band of the measured sound pressure against distance. This frequency band is assumed to be dominated by the second engine order. The first peak occurs when the vehicle front passes the microphone line. The second peak, which is higher in amplitude, occurs when the vehicle is far into the second half of the test track. Thus, it might be assumed that the first peak originates from the front of the vehicle whilst the second peak is related to the rear of the vehicle. However, near-field sound pressure measurements carried out indoors with a microphone array in a plane close to the vehicle result in the identification of the intake system as the noise source with the highest source strength. Thus, in this particular case the measured pass-by noise level in the far-field does not reflect the noise source strengths in the near-field of the vehicle. An illustration of such interference effects can also be seen in the 125 Hz 1/3 octave band of Fig. 2.5 [88].

In contrast to coherent noise sources, the sound pressure signals of incoherent noise sources do not originate from the same physical noise source, which is the case of all four tyres on the vehicle [90]. For the calculation of the overall sound pressure level of several incoherent noise sources, the powers of the sound pressure signals are summed and the phase information is omitted.

The indoor simulated pass-by noise test with microphone arrays does not replace the homologation process of the ISO 362, but it supports the development process from component to vehicle level [27]. A suitable complete vehicle prototype is required. It is of advantage that environmental restrictions due to rain, wind speed, ambient temperature and pressure do not exist. The ground is ideally covered with a material meeting the requirements regarding texture and reflection characteristics according to ISO 10844 in order to increase the comparability with the ISO 362 test [24]. Variations caused by the human driver can be eliminated by automatic control of the accelerator pedal. Free-field conditions between vehicle and microphones are confirmed to be within ±2.5 dB(A) down to the lower cut-off frequency of approximately 50 Hz [24, 27]. In Ref. [32], free-field conditions are verified to be within ±1 dB(A) for one third octave frequencies greater than 100 Hz. Ideal free-field conditions do not exist indoors, hence, deviations from these conditions may impair the experimental results. The background noise of the chassis dynamometer must not contribute to the overall vehicle radiated noise. The measured background noise is less than 40 dB(A) at a height of 1 m above the dynamometer for an equivalent vehicle speed of 50 k.p.h. in Ref. [27]. The wind noise created by a moving vehicle in air is not replicated, since its contribution to pass-by noise is assumed to be negligible in the speed range of the pass-by noise test.

Discrepancies between indoor simulated and real pass-by noise tests remain, irrespective of the layout and characteristics of the indoor test facility, the number of microphones and the algorithm applied to compose the overall signal. However, vehicles equipped with different components can be tested under the same conditions, and then their results can be compared. Vehicle noise sources can be shielded more easily due to the stationary position of the vehicle, thus, providing information about noise source contributions to the overall pass-by noise [24]. Other noise source identification techniques can be applied such as acoustic near-field holography or beam-forming [72]. Beneficially, measurement personnel can walk around the vehicle during testing in order to conduct a subjective evaluation of the pass-by noise characteristics.

2.3.2 Prediction of pass-by noise by experimental source strength quantification and airborne transfer functions

The pass-by noise test arrangement can be described simplistically as a source-transfer-receiver model [84]. This leads generally to two work steps: (1) The strength of each major noise source (engine, intake system, exhaust system, tyre/road

system) has to be quantified acoustically; (2) the transfer paths have to be quantified, since they describe the properties of the medium and space between each noise source and the pass-by microphones at the standard locations for each stage of the test. The physical conditions of the sources as well as the properties of the corresponding transfer paths change constantly during the test in terms of their inherent acoustic characteristics, which has to be considered in the prediction model. The combination of the source strengths and transfer paths is assumed to result in the equivalent of the sound pressure at the ISO 362 microphone locations. This result can also be compared to pass-by noise target values or measured pass-by noise data of the preceding vehicle model and competitors. The prediction model reveals the contributions of the dominant noise sources and critical transfer paths allowing for the implementation of countermeasures in the vehicle development stage.

The operational condition of the vehicle and the relative position of the vehicle to the microphones vary due to the instantaneous nature of the pass-by noise test. The operational source strength can be determined with the noise source installed on a laboratory test rig or locally on the vehicle. The approximation of the transfer functions can be obtained using a vehicle body without operating the original noise sources. The experimental quantification process can be conducted on the official ISO 362 test track or in a semi-anechoic chamber with a chassis dynamometer [36, 40]. The experimental quantification of acoustic source strengths and transfer paths as well as the prediction of pass-by noise is described in detail in the following.

2.3.2.1 Quantification of noise source strengths

In the pass-by noise test, airborne sound is transmitted from the vehicle noise sources to the two pass-by noise microphones. The surfaces and apertures of the real noise sources are considered as sound sources [84]. The quantification of each airborne sound source enables an estimation of the overall real noise source strength.

In general, the sound radiation of an omni-directional monopole source and the sound pressure at an omni-directional monopole receiver appears to be applicable in this case [86]. Therefore, the modelling approach for the determination of the real source strength is the discretisation of the vibrating surfaces and apertures of the main vehicle noise sources with uncorrelated omni-directional monopole sound sources [84]. These point sources are assumed to radiate noise, while the surfaces are assumed to be rigid maintaining the geometry of the real noise source structure. Due to the high impedance of most of the real noise sources, this becomes an

acceptable approach[84]. Volume velocity, which can be obtained through sound pressure measurements in the near-field of the point sources, is selected as a quantity to represent the source strength of the monopoles. Fundamental investigations on this approach are reported in Ref. [59], in which the assumption is that the whole system can be represented as a linear system. It is also required to provide a sufficiently dense arrangement of monopole sources to be spaced by half of the wavelength of the highest frequency of interest occurring in the system [59]. The sound field is assumed to be synthesised accurately, if the number of point sources and their amplitude and phase are chosen correctly [84]. Due to practical reasons, a spacing of half a wavelength between point sources in order to cover the vibrating surfaces of the real noise sources is not always feasible [28]. Consequently, the complex real sound sources are discretised into larger areas or patches [84]. Therefore, it is assumed that the amplitude of the point source volume velocity or the acoustic transfer function must be constant over each patch area [84]. A direct measurement of volume velocity is not possible. However, a measurement of the surface normal velocity is feasible, which is then multiplied by the patch area to obtain volume velocity. It is best suited for the lower frequency range with sound radiation from vibrating structural components [28]. The operational volume velocity of each patch can also be determined indirectly through sound pressure measurements. This is usually done where a measurement of surface normal velocity is not feasible or at regions being difficult to access, for example at nozzles, fans, tyres, and exhaust components. The feasibility of the indirect determination of operational volume velocity makes it the preferred technique in the majority of the reviewed literature.

The quantification of the noise sources can be conducted with the noise sources normally assembled to the vehicle or with the noise sources disassembled from the vehicle and installed on test beds [3, 83]. A free field environment is desirable. Encapsulation of unwanted noise sources may be applied to reduce crosstalk among the diverse noise sources on the vehicle [84]. The volume velocity of the noise source is assumed to be independent from the acoustic boundary conditions [83, 85]. The vehicle noise sources are operated under speed and load conditions corresponding to the pass-by noise test. A small speed gradient can be used to improve readings under instantaneous conditions [67]. The engine speed is recorded to synchronise the operational sound pressure signals with the corresponding vehicle position on the test track [3]. The vehicle position can be estimated by the engine speed in conjunction with the transmission ratio, tyre dimensions and time taken.

Alternatively, the source strength quantification of the main vehicle noise sources can be conducted individually on test rigs independently of the vehicle.

For the evaluation of a powertrain noise source in Ref. [28], a good correlation between the test rig and the full vehicle measurements has been presented. A powertrain is operated in a semi-anechoic environment within the speed and load conditions of the pass-by noise test [66]. The layout of the patches and the measurement procedure remains the same for individual noise source tests and the corresponding complete vehicle tests. However, only one microphone is used on each side of the engine-gearbox-assembly, while it is attempted to isolate intake and exhaust system related noise [3]. Intake and exhaust orifice noise is measured on the vehicle driving on the test track or on the chassis dynamometer in a semi-anechoic chamber with the other noise sources being masked [3]. Specially designed test rigs for intake or exhaust radiated noise present alternative options [66]. Intake orifice noise is recorded by a microphone, which is placed on an extension of the intake orifice axis without interfering with the intake air flow [66]. Exhaust orifice noise is measured by a microphone, which is positioned at a 45° offset from the exhaust orifice axis to protect the microphone from heat and gas flow [67]. Alternatively, the application of 1D CFD simulation of the whole exhaust system is reported in Ref. [3] in order to estimate the exhaust orifice noise. Since it is not possible to replicate the acceleration forces on the tyre/road system without measuring noise from the other major noise sources, tyre/road noise is measured on the vehicle through controlled braking to simulate the load influence on the system [3]. In this case, microphones record sound pressure in the front, rear and on the side of the tyre.

The indirect determination of the operational volume velocity of each path is achieved by a multiplication of the operational sound pressure spectra at the measurement positions in close proximity to the source patches and the transfer function spectra between these microphone positions and all remaining patches [84]. The convolution of the time history of sound pressure and impulse response function data is the equivalent approach in the time domain, which usually implies a higher expenditure of processing time. The transfer functions are determined individually in a direct [48] or reciprocal [84] approach. For areas difficult to access, the reciprocal determination of the transfer function is beneficial by positioning a calibrated point sound source at the original microphone position and a microphone on the patch measuring the sound pressure response of a broad band excitation signal from the point sound source [84]. The radiated volume velocity of the point sound source is calibrated prior to these measurements. For frequency domain data, the division of measured sound pressure and their corresponding broadband volume velocities results in the transfer function matrix. The inverse of the transfer function matrix is then multiplied, or convolved, with the measured operational sound pressure in order to estimate the operational volume velocity or

source strength. The number of microphones should be at least twice the number of patches in order to apply a least squares optimisation of the inverted transfer function matrix, thus, avoiding ill-conditioning and negative values [84, 85, 48]. This approach is also used to reduce errors from resonances in the engine compartment [79]. For all measurements, it is important to ensure microphones remain at their exact positions in order to avoid discrepancies in the sound pressure recordings [86]. The number of patches and microphones vary, for example, from equally sized areas of $0.1\,\mathrm{m}^2$ [84] and $0.04\,\mathrm{m}^2$ [28] up to an area of an engine side [3, 48]. However, subdivisions of the engine into the different sides of the engine block and oil pan, accessories, gearbox are also practiced [73]. For the other main sources, the intake orifice and air intake filter housing, exhaust mufflers and orifice, and leading and trailing edge of the drive wheels are considered as monopole sources [48, 73]. In case of a strong directional radiation characteristic of a surface or noise source, the utilisation of several microphones is recommended [79].

Several variations of this basic approach have been developed. An array of microphones is placed in close proximity around a vehicle measuring operational sound radiation from every noise source simultaneously while source isolation is omitted [73]. This is in contrast to the method presented in Refs. [84, 85, 48] in which microphones are positioned in close proximity to each noise source allowing for individual source strength quantification in turn. In Ref. [73], a monopole source loudspeaker is placed at the microphone position in the array, and microphones measure the sound pressure at discrete locations near the real noise sources, which represent the fictitious locations of the monopole sources. Thus, the transfer functions between microphone array and real noise sources are obtained. Combining transfer functions with their corresponding operational sound pressure measurements result in the volume velocity source strength of each fictitious monopole source. The overall source strength can be numerically separated into the contributions of each individual noise source component. According to Ref. [73], all numerical operations are carried out in the time-domain, since the rapid run-up recordings of the acceleration phase exist in the time domain. A predicted pass-by noise signal allows for audible evaluation.

Alternatively, the determination of the transfer function matrix is omitted in Refs. [36, 40]. Instead of using patches with equal areas and assuming constant surface velocity, operational source pressure is measured at defined positions in the near-field of each source. Then, the source volume velocity is obtained by inserting measured sound pressure into the equation for a monopole point source, which provides a relation between sound pressure, distance and the volume velocity. All noise sources remain assembled on the vehicle. This experimental implementation decreases measurement time. The immediate influence of this method on the

accuracy of the source strength quantification and, hence, the predicted result is unknown. All noise sources are active in this case. The microphone positions have to be selected carefully in order to keep errors regarding sound pressure measurement, source radiation characteristics and cross-talking at a minimum [40]. The term 'cross talk' is regarded to the fact that microphones do not only record the radiated sound pressure from the noise source they are located closest to, but they also measure noise from the other sources. This effect increases, if one or more of the other noise sources have a much greater sound radiation characteristic.

In a case of indoor measurements and where none of the vehicle noise sources is encapsulated or shielded, respectively, during the determination of the operational noise source strengths, a correction function can be applied to improve the predicted pass-by noise signal [36, 40]. If all noise sources are active and unshielded, microphones detect sound pressure not only from the closest noise source, but they also record cross talk contributions from other sources. Furthermore, the complex radiation characteristics of the noise sources may not be captured thoroughly due to the limited number of microphones in the near-field of the sources. In order to improve the prediction result, correction functions are determined in order to account for the different radiation characteristics and cross talk. For the determination of the correction function, only a single group of noise sources is active for that particular group. It is assumed that the radiation characteristic is not affected by the operating condition of a noise source, hence, an operating condition similar to the pass-by noise test procedure is not necessary [36]. Therefore, the powertrain is driven in neutral gear at typical engine speeds, while the front and rear wheels are driven individually by the chassis dynamometer. A few microphones in the line array, which covers the whole distance of a vehicle pass-by, are selected as reference signals to measure noise of the active group. Simultaneously, the microphones at the near-field positions of the non-active noise sources record noise from the active noise source, which is related to cross talk from the active noise source. All near-field sound pressure measurements are combined with their corresponding transfer functions and summed in order to obtain the far-field sound pressure at a particular microphone in the line array. Deviations in the ratio of this synthesised signal to the measured sound pressure at the same position are related to cross talk and inaccuracies in the identification of the source radiation characteristic [36]. It is assumed that the deviations of this ratio are approximately not affected by the location of the far-field microphone position or the operational conditions, hence, allowing them to be used as correction functions [40]. The correction function for the active group of noise sources is established as the ratio of the time-averaged synthesised to measured sound pressure for the

selected microphones in the line array, which are then averaged over all reference positions resulting in a single correction function for each group of noise sources. The final results are spatial and time averaged correction functions for each noise source, which are applied to filter the pass-by noise contributions at each microphone in the line array. The proposed correction measure represents a simplistic approximation and the partial coherence analysis is suggested as a more sophisticated technique [36]. However, the predicted sound pressure of this method deviates up to 5 dB(A) for an approaching vehicle, in comparison to the ISO 362 test. A good agreement can be achieved for the maximum pass-by noise level, which occurs when the vehicle is about to leave the acceleration area. Although, encapsulation measures on vehicle noise sources appear to be more feasible in indoor environments than outdoors, the prediction method is not conducted for encapsulated non-active noise sources. A comparison is also made between the corrected prediction of pass-by noise based upon noise source contributions and an indoor simulated pass-by with microphone line arrays. Both signals correspond well indicating that their underlying techniques achieve results of a similar quality.

Another method relinquishes the determination of the operational volume velocities and uses sound pressure for source quantification instead [67, 66]. Sound pressure on each engine side and at the intake and exhaust orifice is measured on test rigs under pass-by noise test conditions and used as operational source strength quantification [67]. According to Ref. [79], an alternative source strength quantification method is the sound power of each radiating source, which is estimated from sound pressure measurements.

A special case for tyre/road noise quantification is presented in Ref. [66]. It is assumed that radiated tyre/road noise is rather unobstructed in its path to the pass-by microphone. Therefore, the noise of the propelled vehicle is recorded at the standard microphone locations on the ISO 362 test track for several vehicle speed values, which cover the speed range of the vehicle in the pass-by noise test. Then, the test is conducted with the engine switched off and neutral gear selected in order to measure rolling tyre/road noise only. The rolling noise of different speeds are then associated with the corresponding positions of the vehicle on the test track for the real pass-by noise test. A correction which accounts for tyre/road noise due to vehicle acceleration is applied on the recorded data in order to approximate the contribution of tyre/road noise to the overall pass-by noise. Hence, this method is an approximation of the accelerated tyre/road noise under full load through rolling tyre/road noise. Presumably, its accuracy depends on the correction spectrum for accelerated tyre/road noise and the number of speeds utilised in the rolling test. Furthermore, the decrease of vehicle speed in the rolling test needs to be considered.

The establishment of source strength databases can help to evaluate different types of noise sources in combination with different types of vehicle bodies. This may be valuable especially for the tyre/road system according to Ref. [3]. If different engines or intake/exhaust systems are quantified separately on test rigs, their effect on pass-by noise in combination with different vehicle body designs can also be estimated [66, 23].

2.3.2.2 Quantification of transfer path characteristics

After the determination of source strengths, the source-transfer-receiver model requires the identification of the acoustic transfer path characteristics between the location of the vehicle noise source and the pass-by receiver microphones. Transfer path characteristics include the effects of absorption and diffraction of the sound, reflections from the ground and adjacent surfaces, and attenuation over distance [3, 85, 66]. They can be determined either in the direct or reciprocal approach. The number and location of transfer paths are defined by the fictitious monopole sources modelling the real vehicle noise sources.

In the direct approach, a calibrated sound source with monopole characteristic is placed at the position of the real vehicle noise source and excites the surrounding medium over a broadband frequency range. A microphone measures sound pressure at the receiver position. Due to the subdivision of the real noise sources into patches, the transfer functions between each patch and the pass-by microphone have to be determined. For practical implementation, artificial sound sources have to be placed within the original vibrating structure [86], which is hardly feasible. If they are positioned in the close vicinity or on the radiating structure, the whole system is basically falsified and the inaccuracy of the transfer functions is impaired [86]. However, suitable results are achieved in Ref. [48] with the direct approach. Alternatively, the original noise sources can be replaced with noise simulators of a similar shape and geometry in which each loudspeaker is activated individually to determine the whole set of transfer functions [66, 23]. Noise simulators are built for the engine, intake and exhaust orifices as reported in Refs. [66, 23]. Using noise simulators enables the evaluation of different vehicle body designs, for example the effect of an engine compartment under-shield can be studied [66]. The transfer function is calculated by the division of the measured sound pressure spectrum at the pass-by microphone location by the radiated volume velocity.

A ‘noise reduction’ value can also serve as a descriptor of transfer path characteristics [66]. Sound pressure radiated from the noise simulators is measured at the pass-by microphone location with and without the vehicle body. The difference between both sound pressure readings corresponds to the noise reduction value

[66]. The greater is the noise reduction then the greater is the attenuation effect of the vehicle body. However, a system change occurs in this procedure, since the engine is removed from the engine bay for example, which may incur uncertainties or errors.

The idea of the reciprocal approach is to swap the positions of the source and receiver [59]. In practice, microphones are positioned at or as close as possible to the original noise source, while an artificial noise source, usually a loudspeaker with monopole characteristics, is placed at the original receiver microphone location. It is assumed that the microphones located in the vicinity of the sources barely change the system 'vehicle'. The reciprocal approach offers a feasible and quick solution for the determination of transfer function by using the microphones on the patches defined during the source strength determination procedure and powerful sound sources at the ISO 362 microphone locations. Only one sound source is required in the reciprocal approach, while many sound sources are needed in the direct approach, or the recording has to be repeated for every noise source patch with a single loudspeaker. Averaging of the transfer function is recommended [28, 79]. A comparison of directly and indirectly determined transfer functions shows a difference of only ± 1 dB [86] confirming the applicability of the principle of reciprocity. The reciprocal approach appears to be the preferred method [3, 36, 86, 79, 73].

The transfer path measurement procedure is repeated for several positions of the vehicle over the whole length of the test track, usually in increments of 1m. Transfer functions are interpolated three times between two adjacent microphone positions in Ref. [79]. The measurement procedure is carried out analogously in a semi-anechoic chamber, where the artificial sound source is moved through the microphone positions in the line array in sequence. Using a smaller semi-anechoic chamber, corrections based on the inverse square law and the acoustic centre location can be applied [36]. Whether measurements are conducted indoors or outdoors, the asphalt surface should comply with the requirements of the ISO 10844 standard to ensure that comparable conditions regarding the actual pass-by noise test exist [66]. It is recommended to use a vehicle prototype which is equipped with the acoustic insulation material being intended to be used in the final product in order to provide a realistic image of the transfer path behaviour in the pass-by noise test situation [28]. If the acoustic boundary conditions alter, for example, if an acoustic insulation part is added to the vehicle, then the transfer function has to be determined for the altered configuration [85].

Irrespective of the approach for the determination of the transfer functions, the artificial sound sources or loudspeakers have to be sufficiently powerful in order to reduce the effect of sound attenuation with distance from the ISO 362 microphone

locations to the position of each noise source on the vehicle, and, thus, to record a signal with a sufficiently high signal-to-noise ratio, which can be utilised in the prediction technique. The devices are required to provide a spherical radiation characteristic over the frequency range of interest. In the direct approach, the size of the loudspeaker should be small in order to fit into the engine compartment for example [36, 79]. Different signals are utilised in order to excite the surrounding medium over a large frequency range, for example white noise [23] and swept sine [79]. The decisive criterion for the selection of the excitation signal is the signal-to-ratio, which has to be high, in conjunction with the available omni-directional sound source [79].

Transfer function measurements can be influenced by several parameters. In Ref. [86], the influence of temperature is investigated in a direct measurement procedure on a hot and a cold engine resulting in a small shift in frequency, amplitude and phase for the case of higher temperature. Another form of deviation can be caused by the air flow around the real noise sources, which are either a result of ambient air flowing around and into the vehicle or from the cooling process of the fan [86]. The positioning of microphones and sound sources should be precise in order to avoid significant deviations of up to $\pm 3\,\mathrm{dB}$ [86]. However, vehicle motion due to acceleration and the relatively large distance to the standardised microphone locations are of greater influence according to Ref. [86]. Nevertheless, such deviations may not be of practical impact, if they are within the positioning, calibration and measurement accuracy for one-third octave band data [86].

Omni-directional compact tube sound sources or volume velocity sources in rigid housings with a small hole are commercially available and applicable for all measurements of the transfer function determination process. The devices are calibrated in anechoic conditions obtaining a relation between the radiated volume velocity and the loudspeaker input signal or the pressure inside the tube or housing [86, 83]. Sound power is utilised instead of volume velocity in Ref. [79]. Ideally, the source strength is independent of the acoustic boundaries [85], which means that it does not alter if the source is utilised in the vehicle. Alternatively, different types of sound sources can be utilised to analyse different sections of the frequency range [40]. A frequency range of $20 - 4000\,\mathrm{Hz}$ is covered in the measurements reported in Refs. [36, 40]. In Ref. [48], a mid-frequency volume velocity source has been utilised to cover a frequency range of $200 - 8000\,\mathrm{Hz}$. In Ref. [40], three different calibrated loudspeakers are used to provide monopole characteristics for different frequency ranges: a subwoofer ($20 - 100\,\mathrm{Hz}$); a mid-frequency dodecahedron ($100 - 1200\,\mathrm{Hz}$); and a high-frequency dodecahedron ($1200 - 4500\,\mathrm{Hz}$). The measured signals in the three frequency ranges are superposed to obtain a single signal for the whole frequency range of interest. Experimental results of

the mid-frequency dodecahedron show that the monopole characteristic is given within a deviation of 1 dB for its appointed frequency range [40]. Interchanging the position of the dodecahedron and the microphone in a reverberating environment in order to check reciprocity characteristics show a small difference of up to 1 dB, verifying its applicability for reciprocal measurements. However, if the positioning error is greater than 2 cm, the deviations increase to more than 2 dB [40], which emphasises the importance of precise positioning of all devices for an accurate measurement. Thus, the accuracy of the transfer function measurement depends upon the relative position of the loudspeaker to the microphone and the loudspeaker radiation characteristics. The experiments conducted in Ref. [40] lead to the conclusion that an error of about $1 - 2$ dB may have to be inevitable to avoid in the process of transfer function determination.

Transfer functions of the intake and exhaust orifice show the shielding effects of the vehicle body for the frequency range greater than 200 Hz [3, 66]. In the first half of the test track, the transfer function of the intake orifice shows higher amplitude values than the corresponding transfer function of the exhaust orifice, which implies an amplification of the relevant frequency range of the intake orifice noise in comparison to the exhaust orifice noise [3]. The transfer functions show the opposite tendency in the final half of the test track, which, thus, implies amplified exhaust orifice noise in comparison to the intake orifice noise [3]. The transfer function spectra of different positions at the engine, intake and exhaust system have similar values up to 100 Hz. For higher frequencies, the difference between corresponding transfer functions increases by up to 10 dB, which, thus, indicates the different shielding characteristics of the vehicle body at the various measurement positions [8].

2.3.2.3 Evaluation of the pass-by noise prediction

After the identification of source strengths and transfer path characteristics for the source-transfer-receiver model, the final quantity of the receiver, which is the predicted pass-by noise, is determined. The overall pass-by noise signal is composed of the contributions of the vehicle sound sources, which are a combination of source strengths and transfer path characteristics. The source contributions vary according to their condition, which generally depends upon the vehicle or engine speed, and the distance to the pass-by noise microphone. The source contributions are calculated at discrete positions over the whole test track length. The summation of all contributions produces the overall pass-by noise level at this particular position. If this step is repeated for all discrete positions, the result is the prediction of the overall pass-by noise level against track position. The overall pass-by noise

signal of adjacent discrete track positions can be interpolated in order to receive a continuous signal. If the experiments are carried out in a semi-anechoic chamber with microphone line arrays, the noise source contributions are determined for each microphone in the line arrays instead of a discrete track position. The overall pass-by noise signal is obtained by the superposition of each microphone signal.

The calculations can be carried out in the time or frequency domain. In the time domain, the operational source strengths are convolved with the corresponding impulse response functions in order to obtain the noise source contributions [73]. In the frequency domain, the source contributions are calculated at a discrete track position by the product of the operational source strengths and the corresponding transfer functions [28]. The overall sound pressure level of the summed source contributions spectra yields the overall pass-by noise level at that particular position. The maximum frequency range of analysis depends mainly upon the artificial sound source utilised in the determination of the transfer functions.

The predicted results of the reviewed literature are presented either as overall pass-by noise level against track position or as one-third octave frequency spectra. The predicted overall pass-by noise signals correspond well with measured pass-by noise with deviations of the maximum levels within $\pm 1\,\mathrm{dB(A)}$ [36, 66, 48]. However, considering the whole of the pass-by noise signal against track position, deviations between $3-5\,\mathrm{dB(A)}$ occur in Refs. [36, 66, 48]. The predicted pass-by sound pressure deviates by up to $\pm 3\,\mathrm{dB}$ in the one-third octave bands of the frequency range of $200-8000\,\mathrm{Hz}$ [48]. It can be suspected that the deviations in the narrow band frequency spectrum are higher. Although, deviations appear to be high in the frequency spectrum, the corresponding predicted overall pass-by noise level shows less deviation [67, 48]. The methods in which the original noise sources remain on the vehicle and in which they are replaced by noise simulators produce similar outcomes, thus, demonstrating the suitability of both methods for pass-by noise prediction techniques [66, 48, 23]. Deviations occur between measured and predicted pass-by noise levels. Possible causes are likely to be related to the quantification methods for the noise source strengths and the transfer path characteristics as well as the replication of the ISO 362 vehicle pass-by noise test, which is outlined in the following paragraphs.

The strengths of the vehicle noise sources can be determined virtually under operational conditions analogous to the conditions in the ISO 362 test. The radiation characteristics of the noise sources have to be captured comprehensively. The replacement of the real noise sources through a limited number of uncorrelated monopole sources may not be ideal, since the structure as a whole radiates sound. However, the reviewed prediction results indicate that it presents an acceptable approximation for pass-by noise. Furthermore, the number of microphones used

in the measurement of operational source strength can be reduced significantly, to one microphone per engine side, for example, without severely compromising the quality of the predicted signal [28, 48].

The transfer path characteristics are only obtained at a few discrete positions along the test track, which may be due to the vast accumulation of measurement data and the opportunity of interpolation. Suitable approximations of pass-by noise can be expected for the discrete positions at which the transfer functions are determined. Deviations can be expected from the actual pass-by noise signal in the region where interpolation is applied. The loudspeakers used in transfer function determination should possess an omni-directional radiation characteristic and a sufficient sound power output in order to achieve a high signal-to-noise ratio.

If any measurement is carried out repeatedly on a moving vehicle, deviations can be caused by the change in the relative distance between transducer and measurement object, altered source impedance due to temperature variations, and air flow through and around the vehicle body [86]. Measurements with complete vehicle prototypes on chassis dynamometers in semi-anechoic chambers are most frequently used, especially in more recent publications [36, 28, 48, 79, 73]. The ability of the indoor experiments to reproduce the outdoor test relies on the reflection properties of the floor, the absorption capabilities of the walls, the correct source-to-microphone distance, and the replication of the tyre/road noise on the drum surface of the chassis dynamometer [85]. A factor in favour of an indoor implementation is that noise sources can be isolated or shielded, respectively, more easily, thus, reducing their impact on the recording of the noise source of interest [84]. Furthermore, the indoor experiments can be controlled automatically without the need of a driver, which means that the point of acceleration is met accurately and the distance between the vehicle centre line and any microphone does not vary. The radiation characteristics of the noise sources can be captured more thoroughly, since the microphones can be positioned close to the noise sources of the stationary vehicle.

The transient nature of the pass-by noise test may cause measurement errors [23] and a low level of test repeatability, which is an obstacle in providing suitable data for comparison and verification purposes [87]. Averaging of data recorded under non-stationary condition of a rapid run-up process is not advisable. Automatic vehicle control system may represent an improvement in this matter. The close monitoring of vehicle conditions such as engine and wheel speed, vehicle position, cooling fluid temperature, fuel temperature and throttle position provides comparable data of several test runs [87]. Environmental or weather conditions such as ambient temperature and pressure, air density, humidity, rain, wind speed may influence and even prevent outdoor measurements. Test series should be carried

out within the same test facility in order to avoid deviations in the measurement results due to site-to-site variability. Measurement devices should meet the requirements of class one' instruments [11]. The road asphalt of the test track may cause a lack of repeatability and reproducibility. The recently revised standard, ISO 10844 [12], provides guidelines regarding road surface texture and absorption as well as smoothness and evenness of the test track. These factors can cause additional excitation and deformation in the tyre-suspension-system leading to varying noise radiation. The requirement regarding the acoustic property of the asphalt, for example, is an absorption coefficient of less than or equal to 8% determined at the one third octave frequencies within the range of $280 - 1800\,\mathrm{Hz}$ [12]. It is anticipated that variations in the pass-by noise levels will be reduced through the application of the revised standard.

The reviewed methods of the source-path-receiver approach are suitable to predict changes in pass-by noise levels for different vehicle configuration but the exact pass-by noise level cannot be replicated so far. Nevertheless, a knowledge about source strength contributions and transfer path characteristics enables: (1) the analysis of source contributions and transfer paths to the overall pass-by noise [86]; (2) the establishment of a source ranking [28] and noise targets for the major noise sources [66]; (3) the evaluations of encapsulations, absorption properties or other additional countermeasures [86]; and (4) the analysis of road surface reflection on pass-by noise [86]. The technique offers more advanced opportunities than the windowing technique on a noise isolated vehicle due to insufficiencies in the insulation in the low-frequency range and possible small sound level differences between the quietest noise source and the completely noise isolated vehicle [8]. A differentiation between noise sources and transfer paths cannot be achieved if the windowing technique is applied. The technique of experimental source strength quantification and airborne transfer functions is applicable for the requirements of the revised ISO 362 standard, if operational source strength data of a constant-speed pass-by is available.

2.3.3 Numerical methods for the prediction of pass-by noise

This section gives an introduction to pass-by noise prediction by means of numerical methods. Such methods can analyse the pass-by noise characteristics of a vehicle in its early development stage, thus, reducing the experimental effort [46]. The neural networks technique and the Boundary Element Method (BEM) can be categorised as such approaches. The Fast Multipole Method (FMM) was recently applied to simulate very large BEM models without the typical sacrifices

in calculation time and maximum analysable frequency.

2.3.3.1 Neural networks approach

A neural network consists of neurons which are simple processing units, connected to each other to form a network [31]. An output value of a typical artificial neuron is derived from several input values which are multiplied by a weight, summed up, added with a bias and passed on to a transfer function. Advanced neural networks such as the 'multi-layer perceptron' consist of several inputs influencing different layers of neurons. A neural network can provide a predictive model from example data. Vehicle design parameters have a significant influence on pass-by noise, but a suitable prediction of noise is not possible from analytical calculations [30]. The application of neural networks for pass-by noise prediction offers a feasible alternative in an early vehicle design stage [30].

A ranked list of vehicle parameters affecting vehicle pass-by noise was established in Ref. [30], which are practical to collect and applicable to any vehicle. These parameters serve as input values to the neural network model. A sufficiently high number of training examples, which is in the range of several thousand [30], are required to train the network. This data is obtained by the collection of test data of a large number of predecessor vehicles. Further data preparation, such as the definition of weighting factors, has to be conducted. A neural network for the estimation of vehicle performance in combination with the data for vehicle parameters and test conditions are the input to the neural networks model for pass-by noise prediction in Ref. [30]. The averaged error over all test cases of the predicted pass-by noise level in comparison to the actual pass-by noise level is within 1.4%. However, the predicted results show a rather large distribution and deviations of $2 - 4\,\mathrm{dB(A)}$ for many data points. Deviations increase in the case of a new, quieter vehicle. The network has to be retrained constantly with the latest vehicle technology otherwise a possible source of errors may occur due to technology leaps of the most recently developed vehicles. Another disadvantage may be the provision of the vast amount of test data from previous vehicle models, which may be difficult to collect.

2.3.3.2 Boundary Element Method

The BEM calculates the sound pressure level at a specified location in space from the excitation of a medium by a noise source. The source and the receiver locations are modelled by mesh structures. Sufficient computer resources are important prerequisites for the adequate performance of a BEM simulation. Mostly, a trade-off between model accuracy and available computer facilities has to be made [46,

91]. For the prediction of vehicle pass-by noise, a highly complex model would have been to be set up which automatically requires large computer resources.

In general, an acoustical wavelength is required to be modelled by six to ten elements in order to be represented accurately. This has an impact on the maximum analysable frequency and computation time. If a whole vehicle is to be modelled in the analysis of exterior noise propagation, the number of elements is enormous and, hence, the calculation time increases heavily [46]. Therefore, the method is not applicable in practice for frequencies greater than 500 Hz. Another aspect of concern is the frequency resolution. The computation time is increased if the frequency resolution is high. An estimate of the transfer function may be obtained by a small number of frequency data points [46]. However, if the number of frequency points is too small, the quality of the transfer function may be low.

In Ref. [91], a BEM model of the four major noise sources (engine, intake manifold, exhaust tailpipe, tyres) and the vehicle body is established to estimate pass-by noise at 23 specific frequencies in the range of $19.95 - 3162.2$ Hz. Each noise source is modelled via a generic source, which represents an approximated geometry of the real source dimensions. Thus, the build-up of the model is simplified, and the computation time is reduced. The radiated acoustic field of each generic source is reconstructed via sound pressure measurements in the vicinity of the real noise source during a pass-by noise test. Thus, the excitation velocities on the surface elements of the generic source are derived, and the calculated sound pressure values can be assessed against the measured values. Transmission and reflection effects due to the vehicle body and the ground are included in the BEM model. The pass-by noise evaluation points are included as a line of field points along both sides of the vehicle model at 7.5 m distance and 1.2 m height. Since the mesh structure consists of openings and multiple connections, the Indirect BEM is applied to obtain the transfer functions between the generic sources and the evaluation points. The combination of the surface velocities on the generic sources and the corresponding transfer functions result in a pass-by noise prediction. All noise sources are regarded as incoherent. The maximum overall A-weighted sound pressure level of a pass-by in third gear is calculated and compared with the measured value. The deviation is only 1.1 dB(A), with the computed level slightly higher [91]. However, a comparison of a pass-by noise level against track position is not given in Ref. [91]. This technique also depends on sound pressure measurements, otherwise the reconstruction of the acoustic field of the noise sources would not have been feasible.

The sound radiation of an engine-gearbox structure is simulated using BEM in Ref. [39]. A Diesel engine with a manual transmission, used for commercial vehicles, is the foundation of the simulation model, which is limited to noise from

stationary operational conditions. Excitation through combustion forces is considered as well as mechanical excitation through play and dynamic mass inertias. This leads to the calculation of the reaction forces at the bearing positions of the engine-gearbox-structure. The structural transfer characteristics are simulated with a finite element model of the engine-gearbox-unit. As a result, the normal surface velocity distribution is obtained. Boundary element models are generated from the existing finite element models in order to simulate sound radiation. The sound pressure distribution in the far-field at discrete frequencies is calculated from the normal surface velocities. The simulation is carried out only for a few components of the engine-gearbox structure due to intensive computation time. Since not all excitation mechanisms are considered in the simulations, it is difficult to achieve accurate values of the sound pressure distribution. However, the qualitative evaluation represents a good idea of the directivity characteristics of the analysed components.

The Fast Multipole Boundary Element Method (FMBEM) can overcome the trade-off of the limited maximum frequency and high computation time of the traditional BEM [46]. In the application of FMBEM, the model is subdivided into several clusters. The cluster of a noise source contains elements in the near-field of that particular source. In order to obtain the acoustic response in the far-field target cluster, all points of a noise source cluster are collected together to represent a single multipole. The radiated noise from the single multipole is mathematically transferred to the target cluster, then the sound pressure is evaluated on the target points. Clusters, which are far away from the source cluster, can be combined into groups of clusters leading to a hierarchical arrangement and, thus, to a significant reduction in computation time. Therefore, the FMBEM can be applied to BEM problems involving millions of degrees of freedom. This also increases the maximum frequency of analysis up to 2 kHz.

In Ref. [46], the FMBEM is applied to calculate the transfer functions between the source and receiver locations of a pass-by noise test configuration, which utilises two receiver locations, which are in the front and on the side of the vehicle at 4.3 m distance to the vehicle centre line. An experimental setup of a vehicle in a semi-anechoic chamber provides comparison data. The major noise sources are modelled as point sources. Their source strengths, which are quantified by volume velocity, can be obtained by measurements or simulations. Reflections from the ground are considered in the model. An average deviation up to 4 dB occurs for the comparison of simulated and measured pass-by noise level over all transfer paths. Possible causes for the deviations are considered to be mainly related to the poor quality of the modelling of the sources inside the engine compartment.

2.4 Literature survey on acoustic tyre cavity resonances and their impact on noise radiation of the tyre sidewall

The introduction of a constant-speed pass-by noise test in the vehicle homologation process provides a different vehicle pass-by noise characteristic. Noise sources related to the powertrain, which are for example the engine, the intake and exhaust systems, contribute less to the pass-by noise level, since they are operated at stationary conditions with relatively low engine revolutions and low load. In that case, the noise contribution of the tyre/road system becomes relatively dominant. In another scenario, the introduction of a large amount of electrically driven vehicles will change the appearance of vehicle pass-by noise. The noise level of the electric propulsion system is considered to be less than the noise level of conventional propulsion system involving an internal combustion engine. In addition, the noise source radiation characteristics are different as well. However, the tyre/road system remains as the typical noise source. In both scenarios, tyre/road noise sources may be unmasked, which have not been ranked previously as noise contributors to pass-by noise.

The tyre is excited by broadband mechanical distributed forces in the contact region between the tyre and road and responds with the superposition of structural modes at their particular resonance frequencies [51]. The structural waves propagate across the tyre surface in circumferential and cross-sectional directions [16]. In addition, acoustic waves are generated within the air-filled torus-shaped cavity enclosed by tyre and wheel. It is assumed that acoustic and structural waves interact and, thus, sound radiation from the tyre depends on both wave types. The waves in the tyre structure which are entirely due to mechanical force input are called structure-borne waves while the waves due to the acoustic resonances of the tyre air cavity are called airborne waves. The structural modes radiate sound efficiently from the vibrating surface into surrounding air if the structural wave number is less than the acoustical wave number [51]. It is reported in Ref. [16] that the fundamental resonance of the tyre cavity increases sound radiation from a tyre in the low frequency range.

This section presents a literature survey on the resonances of the air column inside the tyre cavity, which are illustrated from various experimental results. Then, the noise radiation characteristics of the tyre sidewall as well as the interaction between the tyre cavity resonances and the tyre sidewall are shown. This is completed by an introduction to various modelling techniques for the tyre cavity as well as the structural/acoustic coupling of the tyre cavity and the tyre sidewall.

2.4.1 Acoustic characteristics of the tyre cavity

The resonances due to the vibration of the air column inside a tyre cavity are shown in various experiments. In Ref. [74], hammer impact excitation is applied on a tyre/wheel combination in free-free condition. The resulting Frequency Response Function (FRF) between the impact force at the tyre contact patch and the acceleration at the centre of the wheel is presented in Fig. 2.25. Whilst the amplitudes near point 'A' and 'C' are related to structural modes of the tyre in cross-sectional direction, the sharp peak near point 'B' is caused by the first acoustic tyre cavity mode. This resonance occurs at the same frequency in several experiments with tyres of the same size but different sidewall stiffnesses and varying tyre inflation pressures. Since the sidewall stiffness and the tyre inflation pressure primarily affect the structural resonances of a tyre, the sharp peak is assumed to be caused by the oscillating air column in the tyre cavity.

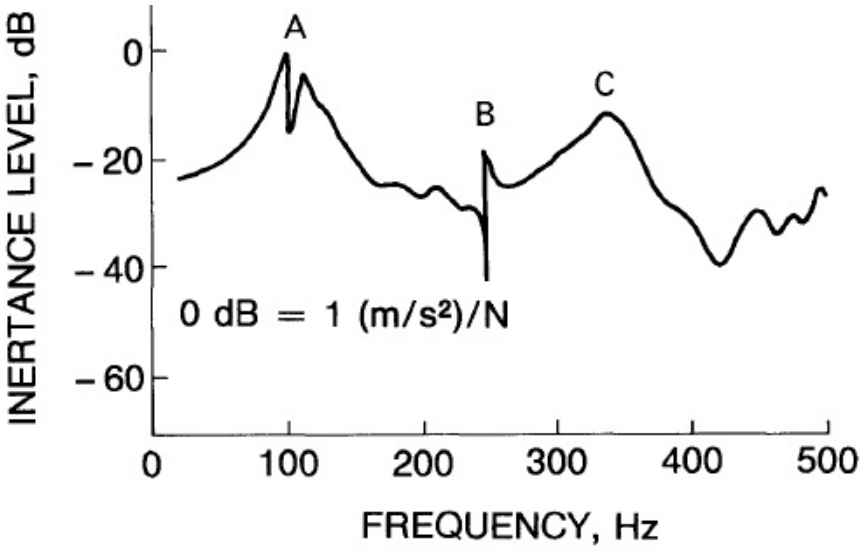

Figure 2.25: Frequency Response Function between the force at the tyre contact patch and the acceleration at the centre of the wheel [74] (reprinted from Sakata T, Morimura H, Ide H. Effects on tire cavity resonance on vehicle road noise. Tire Science and Technology, 18(2):68-79, 1990. With kind permission of Dr Taheri, President of The Tire Society.).

In another experiment in Ref. [74], the air inside the tyre cavity is acoustically excited using a loudspeaker which is attached to the tyre via a hole in the treadband. Two microphones record sound pressure at the centre of the cavity. One microphone is located near the hole for the loudspeaker. The second microphone is located on the opposite side of the tyre cavity. Hence, the distance between the microphones corresponds to approximately half of the length of the circumference of the tyre cavity. The recorded sound pressure levels are presented in Fig. 2.26, where 'point A' refers to the microphone position near the loudspeaker and 'point

B' to the opposite microphone position. The peak at 230 Hz represents the first acoustic cavity mode of the tyre. The peaks at 460 Hz and 690 Hz are multiples of the first cavity mode, thus, representing the second and third acoustic cavity mode.

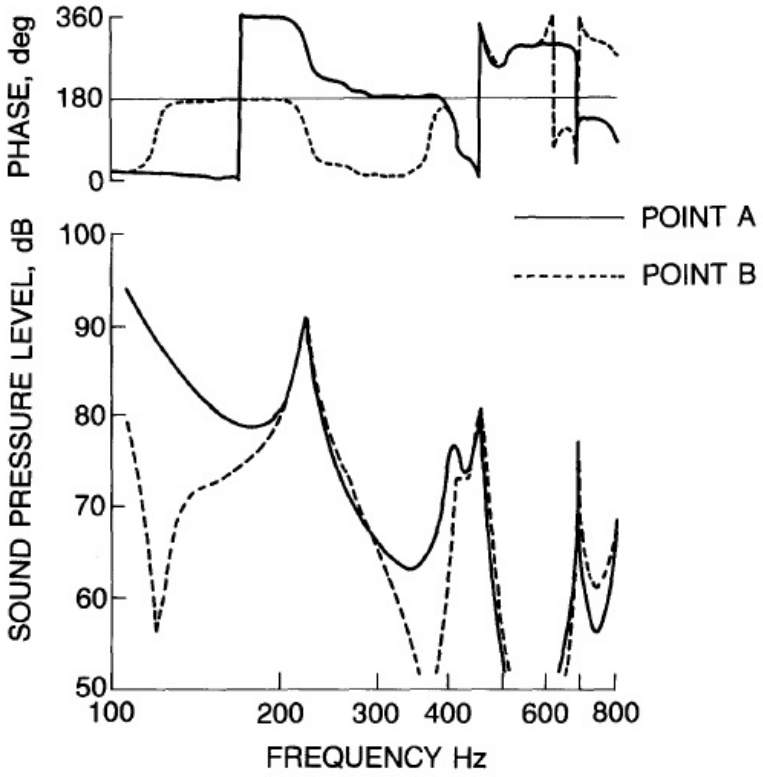

Figure 2.26: Sound pressure level in the tyre cavity during acoustic excitation [74] (reprinted from Sakata T, Morimura H, Ide H. Effects on tire cavity resonance on vehicle road noise. Tire Science and Technology, 18(2):68-79, 1990. With kind permission of Dr Taheri, President of The Tire Society.).

The phase signals of the points 'A' and 'B', also shown in Fig. 2.26, suggest that each cavity mode consist of a specific arrangement of nodes and anti-nodes. For the first and third cavity mode, the phase signal of both measurement locations are in anti-phase, which indicates that anti-nodes with different signs exist at the two microphone locations. For the second cavity mode, the phase signals of the points 'A' and 'B' are in-phase, which indicates that anti-nodes with the same sign exist at the two microphone locations.

An illustration of the first three acoustic tyre cavity mode shapes in free-free condition are presented in Fig. 2.27. The number of anti-nodes increases the higher the resonance frequencies are. In conjunction with the previous phase signals, anti-nodes with different signs can be identified at the bottom and the top of the first and the third cavity mode shape, whilst the anti-nodes are of the same sign for the second mode shape. From the arrangements of positive and

negative anti-nodes, it is concluded in Ref. [74] that a resultant force acts on the wheel in the vertical direction at the frequency of the first cavity mode. This is supported through the experiment in Ref. [44] in which a loudspeaker is placed inside the tyre cavity and the acceleration response is measured on the wheel. The measurement results show that the wheel experiences a forced vibration mode at the frequency of the first cavity mode. It is reported in Ref. [49] that the force is characterised through a sharp peak at the resonance frequency of the first tyre cavity mode, which can also be identified in the FRF spectrum in Fig. 2.25. The sharpness of the peak is due to the small damping properties of the air inside the tyre. The force on the wheel has an effect on the vehicle interior noise since a resonance at the frequency of the first tyre cavity mode can be detected in the vehicle interior noise spectrum in Ref. [74]. For the second and third cavity mode, the resultant force on the wheel is equal to zero due to the arrangements of the positive and negative anti-nodes.

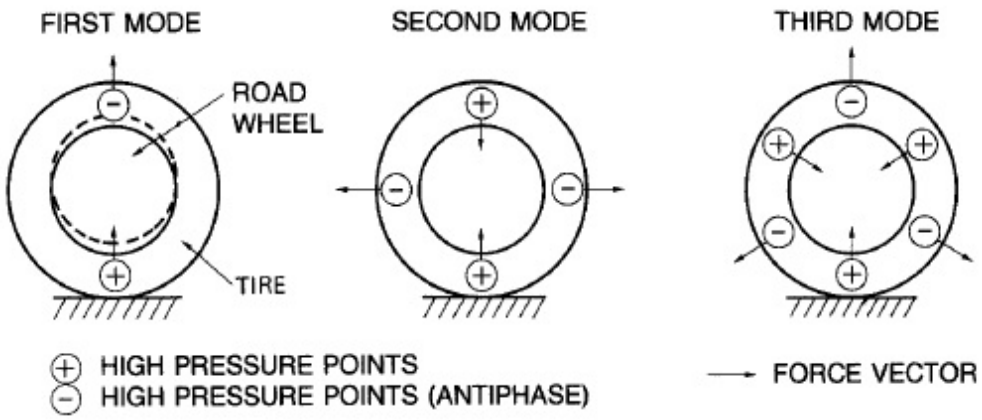

Figure 2.27: Acoustic tyre cavity modes for free-free condition [74] (reprinted from Sakata T, Morimura H, Ide H. Effects on tire cavity resonance on vehicle road noise. Tire Science and Technology, 18(2):68-79, 1990. With kind permission of Dr Taheri, President of The Tire Society.).

The measurement of the transfer function between the hammer impact force on the wheel and the acceleration response on the tread band are carried out for the same tyre/wheel assembly with two different gases, air and helium, in Ref. [77]. The tyres are mounted on a vehicle, which results in a static load on the tyres due to the vehicle weight. For the air-filled tyre, the first acoustic cavity resonance can be identified as two peaks in the spectrum, which is a result of the tyre deformation. No resonance peak is present for the helium-filled tyre since the speed of sound in helium is approximately three times higher than the speed of sound in air. Thus, the first acoustic cavity mode is shifted to a higher frequency. It is further reported in Ref. [77] that a structural-acoustic coupling can occur between the bending mode of the wheel around the longitudinal axis

of the tyre/wheel combination and the first acoustic tyre cavity mode. This is investigated for the vehicle interior noise, which results in higher noise levels.

2.4.2 Noise radiation characteristics of the tyre sidewall for acoustic tyre cavity excitation

This section presents the experimentally determined noise radiation characteristics of the tyre sidewall and the interaction between the tyre cavity resonances and the tyre sidewall vibration and noise radiation.

It is reported in Ref. [53] that the tyre wall is the dominant noise generator of a tyre below 1 kHz. Two experiments are conducted. In the first experiment, a rear tyre is mounted on a vehicle and loaded vertically with the vehicle weight. The excitation is carried out through an electrodynamic shaker. The surface velocity is measured on the surfaces of the tyre treadband and sidewall, which are therefore divided into elements of the length of 40 mm. The measured surface velocities of two adjacent locations on the treadband and the sidewall are presented in Fig. 2.28. The difference between the peaks of both quantities is small up to approximately 650 Hz. Several peaks of both quantities appear at the same frequency which may indicate that a coupling between the treadband and the sidewall occurs. At higher frequencies, the level of the treadband surface velocity is dominating, which indicates that an energy loss occurs for the sidewall modes at higher frequencies. It is also reported in Ref. [53] that the measured surface velocity decays rapidly in regions which are farther away from the force input location. On the treadband at the top of the tyre, which is opposite to the shaker excitation at the bottom of the tyre, a reduction of 15 dB is common.

In the second experiment, the sound pressure is measured on the tyre surface using a microphone whilst a calibrated volume velocity source provides the acoustic excitation. The resulting transfer functions of two adjacent locations on the treadband and the sidewall are presented in Fig. 2.29. The difference between both levels is small over the whole frequency range, which may indicate that the sidewall has a great potential for radiating sound. It is also reported in Ref.[53] that the reduction of inflation pressure results in a decreased sound radiation efficiency of the tyre structure due to a lower stiffness of the sidewall and the carcass.

The waves in the tyre structure are generated in the tyre/road contact area, thus, the waves propagate along the tyre circumference and along the cross-sectional direction along the sidewalls [56]. It is assumed that these waves attenuate for an increasing distance to the point of excitation. Whether these waves radiate sound from the tyre structure depends upon several factors of which the phase velocity, or wave propagation speed, is most important. The phase velo-

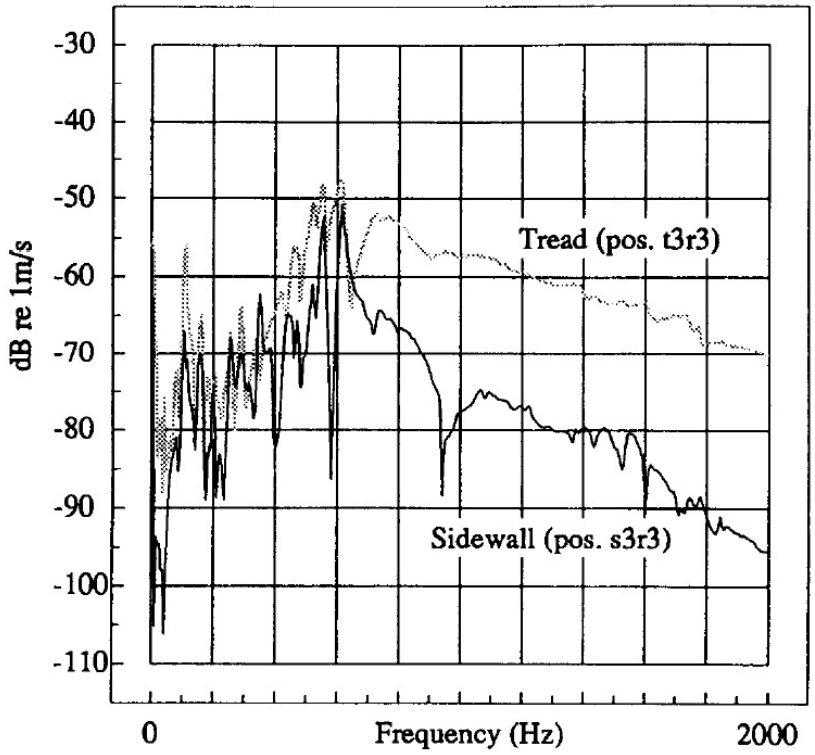

Figure 2.28: The measured surface velocity of two adjacent locations on the tread-band and the sidewall [53] (reprinted from Kim GJ, Holland KR, Lalor N. Identification of the airborne component of tyre-induced vehicle interior noise. Applied Acoustics, 51(2):141-156, 1997. With kind permission of Elesevier Ltd.).

city characterises the propagation speed of a single frequency component of the wave. Since it is a complex wave consisting of many frequency components, the higher frequency components travel at a higher velocity than the low frequency components, which also changes the shape of the wave. If the phase velocity is greater than the speed of sound in air, the wave radiates sound very efficiently into the environment. However, waves with a smaller phase velocity can radiate sound efficiently as well, if damping, edge effects and the association between the structural near-field and the excitation point provide favourable conditions. It is also reported in Ref. [56] that the mode shapes of the carcass are similar to the tyre cavity modes.

A Laser Doppler Vibrometer is applied in the measurements of the surface velocity of a tyre sidewall in Refs. [77, 49]. The surface vibration of a tyre sidewall and wheel is measured at the first tyre cavity resonance frequency by a Laser Doppler Vibrometer as reported in Ref. [77]. A tyre/wheel assembly, with a normal inflation pressure level, is excited by an electrodynamic shaker at the frequency of the first tyre cavity resonance. The measured vibration pattern shows a nodal line which horizontally divides the upper and the lower region of the tyre. Whilst the tyre sidewall in the region of the contact patch is not

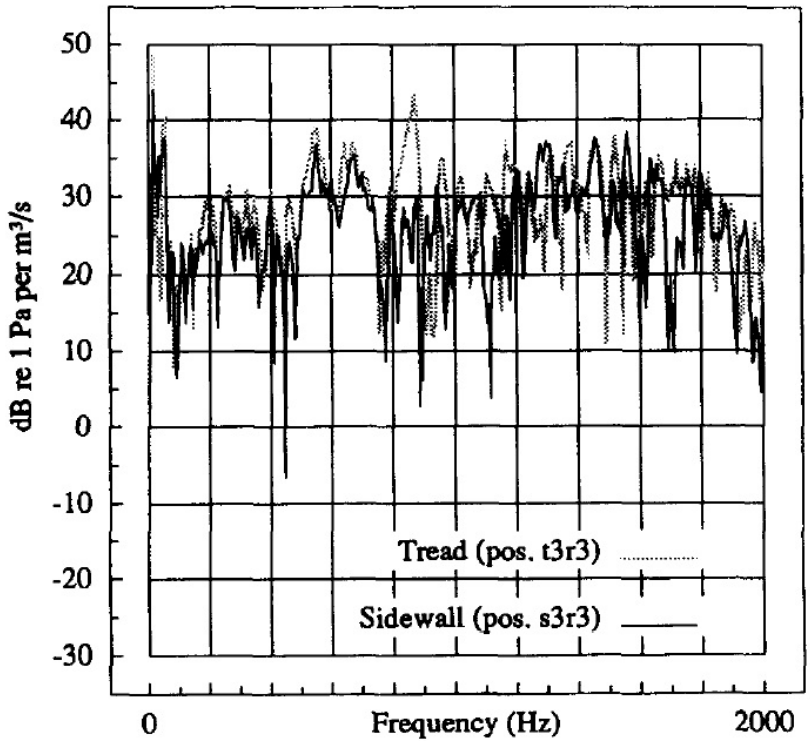

Figure 2.29: The measured sound pressure of two adjacent locations on the treadband and the sidewall [53] (reprinted from Kim GJ, Holland KR, Lalor N. Identification of the airborne component of tyre-induced vehicle interior noise. Applied Acoustics, 51(2):141-156, 1997. With kind permission of Elesevier Ltd.).

displaced significantly, due to the higher stiffnes as a result of vertically loading, the upper region of the tyre sidewall is bended around the nodal line. In Ref. [49], an electrodynamic shaker excites a tyre, without vertical load, at a point on the tyre treadband, and a Laser Doppler Vibrometer is used to measure the surface velocity at 80 locations on the tyre sidewall. It is reported in Ref. [49] that the treadband vibration affect the tyre sidewall. For example, two slow-moving waves with cut-on frequencies at approximately 100 Hz and 250 Hz are identified. The first acoustic tyre cavity mode can be identified in the measured surface velocity of a tyre with high (60 psi) and medium (30 psi) tyre inflation pressures. In a measurement with a tyre being filled with insulation material, the peak of the first acoustic tyre cavity resonance does not appear, according to Ref. [49]. Thus, this particular peak is due to the first tyre cavity resonance. This conclusion is also confirmed in sound pressure measurements in close proximity to the tyre sidewall. The wavespeed of the structure-borne waves is reduced for the lower tyre inflation pressure, since the stiffness of the tyre sidewall is reduced due to lower tyre inflation pressure. A reduction of the wavespeed leads to a change in the corresponding resonance frequency for structure-borne waves. However, the wavespeed of the structure-borne wave at the acoustic cavity resonance frequency

does not seem to be affected. It is approximately equal to the speed of sound in air, thus, it is assumed that it radiates sound efficiently into the environment.

The force input to the tyre is changed from a point force input to an area force input in Ref. [49]. This is realised in a drop test in which the area of the force input is approximately the size of the tyre contact patch, which is more accurate in comparison to the normal tyre operating conditions. The sound pressure of a single bounce is recorded by two microphones at a distance of approximately 30 cm to the tyre sidewall. The peak of the first acoustic tyre cavity mode occurs in its characteristic shape at around 210 Hz for both inflation pressures of 60 psi and 20 psi. The tyre cavity resonance peak as well as the structural resonance peaks are decreased for the lower inflation pressure, which is in line with the previously mentioned dependency of sidewall stiffness and inflation pressure. However, the reduction of the peak of the tyre cavity resonance is relatively small in comparison to the peaks of the structural resonances.

In Ref. [52] the tyre sidewall vibration and sound radiation characteristics are investigated using a stationary tyre/wheel assembly which is acoustically excited by a loudspeaker. The condition of the tyre is free-free. The treadband is smooth and the wheel spokes are removed. Acceleration and sound pressure are measured on the surfaces or in close proximity of 640 discrete areas across the tyre and the rim, which means that 16 measurement locations are distributed in the cross-sectional direction and 40 in the circumferential direction of the tyre/wheel assembly. The measurement locations are chosen to be 50 mm apart in order to cover a frequency range of up to 1000 Hz with six measurement areas. It is assumed that the amplitude and phase are constant for each of the measurement areas. The measured acceleration response spectra due to the acoustic excitation from a loudspeaker inside the tyre cavity are presented in Fig. 2.30, representing all of the measurement locations. The four resonance peaks of the tyre cavity dominate the spectra at every measurement position on the tyre as well as on the rim, covering the cross-sectional as well as the circumferential direction. The cavity resonance frequencies are 237 Hz, 461 Hz, 705 Hz, and 937 Hz according to Ref. [52]. For frequencies higher than 300 Hz, the cavity resonances are the only resonances that can be clearly identified in the spectrum, which may be due to high damping of tyre rubber and high modal density of the whole tyre structure according to Ref. [52]. The tyre cavity resonances are also observed in a similar experiment with a loaded tyre in Ref. [52].

From the measurement data of the surface acceleration, the mode shapes of the tyre sidewall are obtained at the four acoustic tyre cavity resonance frequencies in Ref. [52], which is presented in Fig. 2.31. The mode shapes of the tyre sidewall represent almost the same characteristics as the acoustic tyre cavity modes do,

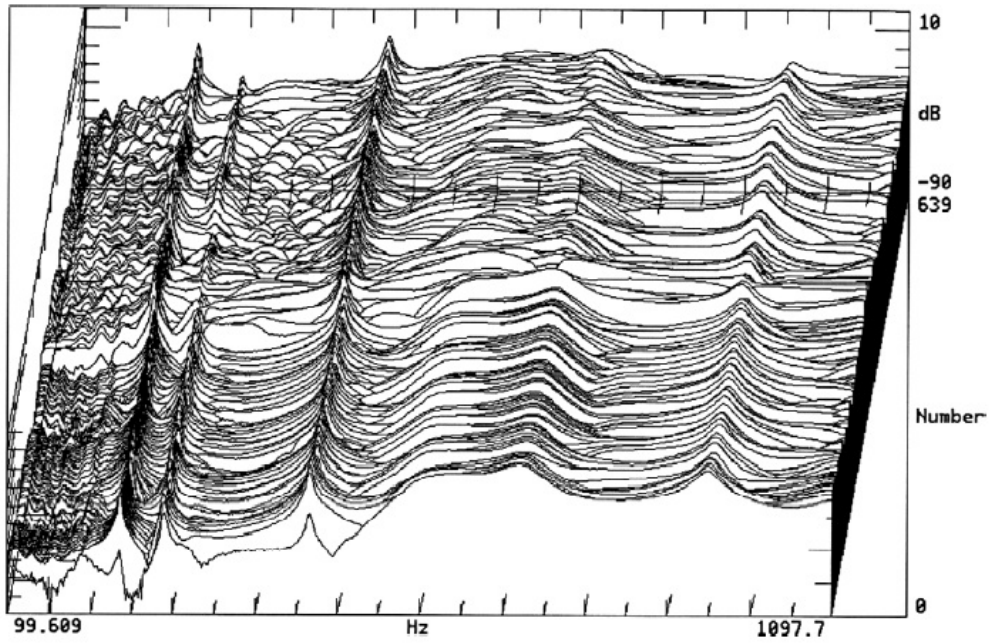

Figure 2.30: Acceleration response spectra of the tyre and rim due to acoustic excitation from the loudspeaker in the tyre cavity (location $0-279$ are on the rim and $280-639$ on the tyre) [52] (reprinted from Kim BS, Kim GJ, Lee TK. The identification of tyre induced vehicle interior noise. Applied Acoustics, 68:133-156, 2007. With kind permission of Elesevier Ltd.).

with only small distortion due to the coupling of acoustic and structural modes. Hence, the influence of the acoustic tyre cavity modes on the tyre sidewall can be clearly identified. It is further reported in Ref. [52] that the transition area between sidewall and treadband shows a similar mode shape characteristic.

The sound pressure contributions of the treadband, sidewall and rim to the overall sound pressure level are determined for a receiver point off the tyre/wheel assembly using a combination of structural and acoustical FRF. Fig. 2.32 presents the sound pressure contributions and the total sound pressure. The sound pressure of the treadband and the sidewall contribute most to the total sound pressure whilst the contributions from the rim are much smaller. While the sound pressure contributions of the treadband and the sidewall are approximately equal at the first and fourth tyre cavity resonance frequencies, the difference is higher at the second and third tyre cavity resonance frequencies. However, the contribution of the sidewall is generally on a significantly high level.

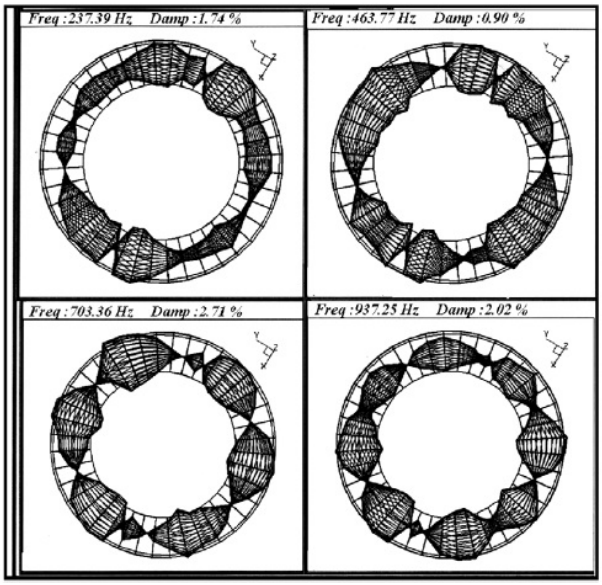

Figure 2.31: Mode shapes of the tyre sidewall at the four acoustic tyre cavity resonance frequencies [52]. (reprinted from Kim BS, Kim GJ, Lee TK. The identification of tyre induced vehicle interior noise. Applied Acoustics, 68:133-156, 2007. With kind permission of Elesevier Ltd.)

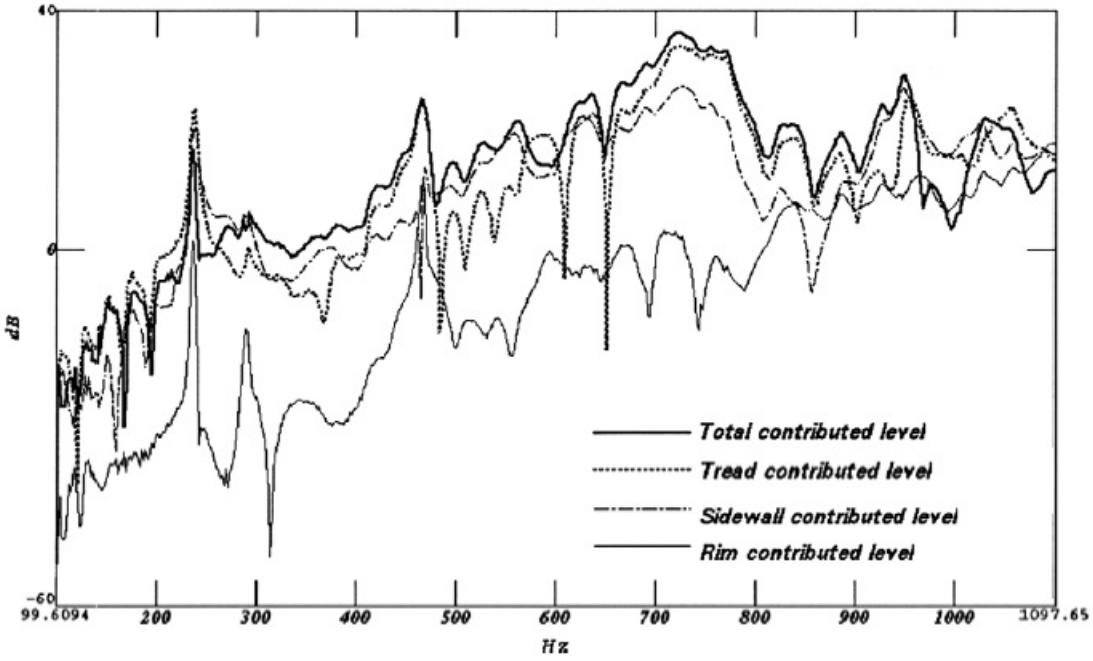

Figure 2.32: Sound pressure contributions of the different tyre regions to the total sound pressure at a receiver point 1.7 m away from the tyre [52] (reprinted from Kim BS, Kim GJ, Lee TK. The identification of tyre induced vehicle interior noise. Applied Acoustics, 68:133-156, 2007. With kind permission of Elesevier Ltd.).

2.4.3 Modelling techniques and simulation results for the tyre cavity and sidewall

The modelling techniques for the tyre cavity range from analytical to numerical models, which can consider tyre deformation as well as structural/acoustic coupling. The following provides an introduction into these techniques and presents their simulation results, which add to the information about the acoustic characteristics of the tyre cavity.

In Ref. [82], the circular tyre cavity is modelled as a straight line duct of finite length and a constant cross-section area. The point at the top of the tyre cavity is represented at both ends of the duct. Hence, continuous boundary conditions must be provided at both ends of the tube since they represent the same point. It is assumed that the wavelengths of the resonance frequencies are much greater than the dimensions of the cross-section area of the duct. Then, the sound propagation in the circumferential direction of the tyre cavity can be treated as plane wave propagation. Cross modes in radial or axial direction of the tyre cavity can be omitted since they occur at higher frequencies which are typically outside the frequency range of interest in the analysis of tyre cavity resonances. The boundaries of the tyre cavity are assumed to be rigid, thus, the particle velocity at the boundaries of the duct is zero as well. For a simple approximation of the acoustic resonance frequencies of the undeformed tyre cavity, it is suggested to use Eq. 2.1 in Refs. [74, 82]:

$$f_i = i \times \frac{c}{l} \tag{2.1}$$

where i is the order of the cavity resonance, f_i is the ith resonance frequency, c is the speed of sound, and l the length of the circumference at the centre of the cross-section of the tyre/wheel assembly. It is reported in Ref. [82] that the accuracy of the calculation of the first cavity resonance frequency is within 1-2 % for four different sized passenger vehicle tyres, which shows the applicability of Eq. 2.1.

Due to the vertically loading of the tyre due to the vehicle weight, the tyre cavity is deformed which is considered in the tyre cavity models presented in Refs. [74, 82, 41]. It is reported in Ref. [74] that two degenerate modes occur at the tyre cavity resonance frequency in an undeformed tyre cavity. The original mode of an undeformed tyre cavity is split into two modes due to the cavity deformation. The cross-section area of the cavity is not constant in the circumferential direction for an undeformed tyre. In the duct model of the tyre cavity, this is considered through a smaller cross-section area of the length of the tyre contact patch in the centre of the duct model. There are two possible boundary conditions to be applied at

both ends of the duct model [82]. The first boundary condition reflects maximum particle velocity at both ends of the duct model, thus, representing a pressure node. The second boundary condition reflects maximum pressure at both ends, thus, representing a pressure anti-node. For matching boundary conditions at both ends of the duct model, which ensures continuous conditions mathematically, the formulas for continuity of mass and conservation of momentum can be applied to calculate pressure and velocity in the duct model.

The two eigenfrequencies of the two degenerate modes of the first tyre cavity mode of the deformed cavity can be estimated using Eq. 2.2, which results in a lower and an upper resonance frequency around the first tyre cavity resonance frequency ($f_{deformed,lower} < f_{undeformed} < f_{deformed,upper}$) [82].

$$f = \frac{c}{l \pm (1-m) l_{cp}} \tag{2.2}$$

where m is the ratio of the deformed cross-section area to the undeformed cross-section area of the tyre cavity, l is the length of the duct, and l_{cp} is the length of the contact patch or the deformed region of the tyre cavity, respectively. It is noticed from Eq. 2.2 that the length of the tyre contact patch l_{cp} determines the distance between the frequencies of the two degenerate modes. The results of Eq. 2.2 show a negligible offset in validation experiments with different sized passenger car tyres under defined tyre deformation conditions [82]. It is concluded in Ref. [77, 82] that the first tyre cavity mode splits into a horizontal and a vertical mode. The frequency of the horizontal mode is less and the frequency of the vertical mode is greater than the first tyre cavity resonance frequency of the unloaded tyre. Both mode shapes correspond to the mode shape of the first tyre cavity mode. However, the mode shape of the horizontal mode is rotated by a quarter rotation relative to the vertical mode shape. Thus, a horizontal and a vertical force is applied on the wheel.

In Ref. [41], the tyre cavity duct model is enhanced through the implementation of smaller waveguide sections, especially in the region of the deformed tyre cavity. For each waveguide section, the pressure and the particle velocity is calculated resulting in an estimated distribution of pressure and particle velocity in the duct model.

A model for the structural/acoustic coupling of the tyre, wheel and cavity is presented in Refs. [61, 60]. Two thin, circular shells are utilised to model the tyre belt and the wheel, whilst two annular plates model the tyre sidewalls. The outer shell is given elastic properties whilst the inner shell and the annular plates are assumed to be rigid. The boundary condition for the outer shell is simply supported. The shells and plates form the structural model for the tyre-wheel

assembly as well as the boundaries of the acoustic model, which represents the tyre cavity. Tyre rotation is not considered in the model. From the equation of motion of the outer shell and the resulting eigenvalue problem, the natural frequencies and the mode shapes of the outer shell can be determined. In order to obtain the natural frequencies and the modal response of the tyre cavity, an acoustic model is developed in which the wave equation is applied under the assumption of rigid surfaces along the annular tyre cavity. In order to consider the effect of the acoustic cavity response on the structural response of the outer shell, a coupling mechanism is implemented at the boundary between the structure and the fluid. The computational procedure combines the external forces on the outer shell and the fluid pressure in the equation of motion of the structural model, which results in the surface velocity of the tyre structure. Since the fluid pressure depends on the velocity response of the structure, the surface velocity leads to a change in the pressure of the cavity fluid. Thus, the fluid loading term is altered. This information is then fed back to the tyre structure model, which completes the coupled structural/acoustic model. Tyre deformation can also be considered in the coupled structural/acoustic model.

The calculation results show that coupling occurs between the first acoustic tyre cavity mode and structural modes of the outer shell in axial direction. It is also shown that the first tyre cavity mode couples with the first structural mode of the outer shell in circumferential direction. Applying the coupled structural/acoustic model, the forces on the wheel due to the interaction of structural and acoustic responses can be estimated. Damping is not considered in the acoustic model. It is assumed in Ref. [61] that the high damping of the structural tyre model has a negligible effect on the acoustic cavity resonance. Since the outer shell and the tyre cavity interact in the radial direction of the tyre, it can be assumed that, in reality, the tyre sidewall is incorporated in the interaction as well.

Other structural/acoustic models of the tyre cavity, the tyre and the wheel are based on numerical methods like the Finite Element Method (FEM), as applied in Refs. [54, 16].

In Ref. [54], a coupled structural-acoustic model is produced utilising the Finite Element Method in conjunction with the indirect Boundary Element Method (IBEM). The surface velocity of the nodes of the FEM mesh of the tyre/wheel assembly are calculated. They are then transferred onto the nodes of the BEM model in order to simulate the acoustic response of the tyre cavity and determine the sound pressure distribution in the tyre cavity model. The acoustic response is eventually transferred back to the FEM model in order to obtain a coupled structural-acoustic response. Utilising another BEM mesh, which covers the exterior of the tyre model, the radiated sound power level is calculated for a hemi-

spherical field point mesh over a reflecting rigid plane. The tyre inflation pressure inside the tyre cavity is represented through a static load on the surface mesh inside the tyre cavity. Then, a harmonic, radial excitation force is added on a single node of the tyre treadband mesh. Tyre deformation through vehicle weight is omitted in the model. The coupled structural/acoustic model is validated against experimental results up to 500 Hz [54].

In the calculated sound pressure spectrum inside the tyre cavity model, the first and second acoustic cavity resonance occur as pronounced peaks. In addition, several peaks occur below the first acoustic tyre cavity resonance frequency, which are approximately 20 dB(A) less than the peaks of the acoustic resonances. These peaks are related to the structural response of the tyre/wheel model. Hence, an effect of the structural response on the acoustic response exist, although it appears to be small. The acoustic tyre cavity resonances are also detected in the result of the radiated sound power level. They are higher in amplitudes than the resonances related to the structural response. Increasing the height of the tyre sidewall results in a 0.6 dB(A) higher mean value of the sound pressure level inside the tyre cavity model [54]. An optimised tyre contour with a flattened curvature in the transition region between the treadband and the sidewall leads to a reduction in the radiated sound power level by 1.4 dB(A), which corresponds to 30% [54]. This is achieved through a reduction in the sound power levels of the structural modes.

In Ref. [16], a FEM model is presented which couples a structural model of the tyre and wheel with an acoustic model of the fluid of the tyre cavity. The treadband and sidewall are modelled using thin shell elements. The wheel model is composed of solid elements with rigid body properties. For the fluid model in the tyre cavity, acoustic fluid elements are utilised for which density and speed of sound are defined. The coupling between the structural and the fluid elements is enabled through the Fluid-Structural-Interaction tool in the Ansys® FEM software. The boundary conditions of the wheel are fixed. Prior to the harmonic analysis, the structural tension in the treadband and sidewall elements, as a consequence of the tyre inflation pressure, is calculated. This can include a vertical load on the tyre due to the vehicle weight. Eventually, a harmonic unit force is applied on an area of the approximate size of the contact patch in radial direction on the tyre treadband mesh.

Since the sidewall has a lower stiffness than the treadband, any effect of the tyre cavity resonances would be revealed more clearly [16]. Thus, the results of the sidewall mesh are selected to primarily present the simulation results. This indicates that the sidewall has generally the potential to radiate noise. In a simulation scenario with an inflation pressure of 30 psi, the radial velocities of the sidewall are generally lower in comparison to the radial velocities of an inflation

pressure of 0 psi, since the sidewall stiffness is increased due to the higher inflation pressure.

In order to identify the propagating waves in the sidewall, the technique of wavenumber decomposition is applied in Ref. [16], which is illustrated in colour maps of frequency against circumferential wavenumber and radial velocity in the sidewall for a point force excitation and for an area force excitation. Structural modes in cross-sectional direction of the tyre model can be identified as curving trajectories. The group phase speed, which is an indicator for efficient sound radiation of a structural wave, can be estimated through the constant slope of each of the curving trajectories. The slope is determined between the origin of the coordinate system and the straight line of a trajectory, which is generally reached at higher circumferential wavenumbers. The group phase speed of the structural-modes in cross-sectional direction is much lower than the speed of sound in air. Thus, their sound radiation is regarded as not efficient. It is further reported in Ref. [16] that, at around 200Hz, 400Hz, 600Hz and 800Hz, relatively high radial velocity amplitudes can be identified as small dots for a low circumferential wavenumber. These are assumed to be associated with the first four acoustic cavity resonance frequencies. Thus, they represent the effect of the acoustic cavity resonances on the tyre sidewall vibration. The group phase speed of the acoustic tyre cavity resonances, determined on the sidewall, is approximately 360 m/s, which is close to the speed of sound in air. Thus, this provides a favourable condition for an efficient sound radiator on the tyre sidewall. The group phase speed is found to be constant for three different radial positions on the sidewall, which makes the acoustic response being independent of the radial position on the sidewall model. It is assumed that an excitation force over a larger area provides a more realistic approximation of the force application on the tyre contact patch in reality than the excitation force on a single node. The radial velocity amplitudes are increased at the acoustic cavity resonance frequencies for the area force whilst the radial velocity amplitudes of structure-borne wave components are reduced at higher frequencies. The radial velocity amplitudes of the third and fourth acoustic tyre cavity resonance become more apparent for the area force excitation. It is concluded in Refs. [16, 15] that the spatial distribution of the force input acts like a spatial low-pass filter for structure-borne wave components in both the circumferential and cross-sectional directions.

In another analysis in Refs. [16, 15], the sound pressure is averaged along three radial positions on the tyre sidewall model, and the radial surface velocity is averaged along the centreline of the treadband mesh as well as on the centreline of the sidewall mesh. In the case of the area force excitation, several peaks occur up to about 400 Hz, which are mainly related to the structural response. However, the

effect of the tyre cavity resonances can be identified clearly in the sound pressure and the radial velocity graphs at around 200Hz, 400Hz, 600Hz and 800Hz. The amplitudes of the third and fourth acoustic tyre cavity resonance are relatively high in both the sound pressure and the radial velocity graphs, which shows that an interaction between structural and acoustic response exists. Since the amplitudes of the radial velocity are higher on the sidewall than they are on the treadband, the importance of the sidewall as a potential noise radiator becomes apparent.

FEM simulations are also conducted with tyre deformation due to a vertical load on the tyre in Refs. [16, 15]. The results for the structural and the acoustic response are again spatially averaged along the treadband, sidewall and the three radial sidewall positions for the case of an area force excitation. The sound pressure response is equal for the radial positions on the sidewall. The frequency split is apparent with the lower and higher frequencies being apart by less than 4 Hz. The structural response of the sidewall shows two peaks for the horizontal and vertical mode. The amplitude of the structural response of the treadband is approximately equal to the amplitude of the sidewall. However, it has a marginal dent at the higher frequency. Again, the interaction between tyre sidewall and tyre cavity fluid is shown.

A wavenumber filtering is applied on the results of the radial velocity of the sidewall at the first acoustic tyre cavity resonance frequency in order to separate airborne components from structure-borne components and, then, to analyse the sound radiation characteristic [16]. The filtered radial velocity shows a dipole-like pattern, which would be in agreement with the mode shape of the first acoustic tyre cavity resonance, which expands on the high pressure side and contracts on the opposite side. This suggests that the sound radiation of the first acoustic tyre cavity resonance in radial direction could be modelled using a dipole source. This can be enhanced to a quadrupole source model in order to consider the reflective properties of the ground. The quadrupole sound radiation model is experimentally verified in Ref. [16] through the measurement of the sound pressure of the first tyre cavity resonance of a rebounding tyre.

In Ref. [51], different approaches, mainly shell and plate theory, are applied in different frequency ranges in order to model the tyre modal behaviour and, then, to estimate the sound radiation of the tyre. In the frequency range below 80 Hz, the tyre structure is modelled like a spring-mass-system, with the treadband being considered the mass and the sidewall being considered the spring. In the frequency range 80-300 Hz, a beam model is used to model the propagation of structural waves in the circumferential direction along the tyre treadband. The beam is elastically supported by springs which represent the sidewall stiffness. Above 300 Hz, two thin cylindrical shell models are coupled in order to calculate

the modal behaviour of the tyre structure. The small shell models the unwrapped structure of the tyre tube. The large shell models the cylindrical shape of the tyre treadband. The structural models are then coupled with the one-dimensional wave equation, which describes the acoustic response of the tyre cavity. The results of the calculations show that there is a significant probability that the acoustic tyre cavity mode coincides with a circumferential structural mode. The acoustically excited wave motion of the tyre structure radiates sound efficiently below 1000 Hz.

The treadband appears to be the major noise generator; it has been subject to several modelling approaches. The tyre sidewall is a major noise generator as well producing noise amplitudes on a similar level compared to the treadband. So far, the tyre sidewall was only subject to initial modelling approaches of which none covers the noise radiation of the sidewall in axial direction of the tyre.

One of the differentiating parameters in the experiments as well as the modelling techniques is the excitation mechanism of the tyre cavity. A loudspeaker can be utilised being positioned inside the cavity. On the other hand, an electrodynamic shaker can be used to excite the tyre structure via a point force input or area force input in radial direction. Then, the tyre cavity is excited by the vibrating tyre structure.

Although the results were mainly analysed in terms of the radial velocity on the sidewall , an interaction between the tyre cavity and the tyre structure was shown. It is assumed that such interaction also affects the sound radiation of the tyre sidewall in axial direction towards the microphone position in the pass-by noise test.

Chapter 3

Methodology for the prediction of pass-by noise

This section presents the basic methodology for the prediction of pass-by noise in this work. The pass-by noise prediction method is applicable to single noise sources under laboratory conditions and is divided into two steps. First, the radiated sound pressure of the noise source is quantified in the static horizontal directivity experiment. Then, that directivity sound pressure is combined with the instantaneous distance between the noise source and the receiving microphone in the inverse square law. This results in an estimate of the predicted pass-by noise of that noise source. In order to test and to validate the prediction method, a pass-by noise test rig was built in order to replicate the pass-by noise test of the international standard ISO 362 on a laboratory scale level. The test rig provides the opportunity to move a noise source on a straight line relative to a stationary microphone. Thus, the emitted pass-by noise is recorded in order to produce a set of validation data that can be compared to the predicted pass-by noise.

3.1 The horizontal directivity method for the prediction of pass-by noise

The pass-by noise prediction method is divided into two steps. First, the circularly radiated sound pressure of a noise source is quantified in the horizontal directivity measurements. Second, the inverse square law is applied in order to combine the directivity sound pressure with the instantaneous distance between source and receiving microphone. Eventually, this results in an estimate of the pass-by noise of the noise source. The prediction method is applicable to single noise sources in anechoic condition.

In the horizontal directivity measurements, the radiated sound pressure of a

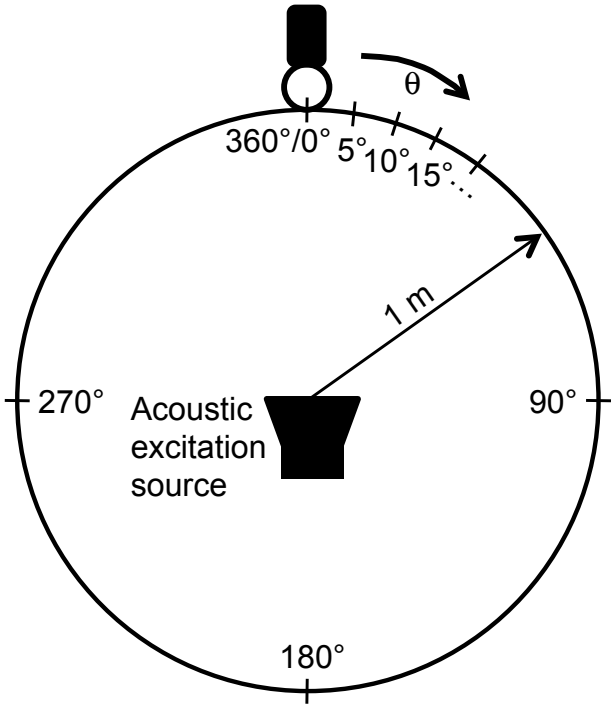

Figure 3.1: Schematic representation of the horizontal directivity measurements of an acoustic source.

noise source is determined at discrete positions on a circle around the noise source. Therefore, a reference point of the acoustic excitation source is chosen and positioned in the centre of the circle, which is parallel to the ground, as illustrated schematically in Fig. 3.1. The radius of the circle is 1 m. Microphones are positioned on the circle in increments of 5° in order to measure the radiated sound pressure of the noise source sequentially. The microphones are on the same height as the reference point of the acoustic source. White noise is selected as an appropriate excitation signal for the noise source in order to generate a broadband response of the noise source and, thus, showing their characteristic acoustic properties. The radiated sound pressure is recorded in the time domain at each of the measurement positions. The data may be subject to low-pass and high-pass filtering. Then, according to the guidelines of the international standard BS EN 61672-1 [13], the frequency A-weighting is applied to the data, which is followed by the calculation of the time-weighted average sound pressure level (SPL) $L_{A\tau}$ using Eq. 3.1 from [13]. The time constant $\tau = 0.125\,\mathrm{s}$ of the time-weighting 'Fast' is applied in Eq. 3.1 since it is also a requirement of the pass-by noise test in Refs. [10, 11].

$$L_{A\tau}(t) = 10 \times \log\left(\frac{\frac{1}{\tau}\int_{-\infty}^{t} p_A^2(\xi)\exp\left(-\frac{t-\xi}{\tau}\right)\mathrm{d}\xi}{p_0^2}\right) \tag{3.1}$$

Eq. 3.1: © British Standards Institution (BSI www.bsigroup.com). Ex-

tract reproduced with permission. Source: BS EN 61672-1:2013 Electroacoustics. Sound level meters. Specifications.

In Eq. 3.1, p_A^2 is the A-weighted instantaneous sound pressure, t is the time variable, ξ is the time integration variable, and p_0 is the reference sound pressure. The exponential function of time with the specified time constant τ is applied to weight the square of the instantaneous sound pressure in Eq. 3.1. Then, the root mean square is produced, which serves as an average value, at any instant of time t. Thus, the time-varying sound pressure signal is continuously averaged, which is based on all past values of the signal. Recent sound pressure data is more weighted than older data due to the exponential function. The frequency-weighting and the time-weighting of the time history of the sound pressure data represents also a requirement in the vehicle pass-by noise test of the international standard ISO 362.

In the second step of the pass-by noise prediction method, the inverse square law is applied. According to the inverse square law, the squared sound pressure p_s^2 of a propagating plane sound wave in free space is inversely proportional to the squared distance r_s^2 between the source of the sound wave and the point of observation: $p_s^2 \propto 1/r_s^2$. Based on this, a relation between the sound pressure at two points of observation, which are located at different distances from the source, can be established as $p_1^2/p_2^2 = r_2^2/r_1^2$. If both distances and one of the sound pressure values are known, the other sound pressure value can be calculated using $p_1^2 = p_2^2 \times r_2^2/r_1^2$. This relation can be applied in the prediction of pass-by noise, if the sound pressure data of the directivity experiments are combined with the instantaneous distance between the noise source and the receiver as well as the distance between the noise source and the measurement positions of the directivity experiments. Therefore, p_2 is substituted with the directivity sound pressure, r_2 with the instantaneous distance and r_1 with the constant distance in the directivity experiments. This results in the prediction of a single pass-by noise level value of the noise source at a specific discrete location of the noise source relative to the receiving microphone. Eq. 3.2 is applied for the pass-by noise prediction; Fig. 3.2 visualises the pass-by manoeuvre schematically.

$$p_r^2\left(\theta\left(t_i - \frac{r_s}{c}\right), r_s\left(t_i - \frac{r_s}{c}\right)\right) = \frac{r_D^2 \times p_s^2\left(\theta\left(t_i - \frac{r_s}{c}\right)\right)}{r_s^2\left(t_i - \frac{r_s}{c}\right)} \tag{3.2}$$

where p_r is the predicted sound pressure at the microphone location for a particular position of the noise source on its path, p_s is the frequency-weighted and time-weighted sound pressure of the source recorded in the horizontal directivity experiments, r_s is the instantaneous distance between the source and the micro-

phone, and r_D is the distance between the noise source reference point and the microphone in the directivity measurements, which is set to 1 m, θ is the instantaneous angle between the direction of motion of the noise source and the distance vector, the variable t_i represents a point in time and c is the speed of sound.

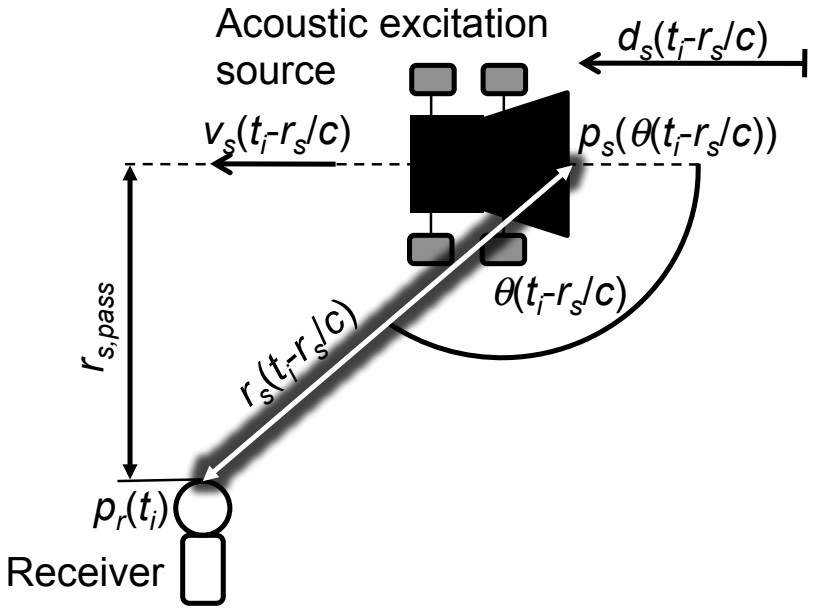

Figure 3.2: Schematic representation of a moving noise source on a straight line relative to a receiving pass-by noise microphone.

Before the pass-by noise can be predicted, a geometrical relation between the instantaneous position of the moving noise source and the static position of the receiver, which is the microphone, is to be established. This is generally based on the test layout of the ISO 362 pass-by noise test. The schematic of the test situation is illustrated in Fig. 3.2 in which an acoustic source moves on a straight line relative to the receiving microphone. The travelled distance of the noise source is d_s and its speed is v_s. The instantaneous distance r_s between the source and the microphone becomes shortest when the reference point on the noise source passes the microphone, which is denoted $r_{s,pass}$.

The travelled distance d_s of the source and its velocity v_s can be detected through various measurement devices. If the distance d_s is known, the angle θ and the distance r_s can be calculated. Since the angle θ has the same reference line and orientation in the directivity measurements and in the pass-by measurements, it can be used to select the sound pressure p_s from the recorded directivity data. Linear interpolation may have to be applied in case of the angle θ lying between

two adjacent directivity measurement positions. Therefore, Eq. 3.3 is utilised.

$$p^2_{s,interp}(\theta_i) = \frac{\theta_i - \theta_{i-1}}{\theta_{i+1} - \theta_{i-1}}(p^2_s(\theta_{i+1}) - p^2_s(\theta_{i-1})) + p^2_s(\theta_{i-1}) \tag{3.3}$$

where $p^2_{s,interp}$ is the interpolated directivity sound pressure at the angle θ_i, the measured directivity sound pressures are $p^2_s(\theta_{i-1})$ and $p^2_s(\theta_{i+1})$ with θ_{i-1} and θ_{i+1} being their corresponding measurement positions on the circle in Fig. 3.1.

With $r_D = 1\,\text{m}$ and both the directivity sound pressure p_s and the distance r_s being available, the sound pressure p_r of the passing acoustic source can be obtained at the microphone position. Eq. 3.2 is repeated for a number of noise source positions in order to produce a graph of discretely distributed pass-by noise prediction values against the source positions on the test track d_s. The prediction method in this form is applicable in anechoic conditions.

3.2 The experimental pass-by noise test rig used for validation

An experimental rig with a moving trolley, on which a sound source can be installed, was constructed and operated on a static track in an anechoic chamber in order to measure validation data and to test the predictive pass-by noise model. A schematic representation of the experimental apparatus is shown in Fig. 3.3. Here, the orifice noise source is installed on the trolley, which is pulled by an electrically powered winch, thus, representing a moving sound source.

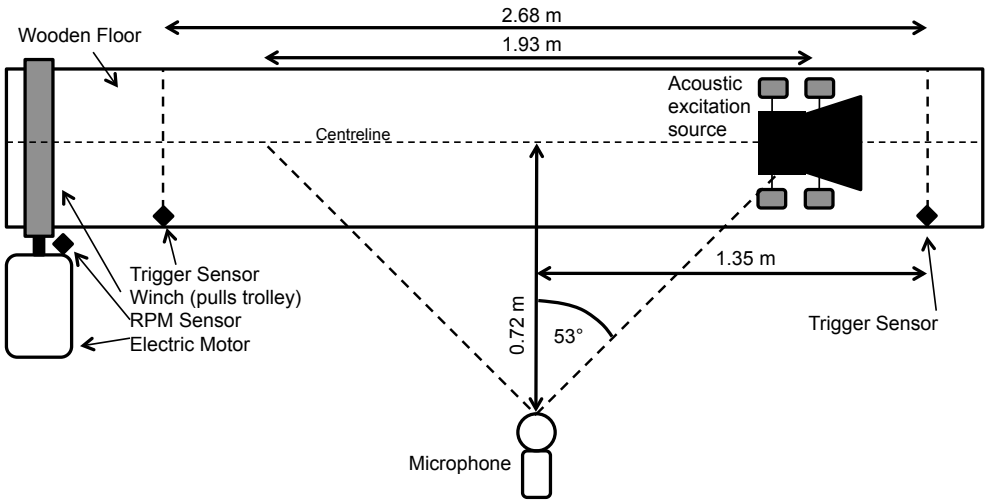

Figure 3.3: Schematic representation of the experimental apparatus for the pass-by noise test.

The test track consists of wooden boards, which are 0.3 m wide. Due to the limited size of the anechoic chamber, which is 6.4 m in length, 5.2 m in width, and 5.3 m in height, the dimensions of the experimental setup are restricted to a maximum length of approximately 3 m. In addition, interferences, which are believed to be due to reflections from the metallic grid floor, have a significant influence on the measured sound pressure of a moving sound source. The grid floor has a different pattern in the lateral direction than it has in the longitudinal direction, which may affect the appearance of interferences. The interferences appear to have a lesser effect when the test rig is lined up in the lateral direction of the chamber, and they are further reduced due to the lifting of the test rig above the floor.

Two photoelectric sensors detect the entry and exit of the noise source into the pass-by noise test area. Each sensor is installed in a retroreflective arrangement in which the sensor combines the transmitter and receiver of a light beam in the same location whilst the emitted light beam bounces back to the transmitter via a reflector. Thus, the photoelectric sensors serve as trigger sensors, which provide distinct signals when the trolley passes by and interrupts the light beams. Thus, the beginning and end of the measurement period can be determined accurately ensuring that only measurement data related to a moving noise source is recorded. The distance between the two trigger sensors is 2.68 m. Due to the restricted length of the test rig, the rear axle of the trolley activates the trigger sensor at the entry position when crossing the light beam. The front axle of the trolley activates the trigger sensor at the exit position. This arrangement provides the largest possible distance over which the trolley can be moved. The actual length of the pass-by noise test zone is reduced to 1.93 m, because the test zone is determined by the positions where the trolley enters and exits the test zone, which corresponds to the conditions of the ISO 362 pass-by noise test. When the wheelbase of the trolley, 0.375 m, is included, data can be recorded over a distance of 2.3 m. The electric motor and winch system are covered by a wooden box with sound insulation material on the inside in order to reduce their operational noise. The sound insulation material has an overall thickness of 32 mm and consists of two layers of polyurethane foam and a lead barrier layer with a density of 10 kg/m^2 between them.

The position and velocity of the trolley can be determined using the geometrical dimensions of the experimental setup and the recordings of the electric motor speed and of the time signal. Beforehand, the measured motor speed signal is corrected since a calibration test revealed small deviations from the linear relation between the motor voltage and the motor speed. Such deviations can result from non-linearities in the electric motor design like friction, for example. In order

to increase the accuracy of the measured motor speed signal, a scale factor is introduced in order to correct the motor speed signal. The scale factor is obtained from spectroscope measurements of the motor speed and its corresponding motor voltage.

In addition, a Savitzky-Golay Finite Impulse Response (FIR) filter is applied to the corrected motor speed data. The filter reduces the noise in a data signal by fitting a polynomial to the signal with a minimal least-square error. The filtered value of a specific data point is calculated utilising a limited number of adjacent data points and fitting the polynomial into the selection of data points. As default values, a fourth order polynomial and 1001 data points were chosen. Thus, it is ensured that the polynomial takes into account the trend of the recorded signal in a broader range. In addition, a sampling rate of up to 20480 Hz and a recording duration of up to 3.5 s lead to a high number of samples, which requires a likewise high number of data points for the curve fit. By inspection, a polynomial of fourth order, in combination with the number of data points, appears to provide accurate results as well as an acceptable computation time. The filtered and unfiltered motor speed signal are presented in Fig. 3.4. In comparison to the unfiltered signal, the clarity and understanding of the diagram have been increased whilst the overall trend of the motor speed signal is maintained. The filtering also improves the calculation of the position and velocity of the moving sound source since likely errors due to noise in the recorded motor speed signal are minimised.

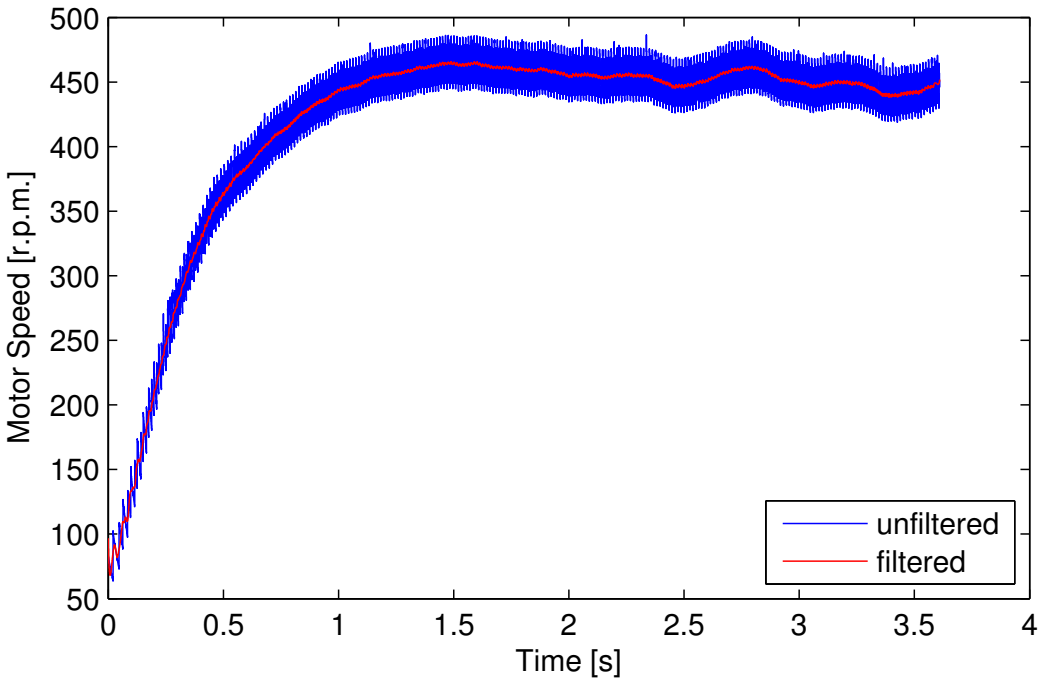

Figure 3.4: The measured motor speed signal without and with the application of the Savitzky-Golay filter.

Using the filtered data of the motor speed n, the velocity of the trolley v can be calculated at each sample point.

$$v(t_i) = 2\pi \times r \times n(t_i) \tag{3.4}$$

The travelled distance s of the trolley can be determined applying Eq. 3.5. The corresponding acceleration a can be obtained using Eq. 3.6.

$$s(t_i) = \frac{1}{2} \times a(t_i) \times t_i^2 + v(t_i) \times t_i \tag{3.5}$$

$$a(t_i) = 2\pi \times r \times \frac{n(t_{i+1}) - n(t_{i-1})}{t_{i+1} - t_{i-1}} \tag{3.6}$$

In Eqs. 3.4 to 3.6, v is the trolley velocity, $r = 15\,\text{mm}$ is the radius of the winch, n is the measured motor speed, which is equivalent to the rotation of the winch, t_{i-1}, t_i and t_{i+1} are the $i\text{th}-1$, $i\text{th}$ and $i\text{th}+1$ sample points in time with the condition of $t_{i-1} < t_i < t_{i+1}$, a is the trolley acceleration, and s is the trolley position on the test track related to the rear axle of the trolley. It is assumed that the acceleration is constant between the time data points t_{i-1} and t_{i+1}.

In order to maintain a geometrical relation between the ISO 362 vehicle pass-by noise test and the laboratory experimental setup, the pass-by noise microphone is positioned midway at a distance of 0.72 m to the centreline of the test track. Thus, the measurement angle between the microphone and the entry and exit lines of the acoustic test zone remains at a value of approximately 53°, as it is the case in the ISO 362 test. Thus, a scaling factor can be determined based on the ratio of the lengths of the acoustic test zones of the ISO 362 test and the laboratory experimental setup, which results in $1.93\,\text{m}/20\,\text{m} = 0.0965$. The value of the scaling factor is confirmed by the ratio of the distances between the microphones to the centrelines of the acoustic test zones, which equates to $0.72375\,\text{m}/7.5\,\text{m} = 0.0965$, including all existing decimal places for the purpose of accuracy. Thus, it is shown that the length of the acoustic test zone as well as the distance of the microphone to the centreline of the acoustic test zone is accurately scaled in the laboratory experimental setup. Despite the accurate geometrical scale, it has to be noted that the combination of the noise source and the experimental rig does not have an exact scaling relation to the combination of the real vehicle noise sources and the ISO 362 test track. Since the whole experimental setup is lifted, the microphone has a height of 1.035 m above the grid floor of the anechoic chamber.

The electric motor is controlled manually. The trolley is accelerated from a standstill with the rear axle just in front of the entry trigger sensor. A time

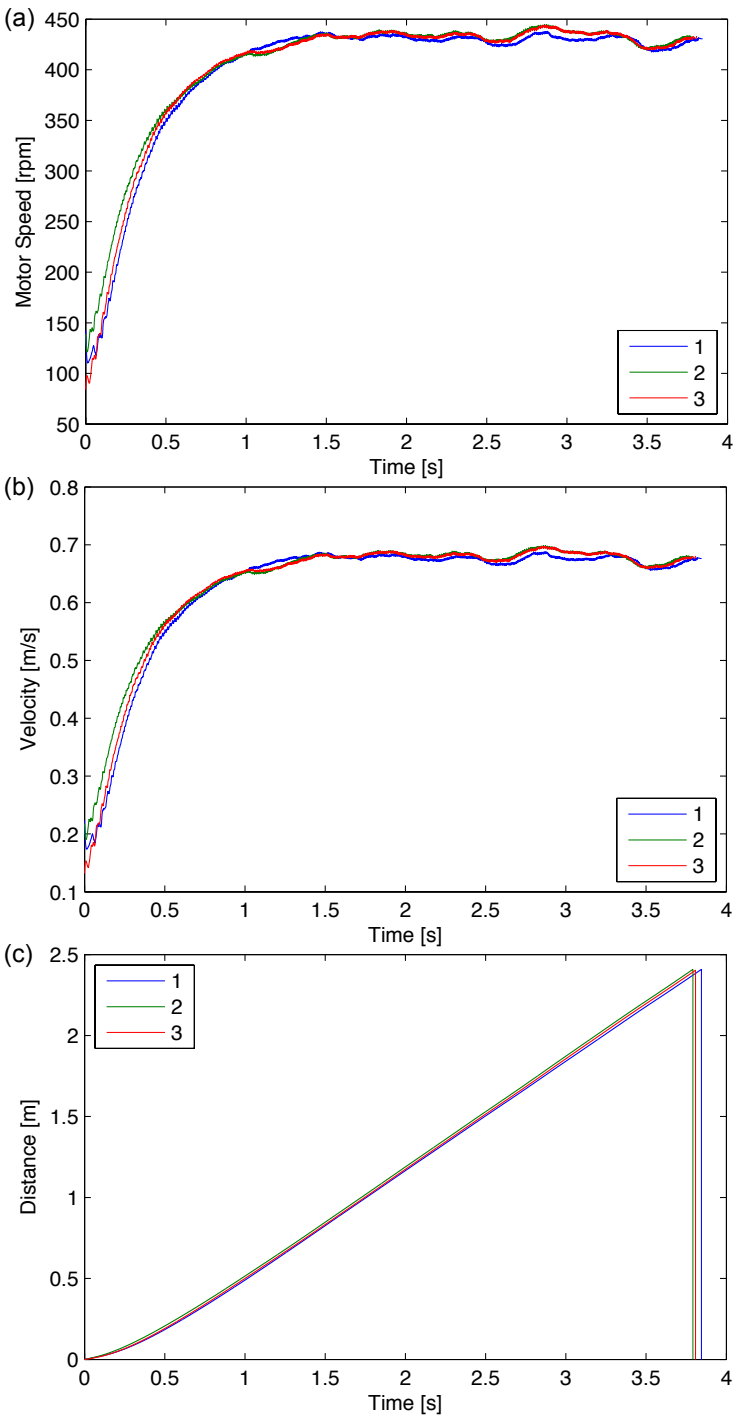

Figure 3.5: (a) Measured motor speed versus time; (b) calculated velocity of the trolley versus time; (c) track position of the moving noise source.

history of the sound pressure is recorded for as long as the noise source moves through the pass-by noise test zone. A typical recording of the motor speed signal is plotted against time for three consecutive pass-by runs in Fig. 3.5 along with the calculated velocity and distance of the trolley. The measurement data for the motor speed shown in Fig. 3.5 (a) indicate that the initial acceleration over the first 1 s of travel can be repeated well. The motor speed then develops into

an approximately constant speed pattern, the trend of which is reproduced in all runs. Overall, a good repeatability could be achieved, which is also reflected in the derived results of the trolley velocity and distance shown in Figs. 3.5(b,c). The maximum speed is about 2.4 k.p.h. Small differences in the start position are the likely reason for the variations in the initial motor speed values between test runs. The variations in the constant speed pattern from 1 to 3.75 s may be caused by flexibilities in the winch system or unevenness of the test track. The duration of a vehicle pass-by in the ISO 362 test varies, since it depends upon the engine power. The measurement duration of the passing trolley can be ranked as a slow pass-by in comparison to the real test situation. Reflection and scattering of sound from the ground and the complex geometric structure of the vehicle are not simulated in this simplified pass-by noise experiment. Reflections from the ground do not occur due to the anechoic environment. Reflections from the test track and the experimental equipment are assumed to be negligible.

3.3 Summary

In this chapter, the pass-by noise prediction method was presented for anechoic conditions. First, a single noise source is subject to the horizontal directivity measurements in which the radiated sound pressure of the noise source is recorded in a circle around the noise source. A reference point on the noise source is selected and is placed in the centre of the circle. The measured sound pressure is frequency-weighted and time-weighted, which is also a requirement of the standard ISO 362. The pass-by noise is eventually predicted through the inverse square law, which combines the directivity sound pressure with the instantaneous distance between the passing noise source and the stationary receiver. The instantaneous distance corresponds to a particular noise source position on the test track, since all objects except the moving noise source have fixed locations. Thus, the predicted pass-by noise can be related to a particular position of the noise source on the test track.

In order to test the prediction method, a scaled pass-by noise test rig was designed and built to be operated under laboratory conditions. The test rig can be utilised to move a noise source on a straight line relative to a stationary microphone, thus, replicating the standardised pass-by noise test. The position of the noise source on the track can be obtained through various sensors, which enables to produce a plot of the measured pass-by noise against the travelled distance. Hence, the measured pass-by noise serves as validation data to which the predicted pass-by noise is to be compared.

The pass-by noise prediction is tested using vehicle noise source replicas under laboratory conditions. The replicated noise sources as well as the comparison

between predicted and measured pass-by noise is presented in Chapters 4, 5 and 6.

Chapter 4

Pass-by noise prediction for an orifice noise source

Orifice noise source is identified as a major contributor to vehicle pass-by noise. Such noise source is represented by the orifices of the intake and the exhaust systems on the vehicle. For the testing of the proposed pass-by noise prediction method of this work in the available laboratory facility, an orifice noise source (ONS) is designed and built in order to replicate the equivalent vehicle orifice noise sources.

In this chapter, the design of the ONS is introduced. The prediction method requires that the radiated sound pressure of the ONS is to be determined in the horizontal directivity measurements. Therefore, the experimental procedure as well as the analysis of the measured directivity sound pressure are presented. Eventually, the prediction method is carried out for four different arrangements of the ONS. A noise source can be mounted on the trolley in order to simulate a moving noise source similar to the vehicle pass-by noise test. The ONS can be arranged in an exhaust orifice configuration, with the duct pointing opposite to the direction of motion, or in an intake orifice configuration, with the duct pointing in the direction of motion. Both configurations can also be realised reciprocally, which means that the ONS remains stationary and the microphone is moved pass the ONS. The corresponding experimental procedure for the recording of the pass-by noise validation data of the ONS is explained. This is followed by the predicted pass-by noise of the ONS which is compared to measured pass-by noise.

4.1 Design of the orifice noise source replica

For the replication of orifice pass-by noise, an orifice noise source (ONS) is built in order to be operated in conjunction with the pass-by noise test rig. Fig. 4.1

illustrates the interior of the ONS and Fig. 4.2 shows a photograph of the ONS. A loudspeaker is positioned at the top of a plastic duct, which has a length of 0.34 m and an inner diameter of 0.152 m. The loudspeaker has an electrical resistance of 8 Ω and operates across a frequency range of 67 Hz to 8000 Hz. A layer of foam on wooden plate is placed right behind the loudspeaker. The remaining duct volume behind the plate is filled with insulation material in order to attenuate the noise radiation on the rear-side of the ONS. The outer radius of the bracket of the loudspeaker diaphragm coincides with the outer radius of the plastic duct. On top of the loudspeaker bracket, a short wooden duct is attached to the bracket of the loudspeaker diaphragm. The wooden duct is open on the loudspeaker end but closed on the opposite end. However, in order to replicate orifice-like noise radiation, as it occurs in vehicle exhaust and intake systems, a small plastic duct is led from the centre of the loudspeaker diaphragm through the closed end of the wooden duct. The duct provides a waveguide through which the sound waves generated by the loudspeaker propagate and, at its open end, radiate into the environment. The length of the duct is 0.155 m and its diameter is 30 mm, which is assumed to be in the range of duct diameters of common exhaust and intake systems of passenger vehicles. The assembly of the ducts and the loudspeaker are covered by layers of insulation material in order to lower the noise radiation on each side and to let the noise radiation from the orifice of the small duct become more apparent.

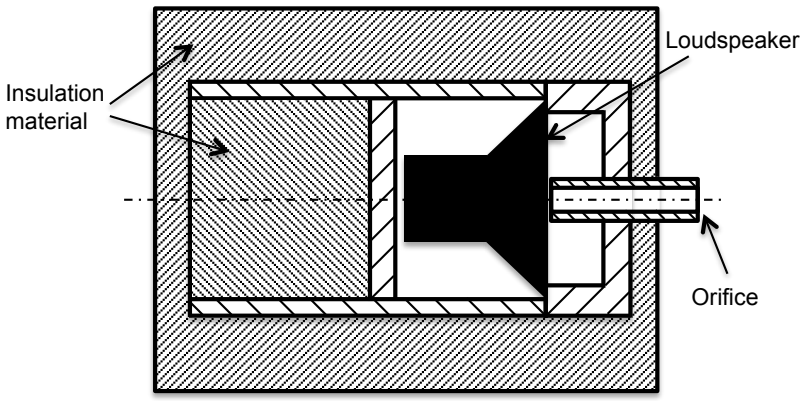

Figure 4.1: Schematic of the orifice noise source replica.

In contrast to real vehicle exhaust and intake systems, mass flux of air or exhaust gases does not occur. Thus, any temperature effect from hot exhaust gases is not considered. Since the speed of sound in a medium is dependent upon its temperature, varying temperatures within a piping system can alter its resonant frequencies significantly. The ONS does not represent the complex piping system of vehicle exhaust and intake systems. It shall replicate the acoustic radiation characteristic of the orifices of the exhaust and intake systems for which the mixing

Figure 4.2: Photograph of the exhaust orifice noise source (orifice on the left).

of hot exhaust gases and ambient air is neglected.

The propagation of a plane wave in a duct is given for the condition of $kr < 1.84$ where the acoustic wave number is k and the duct radius is r [63]. For the radius $r = 15\,\text{mm}$ of the small plastic duct, the condition is fulfilled up to a frequency of 6696 Hz. This also means that higher-order modes only cut-on at higher frequencies than 6696 Hz. Thus, up to 6696 Hz, the radiation characteristic of the orifice of the ONS is assumed to be like a monopole sound source, as it is commonly considered for the acoustic modelling of exhaust and intake system orifices. This frequency range should also generally cover the frequency range of a vehicle pass-by noise test.

For the open duct of the ONS, an end correction Δl is considered for the orifice, which is based on the radiation reactance and the tube impedance according to [63]. The equation for the end correction is $\Delta l = 0.6 \times r$ [63]. With the orifice radius $r = 15\,\text{mm}$, this results in $\Delta l = 9\,\text{mm}$. This means that the acoustic length of the tube is 9 mm longer than the tube itself. Thus, the duct length plus the end correction have tonsidered for the determination of the wavelength of the resonance frequency of an open duct. It also indicates that the location of the acoustic point source is 9 mm in front of the open duct of the ONS.

4.2 Directivity characteristics of the orifice noise source

In this section, the experimental procedure of gaining the directivity sound pressure of the ONS is presented. Then, the acoustic characteristics of the ONS a analysed based on the directivity measurement data in the time and frequency domains.

4.2.1 Experimental procedure

For the determination of the directivity characteristics of the whole ONS assembly, sound pressure measurements were conducted according to Section 3.1. The reference point of the ONS, which is positioned in the centre of the horizontal measurement circle, is the orifice, as illustrated in Fig. 4.3. Sound pressure is measured along the circle of a radius of 1 m at increments of 5° and on the height of the orifice. The height of the orifice is approximately 1 m above the metal grid floor in the anechoic chamber. White noise is utilised as the excitation signal.

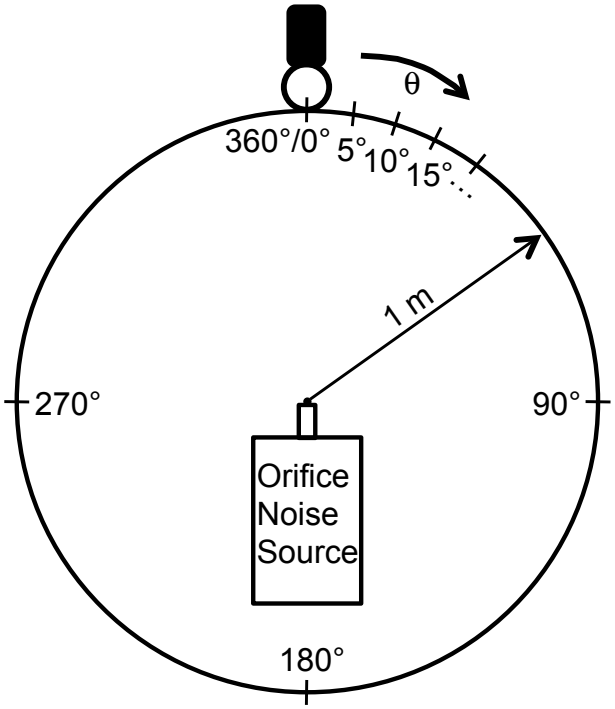

Figure 4.3: Schematic of the horizontal directivity measurements with the orifice of the ONS at the centre of the measurement circle.

For the analysis, the measured sound pressure data is filtered with a high-pass and a low-pass filter. The cut-off frequency of the high-pass filter is chosen to be 150 Hz, which is approximately the lower frequency limit of the anechoic chamber in which the recording takes place. It effectively reduces the high amplitudes in the very low frequency range. The cut-off frequency of the low-pass filter is chosen to be 6696 Hz, which corresponds to the frequency up to which the ONS can be considered as a point source. Then, the filtered sound pressure data is subject to the frequency A-weighting according to guidelines in the international standard BS EN 61672-1 [13]. In the final step, the time-weighted average sound pressure level $L_{A\tau}$ is calculated according to Eq. 3.1 using the time weighting 'Fast' with the time constant $\tau = 0.125\,\mathrm{s}$. The filtering, frequency-weighting and time-weighting is carried out on the discrete sound pressure signal in the

time domain. Both the A-weighting and the time-weighting of the time history of the sound pressure data are also applied in the vehicle pass-by noise test as it is requested in the corresponding standard ISO 362 [10, 11]. Thus, the sound pressure measurement data of the ONS directivity experiment is processed in close relation to the standard ISO 362.

4.2.2 Experimentally determined directivity sound pressure

Conducting the horizontal directivity measurements according to Section 4.2.1, the measured sound pressure data is used to determine the frequency-weighted and time-weighted sound pressure levels for each measurement position on the circle and the power spectral density (PSD) spectra at the 0°, 90° and 180° positions in order to analyse the directivity characteristics of the ONS.

The frequency-weighted and time-weighted sound pressure level serves to characterise the directivity of the ONS. Therefore, the sound pressure levels are plotted against the measurement positions in Fig. 4.4. The distribution of the sound pressure levels is approximately symmetrical around the longitudinal axis of the ONS, which is along the measurement positions of 0°/360° and 180°. The sound pressure levels are much higher at the front of the ONS than the levels at the rear. At the front, between 270° and 90°, the levels vary within a span of 3.2 dB(A). At the rear, between 130° and 225°, the levels vary within a span of 3.9 dB(A). If the SPL at 200° is considered as well, the span increases to 4.3 dB(A). The level difference between the front and the rear regions is between 8-15 dB(A). At the measurement positions between 90° and 130° as well as between 270° and 225° the SPLs decrease rapidly by about 8 dB(A). Comparing the high levels at the front of the ONS, which cover a range of ±90°, and the decreasing as well as the low levels at the other measurement positions, it is assumed that this is the main radiation direction. This is supported by the minimum level difference of 8 dB(A) between the front and the rear regions of the ONS. It is assumed that the level differences between 270° and 90° as well as between 130° and 225° could be caused by non-uniformities in the assembly of the insulation material at the front and the rear of the ONS. For example, gaps between the layers of insulation material could decrease the attenuation capability of the assembly. The measurement positions between 90° and 130° as well as between 270° and 225° may be considered as transition ranges in which the sound radiation of the orifice is still detected but it decreases with angular distance from the front region of the ONS.

For the analysis of the spectral characteristics of the ONS, the estimation of the power spectral density (PSD) is presented for the measurement positions 0°,

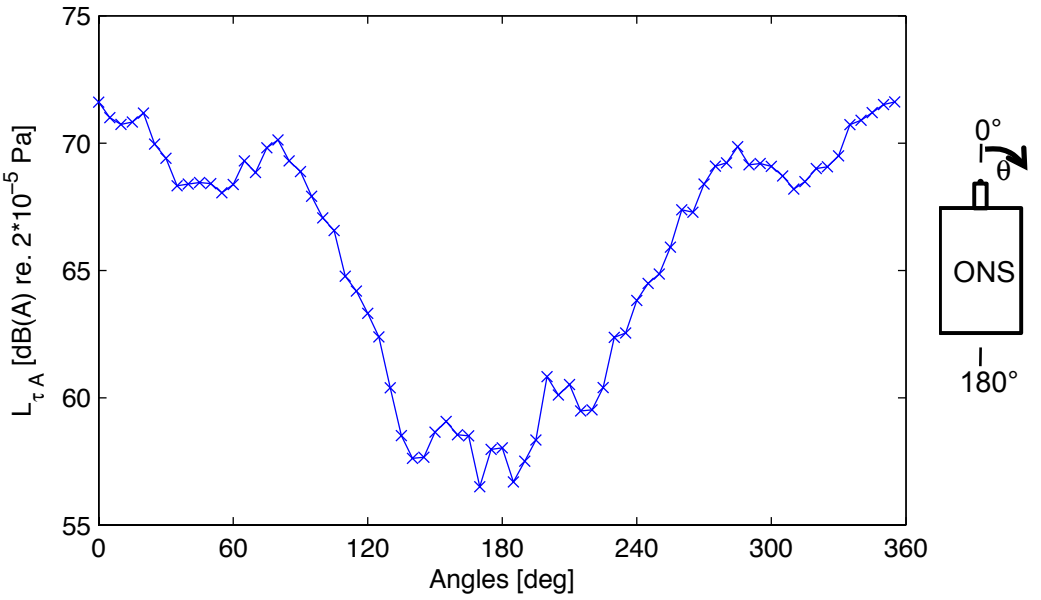

Figure 4.4: The exponential time-weighted sound pressure levels with A-weighting are used to characterise the directivity of the orifice noise source.

90° and 180° in Fig. 4.5. The resonant regions are depicted in Table 4.1.

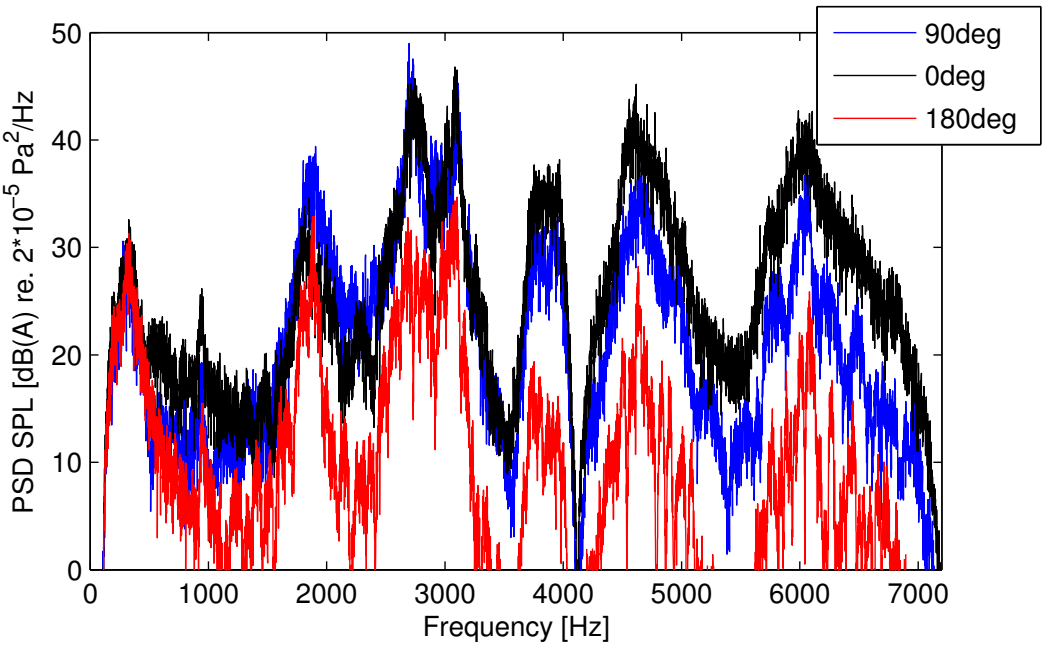

Figure 4.5: The PSD of the measured sound pressure at the measurement positions 0°, 90° and 180°.

The sound pressure levels generally decrease when the measurement position is changed from the 0° position at the front of the ONS to the 90° position on the right-hand side and to the 180° position at the rear. However, the SPLs are approximately constant at the first major resonance peak around 312 Hz for all three measurement positions. In the resonance frequency regions around 1850 Hz

	resonance frequency [Hz]	Multiple of the first resonance (approximately)
1	312	
2	948	3
3	1820 - 1880	6
4	2725	9
5	3020 - 3083	10
7	3710 - 3990	12 to 13
8	4510 - 4780	15
9	5980 - 6100	19 to 20

Table 4.1: Resonance frequencies of the ONS directivity measurements corresponding the resonance regions in the PSD spectra of Fig. 4.5.

and 2725 Hz, the SPLs of the 90° position are slightly higher than those of the 0° position. The assumption that the main radiation direction is towards the front of the ONS is supported by the similar values of the SPLs of the 0° and 90° positions. In addition, their resonances can be identified at the same frequencies in both graphs. The levels of the 90° position decrease relative to the values of the 0° position with increasing frequency. The major resonance frequency regions can also be identified in the graph of the SPL of the 180° position. However, the level differences between the spectra of the 0° and the 90° positions on the one hand and the spectrum of the 180° position on the other hand increase heavily at frequencies of 2000 Hz or higher. This may be due to a combination of the sound radiation of the ONS, which occurs primarily within the ±90° positions and decays towards the rear measurement positions, and to the applied insulation material, which may be more efficient at higher frequencies at the rear region of the ONS.

The width of all resonances are generally similar up to 4500 Hz. At higher frequencies, differences in width occur predominantly for the 180° position. Since the width of a resonance peak generally indicates the damping of a system, it is concluded that the damping is very high for the ONS. Resonance peaks of sound waves, which travel through air within a duct system, are expected to be narrow, since the damping capability of air is low. Thus, it is assumed that the resonances are affected by the whole structure of the ONS, which includes the insulation material, plastic pipes and loudspeaker.

The PSD spectra of the 90° and the 270° positions are almost identical. In order to maintain a neat arrangement in the diagram, only the spectrum of the 90° position is plotted in Fig. 4.5.

Several resonance regions can be identified in the spectra of Fig. 4.5, which are depicted in Table 4.1. However, it seems to be difficult to clearly identify a

single resonance peak in some cases. Instead high amplitudes appear over wide frequency ranges, which span from 60 to 280 Hz. The peak at 948 Hz represents an exception in that regard. In addition, the spectra appear to contain a small amount of noise, which may be due to the low number of six averages for the estimation of the PSD spectra. This may also contribute to the formation of such resonance frequency regions instead of clear single resonance peaks.

It is assumed that, depending on the frequency range of interest, the resonance frequencies are affected by the ONS structure and the applied insulation material, which may result in an acoustic system which is neither an ideal open duct nor an ideal single-sided closed duct but a combination of both. Therefore, the commonly known formulas for the calculation of the resonance frequencies of an open duct or a single-sided closed duct may not lead to accurate results when the theoretical resonance frequencies of the duct lengths of the ONS are compared to the measured resonance frequencies. The resonance frequencies of a single-sided open duct can be calculated applying Eq. 4.1.

$$f_n = \frac{(2n+1)c}{4l} \tag{4.1}$$

The resonance frequencies of a double-sided open or double-sided closed duct can be obtained using Eq. 4.2.

$$f_n = \frac{nc}{2l} \tag{4.2}$$

where f_n is the resonance frequency of the nth mode with $n = 1, 2, ...$, c is the speed of sound and l is the length of the duct.

In general, the resonance frequencies could be approximately interpreted as multiples of the first resonance at 312 Hz, as shown in Table 4.1. However, in case of the single-sided open duct, the resonance frequencies occur in multiples of odd integers only. Applying Eq. 4.1 for a single-sided open duct, it can be found that the resonance frequency 312 Hz occurs at a duct length of 0.275 m. In comparison, applying Eq. 4.2 for a doube-sided closed duct results in a duct length of 0.55 m. Assuming that a resonance does not exist below 312 Hz, both duct lengths relate to the first mode. Only the latter result can approximately be related to the overall length of the ONS, which is 0.495 m for the duct system plus approximately 0.05 m for the insulation material at the rear. Thus, the overall characteristic of the ONS tends to be that of a double-sided closed or open duct. This is doubtful, however, since the ONS can be considered as a open duct end at the orifice and a closed duct end on the opposite side where the loudspeaker and the insulation material is placed. The other resonances in the spectrum and in Table 4.1 occur predominantly at multiples of three, which then appears to be

a set of resonances of a single-sided open duct. However, multiples 10, 19 or 20 do not appear to fit into this pattern.

Table 4.2 presents the theoretical resonance frequencies, which are calculated using Eqs. 4.1 and 4.2. For both equations, the first resonance frequency is the measured first resonance frequency. Similarities occur when the theoretical and the measured resonance frequencies of Tables 4.2 and 4.1 are compared. The calculated frequencies of 936 Hz, 2808 Hz, 4057 Hz, 4680 Hz, 5929 Hz are relatively close to the measured frequencies of 948 Hz, 2725 Hz, 3990 Hz, 4510-4780 Hz and 5980 Hz. Thus, these frequencies may be associated to each other. The corresponding mode numbers are smaller for the theoretical resonances of the single-sided open duct. However, for a distinct conclusion whether the ONS is either a double-sided closed/open duct or a single-sided open duct further experimental investigation would be necessary.

n	Resonance frequency of a single-sided open duct (Eq. 4.1) [Hz]	Resonance frequency of a double-sided closed/open duct (Eq. 4.2) [Hz]
1	312	312
2	936	624
3	1560	936
4	2184	1248
5	2808	1560
6	3432	1872
7	4056	2184
8	4680	2496
9	5304	2808
10	5928	3120
11	6552	3432
12		3744
13		4056
14		4368
15		4680
16		4992
17		5304
18		5616
19		5928
20		6240
21		6552
22		6864

Table 4.2: Theoretical resonance frequencies of the ONS, which are calculated using Eqs. 4.1 and 4.2. It is assumed that the measured resonance frequency of 312 Hz is the first resonance frequency.

A small, narrow peak exists at 526 Hz, which may be associated to the first resonance frequency of the small plastic duct of the ONS through which the sound

waves are radiated into the environment. Considering this as a single-sided open duct and using Eq. 4.1, the frequency corresponds to the acoustic length of the duct, which is composed of the physical length of 0.155 m plus the end correction for an open duct of 0.009 m. Even a small peak exists at 1576 Hz, which could interpreted as the second mode of a single-sided open duct. However, the peaks appear to be unremarkable due to the noise in the signal.

The pattern of the measured resonance frequencies in the spectrum is similar to the pattern of the resonance frequencies of the exhaust and the intake systems in which resonances occur with varying amplitudes at a fundamental frequency and its multiples. However, the resonances of the ONS are spread over a much wider frequency range than the resonances of the vehicle exhaust and intake systems.

4.3 Prediction of orifice pass-by noise

In this section, the experimental determination of the pass-by noise validation data of the ONS is presented. The measured pass-by noise is analysed. Then, the predicted pass-by noise of the ONS is presented and compared to the validation data.

4.3.1 Measurement procedure of orifice pass-by noise validation data

The ONS is assumed to replicate the noise source characteristics of the orifice of the exhaust or the intake system. Since the vehicle exhaust and intake orifices are usually in line with the direction of motion of the vehicle in the ISO 362 pass-by noise test, it is aimed to replicate this form of arrangement in the laboratory scale pass-by noise experiments as well. Four different arrangements are realised for the ONS. These are the exhaust orifice and the intake orifice arrangements in which the noise source is moved along the track and the microphone is stationary off the test track. Fig. 4.6 illustrates that the ONS is in the normal exhaust orifice arrangement. These two normal arrangements are also realised reciprocally in which the noise source is stationary at the previous microphone position and the microphone is moved on the trolley of the pass-by noise test rig along the test track. Fig. 4.7 illustrates the reciprocal arrangement of the ONS being in the intake orifice configuration, since the orifice points towards the microphone at the beginning of the pass-by noise recording.

In order to replicate the orifice of an exhaust system, the ONS is mounted on the trolley of the experimental pass-by noise test rig in such a way that its orifice points in the opposite of the direction of motion of the trolley. This arrangement is

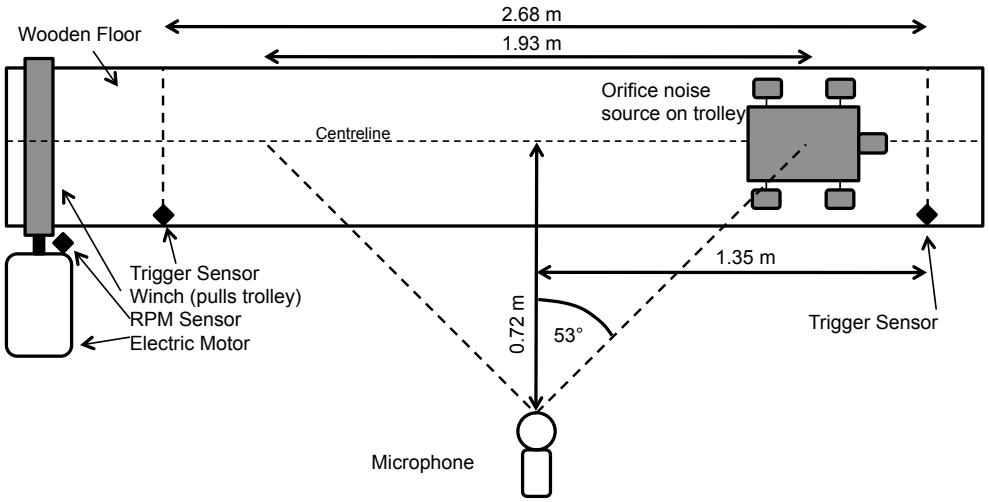

Figure 4.6: Schematic of the pass-by noise validation experiment for the orifice noise source, being mounted on the moving trolley, in the normal exhaust arrangement.

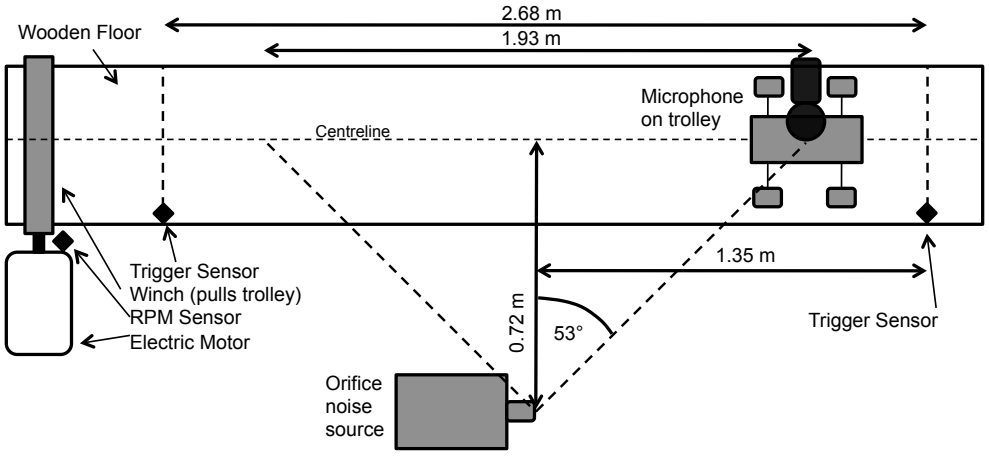

Figure 4.7: Schematic of the pass-by noise validation experiment for the orifice noise source in the reciprocal intake arrangement with the ONS being stationary and the microphone being mounted on the moving trolley.

denoted 'normal exhaust orifice configuration'. The orifice of the ONS is positioned right above the rear axle of the trolley, which is used to trigger the recording of the electric motor speed, which is needed for the estimation of the position of the trolley on the track. Thus, the position of the orifice corresponds to the calculated position of the rear axle. If the orifice of the ONS points in the moving direction of the trolley, the ONS is thought to replicate the orifice of an intake system. This arrangement is denoted 'normal intake orifice configuration'. In this arrangement, the orifice of the ONS is positioned 0.375 m ahead of the rear axle of the trolley. Thus, the position of the noise radiation and the calculated distance do not coincide. Therefore, this offset is incorporated in the graphs of the pass-by noise levels against distance in order to provide the true position from where the measured sound pressure is radiated. For both of the normal arrangements, the microphone is located at the stationary pass-by noise measurement position in the anechoic chamber, which is presented in Fig. 3.3.

Denotation	Position of the ONS	
normal exhaust orifice configuration	orifice points in opposite motion direction	normal arrangement with ONS mounted to the moving trolley
normal intake orifice configuration	orifice points in motion direction	
reciprocal exhaust orifice configuration	orifice points points towards the test track end	reciprocal arrangement with ONS at stationary position off the track
reciprocal intake orifice configuration	orifice points towards the test track entry	

Table 4.3: Overview of the four different arrangements of the ONS in the pass-by noise experiments.

Denotation	Offset in pass-by noise graphs
normal exhaust orifice configuration	-0.009 m
normal normal intake orifice configuration	(0.375+0.009) m
reciprocal exhaust orifice configuration	(0.1875+0.009) m
reciprocal intake orifice configuration	(0.1875-0.009) m

Table 4.4: Overview of the offsets due to the different positions of the orifice of the ONS or the microphone, respectively, which are used to plot the measured SPL against the distance value at which it was measured.

Two other arrangements of the ONS are based on the reciprocal measurement principle. Therefore, the positions of the microphone and the ONS are swapped. The microphone is attached to a bracket, which is mounted to the trolley. There is a 90° angle between the microphone axis and the moving direction of the trolley, which means that the microphone points towards the stationary ONS. The orifice of the ONS is placed at the same position where the microphone is located in the

normal pass-by noise measurements. However, the tube of the ONS is parallel to the moving direction of the trolley. In order to replicate the exhaust orifice configuration reciprocally, the orifice of the ONS points in the moving direction of the trolley. Thus, the relative positions of the microphone and the ONS are identical to the corresponding 'normal exhaust orifice configuration'. This arrangement is denoted 'reciprocal exhaust orifice configuration'. In order to replicate the intake orifice configuration reciprocally, the orifice of the ONS points in the opposite direction of the moving trolley. Thus, the relative positions of the microphone and the ONS are identical to the corresponding 'normal intake orifice configuration'. This arrangement is denoted 'reciprocal intake orifice configuration'. For both reciprocal arrangements, an offset of 0.188 m is considered in the pass-by noise graphs, which corresponds to the distance between the rear axle of the trolley and the position of the microphone in the middle of the trolley. Thus, the measured sound pressure level is plotted against the distance value at which it has been measured.

Table 4.3 summarises the four different arrangements of the ONS in the experiments. Table 4.4 gives an overview about the offsets due to the position of the orifice of the ONS or the microphone, respectively, in the pass-by noise experiments. This also includes the end correction, which has been introduced in Section 4.1 and which is either added to or subtracted from the offset value.

4.3.2 Comparison of measured and predicted pass-by noise

The results of the pass-by noise prediction of the Orifice Noise Source (ONS) are presented in this section. Therefore, the ONS is positioned in four different arrangements for which the pass-by noise is measured in anechoic condition, which serves as the validation data for the predicted pass-by noise. The pass-by noise prediction is carried out for each of the noise source arrangements applying the directivity method.

The four different arrangements of the ONS are 'normal exhaust orifice', 'normal intake orifice', 'reciprocal exhaust orifice', 'reciprocal intake orifice'. An overview of the four arrangements is given in Table 4.3 of Section 4.3.1. The measured pass-by noise of the two normal arrangements is plotted against the source position on the test track in Figs. 4.8, 4.9. For the two reciprocal arrangements, the measured pass-by noise is plotted against the microphone position on the track in Figs. 4.10 and 4.11. The distance values vary due to the location of the orifice of the ONS in the regular arrangements or to the location of the microphone on the trolley in the reciprocal arrangements. Thus, the distance values correspond to

the position when the pass-by noise is detected. In addition, an end correction of 9 mm is considered for the duct of the ONS, as outlined in Sections 4.1 and 4.3.1.

The ONS is excited by a white noise signal over the frequency range of interest. The measured pass-by sound pressure is filtered with a digital high-pass filter, which is of sixth order and has a transition frequency of 150 Hz, and a digital low-pass filter, which is of 20th order and has a transition frequency of 6696 Hz. Since the standard ISO 362 for the measurement of the vehicle pass-by noise requests that the pass-by noise level is to be frequency-weighted and time-weighted, this procedure is applied to the measured sound pressure data, which results in the pass-by noise level $L_{A\tau}$. This approach shall increase the level of reality of the laboratory scale experiments.

Three consecutive pass-by noise recordings were carried out in each configuration. The differences between the three recorded signals in each configuration are generally within 0.5 dB(A) with a few exceptions up to 1 dB(A) only. Thus, the repeatability of the pass-by noise is deemed to be good in general in each experimental configuration.

In all of the four arrangements, the measured pass-by noise level increases rapidly at the beginning of the recording. This is a consequence of the exponential time-weighted average formula for which a time period must elapse before the averaged value becomes accurate. When the trolley has travelled for approximately 0.15 m, it is assumed that accurate $L_{A\tau}$ values can be expected.

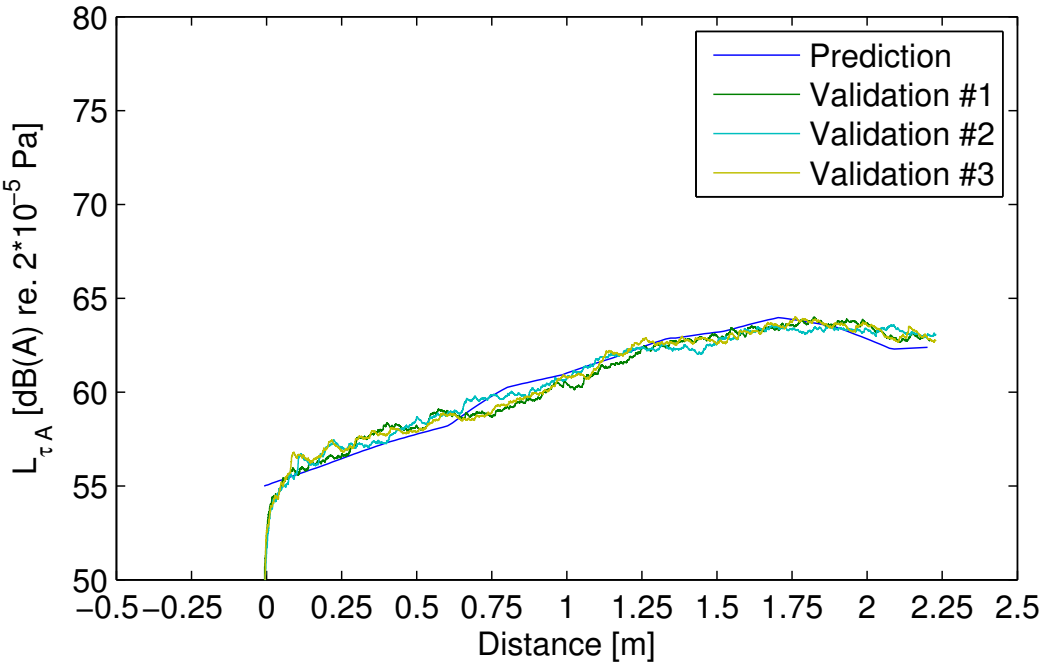

Figure 4.8: Comparison of the predicted and measured pass-by noise signals for the exhaust orifice configuration.

The measured pass-by noise of the 'normal exhaust orifice configuration' arrangement is shown in Fig. 4.8. The pass-by noise level $L_{A\tau}$ increases steadily with distance. Since the orifice of the ONS points away from the pass-by noise microphone at the beginning of the recording, a low pass-by noise level was expected. Then, the noise level rises whilst the ONS is moving. Here, two effects are assumed to contribute to the rising pass-by noise level. First, the distance between the noise source and the receiver decreases. Thus, the attenuation through distance decreases as well. Second, the relative angular position between the noise source and the microphone alters, which changes the influence from the directivity characteristics of the ONS. The measured pass-by noise level potentially rises since the corresponding SPL of the directivity graph in Fig. 4.4 increases at the angles between 120° to 80°, which correspond approximately to the altering angles during the pass-by noise experiment. When the trolley has passed the microphone position, the microphone is directly exposed to the radiated noise from the ONS. According to the directivity characteristics, the SPL is highest within ±90° at the front of the orifice, which is assumed to be reflected in the measured pass-by noise. Also, the maximum level of about 64 dB(A) is reached at 1.76 m. Then, the level begins to decrease slowly whilst the ONS is receding. The difference between minimum and maximum pass-by noise level is approximately 7-8 dB(A). The rising and falling pass-by noise level as well as the maximum pass-by noise level appearing in the second half of the test track generally coincides with the real pass-by noise test, as it can be seen in Figs. 2.1 and 2.8, for example.

The predicted pass-by noise level for the 'normal exhaust orifice configuration' in Fig. 4.8 is generally very close to the measured pass-by noise level. The highest difference between both levels is 1.3 dB(A). However, for the majority of the levels, the difference is less than 1 dB(A). This is seen as a good result for the prediction. Both the directivity SPL and the distance between the noise source and the recording microphone determine the predicted pass-by noise level. It is assumed that some of the directivity characteristics can be recognised in the predicted pass-by noise level. The relative steady increase of the predicted pass-by noise level is related to the relative steady increase of the directivity SPL, which occurs between 130° and 90°, for example. A more rapid change in the gradient at 0.6 m, for example, is caused by a rapid increase in the directivity SPL between 110° to 105° in Fig. 4.4. If the directivity SPL of an angular position is needed in the prediction method, which lies between adjacent directivity SPLs, a linear interpolation is carried out in order to obtain an interpolated directivity SPL, which is then used in the prediction method. Thus, the steady increase of the predicted pass-by noise level is partly due to the linear interpolation of the directivity SPL. The progression of the predicted pass-by noise level between the

1.75 m mark until the end of the test track is mainly determined by the directivity SPL between 90° and 0°, which results in a relative good agreement with the measured pass-by noise level. Only one prediction graph is plotted since the distance between the noise source and the recording microphone is constant for each test run.

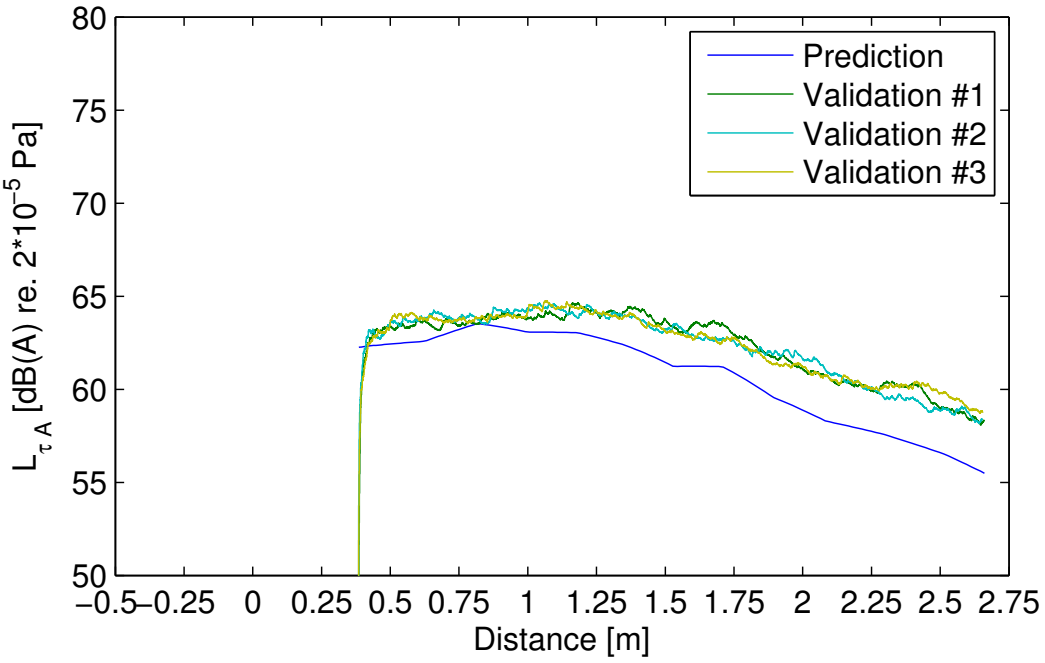

Figure 4.9: Comparison of the predicted and measured pass-by noise signals for the intake orifice configuration.

The measured pass-by noise of the 'normal intake orifice configuration' arrangement is shown in Fig. 4.9. The pass-by noise level $L_{A\tau}$ shows an inverse characteristic in comparison to the level of the 'normal exhaust orifice configuration' in Fig. 4.8. At the beginning of the recording, the pass-by noise level increases slightly by about 1.5 dB(A) to 64.5 dB(A) at 1.15 m, which is the maximum level. In this region of the test track, the front of the ONS with its noise radiating orifice faces the microphone. Thus, higher noise levels are expected. The measured pass-by noise level then starts to decrease until the end of the test track, which is due to the changing directivity characteristics of the moving ONS. In the intake orifice configuration, the angles between 360° to 230° of the directivity measurement in Fig. 4.4 face the pass-by noise microphone. Thus, the directivity SPLs at these positions are assumed to have the significant influence on the pass-by noise level. The measured pass-by noise level decreases with a steeper gradient from around 1.5 m, although the orifice of the ONS has not yet passed the microphone position at approximately 1.75 m. The difference between minimum and maximum pass-by noise level is approximately 5 dB(A), which is less than the difference in

the exhaust orifice configuration. It is assumed that the characteristic rising and falling of the pass-by noise level as well as the maximum level appearing in the first half of the test track generally reflects the pass-by noise characteristics of a vehicle intake orifice noise source.

In Fig. 4.9, the trend of the predicted pass-by noise level of the 'normal intake orifice configuration' generally agrees very well with the measured pass-by noise level. However, the predicted levels are smaller than the measured levels over the measurement distance, which excludes the beginning of the recording when the exponential time-weighting function produces inaccurate values. In the prediction method, the directivity SPLs of the angular positions of 360° to 230° are mainly utilised in conjunction with the calculated distance between the noise source and the receiver microphone. In contrast to the measured pass-by noise level, the maximum level of the prediction, which has a value of 63.5 dB(A), appears earlier at around 0.8 m. The difference between the measured and the predicted values is less than 1.5 dB(A) up to a distance of 1.35 m. Then, the difference increases and varies between 1.5-2.5 dB(A), which depends on the validation data to which the predicted level is compared. From 1.9 m, the difference increases to about 3 dB(A). For the remaining distance on the test track, the difference varies between 2.5-4 dB(A). The highest difference of 4 dB(A) occurs at about 2.4 m at which the orifice of the ONS has passed the microphone position and the directivity SPL at the positions of 270° or less are utilised in the prediction method. From about 1.25 m, the difference between the measured and the predicted pass-by noise level increases very slowly with distance. It almost appears that the level difference remains constant over short stages along the track.

Since the trend of the measured pass-by noise level can be generally reproduced with the predicted pass-by noise levels, it is concluded that the prediction method works well for the ONS in the normal configurations. The differences between both levels increase in the second half of the test track, where potentially the rolling noise of the trolley has a greater influence due to a decreasing SPL of the ONS, which is confirmed by the SPL at the angular positions between 270° to 230° in the directivity graph in Fig. 4.4.

The measured pass-by noise of the 'reciprocal exhaust orifice configuration' is shown in Fig. 4.10. This configuration shall replicate the pass-by noise of an exhaust orifice in a reciprocal measurement arrangement. Thus, the ONS is stationary, with orifice pointing initially away from the microphone, and the microphone is moved along the test track. The pass-by noise level $L_{A\tau}$ is generally higher than in the two normal arrangements which may be due to higher setting in the amplified volume of the loudspeaker inside the ONS. The pass-by noise level $L_{A\tau}$ increases steadily with a relatively high gradient when the microphone

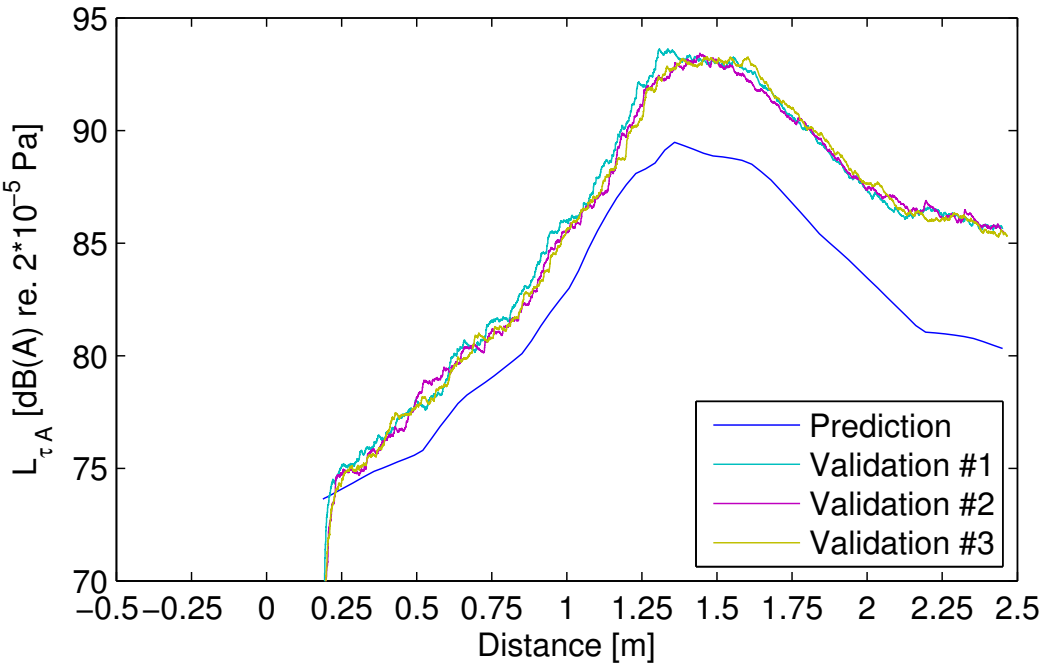

Figure 4.10: Comparison of the predicted and measured pass-by noise signals for the reciprocally arranged exhaust orifice configuration.

is moved forward, approaching the ONS from its rear side. The minimum level is 74.9 dB(A) at 0.32 m. The maximum levels of more than 93.3 dB(A) are measured between 1.33-1.6 m, where the microphone is at the closest distance to the orifice of the ONS. The microphone passes the orifice at approximately 1.54 m. Then, the pass-by noise level decreases to 85.6 dB(A) at around 2.45 m. The gradient of the pass-by noise level of the receding ONS is less steep than the gradient of the approaching ONS. This may be due to the unobstructed noise radiation from the orifice to the microphone. The difference between the minimum and the maximum level is about 18 dB(A), which is more than the difference of 7-8 dB(A) in the 'normal exhaust orifice configuration'. In contrast to the 'normal exhaust orifice configuration' of the ONS in Fig. 4.8, the pass-by noise level of the 'reciprocal exhaust orifice configuration' increases more rapidly having a higher difference between the minimum and the maximum levels as well as higher noise levels.

The trend and the gradients of the measured level are generally reproduced well by the predicted level. The difference between the measured and the predicted levels is less than 0.5 dB(A) at the beginning of the test track. The difference remains at 2 dB(A) for most positions up to 1.3 m, only occasionally rising to approximately 2.7 dB(A) at 0.5 m and 1.0 m for example. Between 1.3 m and 2.2 m the difference is almost constant at about 4 dB(A). For the rest of the test track, the difference between the measured and the predicted pass-by noise level remains between 5-6 dB(A). Rolling noise or background noise, respectively,

originating from the operation of the pass-by noise test rig, is excluded as a cause for the difference between measured and predicted pass-by noise due to the very large difference between rolling noise and pass-by noise. The maximum rolling noise level is less than 65 dB(A), which is about 10 dB(A) less than the minimum pass-by noise level. Thus, the rolling noise level is negligible. A possible cause for the difference between measured and predicted pass-by noise may be reflected sound from the pass-by noise test rig when the ONS is moved along.

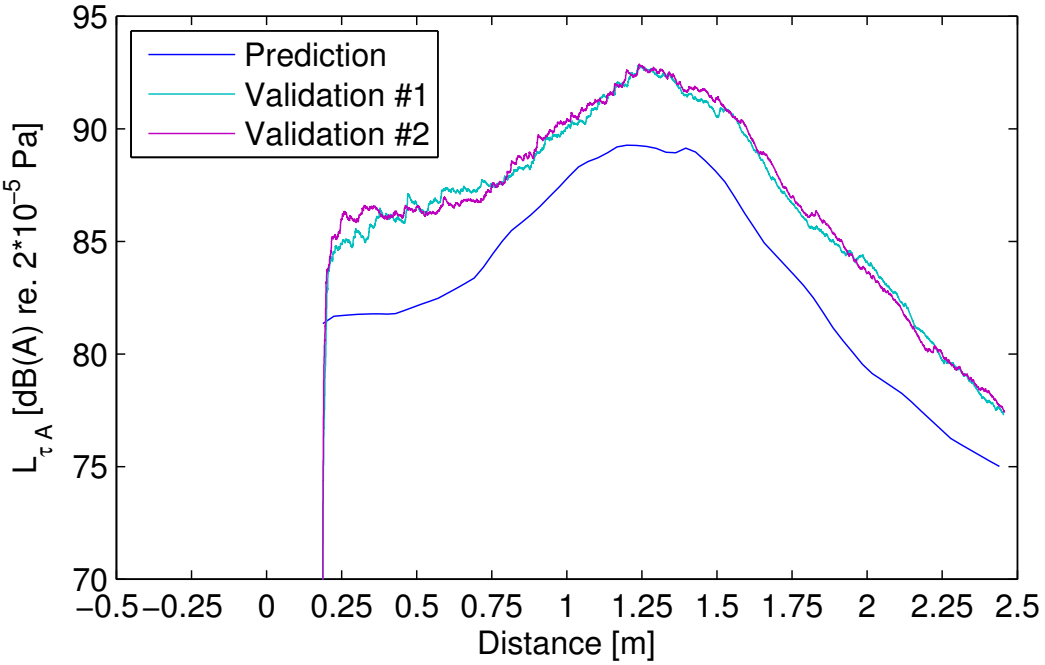

Figure 4.11: Comparison of the predicted and measured pass-by noise signals for the reciprocally arranged intake orifice configuration.

The measured pass-by noise of the reciprocally arranged intake orifice configuration is shown in Fig. 4.11, which appears to be inversely related to the pass-by noise of the 'reciprocal exhaust orifice configuration' in Fig. 4.10. The initial pass-by noise level is higher than the level at the end of the test track. In between, the maximum pass-by noise level occurs. The measured pass-by noise levels are generally very similar with a difference of less than 0.5 dB(A) for the majority of the test track length. Thus, the repeatability is deemed to be good. The measured pass-by noise level $L_{A\tau}$ at the beginning of the test track is approximately 85.5 dB(A). The maximum level 92.5 dB(A) is reached between 1.2-1.35 m. The minimum level is 77.4 dB(A) at 2.45 m. Thus, a difference of approximately 25 dB(A) between the minimum and the maximum level exists. The gradient of the measured pass-by noise level is less steep for the approaching microphone than it is for the receding microphone, which may be influenced by the relative arrangement of the orifice and the microphone. For example, the sound radiated from

the orifice can travel unobstructedly towards the microphone at the beginning of the test track, whilst the microphone faces the rear side of the ONS, where the radiated sound pressure is generally lower than at the front, at the end of the test track. A similar conclusion was suggested in the case in the pass-by noise of the 'reciprocal exhaust orifice configuration'. The noise levels of the 'reciprocal intake orifice configuration' are higher than the noise levels in the 'normal intake orifice configuration' which is assumed to be caused by different settings of the amplified volume of the loudspeaker inside the ONS.

The trend of the measured pass-by noise levels is reproduced well with the predicted pass-by noise levels. However, an almost constant deviation remains between measurement and prediction. The difference between the measured and the predicted pass-by noise levels is similar to the levels in the 'reciprocal exhaust orifice configuration'. The difference is 2-3.5 dB(A) up to where the highest noise levels occur at around 1.25 m. Between 1.4-2.45 m, the difference is 2-4 dB(A).

4.4 Summary

The design and the directivity characteristics of the orifice noise source (ONS) as well as the measured and the predicted pass-by noise of the ONS are presented in this chapter.

The ONS consists of a loudspeaker, being covered in insulation material, and a duct. From the orifice of the duct, the generated noise can radiate into the environment. Thus, a vehicle orifice noise source, as for example the orifices of the intake and the exhaust systems, is replicated.

The experimental procedure of the horizontal directivity measurements is described in which the orifice of the ONS, which is the acoustic reference point of the noise source, is placed in the centre of the measurement circle. White noise is the excitation signal. The radiated sound pressure is measured on the circle at increments of 5°. All experiments are conducted in anechoic conditions. The measured SPLs in the directivity experiment are the foundation of the pass-by noise prediction method. The highest SPLs are measured at the angular positions of ±90°, which represents the front of the ONS. Towards the rear of the ONS, the measured SPL begin to fall. They are lowest at the rear having a difference of at least 8 dB(A) to the measured SPLs at the front. In the PSD spectra of the directivity SPL, the resonances are distributed over the whole frequency range of interest, thus, showing a similarity to real vehicle exhaust systems, for example. However, it was not possible to clearly relate the measured resonance frequencies to the theoretical resonance frequencies of a double-sided open or closed duct or of a single-sided open duct by using any of the duct lengths of the ONS in conjunc-

tion with the corresponding theoretical formulas. The lengths used in the formulas shall correspond to the overall length of the ONS or the length of the duct through which noise is radiated. The directivity SPLs are subject to frequency-weighting and time-weighting, which is in line with the requirements in the standard ISO 362.

Then, the experimental procedure of the pass-by noise measurements of the ONS is presented. The pass-by noise is recorded for four different arrangements. This includes the exhaust and the intake orifice configurations, which are both used in normally and reciprocally conducted experiments. Thus, it is intended to simulate the pass-by noise radiation of an exhaust orifice and an intake orifice in either the normal or the reciprocal arrangement. The repeatability is generally given for each arrangement. The measured pass-by noise levels serve as validation data for the predicted pass-by noise levels.

Comparing the measured and the predicted pass-by noise levels, it seems that the prediction method works well in case of the normal arrangements of the ONS due to the small differences between measured and predicted levels. The deviation between measurement and prediction are smallest for the 'normal exhaust orifice configuration'. The deviation is slightly higher for the 'normal intake orifice configuration'. In case of the reciprocal arrangements, the trend of the measured pass-by noise levels of the ONS is generally very well predicted. However, an offset of 2-4 dB(A) remains. The operational rolling noise of the pass-by noise test rig is excluded as a possible cause for such deviations due to the large difference of more than 10 dB(A) between the maximum rolling noise level and the lowest pass-by noise level. The prediction method is dependent upon the measured directivity SPL of the noise source as well as on the quality of the measured pass-by noise validation data to which the predicted pass-by noise level is compared.

Chapter 5

Pass-by noise prediction for a shell noise source

Shell noise source, such as thin-walled structures in the exterior of a vehicle, is identified as a major contributor to vehicle pass-by noise as well. Therefore, a shell noise source (SNS) is designed and built in order to replicate the equivalent vehicle orifice noise sources and to test the proposed pass-by noise prediction method of this work in the available laboratory facility.

In this chapter, the design of the SNS is introduced. The noise source consists of a thin-walled cylinder, which is acoustically excited. This is followed by the description of the horizontal directivity measurements of the SNS in which the radiated sound pressure is measured in a circle around the SNS. An impact test supports the identification of the resonances of the noise source. After the analysis of the directivity sound pressure, which is required for the prediction method, pass-by noise validation data is obtained utilising the pass-by noise test rig. The validation data is recorded reciprocally only due to the size of the SNS. Eventually, the pass-by noise of the SNS is predicted, which is compared to the measured pass-by noise.

5.1 Design of the shell noise source replica

For the experimental investigation of pass-by noise of shell structures on a laboratory scale, a shell noise source (SNS) is designed and built. The interior of the SNS is illustrated in Fig. 5.1 whilst a photograph of the SNS is presented in Fig. 5.2. A vehicle noise source with a shell-like structure is the muffler of the exhaust system, for example. The SNS was developed for laboratory pass-by noise experimental work as it is reported in Ref. [17]. The SNS consists of a cylinder, which has a length of 0.4 m, an outer diameter of 0.16 m and a wall thickness of 1 mm.

The material of the cylinder is stainless steel. There is no internal structure inside the cylinder. The cylinder is completely closed on one end. On the opposite end, a small opening with a diameter of 0.046 m exists. A connection duct of a length of 3 m is attached to this opening. The ONS is attached to the other end of the connection duct, which serves as a waveguide, in order to acoustically excite the SNS. The connection duct and the ONS are covered thoroughly by insulation material in order to attenuate any noise radiation, which originates from these parts. The dimension of the cylinder or SNS, respectively, is considered to be similar to a real vehicle muffler.

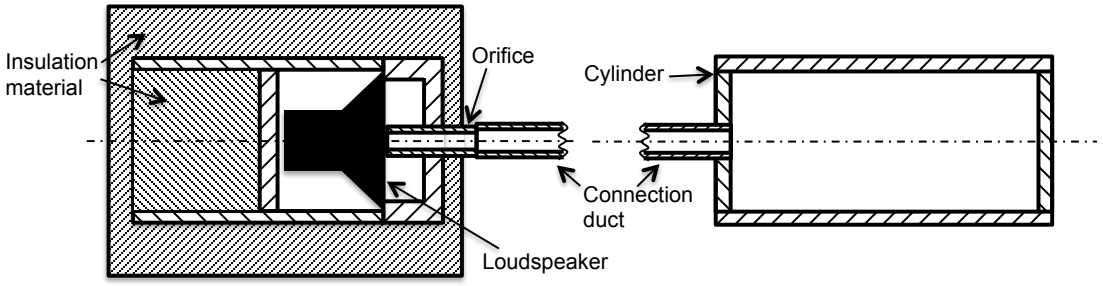

Figure 5.1: Schematic of the shell noise source on the right, which is acoustically excited by the loudspeaker of the orifice noise source.

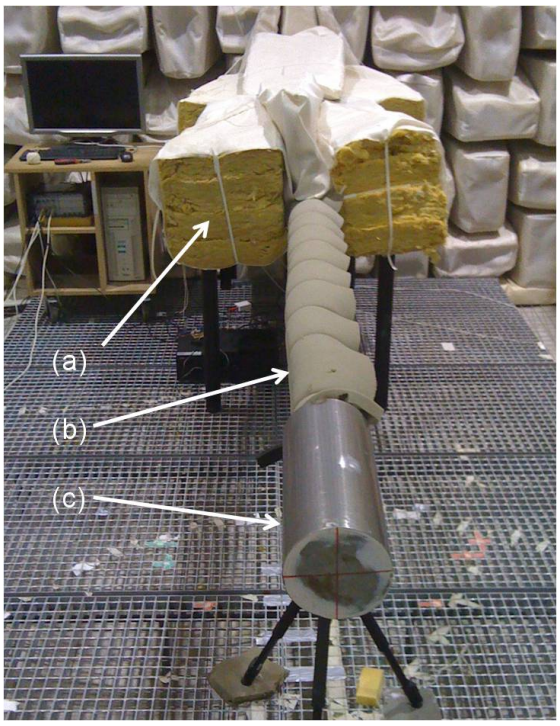

Figure 5.2: Photograph of (a) the shell noise source, (b) part of the connection duct, which is insulated with foam, and (c) the insulation material, which covers the rest of the connection duct as well as the ONS.

The mass flux of air or exhaust gases is not reproduced. Hence, high temper-

atures of hot exhaust gases or temperature shifts of cooling down exhaust gases, as they occur in vehicle exhaust systems, are not reproduced inside the cylinder either. Due to the constant temperature in the experiments of this work, the eigenfrequencies of the air inside the cylinder do not change and the sound radiation of the cylinder is not affected by heat radiation from the hot cylinder surfaces into the surrounding air. The piping system and the filling with insulation wool, which are usually part of a vehicle muffler, are not rebuilt in the SNS in order to limit the complexity of the system and to focus on the noise radiation of the SNS. Thus, the SNS represents a simplified model of a vehicle muffler noise source, where the resonances are assumed to be limited to the cavity inside the cylinder and to the cylinder structure.

5.2 Directivity characteristics of the shell noise source

In this section, the experimental procedure of gaining the directivity sound pressure of the SNS is presented. An impact test is conducted in order to distinguish between the structural and acoustic resonances of the SNS. Then, the acoustic characteristics of the SNS are analysed based on the directivity measurement data in the time and frequency domains.

5.2.1 Experimental procedure

For the determination of the directivity characteristics of the SNS, sound pressure measurements are conducted in a horizontal circle around the SNS, which is the same approach as in the directivity experiment of the ONS. The centre of the cylinder, which is chosen to be the acoustic reference point of the SNS, is positioned in the centre of the circle, which has a radius of 1 m. Sound pressure is recorded at 5° intervals along the circle. The microphone is on the same height as the longitudinal axis of the cylinder, which is approximately 1 m above the grid floor in the anechoic chamber.

A schematic of the experimental setup is presented in Fig. 5.3. It has to be differentiated between the circumferential and radial measurement positions. A single measurement position is specified according to its radial position and its circumferential position. In Fig. 5.3, the definition of the radial measurement positions are presented on the left whilst the circumferential positions are on the right. The sound pressure which characterises the horizontal directivity is measured at each circumferential measurement position. Measuring the sound pressure of the horizontal directivity at all circumferential measurement positions, two of

the four radial positions are automatically covered, which are initially the 0° and the 180° radial positions. Each of the radial position covers half of the circumferential measurement positions. In order to get a more detailed understanding of the noise radiation of the SNS, the horizontal directivity is also measured for the radial positions of 90° and 270° for which the cylinder is rotated by 90° around its longitudinal axis. Since the cylinder is symmetrical, there should not be any difference in the noise radiation. However, non-uniformities in the cylinder structure or material or due to the cylinder manufacturing process might be the cause of any deviation.

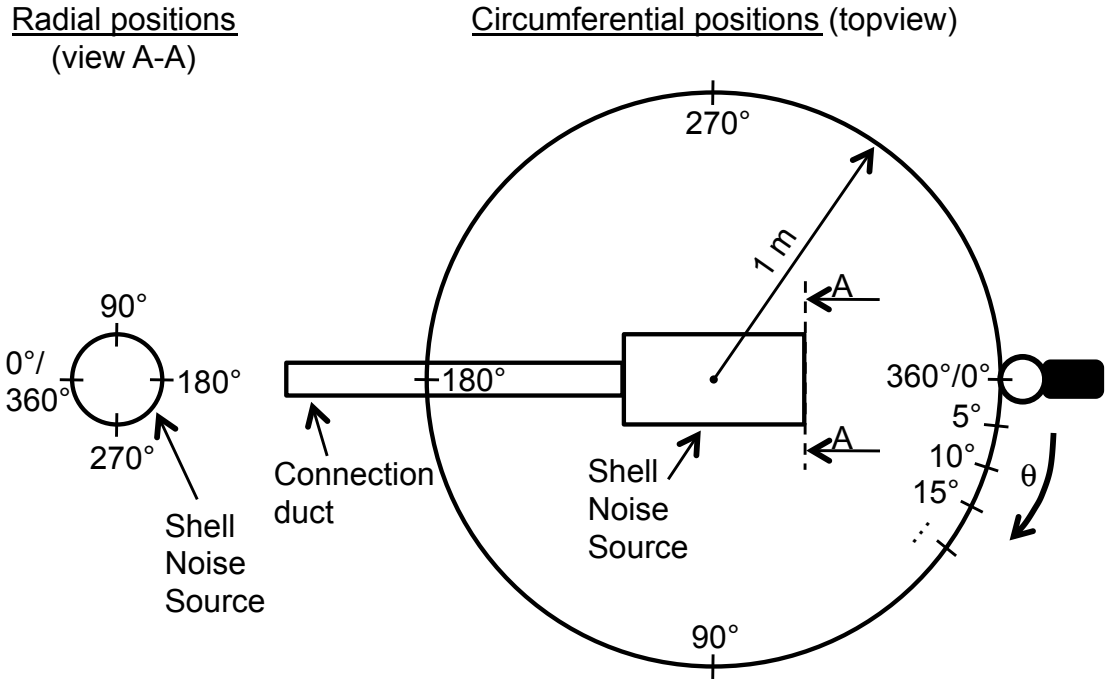

Figure 5.3: Schematic of the horizontal directivity measurement setup of the SNS. Left: view of the radial measurement positions on the SNS. Right: view of the circumferential measurement positions with the SNS at the centre of the measurement circle and the microphone at the 0° position. Note that the directivity measurements are carried out measuring sound pressure at the circumferential measurement positions, which automatically covers two radial positions of the SNS. If the cylinder of the SNS is then rotated by 90°, the directivity characteristics of the other two radial positions can be determined as well.

The directivity characteristics of the SNS are analysed based on the power spectral densities (PSD) of the measured sound pressure. Therefore, the sound pressure is recorded at each measurement position and averaged 20 times before the power spectral density (PSD) is estimated by the analyser. The frequency range 150-3500 Hz is subject to frequency A-weighting before the root-mean-square (RMS) value is calculated.

In the pass-by noise test according to the standard ISO 362 [10, 11], the

frequency-weighted and time-weighted sound pressure level $L_{A\tau}$ is expected. Therefore, for the application of the directivity sound pressure data in the prediction method, the measured time history data is filtered with a high-pass and a low-pass filter with cut-off frequencies at 150 Hz and 3500 Hz. The smaller frequency is approximately the lower frequency limit of the anechoic chamber in which the recording takes place. The higher frequency was chosen in order to stay in the main frequency region of an equivalent real vehicle noise source. The filtered sound pressure data is then frequency-weighted and time-weighted, according to Ref. [13] and as required in Refs. [10, 11]. For the time weighting 'Fast', the time constant $\tau = 0.125\,\mathrm{s}$ is applied in order to calculate the level $L_{A\tau}$.

Since the SPL cannot be measured at the 180° position due to the connection duct, the SPLs at the 175° and the 185° positions are linearly interpolated in order to obtain an estimated SPL at the 180° position. The excitation signal is white noise for all recordings. The measurements are conducted in anechoic conditions.

5.2.2 Experimentally determined directivity sound pressure

The directivity characteristics of the SNS are analysed by means of the overall SPL, which has been measured in a circle around the noise source, and the PSD spectra of selected measurement positions. In the recording process of these experiments, the SNS is excited acoustically with a white noise signal from a loudspeaker. In addition, the identification of the structural resonances of the SNS is accomplished by measuring the acceleration response in an impact test.

Fig. 5.4 presents the directivity graph of the SNS, which consists of the measured SPL plotted against the angular measurement positions in the circumferential direction. The sound pressure is frequency-weighted and the RMS of the PSD spectrum is presented in the diagram. The denotation '0° radial' means that the horizontal directivity was measured when the SNS was in the radial position of 0° and 180°, according to Fig. 5.3. Hence, in Fig. 5.4, the radial position is 0° for the SPL of the circumferential positions between 0° and 180°; for the SPL of the circumferential positions between 180° and 360° the radial position is 180°. The denotation '90° radial' means that the horizontal directivity was measured when the SNS was in the radial position of 90° and 270°, according to Fig. 5.3. Hence, in Fig. 5.4, the radial position is 90° for the SPL of the circumferential positions between 0° and 180°; for the SPL of the circumferential positions between 180° and 360° the radial position is 270°. Thus, looking at the horizontal directivity of different radial positions of the SNS, a comprehensive understanding of the noise radiation characteristics of the SNS can be obtained.

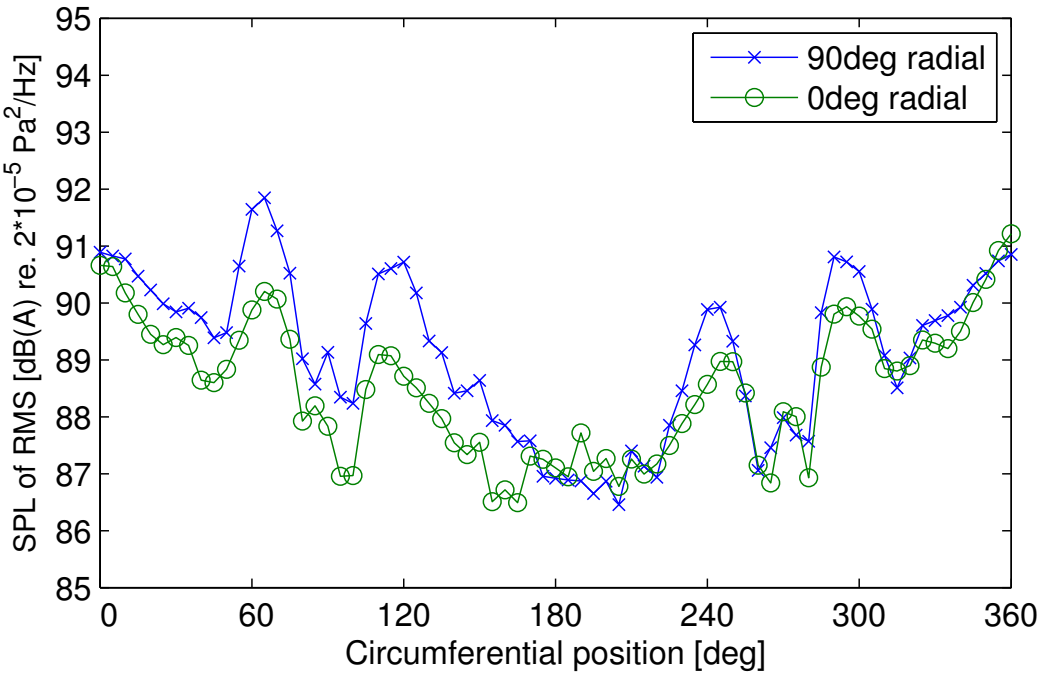

Figure 5.4: The SPL of the RMS at each circumferential measurement position characterises the directivity of the SNS, which has been determined for two radial positions of the SNS.

The largest difference between the lowest and the highest directivity SPL in Fig. 5.4 is less than 5 dB(A) for each of the graphs. The SPL at the 0° circumferential position is one of the highest. Around the 180° circumferential position, the SPL becomes lowest. Between the 0° and the 180° as well as between the 360° and 180° circumferential positions, the trend of the SPL is generally decreasing. However, exceptions occur at approximately the 60°, 120°, 240° and 300° circumferential positions. Here, the SPL rises to a level which is as high as or even higher than the SPL at the 0° circumferential position. It is assumed that these relatively high SPL occur at any radial position, since the 240° and the 300° circumferential positions of the 180° radial position correspond the 120° and the 60° circumferential positions of the 0° radial position. The situation is analogous for the 90° and the 270° radial positions.

The high SPL at the 0° circumferential position may be favoured by the closed end of the SNS, which is a flat, thin, circular plate. In combination with the acoustic wave propagation direction, which originates from the loudspeaker inside the ONS and which is predominantly in the normal direction of the end plate, the end plate may act as an efficient noise radiator. In contrast, the lower SPL around the 180° position may be affected by the annular shape of the plate at this end of the SNS. This end plate has a smaller area,too, since a hole in the end plate is necessary in order to attach the cylinder to the long duct. Due to the attachment,

the weight of the whole cylinder acts on the annular end plate, which imposes different boundary conditions on this end plate in comparison to the opposite end plate. This may influence the vibration properties and, thus, the noise radiation of the end plate.

The directivity SPLs show that the noise radiation of the radial positions is generally of a symmetric characteristic with respect to the longitudinal axis of the SNS, which is along the 0° and the 180° circumferential positions. This means that the noise radiation is of a similar characteristic for each of the radial positions, which corresponds to the symmetric shape of the cylinder. This is supported by the small deviations between the graphs. The SPL of both graphs are generally within 1 dB(A). However, the deviations increase up to approximately 2 dB(A), which is still seen as a very low value, around the 60°, 120°, 240° and 300° circumferential positions. At these positions, the SPL are relatively high in comparison to the SPL at the adjacent positions.

In order to analyse the noise radiation characteristics of each radial position, the directivity SPLs are separated into their respective radial position and are plotted against the circumferential positions in Fig. 5.5. On the abscissa, 0° marks the front of the SNS, 90° marks the measurement position, which faces the long side of the cylinder, and 180° marks the rear of the SNS, which coincides with the location of the long duct. Thus, the SPLs of each radial position can be compared better. The graphs of Fig. 5.5 confirm the previous result that the noise radiation is almost identical regardless of the radial position. The SPLs of the radial positions of 0° and 180° are almost identical. In contrast, the deviations between the SPLs of the radial positions of 90° and 270° rise up to 2 dB(A). Deviations also exist between the SPLs of the 90° and 270° radial positions on the one hand and the SPL of the 0° and the 180° radial positions on the other hand. The deviations are highest at around 60° and 120°, which have been previously identified as positions with high SPLs.

In order to reveal the cause for these deviations, further analyses have to be carried out. In Fig. 5.6, the directivity SPLs of each radial position are plotted without frequency-weighting against the circumferential positions. The trend of the SPLs in Figs. 5.5 and 5.6 are very similar. The differences between the SPLs of the radial positions are approximately within 0.5 dB for most of the measurement positions and increase to approximately 1 dB at around the 60° and the 120° circumferential positions. The differences are generally less than the differences between the SPLs with frequency-weighting in Fig. 5.5. Thus, it is concluded that the frequency-weighting is the cause for some of the deviations by attenuating the low-frequency SPLs and amplifying the SPLs in the higher frequency range. However, the differences between the SPLs of the 0° and the 180° radial positions

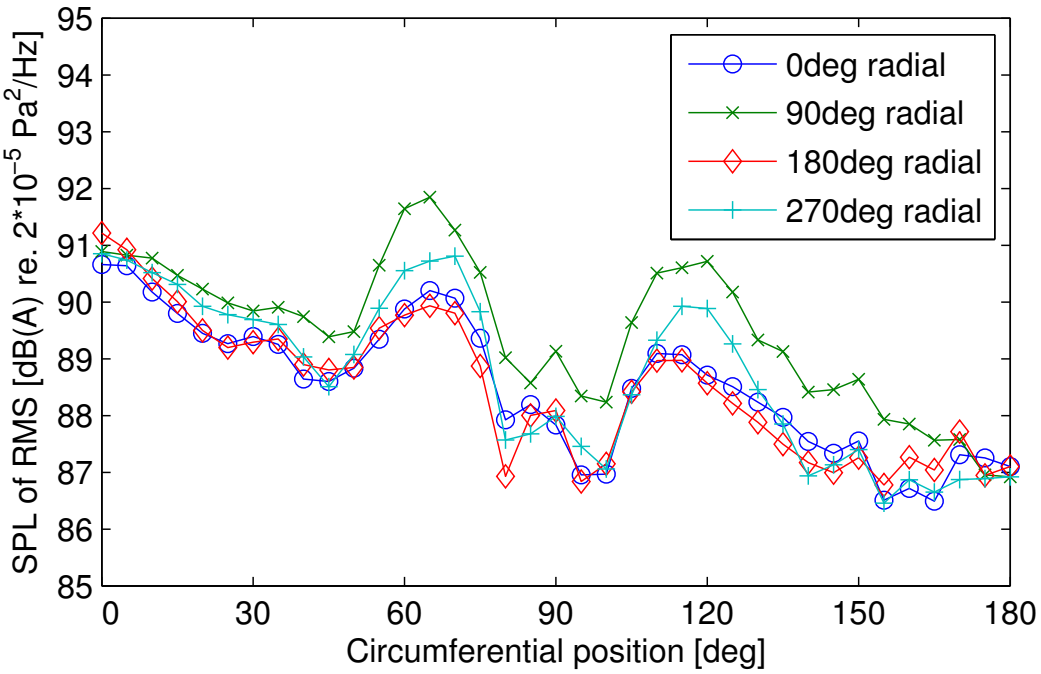

Figure 5.5: The directivity SPLs of Fig. 5.4 are plotted separately in order to distinguish between their radial positions.

on the one hand and the 90° and the 180° radial positions on the other hand remain without frequency-weighting as well as the relatively high SPLs at the 60° and the 120° positions.

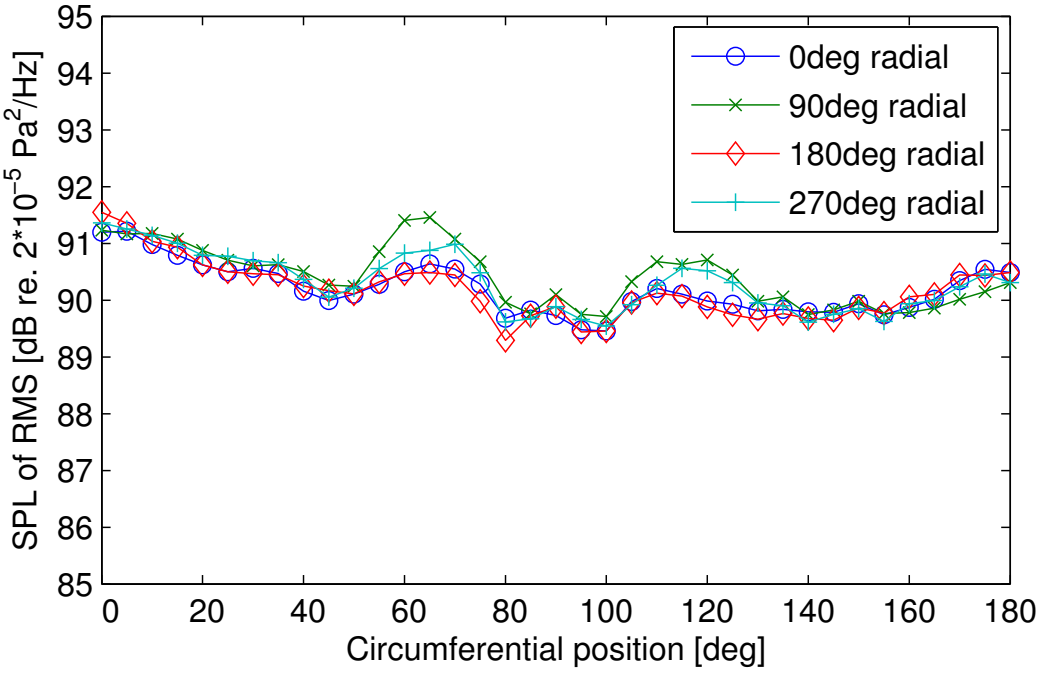

Figure 5.6: The directivity SPLs of Fig. 5.5 are plotted without frequency-weighting.

Fig. 5.7 presents the PSD spectrum of the SPL of the 0° and the 90° radial positions, which were measured at the 120° circumferential position, in order to analyse their spectral characteristics. In Fig. 5.7, minor differences between both graphs occur at frequencies below 450 Hz and they are nearly identical up to 2000 Hz. At higher frequencies, the differences increase and the resonant peaks of the 90° radial position are up to 5 dB(A) higher than the peaks of the 0° radial position. It is assumed that the cause of these differences are related to inhomogeneities in parts of the structure of the SNS, since they do not occur at each radial position. Small gaps may exist between the end plates and the cylinder surface, which may be a consequence of the manufacturing process of the cylinder. Through such small gaps, the noise radiation may be increased at the 60° and the 120° circumferential positions.

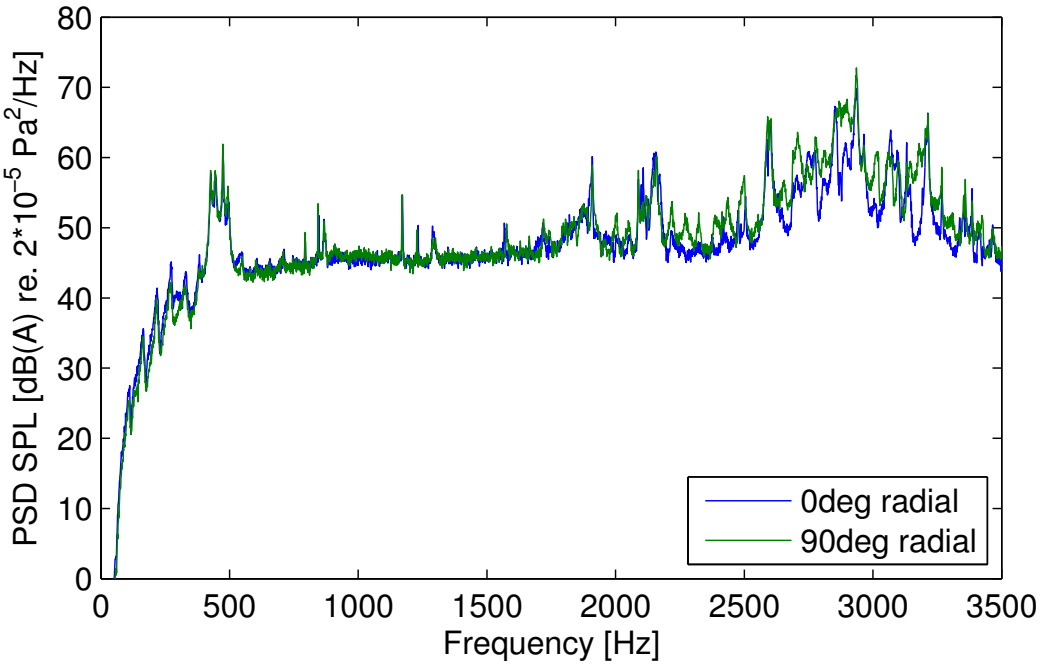

Figure 5.7: The PSD of the SPL at the 0° and the 90° radial positions are plotted for the 120° circumferential position.

In order to visualise the effect of the frequency-weighting on the PSD spectrum, Fig. 5.8 presents the PSD spectrum of the SPLs at the 0° radial and circumferential position, which are plotted with and without the frequency-weighting. As a result, the amplitudes of the frequency range up to about 400 Hz are significantly reduced. The peaks in that frequency range, which occur for example at 29 Hz, 85 Hz, 162 Hz, 218 Hz, etc., can be associated with the long duct. If the long duct is regarded as a single-sided open duct, utilising Eq. 4.1 results in the theoretical resonance frequencies of 29 Hz, 86 Hz, 143 Hz, 200 Hz, etc. Whilst the first two resonance frequencies of the measurement and the calculation match well, the other

two resonances seem to be frequency-shifted. Overall, it seems that the frequency-weighting eliminates the background noise from the long duct, which would have had a negative effect on the determination of the directivity characteristics of the SNS. In contrast to the low frequency range, the amplitudes of the frequency range between 1500-3500 Hz are slightly increased due to the frequency-weighting.

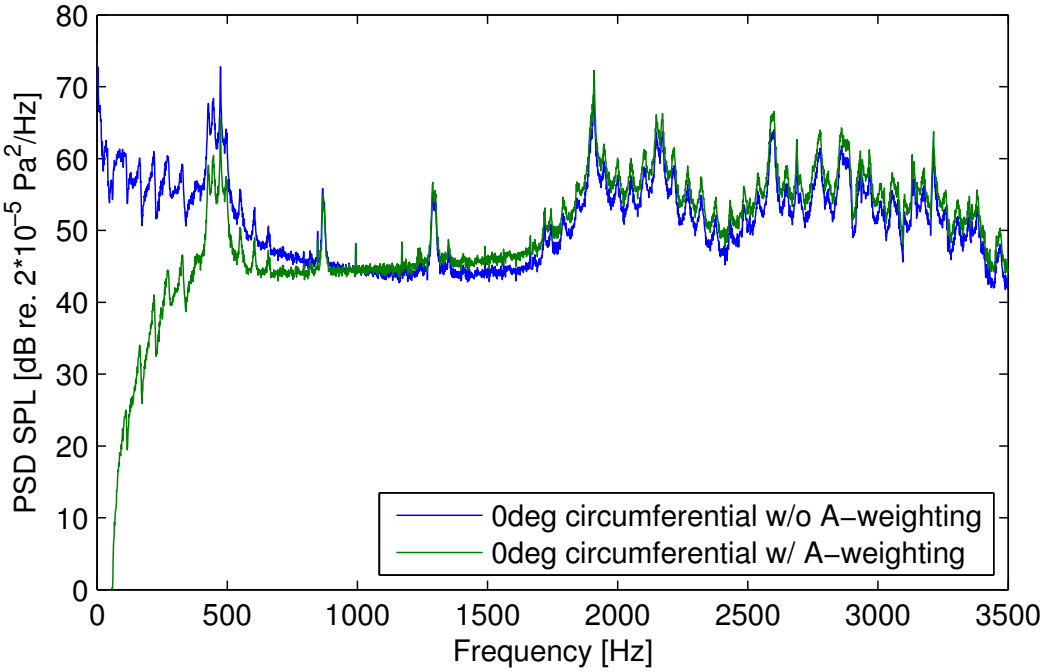

Figure 5.8: The effect of frequency-weighting on the PSD spectrum of the SPL at the 0° radial and circumferential position.

The PSD spectrum of the SPLs, which are measured at the 0° and the 90° circumferential positions of the 0° radial position, are shown in Fig. 5.9. The acoustic excitation from the loudspeaker results in standing waves inside the cylinder and structural resonances of the cylinder, as the cylinder responds to the sound waves. Depending on the noise radiation efficiency of the cylinder, the resonance frequencies of the standing waves and the structural resonances can be detected in the sound pressure measurements.

The majority of the resonance peaks in Fig. 5.9 occur at both of the circumferential positions. However, the amplitudes of both graphs may vary up to 10 dB(A). In the frequency range between 1700-2700 Hz, the SPLs of the 0° circumferential position are generally much higher than the SPLs of the 90° circumferential position. This may indicate that the noise radiation in the longitudinal direction of the SNS is much more efficient than it is in the radial direction. The longitudinal direction of the cylinder also coincides with the direction of the sound wave propagation, which originates from the loudspeaker and moves through the long duct into the cylinder of the SNS. Thus, it may be concluded that the spectral

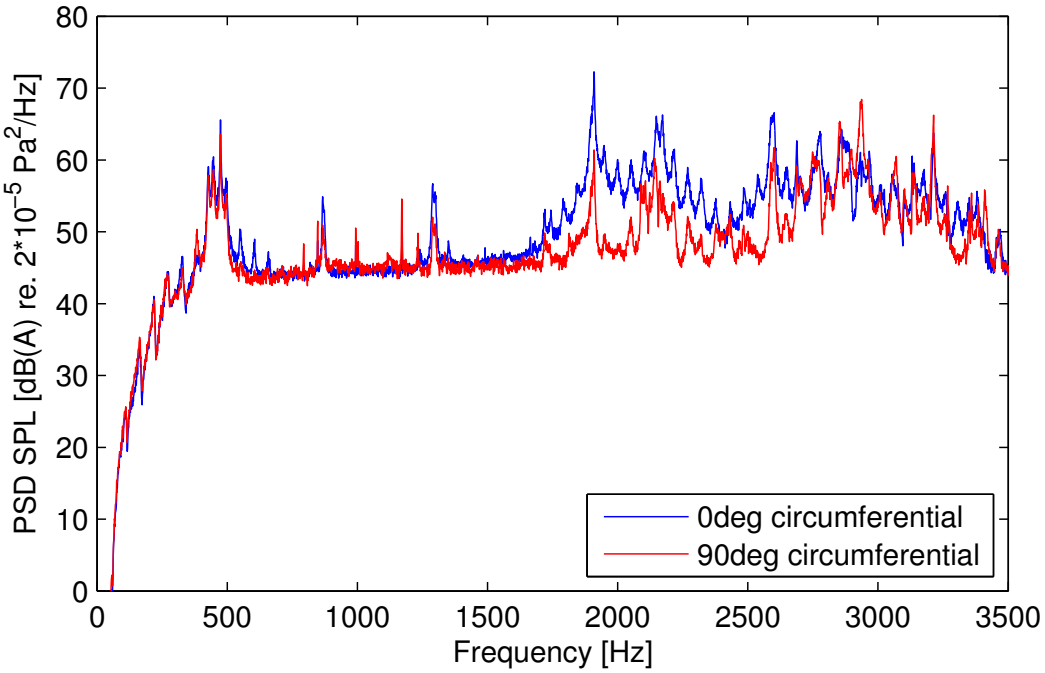

Figure 5.9: The PSD of the SPL at the 0° and the 90° circumferential positions are plotted for the 0° radial position.

differences between both graphs result in the specific directivity characteristics of the overall SPL against the circumferential measurement positions in Fig. 5.4.

A selection of measured resonance frequencies are presented in Table 5.1, which are compared to either the corresponding theoretical duct resonances or the corresponding measured resonances of the impact test, which are considered as the causes of the resonances. If the cylinder of the SNS is regarded as a closed duct with a length of 0.4 m, its theoretical resonance frequency of 429 Hz matches the measured resonance frequency of 427 Hz well. Despite the differences of 2-15 Hz between the theoretical and the measured frequencies of the higher modes, it is still a reasonable assumption that these resonances originate from the standing waves inside the cylinder. In the radial direction of the cylinder, cross modes exist at 2149 Hz and 3214 Hz, which coincide with the second and the third mode of a standing wave across the cylinder diameter of 0.16 m. The first mode at the theoretical frequency of 1072 Hz cannot be clearly identified. In Fig. 5.9, a relatively small peak exists at 1076 Hz, which may be associated with the first mode but which is not significant to the adjacent resonance peaks.

In order to identify the structural resonances of the SNS, an impact test is carried out in which the cylinder is hit with a stiff metal object whilst an accelerometer records the response. The location of the accelerometer is in the middle of the cylinder wall of the SNS, which is illustrated in Fig. 5.10. The impact location is on the opposite side of the accelerometer position on the cylinder. The recorded

Measured resonance	Cause		
427 Hz	closed duct (l = 0.4 m, Eq. 4.2)	1st mode	429 Hz
867 Hz		2nd mode	856 Hz
1288 Hz		3rd mode	1286 Hz
1718 Hz		4th mode	1715 Hz
2150 Hz		5th mode	2144 Hz
2588 Hz		6th mode	2573 Hz
3013 Hz		7th mode	3001 Hz
not identifiable	closed duct (l = 0.16 m, Eq. 4.2)	1st mode	1072 Hz
2149 Hz		2nd mode	2144 Hz
3214 Hz		3rd mode	3216 Hz
Small resonance peaks are barely identifiable	structural resonances impact test, Fig. 5.10)		574 Hz
			763 Hz
			825 Hz
			1161 Hz
			1674 Hz
			1845 Hz
			2016 Hz
			2301 Hz
			2560 Hz
			2990 Hz
			3325 Hz

Table 5.1: Comparison of the resonance frequencies of the measured directivity sound pressure and their possible causes.

data showed good repeatability. The measured spectrum of a single acceleration response, as a result of a 20 times linear averaging, is presented in Fig. 5.10. The structural resonance peaks with the highest amplitudes are listed in the bottom part of Table 5.1. A detailed investigation into the structural mode shapes was omitted. All of the structural resonances of the impact test occur in the sound pressure spectrum of the 90° circumferential position in Fig. 5.9. However, the corresponding amplitudes are very small and, thus, barely identifiable in the sound pressure spectrum. In case of the sound pressure data in Fig. 5.9, which is the result of an acoustic excitation from a loudspeaker, it appears that the acoustic excitation energy is not high enough in order to excite the structural resonances and to radiate their sound distinctively. Instead, the sound radiation is determined by acoustic resonances, which are caused by the sound waves travelling through and being reflected within the geometrical boundaries of the SNS.

The spectral analysis of the structural resonances as well as of the sound radiation contributes to the overall understanding of the SNS, although the pass-by noise test regulation requires the overall noise level only.

It is assumed that the SNS replicates an exhaust system muffler of a real vehicle relatively well within limitations. Due to the broadband excitation, stand-

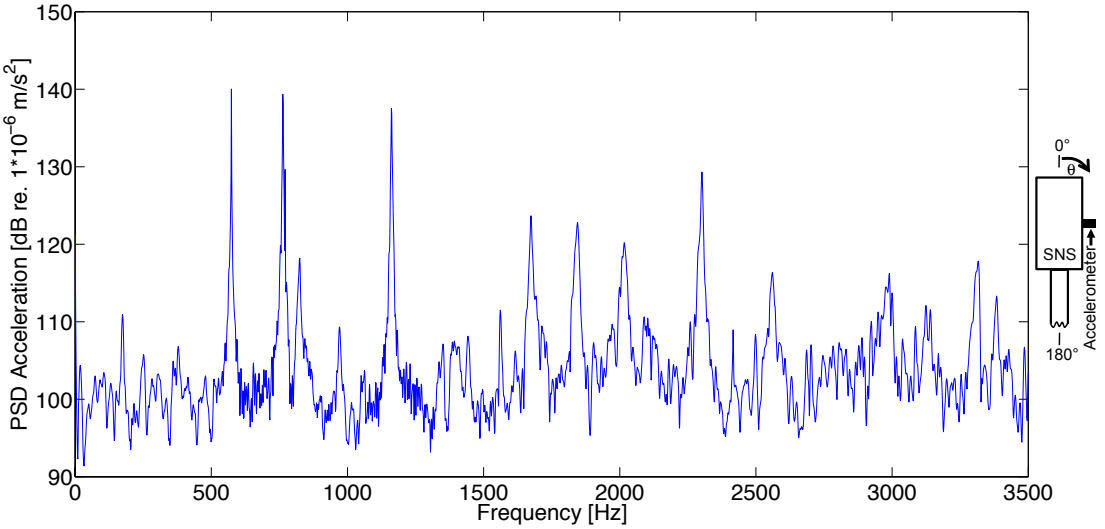

Figure 5.10: The PSD of the measured acceleration response of the impact test of the cylinder of the SNS.

ing wave resonances and structural resonances of a muffler-like structure are replicated. However, the influence of hot exhaust gases is neglected. Any excitation from engine vibrations, which are transferred via the exhaust system parts to the muffler, are not explicitly replicated. The structural vibrations of the SNS are a result of the acoustic excitation from the loudspeaker.

5.3 Prediction of shell pass-by noise

In this section, the experimental determination of the pass-by noise validation data of the SNS is presented, which is carried out for four different rotational positions of the SNS. The measured pass-by noise is analysed. Then, the predicted pass-by noise of the SNS is presented and compared to the validation data.

5.3.1 Measurement procedure of shell pass-by noise validation data

Most mufflers are assembled with their longitudinal axis in the driving direction of the vehicle. This configuration shall be replicated with the SNS in the pass-by noise experiments of this work. Due to the dimension of the SNS, including the connection duct and the ONS, the apparatus cannot be attached to and moved on the trolley of the experimental pass-by noise test rig. Therefore, the SNS is positioned stationary at the previous microphone location and the microphone is mounted on the trolley of the test rig. Then, the pass-by noise measurements are conducted reciprocally. The schematic of the experiment is presented in Fig.

5.11 whilst Fig. 5.12 shows a photograph of the experimental setup. Despite the symmetry of the cylinder of the SNS, pass-by noise measurements are recorded for four radial positions of the SNS. Therefore, the SNS is turned by 90° around its longitudinal axis in order to measure the pass-by noise when the radial positions of 0°, 90°, 180° and 270° are closest to the test rig. The radial positions were introduced in Fig. 5.3. Since the travelled distance of the trolley is referred to the rear axle of the trolley and since the microphone is positioned in the middle of the trolley, the measured pass-by noise will be plotted with an offset of 0.1875 m in the corresponding pass-by noise diagrams.

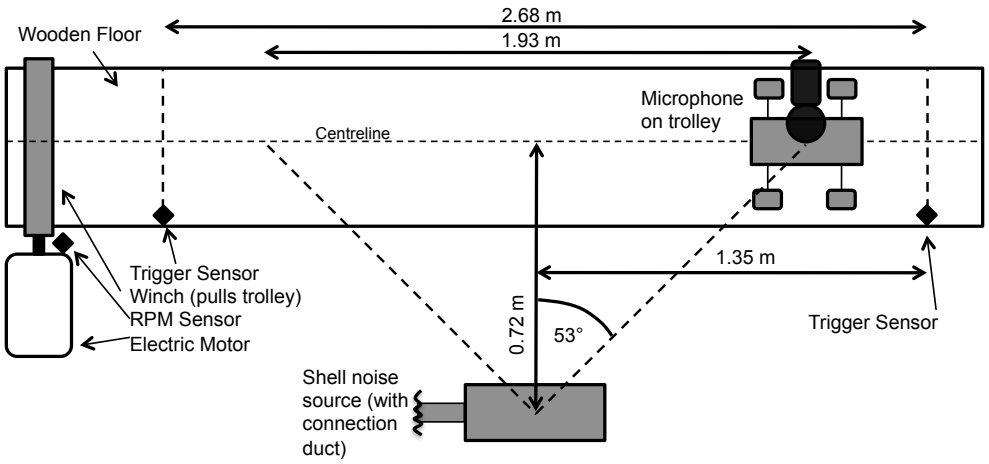

Figure 5.11: Schematic of the pass-by noise validation experiment of the SNS, which is conducted reciprocally with the microphone being mounted on the trolley and the SNS at a stationary position off the test track.

5.3.2 Comparison of measured and predicted pass-by noise

The pass-by noise of the SNS is predicted by means of the horizontal directivity method of Section 3.1 and presented in this section. An alternative pass-by noise prediction method based on transfer functions between the noise source and the microphone was applied for the pass-by noise prediction of the SNS as well, as reported in Ref. [17]. However, the discrepancies between the measured and the predicted pass-by noise were high. Therefore, the directivity method is selected for the pass-by noise prediction in this work, which is compared to the reciprocally measured pass-by noise validation data of the SNS.

Since the deviations between the directivity sound pressure characteristics of the four radial positions are small, the reciprocal pass-by noise of the SNS is measured just for the 90° radial position. Fig. 5.13 presents the measured and

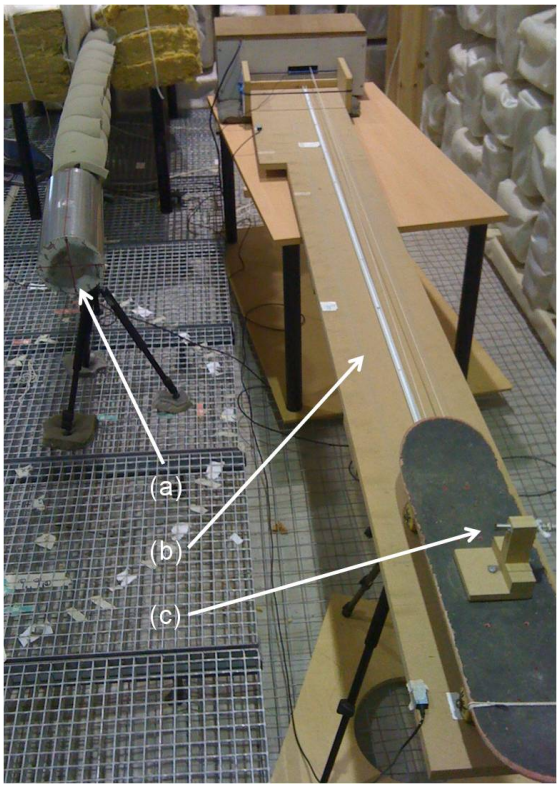

Figure 5.12: Photograph of the SNS in the reciprocal arrangement of the laboratory scale pass-by noise experiment: (a) SNS; (b) pass-by noise test track; (c) microphone attached to the trolley.

predicted pass-by noise as well as the averaged rolling noise (RN). Three consecutive recordings were carried out for the measured pass-by noise for which the SNS was excited with a white noise signal over the frequency range of interest. The rolling noise, or background noise respectively, is obtained when the microphone, mounted on the trolley, is moved along the test track measuring the noise due to the operation of the pass-by noise test rig. Such noise is assumed to be composed of the rolling noise of the trolley wheels of the test rig, the electric motor as well as the winch system. The rolling noise is averaged from three recordings. The measured pass-by noise validation data contains a contribution of the rolling noise. The green coloured graph represents the sum of the predicted pass-by noise and the measured rolling noise. The noise graphs are plotted against the microphone position on the track, which has an offset of 0.1875 m relative to the rear axle of the trolley, which is the reference point for the measurement of the travelled distance. The measured sound pressure data is filtered with a digital high-pass and low-pass filter with cut-off frequencies at 150 Hz and 3500 Hz. In accordance with the standard ISO 362, the measured pass-by noise is frequency-weighted and time-weighted, which results in the pass-by noise level $L_{A\tau}$. This approach shall increase the level of reality of the laboratory scale experiments.

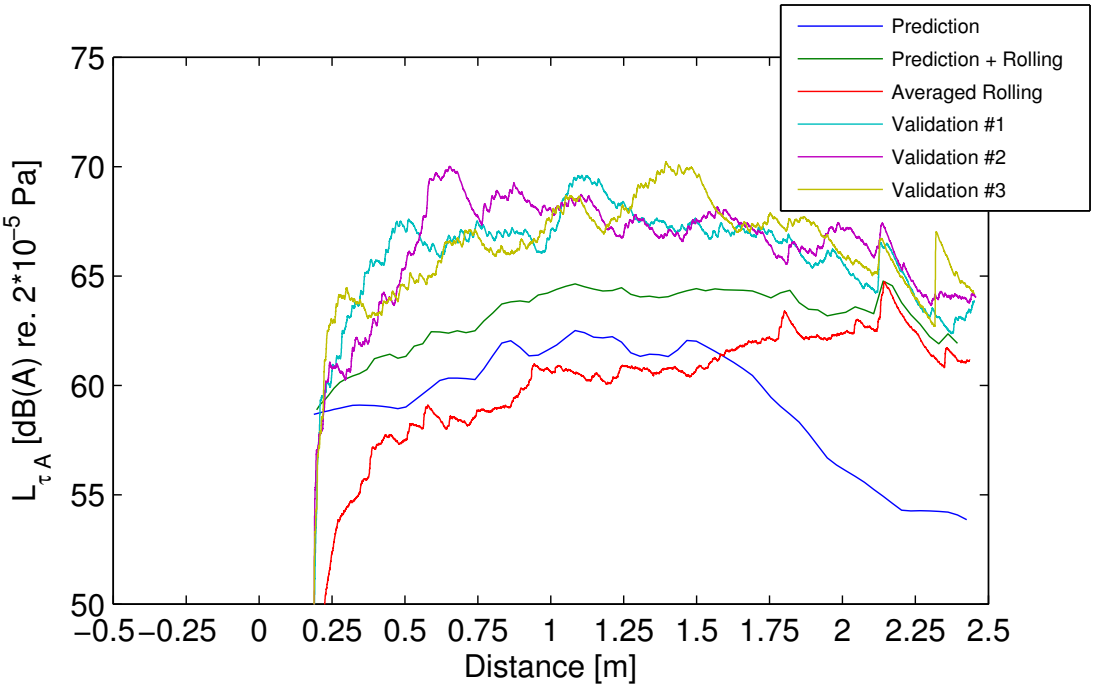

Figure 5.13: Comparison of the predicted and the measured pass-by noise signals for the 90° radial position.

The trends of the measured pass-by noise levels are similar. At the beginning of the recording, the measured pass-by noise levels increase rapidly, as a consequence of the exponential time-weighted average formula for which a time period must elapse before the averaged value becomes accurate. It is assumed that the values of $L_{A\tau}$ become accurate after the trolley has travelled for approximately 0.15 m, which is the same assumption as mentioned in Section 4.3.2. The measured pass-by noise validation data increases in level from approximately 60 dB(A) at the beginning of the test track to the highest values of 67-70 dB(A), which occur in the region of the 1.4 m mark, where the distance between the microphone and the cylinder of the SNS becomes shortest. From approximately the 1.6 m mark, the trend of the validation data is of a decreasing characteristic. However, a relatively high peak occurs at approximately 2.1 m. Here, the measured pass-by noise level increases suddenly by up to 3.5 dB(A) to a level of 67 dB(A). It is assumed that the peak is caused by an impact incident, when the front axle of the trolley rolls over a small cross groove on the test track. The cross groove exists at the place where two boards are joined. Since the microphone is attached to the trolley, the impact incidence may be recognised by the microphone to such an extent through the airborne as well as the structure-borne transfer paths. The impact between the test track and the trolley wheels would be the origin or source of the peak. The structure-borne path would begin at the wheels to be continued through the remaining structures of the trolley and the microphone holder to which the

microphone is attached. The measured pass-by noise levels at the end of the test track are approximately 63 dB(A) and, thus, higher than at the beginning. Over the whole test track length, the deviations among the validation pass-by sound pressure is small. However, they can reach values up to 2-3 dB(A) at the marks around 0.5 m, 0.65 m and 1.4 m.

The initial rolling noise levels increase less rapidly in comparison to the measured pass-by noise. It rises rather slowly up to 57 dB(A) at the 0.4 m mark. In this region, the trolley is in the accelerating phase, as shown in Fig. 3.5. Thus, it is assumed that the increasing speed of the wheels of the trolley of the pass-by noise test rig contributes significantly. Then, the rolling noise increases almost constantly by approximately 3 dB(A)/m whilst the trolley approaches the end of the test track, where the electric motor and the winch system is located within an insulation box. A level of 62.5 dB(A) is reached at the 2 m mark. Between the marks of 0.4-0.75 m, the acceleration is decreasing and becomes approximately zero for the rest of the distance to travel, which means that the trolley travels at approximately constant speed. In that case, the noise contribution from the trolley may be assumed constant as well. The smaller peaks along the travelled distance may be caused by little impact incidents between the wheels and the track. Since the microphone on the trolley is moved closer to the electric motor and the winch system, it may be assumed that their contribution to the recorded rolling noise increases the closer the microphone gets to them. The relatively high impact at 2.1 m is also detected in the rolling noise measurement, which supports the previously made conclusion that the peak is caused by an impact incident between the trolley wheels and the cross groove on the test track.

The predicted pass-by noise level shows a similar trend in comparison to the measured pass-by noise validation data. However, the differences between both levels becomes up to 6 dB(A) until the 1.5 m mark and even increases up to 10 dB(A) in the final part of the test track. The peaks of the predicted pass-by noise levels at around 1.1 m, 1.3 m and 1.6 m are assumed to be related to the relatively higher directivity SPLs at the 60°, 90° and 120° circumferential positions. It is assumed that these SPLs are caused through edge effects of the sound radiation of the cylinder of the SNS. However, their effect is reduced in the summed level of the predicted pass-by noise and the rolling noise.

Between 0.4-1.6 m, the predicted pass-by noise level and the rolling noise level are in the same range, having a small deviation of 0.5-3 dB(A). After the 1.6 m mark, the rolling noise level becomes the higher of the two levels, with a difference of up to 10 dB(A) due to the decreasing predicted pass-by noise level. The rolling noise may have a significant influence on the pass-by noise, since both noise levels lie in close range or the rolling noise level is higher than the predicted pass-by

noise level. In addition, the rolling noise is also recorded by the microphone when the pass-by noise validation data is measured. Thus, the validation data contains a contribution of the rolling noise. As a consequence, in order to improve the prediction result, the rolling noise and the predicted pass-by noise are summed up resulting in a corrected pass-by noise prediction in Fig. 5.13. The highest deviation between the measured and corrected predicted pass-by noise is reduced to 4 dB(A) up to the 1.6 m, which is in the range of the shortest distance between the microphone and the reference point of the SNS. The smallest deviations become approximately 2.5-3 dB(A) around the 0.45 m, 0.85 m and 1.5 m marks. After the 1.6 m, the difference reduces further from about 3 dB(A) to 2 dB(A) at the end of the test track. It seems that the rolling noise becomes dominant in the corrected pass-by noise prediction in the latter part of the test track. Therefore, the effect of any noise radiation of the connection duct or the ONS, which provides the acoustic excitation for the SNS and is covered in insulation material, may be assumed to be small.

5.4 Summary

The design of the shell noise source (SNS) and its directivity characteristics are presented in this chapter. This is complemented by the measured and the predicted pass-by noise of the SNS.

The SNS consists of a thin-walled cylinder structure, which is acoustically excited by the orifice noise source (ONS) of Chapter 4. The acoustic waves propagate from the ONS through a connection duct into the cylinder of the SNS. Both the ONS and the connection duct are covered in insulation material in order to minimise their sound radiation. The radiated sound from the cylinder of the SNS is the main factor of interest. Thus, a vehicle shell noise source, as for example the muffler of the exhaust system, is replicated.

The experimental procedure of the horizontal directivity measurements is described. The centre of the cylinder of the SNS is chosen to be the acoustic reference point of the noise source. The reference point is positioned in the centre of the measurement circle. The excitation signal is white noise. The radiated sound pressure is measured on the circle at increments of 5°. A constant sound radiation pattern is expected due to the symmetrical shape of the cylinder of the SNS. However, the horizontal directivity measurements were conducted for two rotational positions of the cylinder. This means that the cylinder was rotated by 90° after the sound pressure had been measured for a whole circle. All experiments are conducted in anechoic conditions.

All sound pressure measurement data is high-pass and low-pass filtered before

the frequency A-weighting and the time-weighting 'Fast' is applied, resulting in the sound pressure level (SPL) $L_{A\tau}$. Both the frequency-weighting and time-weighting are required in the standard ISO 362 as well. The measured directivity SPLs are highest at the front of the SNS. The SPLs of the different rotational positions of the SNS decrease slightly for the measurement positions between the front of the SNS along the measurement circle to the back, where the connection duct is located. The sound radiation pattern of the cylinder appears to be symmetrical since the measured SPLs are in close range to one another. At the 60°, 120°, 240° and 300° measurement positions, the SPLs are raised in comparison to the SPLs of the adjacent measurement positions. Since the edges of the cylinder of the SNS are approximately located in this region, it is assumed that edge effects, where longitudinal waves in the cylinder structure may change to bending waves which radiate sound efficiently, cause this increase. The spectral analysis of the sound radiation and of the structural resonances contributes to the overall understanding of the noise source characteristics. The spectrum of the acoustically excited SNS consists of a number of discrete resonance peaks, which are caused by standing waves inside the cylinder or the connection duct as well as by structural resonances of the SNS. The frequency A-weighting reduces the resonances in the low frequency range, which are associated to the connection duct and, thus, would have been unwanted noise. From the spectra, such details as the SPLs in the frequency range of 1700-2700 Hz, which are higher at the 0° measurement position than they are on the side of the SNS cylinder at the 90° position, can be identified. It is shown that many resonances can be related theoretically to the length and the diameter of the SNS cylinder. An impact test revealed the structural resonances of the cylinder of the SNS, which appear as very small peaks and, thus, are barely identifiable in the sound pressure spectrum of the acoustic excitation. Thus, it is concluded that the resonances of the SNS are predominantly acoustic resonances, which are caused by sound waves travelling and being reflected inside the SNS. It is assumed that the shell noise source replicates an equivalent vehicle noise source sufficiently well. However, the effect of hot exhaust gas stream is not neglected as well as vibration excitation from the combustion engine.

The pass-by noise experiments of the SNS are conducted reciprocally with the SNS at a stationary position off the test track and the microphone being mounted on the trolley. Since the directivity SPLs are approximately constant regardless of the rotational position of the cylinder, the pass-by noise experiment is carried out for one rotational position only. The longitudinal axis of the SNS is parallel to the direction of motion of the microphone, which is assumed to correspond to the fitting position of most vehicle mufflers. The repeatability of the measured pass-by noise validation data is generally acceptable.

The pass-by noise is predicted using the directivity sound pressure and the instantaneous distance between the noise source and the microphone. The trend of the measured levels can be slightly reproduced only with the prediction method, although the deviation is high and the predicted level is below the measured level. Adding the average of the measured rolling noise, which is the operational noise due to the moving trolley as well as the electric motor and the winch system and which increases slightly along the travelled distance, to the predicted pass-by noise, an improvement can be achieved. The difference between the measurement and the corrected prediction is reduced to 2-3 dB(A) and the trend of the measured pass-by noise can be reproduced more accurately.

Chapter 6

Prediction of tyre sidewall radiation for pass-by noise

The tyre sidewall can be excited by the cavity modes of the toroidal shape of the interior of the tyre/wheel assembly within the boundaries of the tyre sidewalls, the tyre treadband and the wheel. Thus, the tyre sidewall vibrates and consequently radiates sound into the environment. In the case of a perpendicular radiation direction relative to the sidewall, the radiated sound may reach the microphone in the pass-by noise test. Thus, the tyre cavity resonances, via the sound radiation of the tyre sidewall, have an effect on the pass-by noise test. This may be recognisable in particular in the proposed constant-speed pass-by noise test. Therefore, a tyre sidewall replica (TSR) test rig is designed and built in order to replicate the tyre cavity resonance excitation and the tyre sidewall sound radiation. The TSR test rig or noise source, respectively, is utilised to test the proposed pass-by noise prediction method of this work in the available laboratory facility.

After introducing the design of the TSR test rig, the result of an experiment for the identification of the cavity modes of the TSR test rig is presented. The sidewall is replicated through a membrane. Therefore, the annular membrane model (AMM) is devised in order to identify the membrane tension resulting in a match of the eigenfrequencies of the membrane and the cavity. Thus, it is assumed that the coupling of the tyre cavity resonances and the tyre sidewall radiation can be replicated sufficiently well. This is followed by the presentation of the experiments in which the membrane tension of the TSR test rig is tuned and estimated via measured strain fields, which are acquired using the Digital Image Correlation (DIC) technique. Sound radiation experiments are conducted in the close proximity to the membrane in order to confirm that the cavity resonance frequencies are radiated via the membrane being a substitute for the sidewall. This is then complemented by the horizontal directivity measurements of the TSR

test rig, in which the radiated sound pressure is measured in a semi-circle around the TSR test rig. After the analysis of the directivity sound pressure, which is required for the prediction method, the pass-by noise validation data is obtained utilising the pass-by noise test rig. Due to the size and weight of the TSR test rig the validation data is recorded reciprocally. Eventually, the pass-by noise of the TSR is predicted and compared to the measured pass-by noise data.

6.1 Design of the tyre sidewall and cavity test rig

In this section, the design of the tyre sidewall replica (TSR) test rig is presented. For the investigation of the sound radiation of a tyre sidewall due to the excitation of the tyre cavity resonances, a test rig is designed which replicates the outer tyre structure and sidewall.

The purpose of the TSR test rig is to replicate the excitation mechanism of the tyre sidewall due to the tyre cavity resonances and the resulting exterior sound radiation of the tyre sidewall. Thus, the TSR test rig can be used as a substitute noise source in the development of the pass-by noise prediction model in order to estimate the contribution of the tyre sidewall noise due to tyre cavity resonance excitation. A photograph of the test rig is shown in Fig. 6.1.

In the test rig, the shape of the tyre air cavity is formed by two wooden shells in circular shape, thus, representing the inner and outer boundary. The diameters of both the inner and outer shells as well as their width were chosen to match the size of a real tyre air cavity closely. The diameter of the outer shell is 609.6 mm, the diameter of the inner shell is 355.6 mm, and the width of the shells is 203.2 mm. Subtracting the wall thickness of 13 mm from the diameter of the outer shell, the outer diameter of the cavity becomes 583.6 mm. These dimensions approximate the tyre air cavity of a common radial tyre of the size 195/65R14 generally well. Assuming a tyre wall thickness of 10 mm, the outer diameter of the tyre cavity is 589.1 mm which is just 5.5 mm larger than the outer diameter of the cavity of the TSR test rig. The inner diameter of the cavities are the same. The width of the tyre is 195 mm which is just 8.2 mm shorter than the width of the cavity of the TSR test rig. It is further assumed that the unwrapped length of the cavity is decisive for the development of cavity noise in the frequency range of interest up to 1 kHz at which cross modes along the radial height or the width of the cavity begin to occur. Therefore, the effect of small discrepancies between the real cross-sectional shape of the tyre cavity, which is not only characterised by the aforementioned quantities but also by the shape of the rim and tyre, and the rectangular cross

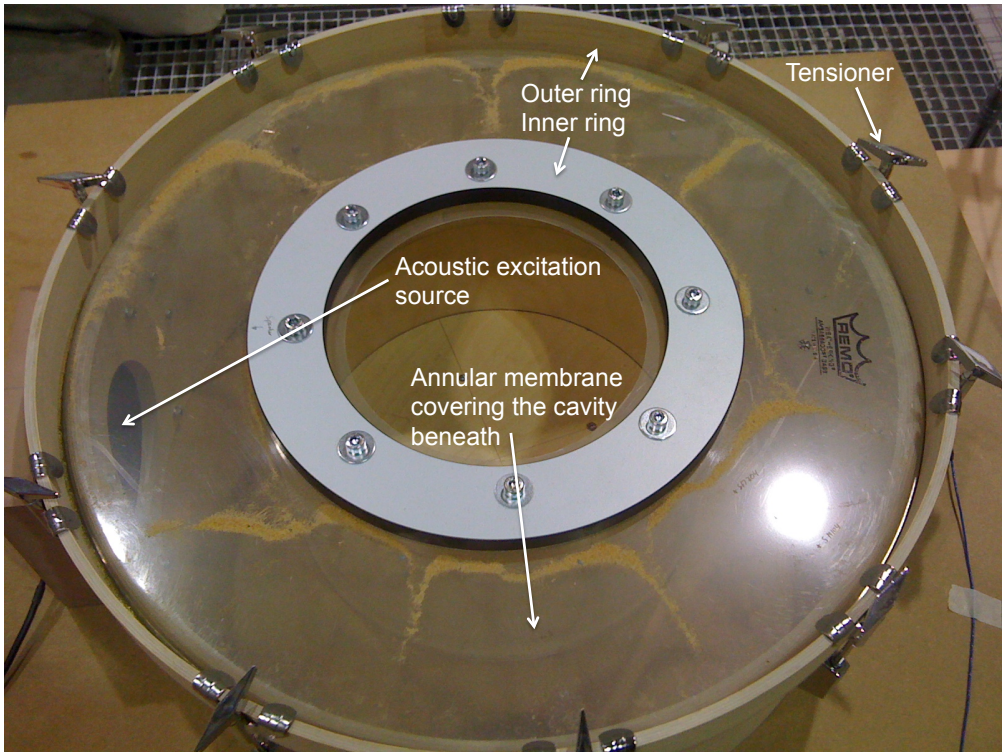

Figure 6.1: The tyre sidewall replica test rig with the acoustic excitation source on the left-hand side.

section of the cavity of the TSR test rig is assumed to be negligible.

The shells are attached to a massive wooden back board, which confines the cavity on one side. It is anticipated that the large wall thicknesses and weight of the shells and the backboard provide sufficiently high level of rigidity in order to avoid unwanted impact on the acoustic properties of the cavity and the membrane. On the opposite side of the cavity, Mylar® polyester film of an annular shape, which is utilised to replicate the tyre sidewall, confines the cavity. The annular polyester film or membrane, respectively, covers the whole area between the inner and outer shells, which approximately corresponds to the area of the sidewall and the shoulder of the real tyre. The physical and thermal properties of the Mylar® material are published by the manufacturer in Ref. [26].

A tension has to be applied on the annular polyester film, otherwise it cannot vibrate nor radiate sound at all. If tension is applied, the polyester film is considered to have the properties of a membrane. The tensioning mechanism is shown in Fig. 6.2. On its outer diameter, the polyester film is molded into a ring. The ring is slightly larger than the outer shell and, thus, just fits around it whilst the membrane lies on the edge of the outer shell. In the assembled TSR test rig, a wooden hoop is laid on top of the ring, which provides a hardpoint for the claw of the tensioning system, as shown in Fig. 6.2. The tensioning system consists of a metal claw, bolt and lug, where the latter one is attached to the outside of

the outer shell. The claw is guided through the bolt. Fastening the bolt into the lug, the hoop and the membrane ring is pulled downwards by the claw, which ultimately increases the tension in the membrane. At the inner shell, the membrane is clamped between two rings, which avoids the membrane from moving when the tension is increased. The lower ring is attached to and supported through the inside of the inner shell whilst the upper ring is laid on its top (Fig. 6.2). The outer diameters of the upper ring and of the inner shell are mutually-flush, thus, providing an appropriate clamping condition. The rings are held together via eight bolted connections providing approximately even clamping conditions along the circumference. Overall, the annular membrane is tensioned by ten bolts which are distributed evenly along the outside of the outer shell except at the position of the loudspeaker. Basically, the loudspeaker replaces the tyre/road contact patch, which is assumed to be the main excitation source for a rolling tyre in reality. The loudspeaker is mounted on a bracket which is attached to the outside of the outer shell. Located closely to the outer shell, the loudspeaker generates sound waves which travel through a circular hole in the outer shell, which is of the size of the loudspeaker membrane, into the cavity of the TSR test rig. A suitable acoustic excitation signal is white noise, for example, which generates constant sound pressure amplitudes over a broad range of frequencies. Thus, the acoustic excitation of the cavity resonance frequencies is ensured.

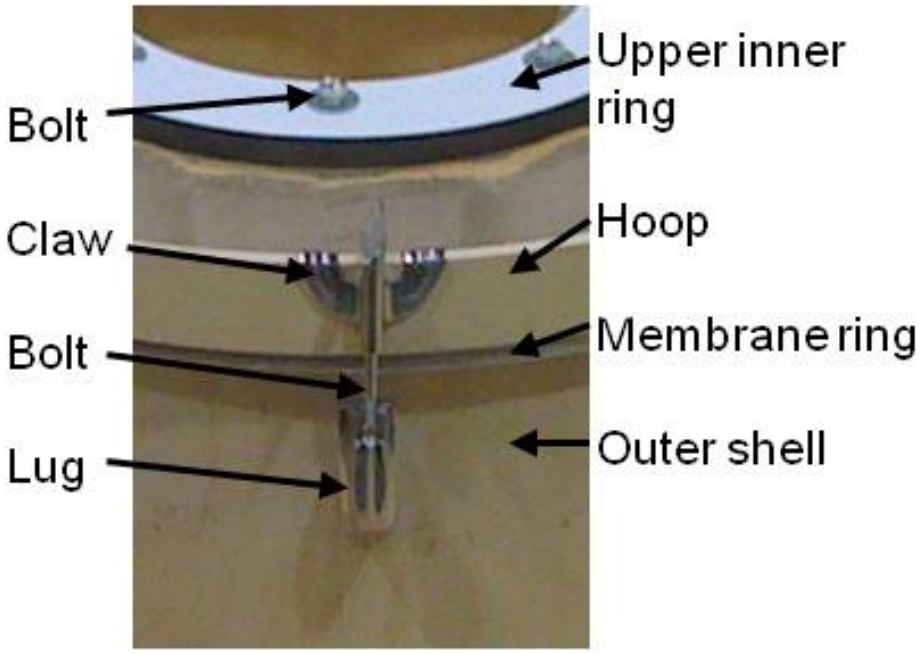

Figure 6.2: The tensioning system for the annular membrane of the tyre sidewall replica test rig in detail.

The polyester film material is of a lightweight design and is supposed to provide excellent responsiveness in case of acoustic excitation from the cavity resonance.

The consequence is a suitable sound radiation generation. Thus, the membrane material may be advantageous in this test rig solution in comparison to a rubber material, which originates from a real tyre or shares similar specifications to tyre rubber material. The integration of such rubber material in the test rig and the design of the tensioning system would have been more complex. In addition, using the tensioning system, the tension can be adjusted in the annular membrane resulting in a specific set of eigenfrequencies. Thus, the eigenfrequency and mode shape of the annular membrane can be matched with the eigenfrequency and the mode shape of the cavity. Then, the excitation of the membrane due to the cavity resonance is replicated successfully.

6.2 The cavity resonances of the tyre sidewall replica test rig

The cavity resonances of the TSR test rig are investigated in this section. Therefore, the experimental procedure is explained and the spectrum of the sound pressure measured inside the cavity is presented. This is in support of the analysis of the excitation mechanism of the sidewall replica, which is the annular membrane.

A microphone is inserted into the cavity of the TSR test rig through a hole in the TSR test rig. The hole is located midway on the outer shell on the opposite side to the loudspeaker. The depth of the microphone position inside the cavity is varied between 25 mm and 75 mm. The loudspeaker radiates a white noise excitation signal in the frequency range of interest. The measured sound pressure is averaged and the power spectral density spectrum is produced.

The measured cavity resonances are presented in this section, which are then compared to the estimated cavity resonances from the Cartesian periodic duct theory. Fig. 6.3 presents three graphs of the power spectral density of the measured sound pressure inside the cavity of TSR test rig. Each graph was averaged 20 times. In Table 6.1, the first few resonance frequencies of the spectrum, which are associated with the mode shapes of the sound waves in the circumferential direction of the cavity, are compared to the calculated cavity resonance frequencies. These were determined through the application of the Cartesian periodic duct theory for which it was assumed that the cavity is not rotating and that its inner and outer radii are not varied and that no resonators are attached to the cavity.

From the spectrum in Fig. 6.3 it is assumed that the peak at 208 Hz is the resonance frequency of the first mode in the circumferential direction of the cavity of the TSR test rig. The frequencies at which the second, third and fourth mode

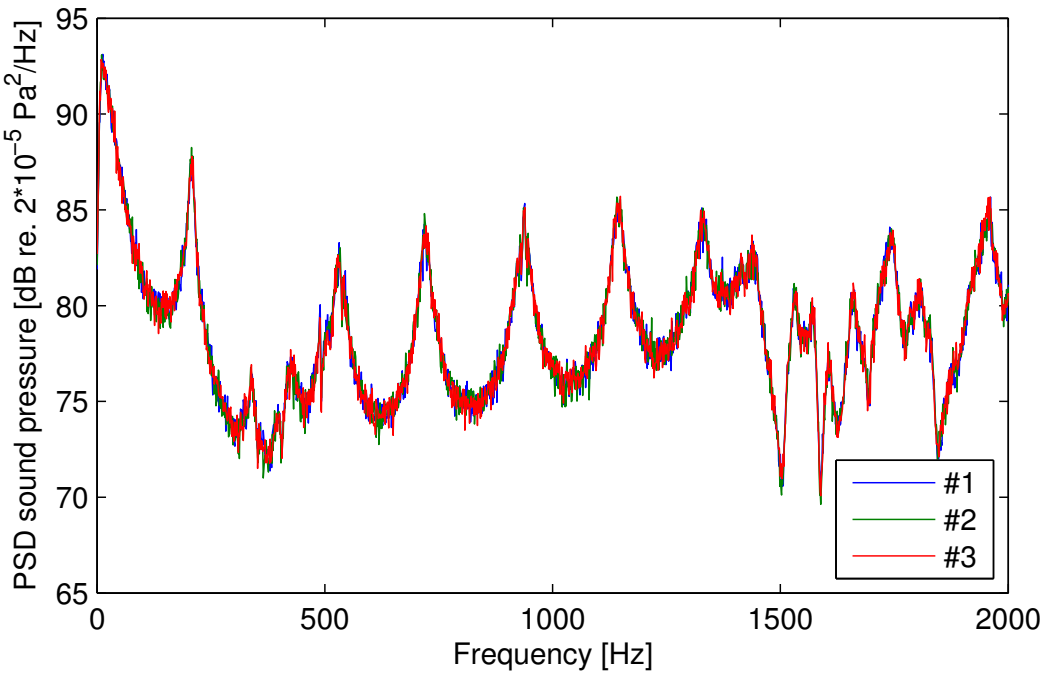

Figure 6.3: The power spectral density of the measured sound pressure inside the cavity of the TSR test rig.

n	Calculated $f_{0,c,n}$ [Hz]	$f_{0,c,n} - f_{0,c,n-1}$ [Hz]	Measured $f_{0,m,n}$ [Hz]	$f_{0,m,n} - f_{0,m,n-1}$ [Hz]	$f_{0,c,n} - f_{0,m,n}$ [Hz]
1	230	-	208	-	22
2	459	230	531	323	-72
3	689	230	719	188	-30
4	919	230	939	220	-20
5	1149	230	1141	202	8
6	1379	230	1325	184	54

Table 6.1: Comparison of the calculated and measured resonance frequencies of the cavity of the TSR test rig. (Values are rounded.)

shapes occur are 531 Hz, 719 Hz and 939 Hz. Applying the Cartesian periodic duct theory, the calculated first resonance frequency is 230 Hz, which is 22 Hz higher than the measured resonance frequency. Alternatively, the circular annular duct theory is applied resulting in the calculated first resonance frequency of 229 Hz, which is just 1 Hz below the result of the Cartesian periodic duct theory. The calculated frequencies of higher resonances occur at constant intervals of approximately 230 Hz, making them multiples of the first harmonic. The multiples appear at integer ratios. In contrast, the ratio between the measured resonance frequencies to the first resonance frequency are not integers for $n \geq 2$. For the second to the sixth resonance frequency, the ratios, rounded to the first decimal place, are 2.6, 3.5, 4.5, 5.5, 6.4. Although the ratios vary slightly, it seems that they are equivalent to $(n + 0.5)$ with $n = [2, 3, 4, 5, 6]$. The differences between the measured

resonance frequencies, presented in the fifth column of Table 6.1, show that the difference between the first and the second resonance frequency is 323 Hz. This is a relatively large value in comparison to the other differences between adjacent resonance frequencies, which only vary between 184-220 Hz. Thus, it seems that the large difference between the first and the second resonance frequency define the $(n + 0.5)$ ratio of the first resonance frequency and its multiples. This is also supported by the smaller distances between the second and the sixth resonance frequencies, which are between 184-220 Hz and, thus, are closer to the value of the first measured resonance frequency of 208 Hz.

The highest amplitude of the cavity resonances in Fig. 6.3 is 87.8 dB and occurs at 208 Hz, which confirms that this resonance belongs to the first mode in the circumferential direction of the cavity. The amplitude of the second resonance has a value of 83 dB, and is therefore the smallest among the first six resonance frequencies. Up to the fifth resonance, the amplitudes increase up to a value of 85.5 dB whilst the sixth amplitude is 0.5 dB smaller than the previous one. The amplitudes are generally much smaller than the reported value of 140 dB, which develops in a real tyre due to the excitation of the cavity resonances. However, the magnitude of the amplitudes is deemed to be sufficiently high for the application in this work.

The damping of the resonance peaks can be characterised through the width of the resonance peaks. For resonances originating from the air column in the cavity of the TSR test rig, a very low damping is expected, as it occurs for the first resonance frequency. For the second to the sixth resonance frequencies, the damping is slightly higher than the damping for the first resonance frequency. However, the damping is approximately constant for these resonances when the width of the resonance is estimated at amplitudes which are 3 dB less than the resonance peak. Maybe, the annular membrane has an influence on the damping of the second to the sixth resonance frequency.

The comparison of the calculated and the measured resonance frequencies in Table 6.1 shows that the measured first resonance frequency is smaller than the corresponding calculated resonance frequency. However, the measured second, third and fourth resonance frequencies are higher than their corresponding calculated resonance frequencies. The difference between the measured and calculated resonance frequencies decreases from 72 Hz for the second resonance frequency to 20 Hz for the fourth. At the fifth resonance frequency, the calculated and the measured frequencies are closest with a difference of just 8 Hz. For the sixth resonance frequency, the distance between the calculated and the measured resonance frequency increases again to 54 Hz. The measured resonance frequencies are smaller than the corresponding calculated resonance frequencies for the first, fifth and

sixth resonance whilst they are higher for the second, third and fourth resonance.

The temperature varies between the calculated and the measured resonance frequencies. In the calculation, a temperature of 20°C is used. During the sound pressure measurement, the temperature is estimated to be 12°C. Due to the lower temperature the speed of sound in the experiment is lower than the speed of sound in the calculation. Thus, a lower resonance frequency is expected in the experiment, since the wavelength of the corresponding resonance frequency remains constant due to the fixed length of the circumference of the cavity. This follows the basic equation $f = c/\lambda$, where the frequency f is equal to the quotient of the speed of sound c and the wavelength λ. However, a decrease of 22 Hz between the calculated and the measured first resonance frequency is deemed to be too high to be caused entirely by a shift in temperature of 8°C. Using the geometries of the cavity of the TSR test rig, the effective circumferential length or the wavelength becomes approximately 1.5 m. For a temperature of 20°C, the circumferential length equates to a frequency of 230 Hz using the Cartesian periodic duct theory. Decreasing the temperature to a value of 12°C results in a frequency of 227 Hz, which is just a reduction of 3 Hz.

Modes across the width or the radius of the cavity begin to appear at higher frequencies. Using the cavity width in conjunction with the Cartesian periodic duct theory, a frequency of 936 Hz is estimated to be the limit up to which plane wave propagation is assumed to occur in the circumferential direction and from which cross modes begin to develop. The measured resonance frequencies, which are also listed in Tab. 6.1, basically show a harmonic behaviour up to approximately 1400 Hz in Fig. 6.3. They are deemed to characterise plane waves in the circumferential direction of the cavity. Thus, it is assumed that modes across the width or across the radius do not occur below 1400 Hz. This is supported through Fig. 6.4, which presents the measured cavity resonances of two microphone positions, which are inserted either 25 mm or 75 mm into the cavity. The recorded sound pressure data of both positions only differs marginally up to 1200 Hz. Larger variations occur at higher frequencies. From approximately 1500 Hz, the two signals show opposite characteristics which means that a resonance occurs for one signal and an anti-resonance for the other signal. This can be observed well in the frequency range of 1500-1800 Hz. Thus, this may indicate the modes across the width or the radius of the cavity. This is under the assumption that such cross modes are detectable with a microphone at the measurement position in use and that the resonance frequencies of the cross modes are not masked by or develop at the same frequency as any of the resonance frequencies of the circumferential modes below 1400 Hz.

The coherence between the sound pressure inside the cavity of the TSR test rig

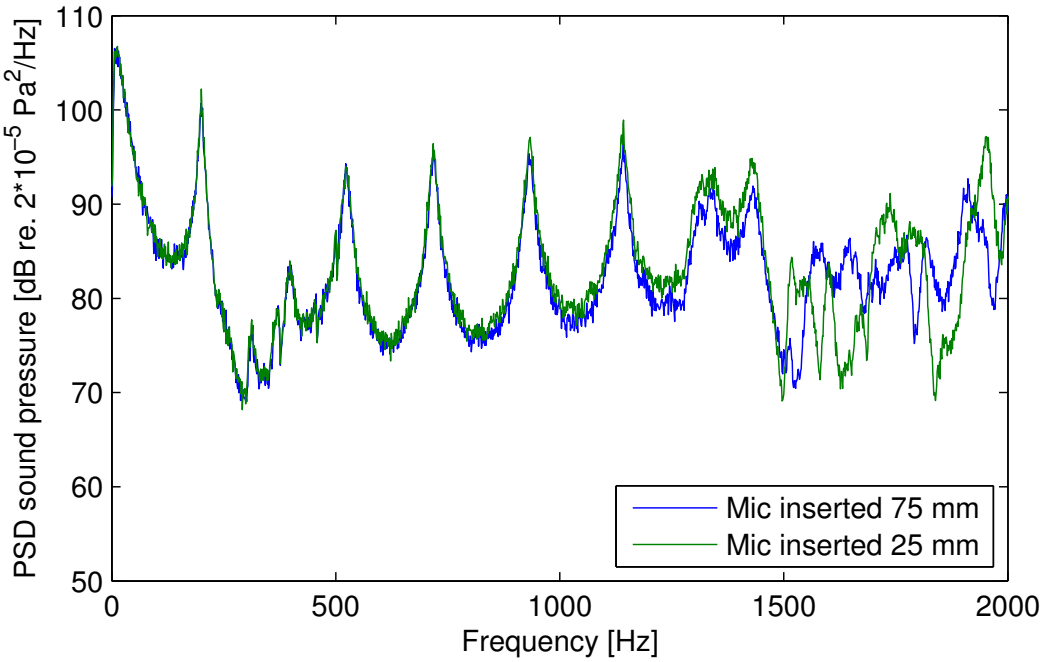

Figure 6.4: The power spectral density of the measured sound pressure of two measurement positions inside the cavity of the TSR test rig. The measurement positions vary in the distance between the microphone and the inside of the outer shell.

and the voltage signal of the electric current sensor, which measures the electric current into the loudspeaker, is presented in Fig. 6.5. The results for the coherence, which is plotted against frequency, are deemed to be generally good. The majority of the values of the coherence are above 0.9, which indicates that the sound pressure signal originates from the white noise excitation signal of the loudspeaker. Low coherence values indicate a poor correlation between two signals. Although, a decline of the coherence occurs in the frequency ranges 240-330 Hz, 345-415 Hz, 491 Hz, 539 Hz, 1485-1514 Hz, 1615-1639 Hz, 1698 Hz and 1838-1860 Hz, this cannot be correlated to any resonances in the sound pressure spectrum of Fig. 6.3.

The three consecutive recordings, which have been made and which are displayed in the sound pressure spectrum in Fig. 6.3 and in the coherence in Fig. 6.5, show similar results. This indicates that the experiment has a high level of repeatability.

The spectrum of the measured voltage signal of the electric current sensor, which measures the electric current into the loudspeaker, is presented in Fig. 6.6. A sharp peak occurs at 10 Hz, which is the cause for the corresponding sharp peak in the sound pressure spectrum in Fig. 6.3. After the sharp peak, the amplitude of the voltage signal decreases further up to approximately 200 Hz. Between 200-500 Hz, the signal remains approximately constant. Then, it starts to increase slowly up to a frequency of 1600 Hz, after which it remains constant

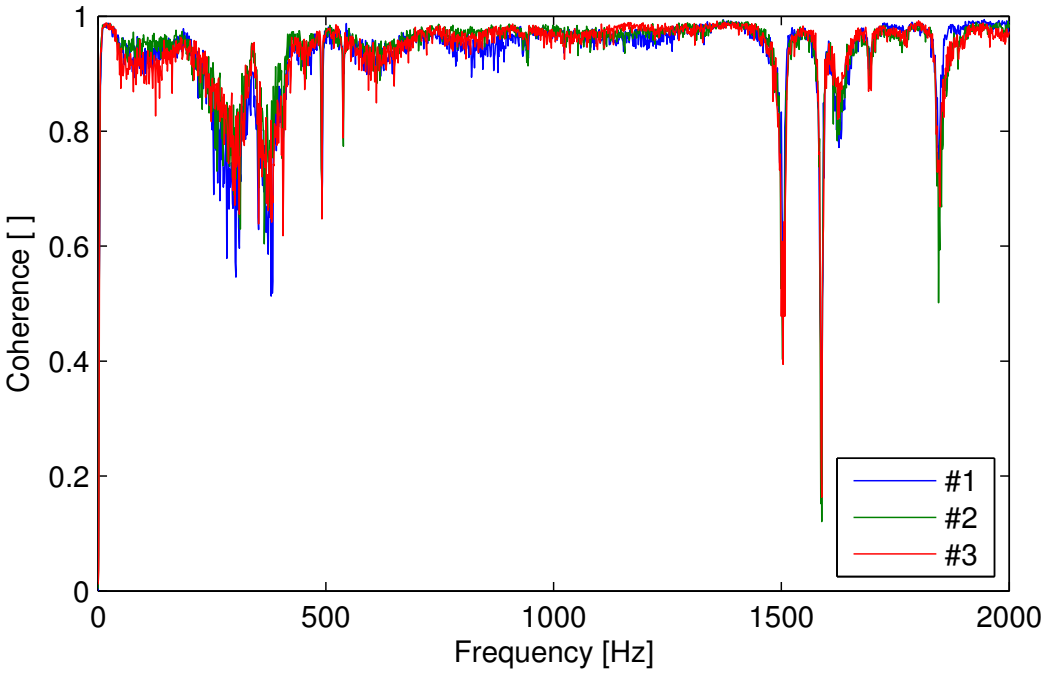

Figure 6.5: The coherence between the sound pressure inside the cavity of the TSR test rig and the voltage signal of the electric current sensor, which measures the electric current into the loudspeaker.

again. Despite the small amplitude variations, the excitation signal appears to be relatively constant with no distinctive peaks except the one at 10 Hz. The voltage signal is proportional to the electric current into the loudspeaker, which is a measure of the acoustic output of the loudspeaker. It is assumed that the alterations in the voltage signal are related to the electrodynamic characteristics of the loudspeaker. Since the amplitudes in Fig. 6.6 increase with frequency, the dynamic output of the loudspeaker should increase as well. Thus, the sound pressure amplitudes slightly increase between the second and the sixth resonance frequencies in Fig. 6.3.

Although the measurement results of this section seem to be plausible, discrepancies exist between the resonance frequencies of the measured sound pressure and the cavity resonance frequencies, which are determined using the Cartesian periodic duct theory. Possible influences could originate from the geometrical shape of the cavity, the cavity boundaries or the acoustic excitation source. The geometry of the cavity, which is bordered by the inner and outer shells, the backboard and the annular membrane, is the decisive element in the development of the resonance modes. Both the inner and outer shells are of a circular shape. Even during the tensioning process of the annular membrane, the shape of the shells were not distorted to an extent where it would be visually recognisable. The cavity may not be ideally sealed. Whilst the backboard is bolted to the shells, which should

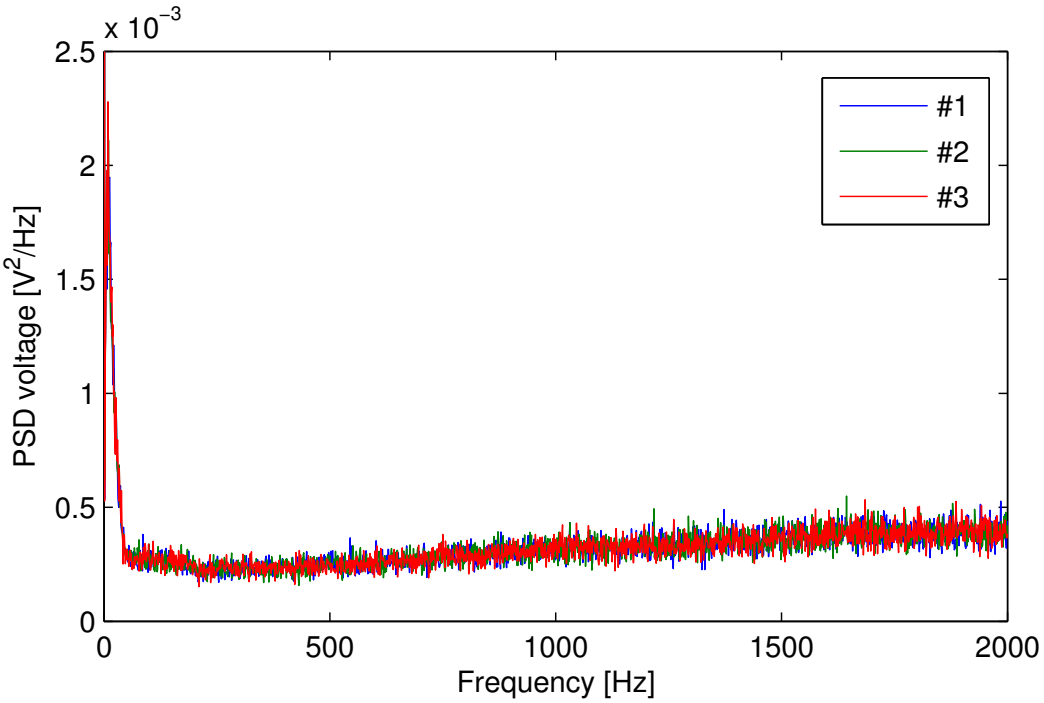

Figure 6.6: The spectrum of the measured voltage signal of the electric current sensor, which measures the electric current into the loudspeaker.

provide a suitable sealing, small gaps might develop between the annular membrane and the outer shell between two tensioning positions, where the force may be less than at the tensioning position directly. Since the annular membrane is an elastic part, it might interact with the oscillating air column inside the cavity. There are no indications that the excitation mechanism does not work out.

6.3 Annular membrane model of the tyre sidewall

The annular membrane model (AMM) is devised for the modelling of the annular membrane of the tyre sidewall replica (TSR) test rig. Since the annular membrane replicates the tyre sidewall, the eigenfrequencies of the TSR test rig cavity and the annular membrane shall match in order to replicate the excitation mechanism of the acoustic tyre cavity resonances onto the tyre sidewall. By means of the annular membrane model (AMM), the eigenfrequencies of the annular membrane of the tyre sidewall replica (TSR) test rig can be estimated and the corresponding mode shapes can be visualised. Thus, it will be possible to adjust the tension within the annular membrane in order to match a particular eigenfrequency of the membrane with a cavity resonance frequency of the TSR test rig.

Certain assumptions and requirements apply to a membrane model in general.

A membrane is described as a planar elastic continuum in Ref. [42]. The membrane expands in two dimensions and is pre-tensioned and its wall thickness is assumed to remain constant. However, due to the thin membrane wall the bending stiffness will be very small. Therefore, the transmission of bending moments is assumed to be negligible. Shear forces in the orthogonal direction to the plane of the membrane are neglected as well. In order for the membrane to vibrate, a tension must exist within the plane of the membrane. The tension, which is determined from the product of the principal stress and the membrane thickness, is assumed to be constant and evenly distributed throughout the membrane. Other assumptions are that any displacement of any point of the membrane are small and perpendicular to the plane of the deflected membrane. The membrane material is assumed to be of homogeneous and isotropic characteristic.

The equation of motion of the annular membrane will be derived in the polar coordinate system, which is the preferred coordinate system due to the circular shape of the annular membrane. In addition, initial and boundary conditions can be formulated conveniently as well.

Considering the deflection of a pre-tensioned annular membrane, the equilibrium of forces within the membrane can be viewed on an infinitesimal element of the annular membrane, as it is illustrated in Fig. 6.7. The cross-sectional views of the infinitesimal element in the vertical-radial z-r and the vertical-circular z-$r\varphi$ plane is shown in Fig. 6.8. The deflection $\mathrm{d}z$ is small, however the tension in the membrane results in a restoring force, which returns the membrane to the state of equilibrium. The tension per unit length T is defined by the product of the principal stress and the thickness of the membrane

$$T = \sigma_{r/\varphi} \times h \tag{6.1}$$

where $\sigma_{r/\varphi}$ is the principal stress in the radial or tangential direction and h is the thickness of the membrane. The assumption of a constant and evenly distributed tension as well as a constant membrane thickness results in a constant principal stress throughout the membrane, which is $\sigma_r = \sigma_\varphi = \text{constant}$.

The field variable is denoted $z = z(r, \varphi, t)$, which is a function of time t, the radial coordinate r and the polar coordinate φ. The equation of motion can be determined as the sum of the forces F in the vertical direction z

$$\begin{aligned} \sum F_{(z)} = m\ddot{z} = {} & T\left(r + \mathrm{d}r\right)\mathrm{d}\varphi \sin\left(\vartheta(r + \mathrm{d}r)\right) - T\, r\, \mathrm{d}\varphi \sin\left(\vartheta(r)\right) \\ & + T\, \mathrm{d}r \sin\left(\alpha(r(\varphi + \mathrm{d}\varphi))\right) - T\, \mathrm{d}r \sin\left(\alpha(r\varphi)\right) \end{aligned} \tag{6.2}$$

where the mass of the membrane is m, the acceleration in the z direction is $\ddot{z}$,

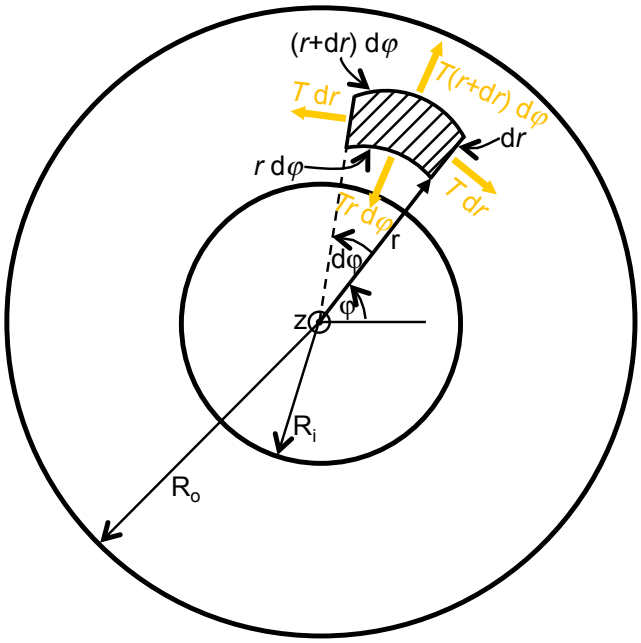

Figure 6.7: An infinitesimal element of an annular membrane in the polar coordinate system.

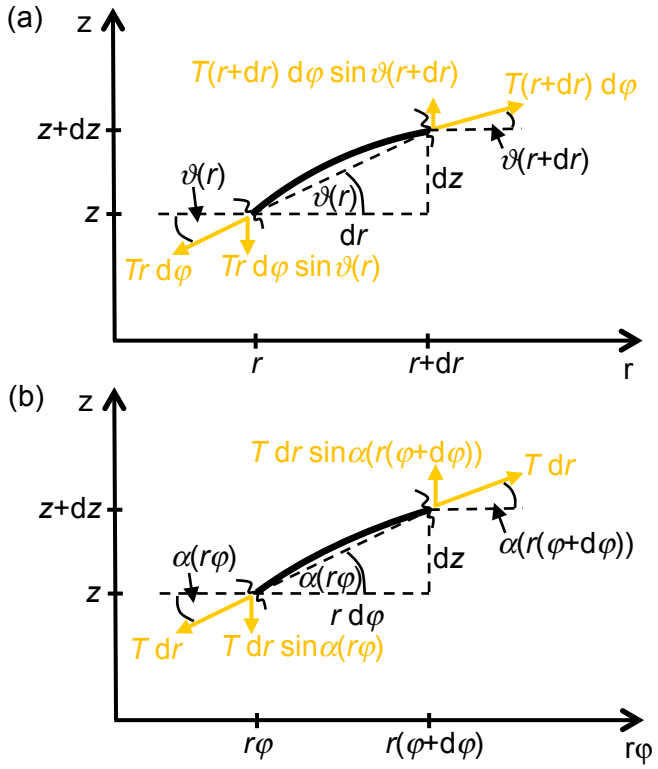

Figure 6.8: Cross-sectional view of the infinitesimal element of an annular membrane in the (a) z-r and (b) z-$r\varphi$ coordinate systems.

the dimensions of the infinitesimal element in the radial and tangential directions are denoted dz and dφ, and the deflection angles in the z-r and z-$r\varphi$ coordinate systems are denoted ϑ and α, as shown in Fig. 6.8.

For small displacements and, thus, small angles, the following simplifications can be implemented, introducing the notation of partial derivatives for the dependent variable z

$$\sin\left(\vartheta(r)\right) \approx \tan\left(\vartheta(r)\right) = \left.\frac{\partial z}{\partial r}\right|_{r} \tag{6.3}$$

$$\sin\left(\vartheta(r+\mathrm{d}r)\right) \approx \tan\left(\vartheta(r+\mathrm{d}r)\right) = \left.\frac{\partial z}{\partial r}\right|_{r+\mathrm{d}r} \tag{6.4}$$

$$\sin\left(\alpha(r\varphi)\right) \approx \tan\left(\alpha(r\varphi)\right) = \left.\frac{1}{r}\frac{\partial z}{\partial \varphi}\right|_{r\varphi} \tag{6.5}$$

$$\sin\left(\alpha(r(\varphi+\mathrm{d}\varphi))\right) \approx \tan\left(\alpha(r(\varphi+\mathrm{d}\varphi))\right) = \left.\frac{1}{r}\frac{\partial z}{\partial \varphi}\right|_{r(\varphi+\mathrm{d}\varphi)} \tag{6.6}$$

The mass m can be substituted with the mass per unit area, which is defined as $\hat{\mu} = \rho h$, where ρ is the density per unit volume. The area of the infinitesimal element is substituted with $\mathrm{d}r\, r\, \mathrm{d}\varphi$.

$$\begin{aligned}\hat{\mu}\,\mathrm{d}r\, r\,\mathrm{d}\varphi\,\frac{\partial^2 z}{\partial t^2} = T\Bigg(r\,\mathrm{d}\varphi \underbrace{\left(\left.\frac{\partial z}{\partial r}\right|_{r+\mathrm{d}r} - \left.\frac{\partial z}{\partial r}\right|_{r}\right)\frac{1}{\mathrm{d}r}}_{\text{Partial differential quotient}}\mathrm{d}r + \mathrm{d}r\,\mathrm{d}\varphi\left.\frac{\partial z}{\partial r}\right|_{r+\mathrm{d}r} \\ + \frac{\mathrm{d}r}{r}\underbrace{\left(\left.\frac{\partial z}{\partial \varphi}\right|_{r(\varphi+\mathrm{d}\varphi)} - \left.\frac{\partial z}{\partial \varphi}\right|_{r\varphi}\right)\frac{1}{\mathrm{d}\varphi}}_{\text{Partial differential quotient}}\mathrm{d}\varphi\Bigg)\end{aligned} \tag{6.7}$$

After substituting the partial differential quotients with the second partial derivative of z with respect to r and φ, respectively, and rearranging of Eq. 6.7, the equation of motion of an annular membrane in polar coordinates becomes

$$\frac{\partial^2 z}{\partial t^2} = \frac{T}{\hat{\mu}}\left(\frac{\partial^2 z}{\partial r^2} + \frac{1}{r}\frac{\partial z}{\partial r} + \frac{1}{r^2}\frac{\partial^2 z}{\partial \varphi^2}\right) \tag{6.8}$$

Eq. 6.8 is a hyperbolic linear partial differential equation of second order with two space variables and represents the two-dimensional wave equation for an annular membrane in polar coordinates. The square root of the quotient of tension and mass per area in Eq. 6.8 is denoted the wave propagation speed of the annular membrane

$$c = \sqrt{T/\hat{\mu}} \tag{6.9}$$

The wave equation describes the characteristics of a transverse wave type. The

solution of the wave equation, Eq. 6.8, is known and given in Ref. [70] as follows

$$\begin{aligned} z(r,\varphi,t) \;=\; & \frac{\partial}{\partial t}\int_0^{2\pi}\int_{R_i}^{R_o} f_0(\xi,\eta)G(r,\varphi,\xi,\eta,t)\xi \mathrm{d}\xi \mathrm{d}\eta \\ & + \int_0^{2\pi}\int_{R_i}^{R_o} f_1(\xi,\eta)G(r,\varphi,\xi,\eta,t)\xi \mathrm{d}\xi \mathrm{d}\eta \\ & + c^2 R_i \int_0^t \int_0^{2\pi} g_1(\eta,\tau)\left[\frac{\partial}{\partial \xi}G(r,\varphi,\xi,\eta,t-\tau)\right]_{\xi=R_i} \mathrm{d}\eta \mathrm{d}\tau \\ & - c^2 R_o \int_0^t \int_0^{2\pi} g_2(\eta,\tau)\left[\frac{\partial}{\partial \xi}G(r,\varphi,\xi,\eta,t-\tau)\right]_{\xi=R_o} \mathrm{d}\eta \mathrm{d}\tau \end{aligned} \tag{6.10}$$

where R_i and R_o are the inner and the outer radius of the membrane, G is the Green's Function, ζ, η and τ are the integration variables for the angle ϕ, the radius r and the time t, respectively.

The solution of the wave equation requires two initial conditions and two boundary conditions. The initial conditions are given by a function of the vertical displacement $f_0(r,\varphi)$ and its first derivative with respect to time $f_1(r,\varphi)$. Both functions are valid at the time $t = 0$ for every coordinate (r,φ). The boundary conditions are given by two displacement functions $g_1(\varphi,t)$ and $g_2(\varphi,t)$, which are valid at the two circumferential boundaries $r = R_i$ (inner radius) and $r = R_o$ (outer radius) of the annular membrane for any point in time t and every angular position φ. A zero displacement at the inner and outer boundaries is deemed to be the suitable boundary condition, which represents the clamped membrane material at the boundary of the TSR test rig.

In the solution of the wave equation, Eq. 6.10, Green's Function G is applied, which is defined in Ref. [70] as

$$G(r,\varphi,\xi,\eta,t) \;=\; \frac{\pi}{2a}\sum_{n=0}^{\infty}\sum_{m=1}^{\infty} A_n B_{nm} Z_n(\mu_{nm} r) Z_n(\mu_{nm}\xi)\cos[n(\varphi-\eta)]\sin(\mu_{nm} c t) \tag{6.11}$$

Where

$$A_n \;=\; \begin{cases} 1/2 \text{ for } n = 0 \\ 1 \text{ for } n \neq 0 \end{cases} \tag{6.12}$$

$$B_{nm} \;=\; \frac{\mu_{nm} J_n^2(\mu_{nm} R_o)}{J_n^2(\mu_{nm} R_i) \;-\; J_n^2(\mu_{nm} R_o)} \tag{6.13}$$

$$Z_n(\mu_{nm} R_1) \;=\; J_n(\mu_{nm} R_i) Y_n(\mu_{nm} r) \;-\; Y_n(\mu_{nm} R_i) J_n(\mu_{nm} r) \tag{6.14}$$

Where $J_n(r)$ and $Y_n(r)$ are the Bessel functions of the first and second kind.

Thus, the index n represents the order of the Bessel functions whilst the index m gives the mth zero of the Bessel function. The variable μ_{nm} represents the positive roots of the equation

$$J_n(\mu_{nm}R_i)Y_n(\mu_{nm}R_o) - Y_n(\mu_{nm}R_i)J_n(\mu_{nm}R_o) = 0 \tag{6.15}$$

The root (n, m) is defined by the quotient of the natural frequency of the (n, m) mode and the wave speed of the membrane, which is equivalent to the wave number k_{nm}.

$$\mu_{nm} = \frac{\omega_{nm}}{c} \tag{6.16}$$

In order to study the inherent characteristics of the annular membrane model, the free response of the annular membrane is to be calculated. The eigenfrequencies of the annular membrane are obtained from Eqs. 6.15 and 6.16. The corresponding mode shapes can be visualised utilising the numerical solution of the wave equation Eq. 6.10, as it is exemplarily shown in Fig. 6.11. This is programmed in Matlab®, in which the annular membrane is represented by a finite coordinate mesh. A zero displacement is required on both the inner and outer radius of the annular membrane, which is considered through the boundary conditions $g_1(\varphi, t) = g_2(\varphi, t) = 0$ in Eq. 6.10. For the definition of the initial conditions in Eq. 6.10, a small deflection of a single point of the annular membrane is chosen for the first initial condition $f_0(r, \varphi)$ whilst the second initial condition $f_1(r, \varphi)$ is set to zero. The value of the mass per area $\hat{\mu}$ is determined from the density of the membrane material of the TSR test rig. According to the material specifications in Ref. [26], the density per unit volume is $\rho = 1390\,\mathrm{kg/m^3}$. Considering the membrane thickness of 0.254 mm of the TSR test rig, which is assumed to be a sufficient low value for the wall thickness of a membrane, the mass per area results in $\hat{\mu} = 0.3531\,\mathrm{kg/m^2}$.

Some of the characteristics of the annular membrane model are to be discussed in the following. Fig. 6.9 presents the eigenfrequencies of the annular membrane model plotted against the order of the Bessel functions with the parameters of the tension and the zeros of the Bessel function. The eigenfrequencies are determined using Eq. 6.15 in which the term μ_{nm}, which contains the value of the natural frequency, is varied, whilst the order of the Bessel functions remain constant, until the equation is satisfied. Then, using Eq. 6.16, the roots μ_{nm} are converted into the natural frequency ω_{nm} or eigenfrequency $f_{nm} = \omega_{nm}/(2\pi)$, respectively. The index nm specifies the eigenfrequency or the mode shape, respectively, which corresponds to the nth order and the mth zero of the Bessel functions in Eq. 6.15. The inner and outer radius of the boundaries of the annular membrane as well as the wave speed, which is the quotient of the tension and mass per area of the

membrane material, are constants in Eq. 6.15. They are also the sole parameters on which the eigenfrequencies of the annular membrane depend on. In Fig. 6.9, the eigenfrequencies are a function of the order of the Bessel functions of the first and second kind, the zero of Eq. 6.15 and the tension. The tension values vary between 500 N/m, 1000 N/m and 2000 N/m, which are plotted in their distinctive colour in Fig. 6.9. For each tension value, the eigenfrequencies are displayed for 25 orders of the Bessel functions and for four zeros of Eq. 6.15, which means that four zeros are determined for a single order of the Bessel functions. Overall, this results in 100 eigenfrequencies for a single tension value. As it is shown in Fig. 6.9, the eigenfrequencies increase the higher is the tension or wave speed, respectively. The eigenfrequencies also increase, if either the order or the zeros of the Bessel functions or both of them increase. For an increasing order of the Bessel functions, diametrical nodal lines are added to the mode shape, as it can be seen in the mode shapes of Fig. 6.10. For an increasing number of the zeros of the Bessel functions, circumferential nodal lines are added to the mode shape. For a given tension, the higher the zero is the less the eigenfrequencies increase with increasing order. If the order of the Bessel functions is small, the three eigenfrequencies of the three different tension values of the same zero are located closely together. If the order is increasing, the spacing between the three eigenfrequencies increases as well. This characteristic can also be identified for the other zeros. Further, it can be observed for each of the tension values that higher eigenfrequencies are close together for different values of the order and zeros of the Bessel functions. It is concluded from Eq. 6.11 that the number of mode shapes is indefinite. Therefore, a high modal density is indicated the higher is the frequency. In testing however, a high modal density can make it potentially more difficult to identify any particular mode shape due to insufficient frequency resolution or masking effects. Different kind of mode shapes can occur at the same eigenfrequency if the tension in the membrane is changed.

Fig. 6.10 illustrates a few mode shapes of the annular membrane by means of diametrical and circumferential nodal lines. In Fig. 6.11, a three dimensional view of the mode shapes is presented, which was produced using the annular membrane model described in this section. Each of the eigenfrequencies belong to a particular mode shape, which are denoted according to the nm indices of the eigenfrequencies. The index n indicates the number of diametrical nodal lines in the mode shape whilst the index m indicates the number of circumferential nodal lines. The lowest number for n is zero, which is related to the order of the Bessel function starting at zero. No diametrical nodal line occurs for $n = 0$. The lowest number for m is one, which is related to the first index of the zero of the Bessel function. If $m = 1$, there is no additional circumferential nodal line in the mode

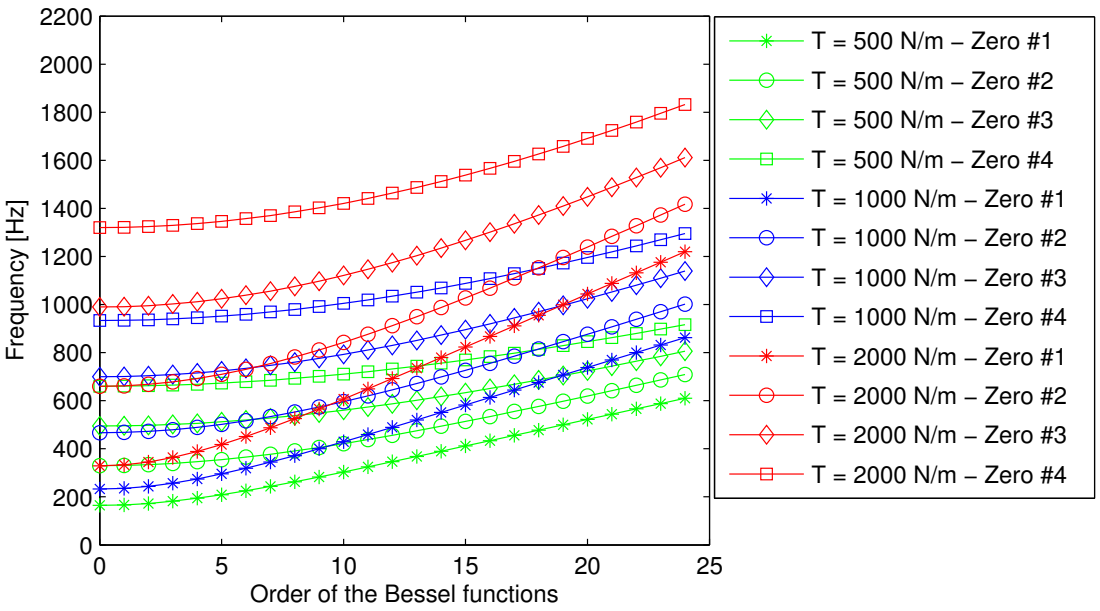

Figure 6.9: Comparison of the eigenfrequencies of the annular membrane model as a function of the tension, and the order and zeros of the Bessel functions of the first and second kind.

shape except that the inner and outer circumferences of the annular membrane experience a zero displacement. Thus, $m-1$ gives the number of circumferential nodal lines in the mode shape.

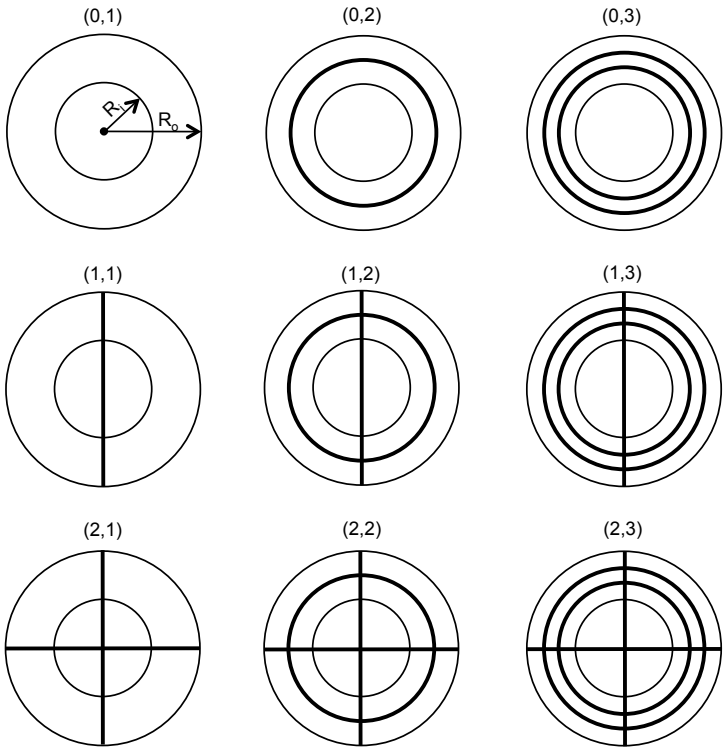

Figure 6.10: Illustration of nine principal mode shapes of the annular membrane.

In Fig. 6.10, the mode shape with the lowest eigenfrequency belongs to the $(0,1)$ mode, which does not show any diametrical nor circumferential nodal lines. Although, the displacement at the inner and outer circumferences of the annular membrane are zero, which is due to the boundary conditions, they are not interpreted as nodal lines since the boundary conditions can change. Thus, the denotation of the mode shape with $m-1$ giving the number of circumferential nodal lines does not need to be changed. The $(0,1)$ mode shows a deflection in the shape of a sinusoidal curve between the inner and outer radius. In the shape of the $(1,1)$ mode, a diametrical nodal line occurs splitting the annular membrane in half with displacements in both the positive and negative vertical directions. For modes with a higher n-index, the number of diametrical nodal lines increases. The areas between nodal lines remain equally large if a nodal line is added. In the shape of the $(0,2)$ mode, a circumferential nodal line occurs midway between the inner and outer radius with displacements in both the positive and negative vertical directions, which essentially corresponds a sine curve in radial direction. For modes with a higher m-index, the number of circumferential nodal lines increases. The areas between the circumferential nodal lines remain equally large if a circumferential nodal line is added. For modes with higher n and m values, the mode shape is more complex combining the characteristics of diametrical and circumferential nodal lines. For the chosen values of the inner and outer radius as well as the tension and the mass per area, the eigenfrequencies of the mode shape having only circumferential nodal lines are higher than the eigenfrequencies of the mode shapes with only diametrical nodal lines.

6.4 Experimental estimation of the tension in the annular membrane

The procedure of the estimation of the tension in the annular membrane is presented in this section. Therefore, the theoretical formulations for the tension calculation are introduced. Then, the experimental procedure is demonstrated in which the tension in the annular membrane is tuned. Eventually, the experimental results of the annular membrane deformation as well as the estimated tension are presented.

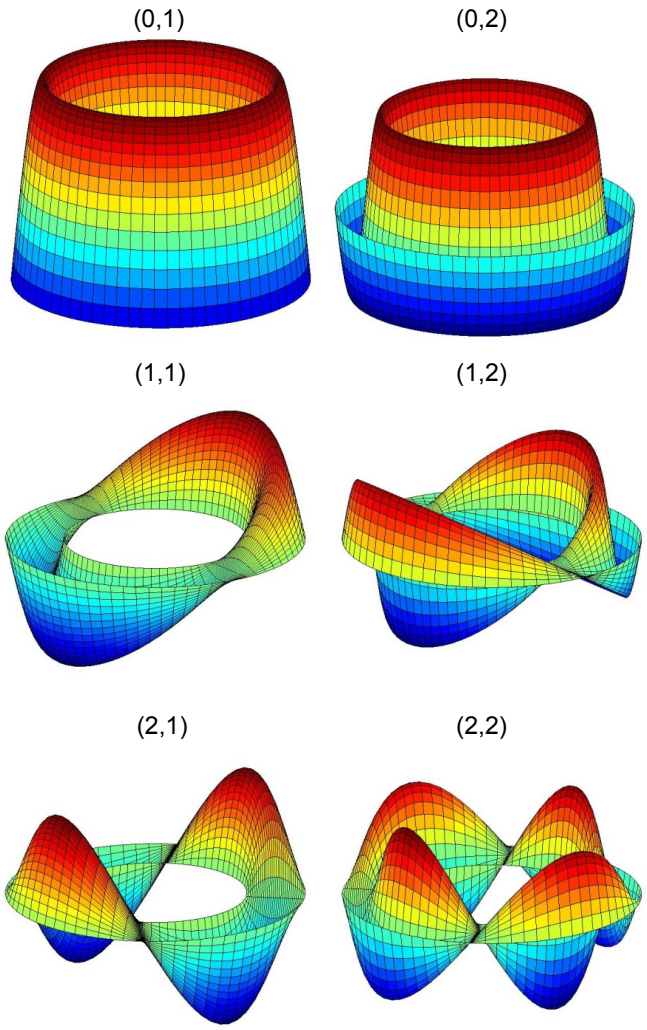

Figure 6.11: Mode shapes produced with the annular membrane model.

6.4.1 Theoretical foundation for the estimation of the tension in the annular membrane

In this section, it is described how the tension in an annular membrane can be estimated based on strain data.

Two assumptions, which were made for the annular membrane model (AMM) in Sec. 6.3, are to be applied for the determination of the tension in an annular membrane. The assumptions are that the tension is equal across the membrane wall and that the wall thickness of the annular membrane is constant. Then, the tension T can be calculated using Eq. 6.1, which is the product of the principal stress $\sigma_{r/\varphi}$ and the membrane thickness h, i.e. $T = \sigma_{r/\varphi} \times h$. The principal stresses point in radial (r) and tangential (φ) directions.

The wall thickness of the membrane is given as $h = 0.254\,\text{mm}$ due to the membrane which is used in the experiment in Sec. 6.1. Hence, if the principal

stresses in the membrane $\sigma_{r/\varphi}$ are known, the tension in the membrane can be determined. Therefore, if linear elastic deformation is assumed for the annular membrane in the tensioning process, the well-known Hooke's law is applied in order to determine the stress σ.

$$\sigma = E \times \varepsilon \tag{6.17}$$

with E being the modulus of elasticity and ε the strain.

The modulus of elasticity is known from the membrane material specifications in Ref. [26], which also states that elasticity is given up to a strain of 3% at 0°C and 2.5% at 35°C. The temperature range from 0°C to 35°C is deemed suitable for the application in this work. Thus, if the strain, ε, in Eq. 6.17 can be measured during the tensioning procedure of the annular membrane, the tension in the membrane can be calculated.

The strain is made available in horizontal and vertical directions as a result of the experiment utilising the Digital Image Correlation technique, as described in Sec. 6.1. Due to the circular shape of the membrane it is advisable to transform the horizontal and vertical strain data into radial and tangential strain data. This is achieved by a transformation of coordinates in which the Cartesian coordinate system is rotated and becomes the polar coordinate system. The origin of both coordinate systems remains unchanged in the centre of the annular membrane. Eqs. 6.18 to 6.20 present the required formulas, which are well-known and can be found in Ref. [50], for example.

$$\varepsilon_{rr} = \varepsilon_{xx} \times \cos^2\vartheta + \varepsilon_{yy} \times \sin^2\vartheta + \varepsilon_{xy} \times \sin 2\vartheta \tag{6.18}$$

$$\varepsilon_{\varphi\varphi} = \varepsilon_{xx} \times \sin^2\vartheta + \varepsilon_{yy} \times \cos^2\vartheta - \varepsilon_{xy} \times \sin 2\vartheta \tag{6.19}$$

$$\varepsilon_{r\varphi} = (\varepsilon_{yy} - \varepsilon_{xx}) \times \sin\vartheta \times \cos\vartheta + \varepsilon_{xy} \times \cos 2\vartheta \tag{6.20}$$

where ε_{xx} is the horizontal strain, ε_{yy} the vertical strain and ε_{xy} is the shear strain in the Cartesian coordinate system whilst ε_{rr} is the radial strain, $\varepsilon_{\varphi\varphi}$ is the tangential strain and $\varepsilon_{r\varphi}$ is the shear strain in the polar coordinate system. The polar angle between the axes of the Cartesian and the polar coordinate systems is denoted by ϑ. The normal strains represent the change in length per unit length of a line element, which originally lies in their corresponding radial, tangential, horizontal or vertical direction. In case of an elongated line element the normal strain is positive. In case of a compressed line element the normal strain becomes negative. The shear strains represent half the change in the original right angle

between two perpendicular lines in the corresponding xy or $r\varphi$ plane, respectively. The shear strain is positive when both lines face either positive or negative coordinate directions and the angle is decreased. The shear strain is negative when both lines face either positive or negative coordinate directions and the angle is increased. When one line faces a positive coordinate direction and the other a negative direction, the shear strain is positive for increased angle and it is negative for a decreased angle. Temperature dependent strain is deemed negligible in this work since large temperature changes do not occur during the experimental phase.

Then, based on Hooke's law, the normal stresses in the annular membrane can be obtained for the radial and tangential directions from Eqs. 6.21 and 6.22 whilst Eq. 6.23 gives the shear stress. The equations can also be found in Ref. [50]. The stresses acting on an infinitesimal element of the annular membrane are illustrated in Fig. 6.12 (a).

$$\sigma_{rr} = \frac{E}{(1+\nu)(1-2\nu)} \times \Big((1-\nu)\varepsilon_{rr} + \nu(\varepsilon_{\varphi\varphi} + \varepsilon_{zz})\Big) \tag{6.21}$$

$$\sigma_{\varphi\varphi} = \frac{E}{(1+\nu)(1-2\nu)} \times \Big((1-\nu)\varepsilon_{\varphi\varphi} + \nu(\varepsilon_{rr} + \varepsilon_{zz})\Big) \tag{6.22}$$

$$\sigma_{r\varphi} = \frac{E}{1+\nu} \times \varepsilon_{r\varphi} \tag{6.23}$$

where σ_{rr} is the radial stress, $\sigma_{\varphi\varphi}$ is the tangential stress, $\sigma_{r\varphi}$ is the shear stress in the plane of the annular membrane. Poisson's number is constant and given as $\nu = 0.38$ in the membrane material specifications in Ref. [26]. The strain in the orthogonal direction to the plane of the annular membrane is denoted ε_{zz}, which is zero due to the assumption that the wall thickness of the membrane remains constant. Since it was further assumed in Sec. 6.3 that the stress in the orthogonal direction to the plane of the annular membrane is negligible, any normal and the shear stresses in the orthogonal direction are assumed to be zero. Thus, the problem becomes two-dimensional plane stress problem.

From the normal and shear stresses in the polar coordinate system, the principal stresses $\sigma_{1/2}$ are determined using Eq. 6.24, according to Ref. [50]. The principal stresses are normal stresses and occur if the shear stresses become zero. Thus, the principal stresses present the maximum and minimum values of the normal stress.

$$\sigma_{1/2} = \frac{1}{2}(\sigma_{rr} + \sigma_{\varphi\varphi}) \pm \sqrt{\frac{1}{4}(\sigma_{rr} - \sigma_{\varphi\varphi})^2 + \sigma_{r\varphi}^2} \tag{6.24}$$

The planes at which the principal stresses occur are called the principal planes.

The polar angle φ_0 in Eq. 6.25 gives the location of the principal planes relative to the planes of the normal and shear stresses, which is illustrated in Fig. 6.12 (b).

$$\varphi_0 = \frac{1}{2} \arctan\left(\frac{2\sigma_{r\varphi}}{\sigma_{rr} - \sigma_{\varphi\varphi}}\right) \tag{6.25}$$

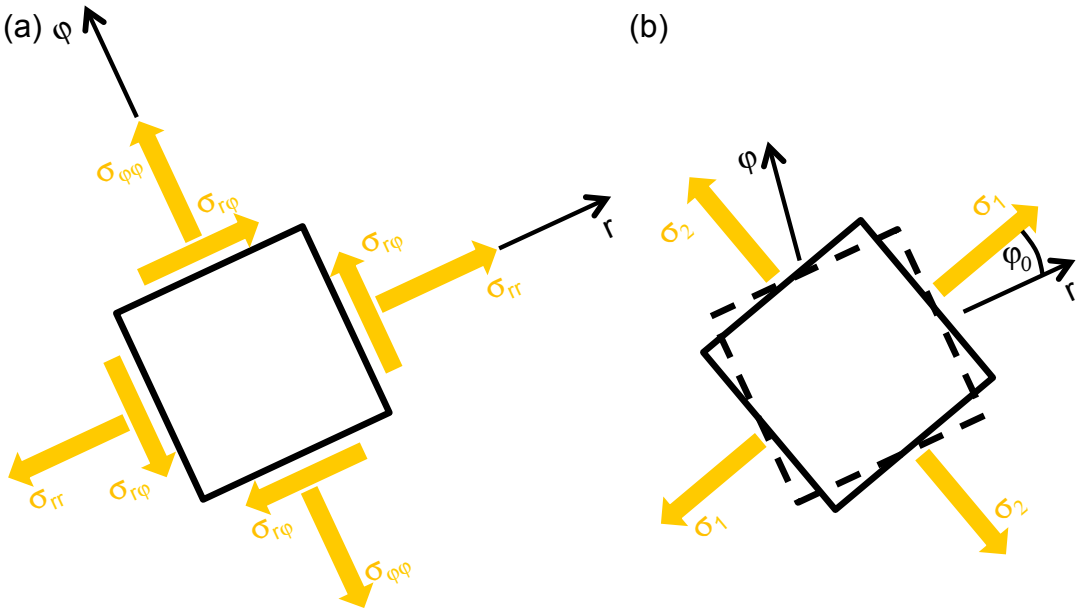

Figure 6.12: An infinitesimal area of the annular membrane illustrating (a) the normal and shear stresses in radial and tangential directions and (b) the principal stresses and their relative position relative to the radial normal stress.

Thus, the angle is zero if the principal stresses σ_1 and σ_2 and the normal stresses σ_{rr} and $\sigma_{\varphi\varphi}$ point in the same direction. Hence, the shear strain $\sigma_{r\varphi}$ would be zero. This leads to equal stresses $\sigma_1 = \sigma_2 = \sigma_{rr} = \sigma_{\varphi\varphi}$, according to Eq. 6.24. Hence, the principal stresses point exactly in radial and tangential directions, which confirms that the stresses are introduced uniformly at the inner and outer boundaries of the annular membrane and, thus, they are evenly distributed throughout the annular membrane. Equal and constant principal stresses, $\sigma_1 = \sigma_2$, are in conjunction with the assumptions made for the AMM in Sec. 6.3.

On the basis of Eq. 6.1, the tension per unit length $T_{1/2}$ is estimated in the principal stress directions utilising the principal stresses $\sigma_{1/2}$ and the membrane thickness h in Eq. 6.26.

$$T_{1/2} = \sigma_{1/2} \times h \tag{6.26}$$

For an ideal membrane, the membrane thickness h and the principal stresses $\sigma_{1/2}$ are assumed to be constant. In addition, the principal stresses are assumed

to be uniformly distributed throughout the membrane. Therefore, the tensions $T_{1/2}$ are constant and uniformly distributed as well.

6.4.2 The experimental tuning procedure of the tension in the annular membrane

The experimental determination of the tension serves two purposes which are (i) to identify whether the tension is uniformly distributed throughout the annular membrane, and (ii) to quantify the tension. The first purpose shall increase the comparability of the TSR test rig with the annular membrane model (AMM) of Section 6.3, in which a uniform tension is assumed. If the tension is uniformly distributed throughout the annular membrane of the TSR test rig, the AMM can be used to determine a particular eigenfrequency, which matches the eigenfrequency of the cavity resonance frequency, as a function of the tension. Then, the second purpose of quantifying the uniform tension supports the tuning of the annular membrane of the TSR test rig in order to be resonance at that particular eigenfrequency. It is envisaged that, in case of matching eigenfrequencies of the annular membrane and the cavity of the TSR test rig, the degree of replication is increased further since a coupling between the cavity and the replicated sidewall occurs, as it does in a real tyre. In a real tyre, the tyre sidewall is excited by and radiates sound at the tyre cavity resonance frequencies.

For the experimental determination of the strain field of the annular membrane, the Digital Image Correlation (DIC) is applied, which is a non-intrusive, non-destructive and non-contacting method for the measurement of deformation. DIC is an optical tool, which measures the deformation of a solid object from a series of images [58]. A single camera produces images of the deformed test object in order to record its two-dimensional in-plane deformation. From a sequence of images, which are acquired during the deformation experiment (with the first image normally being the case of zero applied load), the displacement of the surface pattern of the specimen is determined. In each image, the surface of the specimen is discretised into a grid with small cells or tiles. A cross-correlation analysis is carried out on two consecutive images of each cell using Fast Fourier Transformation. The maximum correlation corresponds to the deformation and gives information of the length of the deformation as well as its direction. The deformation of each cell is then described by a deformation vector field from which the strain field is derived. Due to the many evaluation cells for the test object in this work, the results are presented in colour maps in order to appropriately visualise the deformations or the strain fields, respectively.

The deformation of the surface of the specimen is estimated from a speckle

pattern, which is usually spray painted on the surface. It is assumed that the specimen and the speckle pattern are deformed simultaneously. The states of deformation are then detected by the DIC measurement analyser. The adequate size and distribution of the speckles are decisive criteria for the DIC camera and post-processing software to detect and estimate the displacement of the speckles, which represents the deformation of the specimen.

The experimental setup and equipment is illustrated in Figs. 6.13, 6.14 and 6.15. The measurement equipment from LaVision GmbH, Germany, consists of a tripod-mounted CCD (charge-coupled device) camera which is connected to a computer via an A/D converter. The data acquisition and post-processing is done by the software DaVis 8.1.4. In order for the camera to capture images of the whole surface of the annular membrane, the camera is positioned at a 3 m distance in front of the vertically arranged TSR test rig. In order for the DIC measurement equipment and software to recognise the deformation accurately, the surface of the clear annular membrane is spray painted in black with a white non-uniform speckle pattern on top, as it is shown in Fig. 6.15. If the annular membrane is deformed due to the applied tension, the speckle pattern will change its position. Thus, the deformation is detected and quantified by the measurement software. Sufficient illumination is provided for the camera during the image recording phase. Before the actual measurement process can be started, the camera is focused on the measurement object and a calibration procedure is carried out. Thus, the boundaries of the specimen, the origin of a reference coordinate system and an image scale are defined. The image scale in pixel per millimetre ensures that results shown in scaled units are represented in their true dimensions.

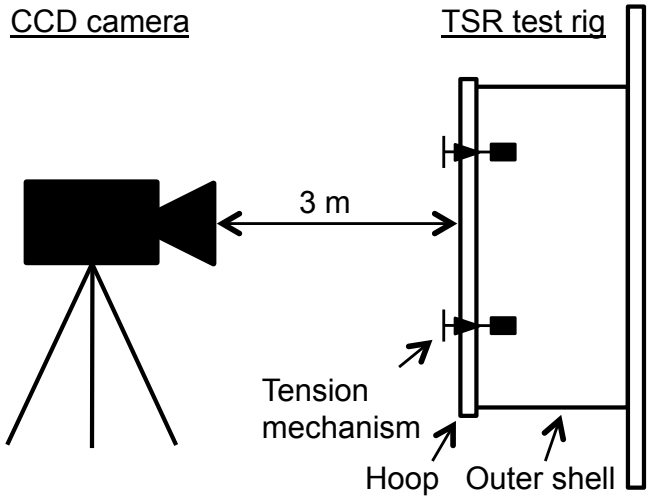

Figure 6.13: Schematic of the DIC experiment.

The inner boundary of the membrane is clamped. The tension is increased via

Figure 6.14: Position of the camera in the DIC experiment.

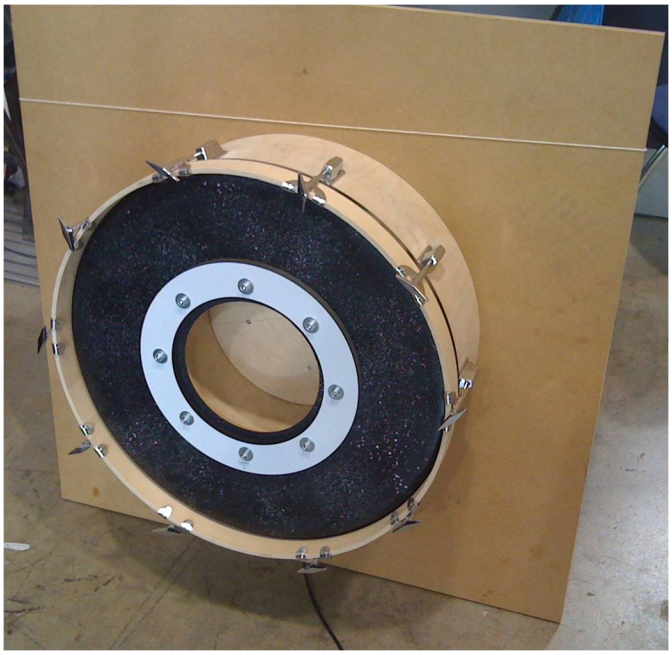

Figure 6.15: Arrangement of the TSR test rig in the DIC experiment.

ten bolts, which are distributed along the outer boundary of the annular membrane. The initial state or zero strain state, respectively, represents the condition of the annular membrane with no tension applied. It is documented with the very first image and provides the basic data from which the relative deformation captured with the subsequent images is calculated. For the zero strain state image, the bolts are slightly tensioned in order to create a plane surface of the annular membrane and to avoid the building-up of wrinkles, which would lead to false measurement results. It is assumed that the applied tension is small and, thus,

does not interfere greatly with the measurement results.

In the actual testing phase, the tension in the annular membrane is increased via the bolts first. The bolts are tightened by half a turn in a pre-determined order which is specified in Fig. 6.16. Following that order, which is based on turning the bolts in pairs which are located opposite to each other, it is envisaged that the tension will be uniformly distributed throughout the annular membrane. Then, an image of the deformed membrane is taken. In the post-processing stage, the deformation of the membrane is calculated from two consecutive images in order to enable the analysis of the strain field. If the strain field shows a uniform pattern, the previous steps are repeated. If the strain field reveals a non-uniform pattern, the tension is subsequently adjusted in such a way in order to compensate for the non-uniformity and to produce a uniform deformation instead. The previous steps are repeated iteratively until the desired tension setting has been adjusted, which corresponds to a particular set of eigenfrequencies of the annular membrane.

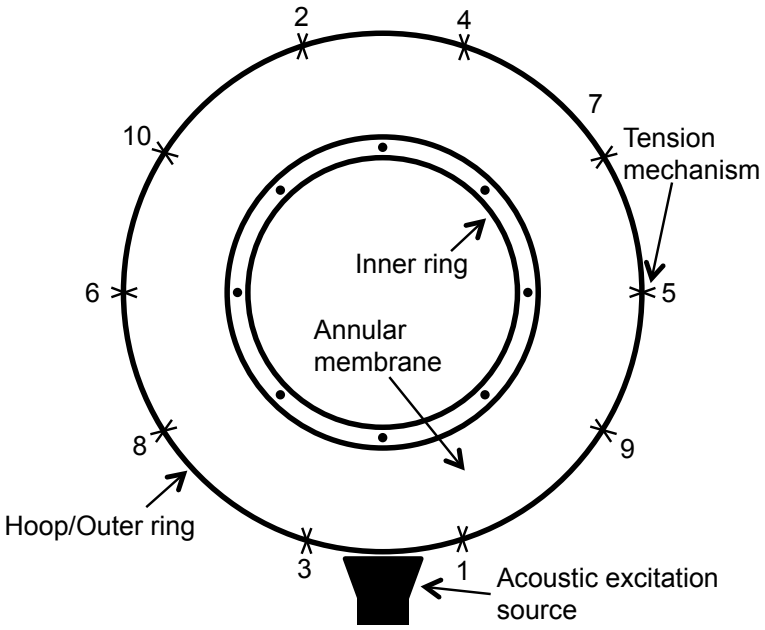

Figure 6.16: Illustration of the order of the bolts in the tensioning process.

The DIC method has several advantages in comparison to alternative methods like the application of strain gauges. If strain gauges are attached to a test object, they add additional weight to it, which is not the case for the DIC measurement method. Since the membrane is very light, the additional weight of the strain gauges located at discrete positions across the annular membrane would interfere with the vibration and sound radiation characteristics of the membrane. Furthermore, the backing sheet of the strain gauge, which is glued onto the membrane surface, produces local stiffening, which would have an impact on the mechanical characteristics of the membrane as well. This ultimately leads to significant inac-

curate readings. Using the DIC method a detailed strain field can be obtained, which cannot be achieved through a discrete number of strain gauges distributed across the annular membrane. Each of the strain gauges only reflects the local strain state at its position. The application of strain gauges usually involves the preparation of the surface of the test object in order to provide an adequate bonding between the surface and the strain gauge. However, the thin membrane is at risk to be damaged through cleaning solvents and abrasive paper, which does not exist in the non-contacting DIC method.

6.4.3 Experimental results of the deformed annular membrane

The results of the Digital Image Correlation (DIC) experiment are presented in this section. The results of the DIC experiment do not represent the dynamic response of the annular membrane to a frequency-dependent excitation but the static deformation due to the force application at the boundaries of the annular membrane. The results of the DIC experiment comprise the horizontal and vertical deformations of the annular membrane of the TSR test rig as well as the corresponding strain fields. The strain field results are transformed from the Cartesian to the polar coordinate system in order to calculate the corresponding stresses. Then, the principal stresses and, thus, the tension can be determined.

6.4.3.1 Measured deformation and strain field

Fig. 6.17 illustrates the physical displacement of the white speckle pattern on the surface of the annular membrane. The enlarged areas present the white speckle pattern in the zero strain state and in the final deformation state. The circular arc enables the identification of the displacement of a group of speckles.

The measured deformations in the annular membrane are represented in the horizontal, vertical and radial directions in Figs. 6.18, 6.19 and 6.20. The figures show the absolute deformation relative to the zero strain state, which is the undeformed state. The deformation data on the inner and outer boundary may be treated with caution since the coloured areas, which represent the deformation of the membrane, overlap with fixed, non-moving parts. This applies for the inner and outer rings, as illustrated in Figs. 6.19 and 6.20. The two rings are excluded from the deformation measurement since the white speckle pattern is not applied on them. In addition, they can be regarded as rigid in comparison to the elastic annular membrane. The overlapping ensures that the annular shape of the membrane is covered in the analysis routines of the DIC measurement system. The acoustic excitation source is located on the right-hand side in each figure. The

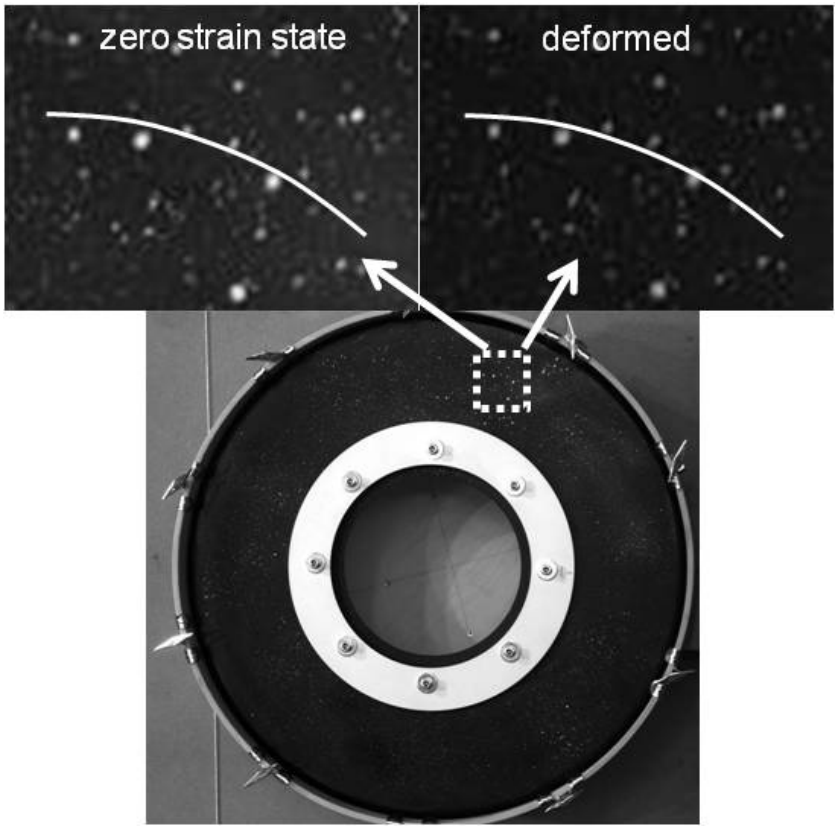

Figure 6.17: Illustration of the displacement of the white speckle pattern of the annular membrane.

horizontal axis is denoted x-axis, and the vertical axis is denoted y-axis. In Fig. 6.18, the highest horizontal deformation values occur in positive and negative direction of the horizontal x-axis. Towards the top and the bottom regions of the annular membrane, the horizontal deformation is reduced with the lowest deformation values at the top and the bottom. Generally, it appears that the horizontal deformation is axially symmetric around the vertical axis. However, the region at the bottom tends to be more deformed towards the left-hand side. Further, a slight imbalance is caused by the deformation values, which vary between the left-hand and right-hand side of the annular membrane. The highest deformation values of up to 1.2 mm occur on the right-hand side. On the left-hand side, the highest deformation values are approximately 0.7 mm, which is about 40% smaller than on the opposite side.

A similar characteristic can be observed for the vertical deformation in Fig. 6.19. The highest vertical deformation values occur in positive and negative direction of the vertical y-axis. Towards the left-hand and the right-hand side of the annular membrane, the vertical deformation decreases with the lowest deformation values in the close vicinity of the horizontal axis. It generally appears that the vertical deformation is axially symmetric around the horizontal axis with a slightly

more even deformation distribution as it is shown for the horizontal deformation in Fig. 6.18. The highest vertical deformation values lie close together between 0.7 - 0.8 mm in both the positive and negative vertical directions.

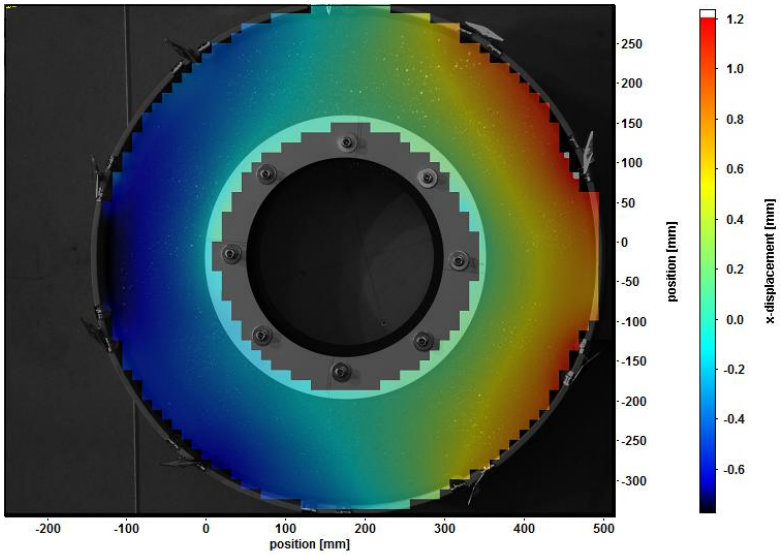

Figure 6.18: Illustration of the measured deformation V_x in horizontal direction. The raw image of the deformed annular membrane is shown in the background.

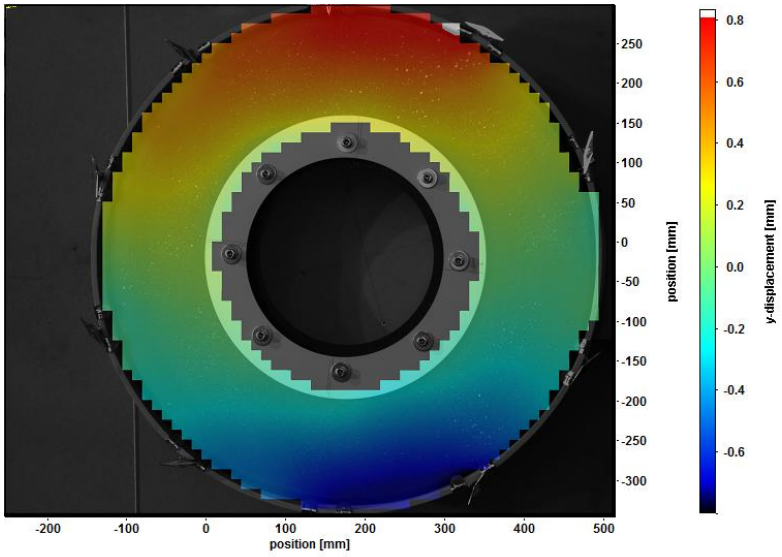

Figure 6.19: Illustration of the measured deformation V_y in vertical direction. The raw image of the deformed annular membrane is shown in the background.

Since the inner boundary of the annular membrane is clamped and the tension is applied at the outer boundary, the deformation direction should be mainly in the outwards radial direction with reference to the centre of the annular membrane. This is confirmed by the measured deformation in horizontal and vertical directions as the deformation occurs in their respective horizontal and vertical

directions. In regions off the main deformation directions, the deformation values generally decrease. In regions which are 90° off-axis the main deformation directions, the deformation values are smallest. In contrast to the horizontal and vertical deformations, the radial deformation is illustrated in Fig. 6.20. Since the membrane is of a circular shape, the radial deformation might be more suitable for the visualisation of the deformation results. The deformation values increase circularly from the inner towards the outer boundary of the annular membrane. Slightly higher deformation occurs around the acoustic excitation source on the right-hand side of the test rig. There, maximum deformation values reach up to 1.1-1.2 mm. In other regions of the outer boundary, the deformation values are less and vary between 0.6-0.9 mm. Since the inner boundary of the annular membrane is clamped, almost no deformation can be identified there. Since the annular membrane is stretched towards the outer boundary, where the tension is applied, the deformation values generally increase in that direction.

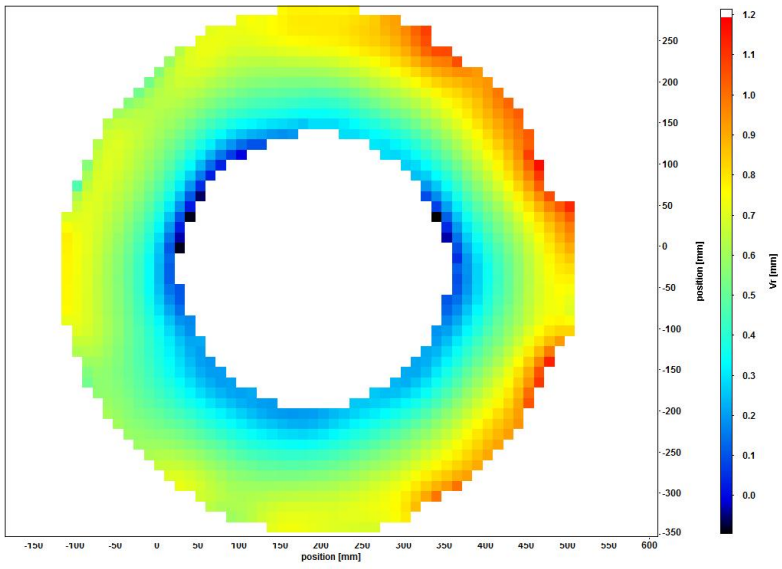

Figure 6.20: Illustration of the measured deformation V_r in radial direction.

From the measured deformations in the horizontal and vertical directions, the normal and shear strain fields are obtained in the Cartesian coordinate system using the DIC post-processing software DaVis 8.1.4. In Fig. 6.21, the normal strain fields are illustrated in the horizontal (top) and vertical (middle) directions whilst the shear strain is shown at the bottom of the figure. In comparison to Figs. 6.18 and 6.19, it is noticed that the coloured evaluation region is slightly truncated on the inner and outer boundaries of the annular membrane, which may be related to the algorithm used to calculate the strain fields from the measured deformation data. Therefore, the results on the boundaries should be treated with care. In general, the normal strain fields reflect the tendency of the deformations

in their corresponding directions. The horizontal strain field shows higher strain values of about 0.5% on the right-hand side of the annular membrane and lower values between approximately 0.2-0.5% on the left-hand side, which corresponds to the tendency of the horizontal deformation. At the top and bottom regions of the annular membrane, the strain values are less than those on the left-hand and right-hand sides. A similar characteristic appears for the vertical strain field, which presents higher strain values of approximately 0.3-0.5% at the top and bottom regions of the annular membrane than on the left-hand and right-hand side, where strain values are approximately between 0.1-0.2%. As illustrated in the bottom plot of Fig. 6.21, the shear strain field is not zero. The shear strain values are within $\pm 0.2\%$ for the majority of the annular membrane area, which is regarded as a small shear strain. The occurence of shear strain may be linked to the force application, which does not only appear in the normal directions but also in the shear directions of the tiles within the evaluation grid of the DIC post-processing software.

The elongation of a specimen is generally characterised by positive strain, which occurs in the most regions of the annular membrane. Conversely, negative strain represents the compression of a specimen. In some regions of the annular membrane, negative strain occurs in the black and dark blue areas in the normal and shear strain fields of Fig. 6.21. In the normal strain fields, the negative strain regions lie on the outer boundary of the annular membrane. It is assumed that this region is not adequately detected by the camera when the membrane is stretched and pulled over the boundary in the radial direction. Thus, part of the speckle pattern is moved over the boundary and cannot be detected and used for the deformation calculation. A compression of the annular membrane is hardly imaginable since the membrane is stretched in the radial direction. Positive and negative shear strain characterises the decrease and increase from the right angle between two perpendicular line elements of an evaluation grid tile. Negative shear strain values may not be as uncommon as negative normal strain values for a stretched membrane. However, it is assumed that this depends upon whether shear forces occur.

In all of the three strain fields in Fig. 6.21, minimum and maximum strain occurs at the inner and outer boundaries of the annular membrane, which may not reflect the true strain. This may be influenced by the overlapping of the coloured evaluation area and the fixed parts such as the inner or outer rings. This may have an impact on the strain results. On the other hand, a large displacement of parts of the annular membrane can possibly occur if the fastening of the tensioner bolts is insufficient. However, due to the firm tightening of the bolts at the inner ring this is recognised an unlikely case. Two tensioner bolts are located at the two

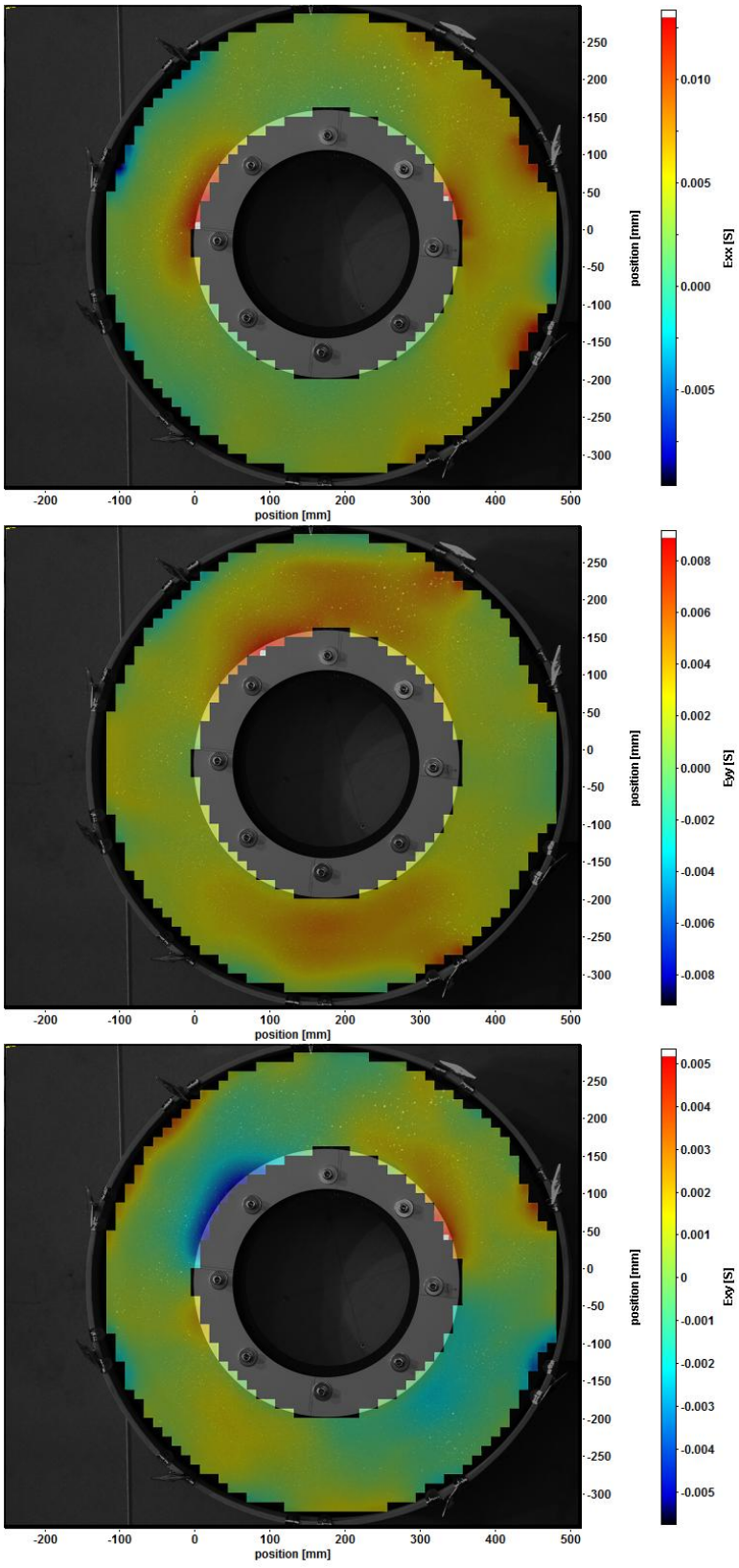

Figure 6.21: Illustration of the measured strain fields in horizontal (top) and vertical (middle) directions as well as the plane shear stress (bottom). The raw image of the deformed annular membrane is shown in the background.

orange and red coloured regions on the right-hand side of the annular membrane. The strain is rather high in the vicinity of the two locations; this may be due to high tension applied at the locations of the bolts. The cause for the appearance of the maximum and minimum strain values on the boundaries may also be affected by the algorithm, which the calculation of the strain fields is based on, resulting in deviations from the true strain. In addition, irregularities in the arrangement of the evaluation tiles can be identified at the inner and outer boundaries in the plots of Fig. 6.21, which are inconsistently arranged for both the normal strain fields. Therefore, it may be advisable not to consider the boundaries for the analysis of the strain fields and focus on the areas between the inner and outer boundaries instead.

Switching to a polar coordinate system with its origin at the centre of the annular membrane, the radial and tangential strain fields are represented in Figs. 6.22 and 6.23, respectively, and the shear strain field is shown in Fig. 6.24. Applying Eqs. 6.18, 6.19 and 6.20 of Sec. 6.4.1, the strain fields are transformed from the Cartesian to the polar coordinate system. The polar strain fields are required in a subsequent step when the principal stresses and the tension in the annular membrane are estimated. Due to the symmetry of the annular membrane, it is appropriate to analyse the strain, stress and tension in the polar coordinate system.

The radial strain field in Fig. 6.22 shows similarities to the horizontal strain field in Fig. 6.21. This applies to the four red coloured regions, which present maximum strain values, and the dark blue coloured region on the upper left-hand side, which represents negative strain values, i.e. compression. Since these regions are located on the boundaries of the annular membrane, they are not taken into further consideration. An almost uniform strain of approximately 0.5% occurs on the right-hand side of the annular membrane, thus indicating constant radial elongation. On the left-hand side of the annular membrane, the strain is slightly less uniform but strain values of about 0.25-0.5% are close to those on the opposite side. Overall, the radial strain tends to be uniform, thus confirming the radial direction as the dominant deformation direction, which is also illustrated in the radial deformation plot in Fig. 6.20.

The tangential strain, illustrated in Fig. 6.23, is less than the radial strain for the majority of the annular membrane area, with strain values between 0.1-0.2%. However, two areas with high strain are located at the upper and lower regions of the right-hand side of the annular membrane, where strain values vary between 0.3-0.6%. Due to the high strain values in the radial direction and the low strain values in the tangential direction, the dominant deformation is confirmed to be in the radial direction. Strain in the tangential direction may be inevitable in case

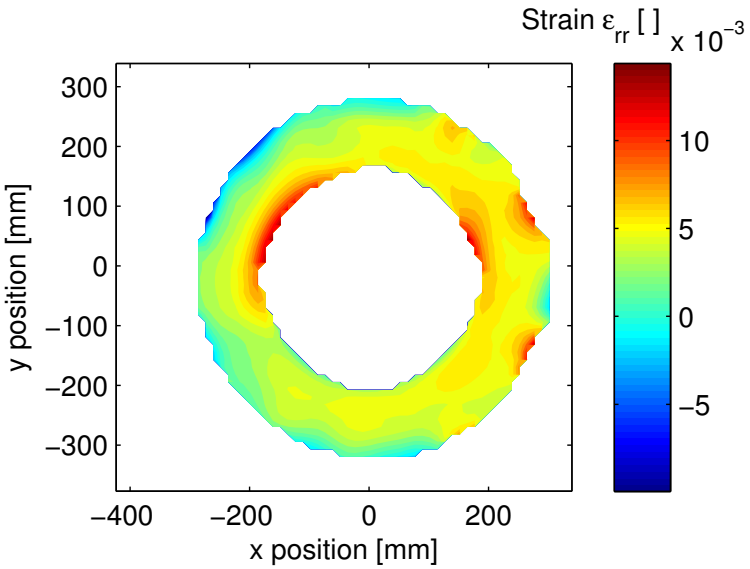

Figure 6.22: Illustration of the radial strain ε_{rr} in the annular membrane.

of a radially deformed membrane since the material is stretched in the tangential direction as a consequence of the stretching in the radial direction.

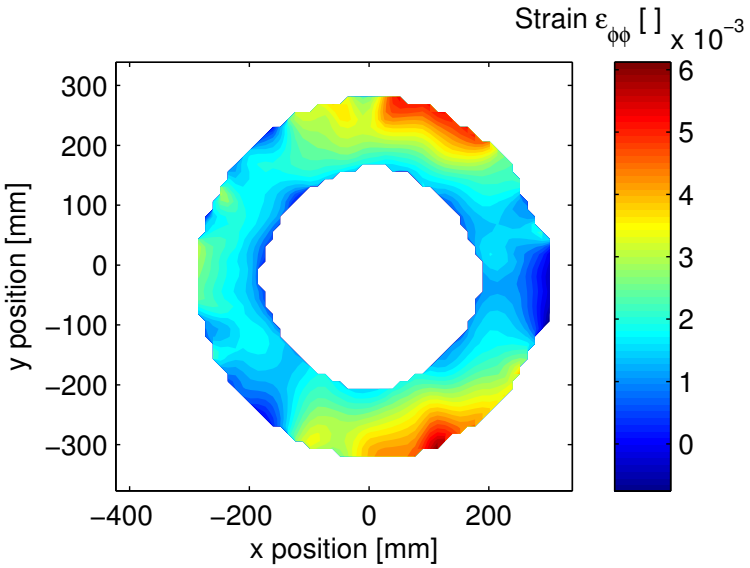

Figure 6.23: Illustration of the angular strain $\varepsilon_{\varphi\varphi}$ in the annular membrane.

The shear strain in the polar coordinate system is illustrated in Fig. 6.24. For the vast majority of the area of the annular membrane the shear strain values range between $\pm 0.1\%$ indicating that the shear is small. Comparing the shear strain in Fig. 6.24 with the position of the tensioner bolts in Fig. 6.17, it appears that the shear strain has negative values at the positions of the bolts and that positive shear strain values occur between the positions of the bolts. This indicates that the force for the tensioning of the annular membrane is not evenly applied

on the outer ring. Instead, the force varies along the outer ring with higher force application at the position of the tensioner bolts and less force application between them. This apparently causes the shear strain to change from negative to positive values. In case of a uniform force application at the outer ring, shear strain will be avoided.

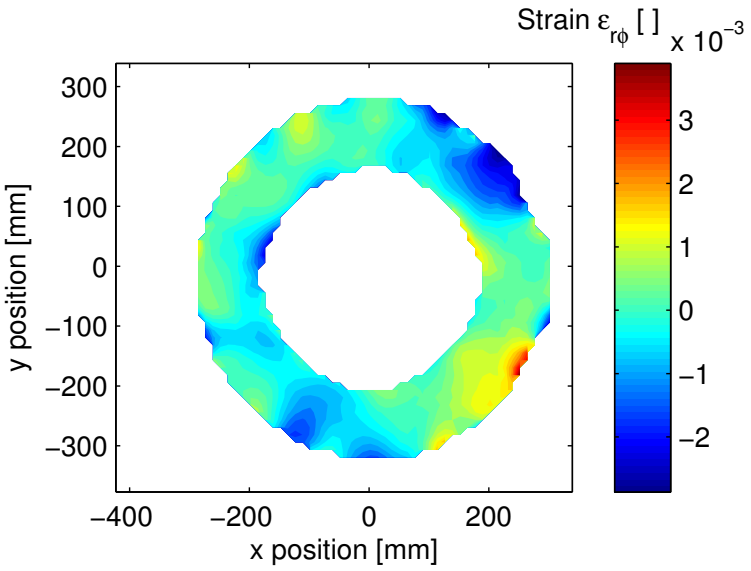

Figure 6.24: Illustration of the shear strain $\varepsilon_{r\varphi}$ in the annular membrane.

6.4.3.2 Estimated stress and tension

The tension in the annular membrane is estimated using the principal stresses, which are calculated using the radial, tangential and shear stresses. These normal and shear stresses are obtained applying Eqs. 6.21, 6.22 and 6.23, which are functions of either the normal strains in the radial and tangential directions or the shear strain, respectively, whilst the modulus of elasticity and the Poisson's number are constants in the equations. The normal and shear strains were presented in Sec. 6.4.3.1. Conducting the DIC experiment, it is the aim to obtain a constant and evenly distributed tension throughout the annular membrane in order to be consistent with the assumptions made for the AMM in Sec. 6.3. If the experimental results of the tension satisfy the assumptions, the AMM shall predict the same resonance frequencies for the annular membrane as they occur in reality. Two other assumptions for the AMM shall be in effect for the evaluation of the DIC experimental data as well: these are, a constant wall thickness, which results in zero strain ε_{zz} in the orthogonal direction, and, zero normal and shear stresses in the orthogonal direction.

The radial stress σ_{rr}, which is calculated according to Eq. 6.21, is represented

in Fig. 6.25. The contour plot of the radial stress in Fig. 6.25 appears to have similarities with the contour plot of the radial strain in Fig. 6.22. In Eq. 6.21, the radial strain ε_{rr} contributes more to the radial stress than the tangential strain $\varepsilon_{\varphi\varphi}$, since the radial strain is generally higher than the tangential strain, which is illustrated in Figs. 6.22 and 6.23. Further, the term $(1-\nu) = 0.68$ is greater than the term $\nu = 0.38$ in Eq. 6.21. Thus, when these terms are multiplied with their corresponding strains ε_{rr} and $\varepsilon_{\varphi\varphi}$ respectively, the contributions of the radial strain are generally higher overall than the contributions of the tangential strain to the radial stress. Fig. 6.26 illustrates the theoretical change of the radial (left) and the tangential (right) stress as a function of the radial and the tangential strain. In order to produce such diagrams, Eqs. 6.21 and 6.22 are utilised and the strain values are chosen according to the measured strain values in the DIC experiment. The modulus of elasticity and the Poisson's number remain unchanged. From the diagram of the radial stress σ_{rr}, one can infer that the radial stress generally increases more with an increasing radial strain ε_{rr} than with an increasing tangential strain $\varepsilon_{\varphi\varphi}$. But from the diagram of the tangential stress $\sigma_{\varphi\varphi}$ it can be concluded that the tangential stress generally increases more with an increasing tangential strain $\varepsilon_{\varphi\varphi}$ than with an increasing radial strain ε_{rr}. Therefore, the term $(1-\nu)\varepsilon_{rr}$ predominantly affects the radial stress whilst the term $(1-\nu)\varepsilon_{\varphi\varphi}$ predominantly affects the tangential stress.

The relatively uniform distribution of the radial stress field is disturbed by a small section of lower stress values in the vicinity of the loudspeaker on the right-hand side of the annular membrane. Here, the influence of the tangential strain, as shown in Fig. 6.23, becomes apparently noticeable. As it is mentioned in the discussion of the strain fields, the results at the boundaries of the annular membrane have to be treated with caution. Reaching maximum stress values of up to $140\,\mathrm{N/mm^2}$ in the red coloured regions, the stress values decrease quickly down to less than $70\,\mathrm{N/mm^2}$ within a distance of less than 40 mm, which is assumed to be a steep gradient. For the majority of the area of the annular membrane, the radial stress ranges between 40-70 $\mathrm{N/mm^2}$. In some regions, where the colour is uniform, the stress is almost evenly distributed with a deviation of less than $\pm 5\,\mathrm{N/mm^2}$, which is assessed as a good result.

The tangential stress $\sigma_{\varphi\varphi}$, calculated according to Eq. 6.22, is illustrated in Fig. 6.27. It appears that the pattern of the tangential stress field in the contour plot in Fig. 6.27 is influenced by both the radial and the tangential strain fields. Although the radial strain field consists of higher strain values than the tangential strain field, the strains are weighted differently due to the multiplication with $(1-\nu)$ and ν, respectively, where $(1-\nu)$ is greater than ν. Therefore, it is assumed that the terms $(1-\nu)\varepsilon_{\varphi\varphi}$ and $\nu\varepsilon_{rr}$ contribute equally to the tangential

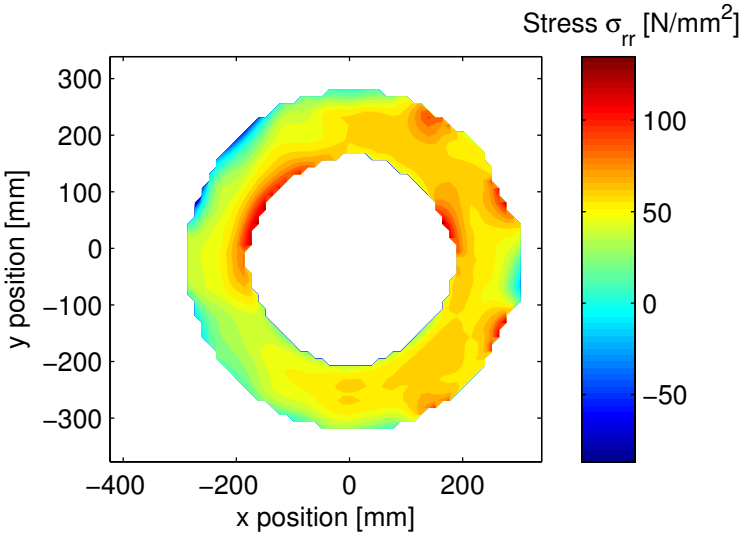

Figure 6.25: Illustration of the radial stress σ_{rr} in the annular membrane.

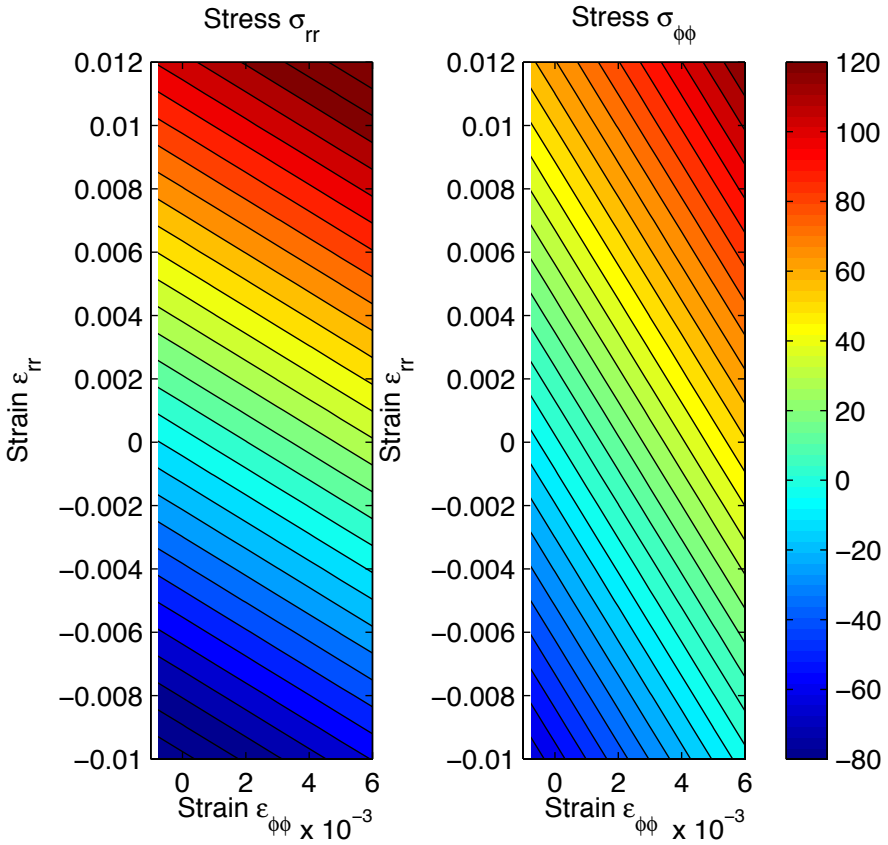

Figure 6.26: Theoretical changes of the radial stress σ_{rr} (left) and the tangential stress $\sigma_{\varphi\varphi}$ (right) as a function of the radial strain ε_{rr} and the tangential strain $\varepsilon_{\varphi\varphi}$.

stress values in Eq. 6.22. However, comparing the levels of the tangential and the radial stresses in Figs. 6.27 and 6.25, it appears that the tangential stress level is generally lower than the level of the radial stress. This has to be attributed to the

relatively large radial strain values. For the majority of the area of the annular membrane, the tangential stress values are between 30-60 $\mathrm{N/mm^2}$.

Both the radial and tangential stress fields show lower stress values in the lower left region of the annular membrane, where the stress values switch from decreasing to increasing in the tangential direction. Higher, but stable, stress values occur in the lower and upper regions of the right-hand side. In the vicinity of the loudspeaker, the stress values are generally lower than they are in the adjacent regions. The upper left region represents a transition area from high to low stress values in the radial outwards direction for both the radial and tangential stress fields, even if the boundary region is excluded in the analysis.

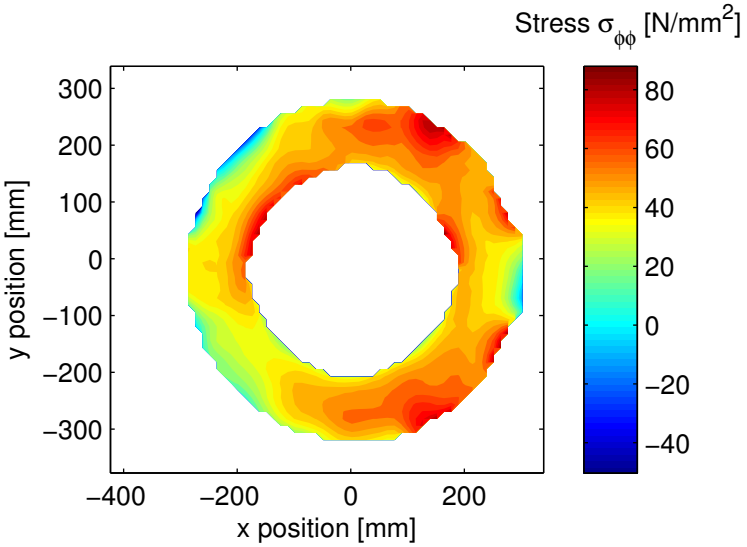

Figure 6.27: Illustration of the tangential stress $\sigma_{\varphi\varphi}$ in the annular membrane.

The shear stress is calculated according to Eq. 6.23 and illustrated in Fig. 6.28. Assuming that the modulus of elasticity and the Poisson's number are constant, the shear stress is a function of the shear strain. Therefore, the contour plots of the shear strain and that of the shear stress show a similar contour pattern. The shear stress values are generally on a very low level ranging between $\pm 2\,\mathrm{N/mm^2}$ in the majority of the area of the annular membrane. This indicates that the shear stress may be negligible. Slightly higher shear stress, which tends either towards positive or negative values, occurs at the upper and lower right-hand side of the annular membrane. It appears that the shear stress increases towards positive values between the two tensioner bolt positions whilst the shear stress tends towards negative values at the position or in the close vicinity of a tensioner bolt. Such a change between positive and negative shear stress values does not occur at the inner boundary of the annular membrane, and the positions of the tensioner bolts seem to affect the pattern of the shear stress. Since elastic parts,

like the wooden outer ring, the metal outer ring of the annular membrane, or the tensioner bolts, and a limited number of tensioner bolts are involved in tensioning the annular membrane, this may lead to an uneven force application at the outer ring, which may cause that particular shear stress pattern.

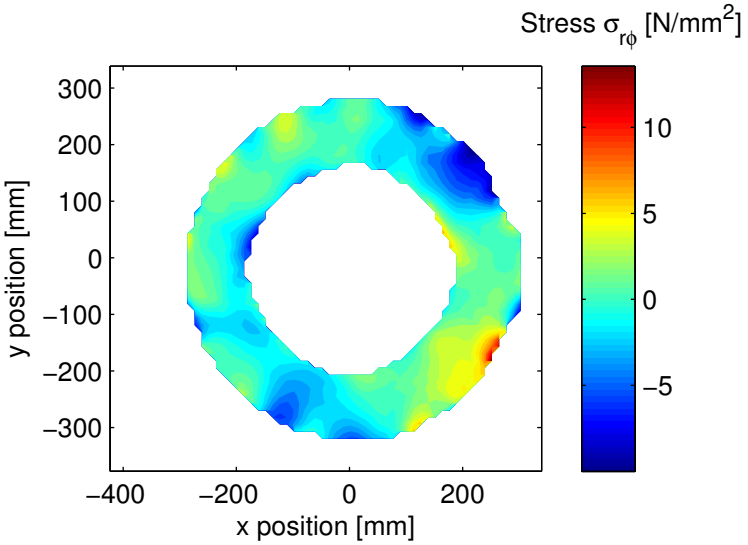

Figure 6.28: Illustration of the shear stress $\sigma_{r\varphi}$ in the annular membrane.

The principals stresses are obtained using Eq. 6.24. The principal stress σ_1 is illustrated in Fig. 6.29, and the principal stress σ_2 is shown in Fig. 6.30. Due to the low shear stress values, the contribution of the shear stress to the principal stress is small in comparison to the contributions of the radial and tangential stresses. The pattern of both principal stress fields appear to be similar to each other and to the radial and tangential stress fields. The latter is due to the high radial and tangential stress values, which contribute most to the principal stress in Eq. 6.24. The values of the principal stress σ_1 generally appear to be slightly higher than the values of the principal stress σ_2, because the difference between the radial and the tangential stress in Eq. 6.24 is subtracted in the calculation of the principal stress σ_2. In both Figs. 6.29 and 6.30, the right-hand side has higher stress values except in the vicinity of the loudspeaker. On the left-hand side the principal stress values are less in general. The lowest values occur in the lower left region as well as close to the outer boundary in the upper left region.

For the majority of the area on the right-hand side of the annular membrane, the principal stress σ_1 ranges from approximately 55-70 $\mathrm{N/mm^2}$ in Fig. 6.29. In the lower left region, most values lie within 30-55 $\mathrm{N/mm^2}$. In the upper left region, a steep gradient occurs with principal stress values between 30-70 $\mathrm{N/mm^2}$. The values of the principal stress σ_2 are approximately between 40-60 $\mathrm{N/mm^2}$ for the majority of the area on the right-hand side of the annular membrane in Fig. 6.30.

In the lower left region, most values range from 25-45 $\mathrm{N/mm^2}$. In the upper left region, a steep gradient occurs as well with principal stress values ranging from 25-60 $\mathrm{N/mm^2}$. In their corresponding regions, the values of the principal stress σ_2 are significantly less than the values of the principal stress σ_1. The results at the inner and outer boundaries are not taken into consideration for this analysis due to suspected measurement or post-processing errors.

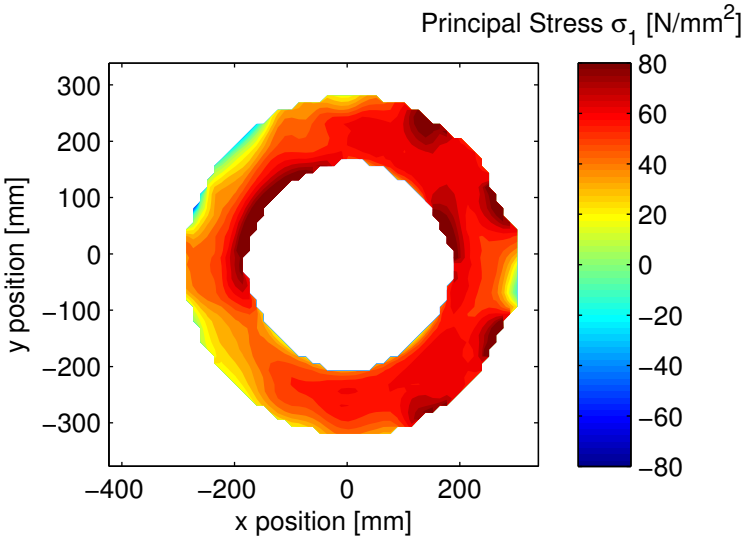

Figure 6.29: Illustration of the principal stress σ_1 in the annular membrane.

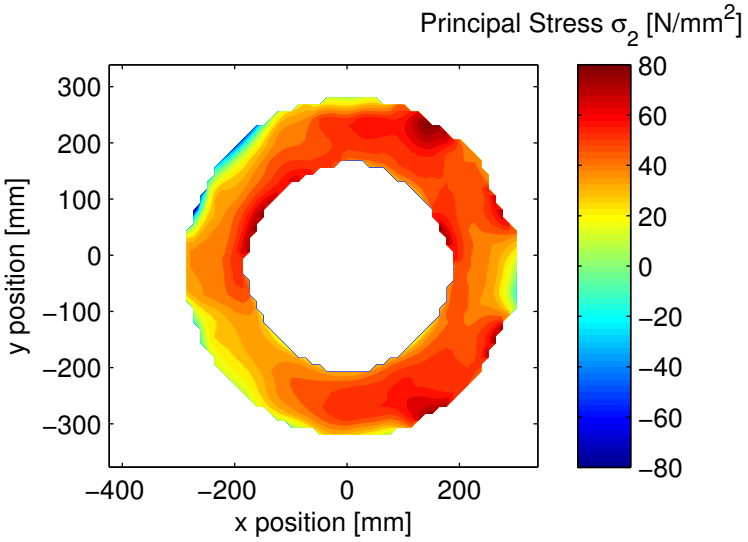

Figure 6.30: Illustration of the principal stress σ_2 in the annular membrane.

Fig. 6.31 illustrates the angle between the normal radial stress and the principal stress according to Eq. 6.25, which gives the direction of the principal stress relative to the radial direction. If the angle is zero, the principal stress σ_1 would

point in the radial direction whilst the principal stress σ_2 would point in the tangential direction. This would match the ideal case and would confirm that the exterior force is evenly applied on the outer boundary of the annular membrane stretching the membrane uniformly in the radial and tangential direction. For the majority of the annular membrane area the angles are within $\pm 15°$. This means that the direction of the principal stress deviates slightly from the radial direction and also varies depending on the location on the annular membrane. However, the direction of the principal stress σ_1 still points towards the outer boundary, which indicates that this is the major direction of the tension.

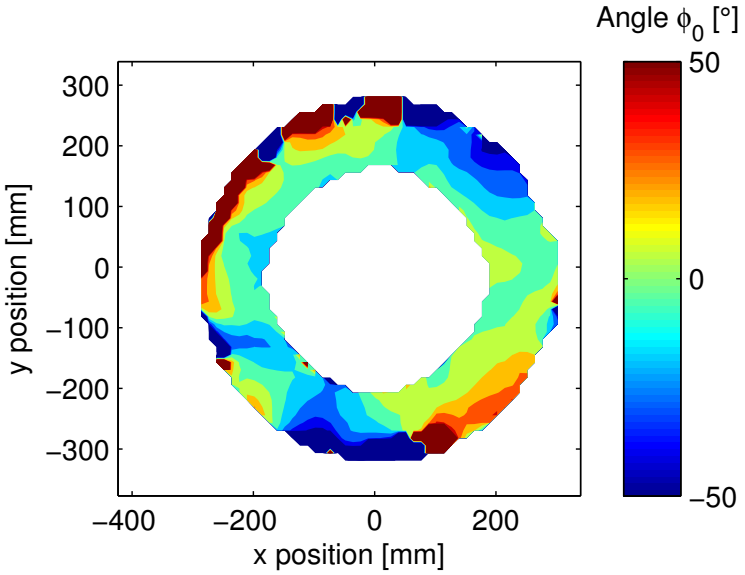

Figure 6.31: Illustration of the angle φ_0 between the normal and principal stresses in the annular membrane.

The tension in the annular membrane is estimated using Eq. 6.1. Since the thickness of the annular membrane is assumed to be constant, the tension becomes a function of the principal stress. Due to the different results in both principal stresses σ_1 and σ_2, the tension will not be exactly uniformly distributed, as it is assumed for the AMM. The tension T_1, which is calculated using the principal stress σ_1, is presented in Fig. 6.32. The tension T_2 is calculated using the principal stress σ_2 and shown in Fig. 6.33.

Since the tensions are functions of the principal stresses, $T_1 = \mathrm{f}(\sigma_1)$ and $T_2 = \mathrm{f}(\sigma_2)$, they point in the same directions as their corresponding principal stresses. Information about the direction of the principal stress has been illustrated in Fig. 6.31. The tension T_1 approximately points in the radial direction whilst T_2 is perpendicular to T_1, which is then approximately in the tangential direction of the annular membrane.

The distribution pattern of both tensions T_1 and T_2 appear to be similar.

Strong similarities exist between the patterns of the tensions and the corresponding principal stresses, which is explainable via Eq. 6.1. The values of the tension T_1 are on a generally higher level than the amplitudes of the tension T_2. The tension values of T_1 and T_2 are generally higher on the right-hand side of the annular membrane except around the location of the loudspeaker, where the values decrease. In the lower left region, both tension values decrease in the tangential direction before increasing again. In the upper right region, the tension values decrease in a radially outwards direction. Tension values appear to be high due to their unit, which is N/m. The average values and the corresponding standard deviations are calculated for both tensions, giving $13912 \pm 5025\,\mathrm{N/m}$ for tension T_1 and $10972 \pm 4256\,\mathrm{N/m}$ for tension T_2. The average values and standard deviations are calculated using every available tension value, including the highest absolute tension values, which occur at the boundaries of the annular membrane. The values at the boundaries should be treated with caution due to possible experimental or post-processing errors. Such errors may be indicated due to the relatively high standard deviations, which equate to 36% and 39% of their corresponding average values. However, such high tension values indicate that a firm tension of the annular membrane is present.

Neglecting the boundary sections of the annular membrane, an inspection of the tensions T_1 and T_2 shows that their values are within 9000-17000 N/m and 8000-16000 N/m, respectively, for the majority of the membrane area. However, comparing various selected coordinates of both tension diagrams, the values of the tension T_1 is usually about 2000-4000 N/m higher than the corresponding values of T_2. Nevertheless, in areas of the annular membrane with the same colour, the tension is approximately uniform. In particular, this is the case for both tensions T_1 and T_2 for large areas on the right-hand side of the membrane. In the transition to the left-hand side, the tension values decrease and a tension pattern with higher variations is formed on the left-hand side.

In Figs. 6.32 and 6.33, the tension T_1 and T_2 appear to be affected by the tensioner bolts on the outer ring. On the right-hand side of the annular membrane, high tension values occur at the positions of the bolts. The tension is higher than the tension in the adjacent areas. This may be related to the application of the force at these locations, thus, leading to high tension in the annular membrane in the vicinity of the bolts. On the left-hand side, the tension at the bolts reaches smaller or high negative values, which are generally less than the tension values in the adjacent areas. There, the tension increases approximately in the radially inward direction away from the bolting positions on the outer ring. Negative tension means that the tension vector is inverted, and tension becomes compression. Since the tension mechanism stretches the annular membrane, a compression cannot oc-

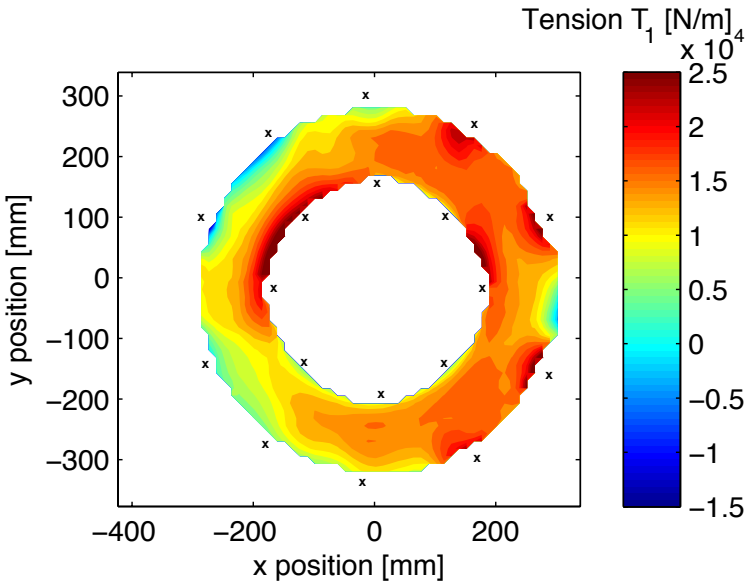

Figure 6.32: Illustration of the tension T_1 in the annular membrane, with x marking the positions of the tensioner bolts.

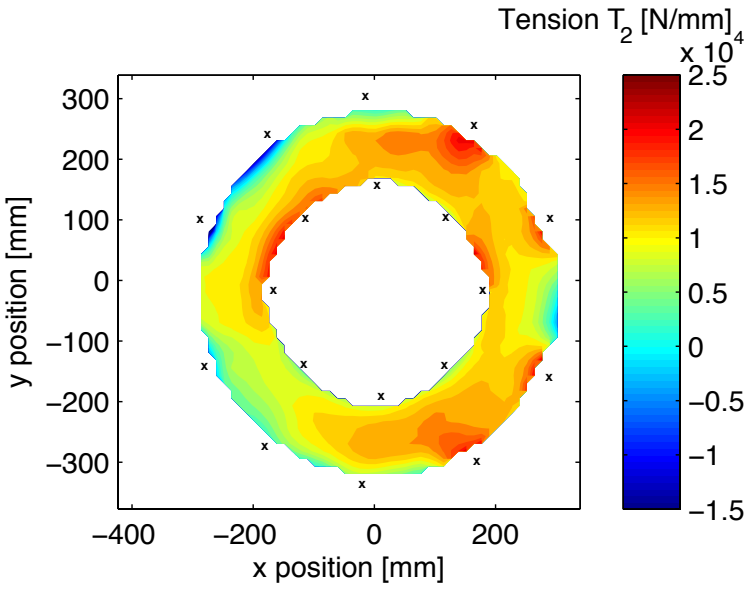

Figure 6.33: Illustration of the tension T_2 in the annular membrane, with x marking the positions of the tensioner bolts.

cur. Thus, it is assumed that a measurement or post-processing error occurred, which just affected a small area on the outer boundary in the upper left region of the annular membrane. At the inner ring it appears that the tension values are generally higher between two adjacent bolts. The purpose of the inner ring is to clamp the annular membrane on its inner boundary. Due to the applied method to determine the tension from optical deformation measurements, the results of the tension depend upon the measured deformation data. If distinctive peculiarities

develop in the data of the deformation, strain or stress fields, they are likely to affect the result of the tension distribution.

6.4.3.3 Discussion of cause of errors and conclusion

The measurement results of the deformation are an approximate assessment criterion in order to achieve a uniformly distributed tension in the annular membrane of the TSR test rig. During the DIC experiment, the tension was adjusted according to the measurement results of the horizontal and vertical deformation, which are presented in Figs. 6.18 and 6.19. If both results are combined, they approximately indicate a uniform deformation in the radial direction. This is confirmed by the radial deformation shown in Fig. 6.20, which was produced after the experiment. Since the deformation approximately increases linearly, a nearly constant strain was expected during the experiment. However, the calculated strain fields show deviations from a constant strain. Such non-uniformities occur again in the subsequent calculations of the strain and the stress in the cylindrical coordinate system as well as the principal stress and the tension. Adjacent deformation values on the evaluation grid pattern are used to estimate the rate of change in deformation, which is then used to calculate the strain. Therefore, the origin of the non-uniformities lies in the uneven increase of the deformation values, which results in an uneven rate of change in deformation.

The sequence of how the tension is increased via the bolts and clamps seems to be appropriate for the annular membrane, since local deformation non-uniformities could be evened out via the adjustment of the corresponding bolts.

Ideally, the tension would be constant throughout the whole annular membrane. However, small deviations are to be expected in reality. The objective of a uniformly distributed tension is deemed to be achieved in the area of the annular membrane in which the colour remains unchanged, although each of the colours represent an interval of tension values. This is the case for a large section of the annular membrane. Figs. 6.34 and 6.35 present the relative frequency distribution of the tension using a class interval of 3776 N/m for T_1 and 3490 N/m for T_2. The number of classes is determined according to $k \leq 5 \times \log n$, with the number of classes k and the number of data elements n, which is a recommended rule of thumb for such a large number of data elements in Ref. [64]. For the tension T_1, 43% of the tension values lie within the class mark 15612 N/m. Adding the adjacent class on the left to that, 68% of the tension values are within 9948-17500 N/m. For the tension T_2, 40% of the tension values lie within the class mark 11040 N/m. Adding the adjacent class on the right, 69% of the tension values lie within 9295-16275 N/m. Although there is a small shift between the

absolute tension values, i.e. the values of the tension T_1 are slightly higher than the values of T_2, more than two-thirds of the values of both tensions T_1 and T_2 are within a range of 7552 N/m for T_1 and 6980 N/m for T_2, respectively.

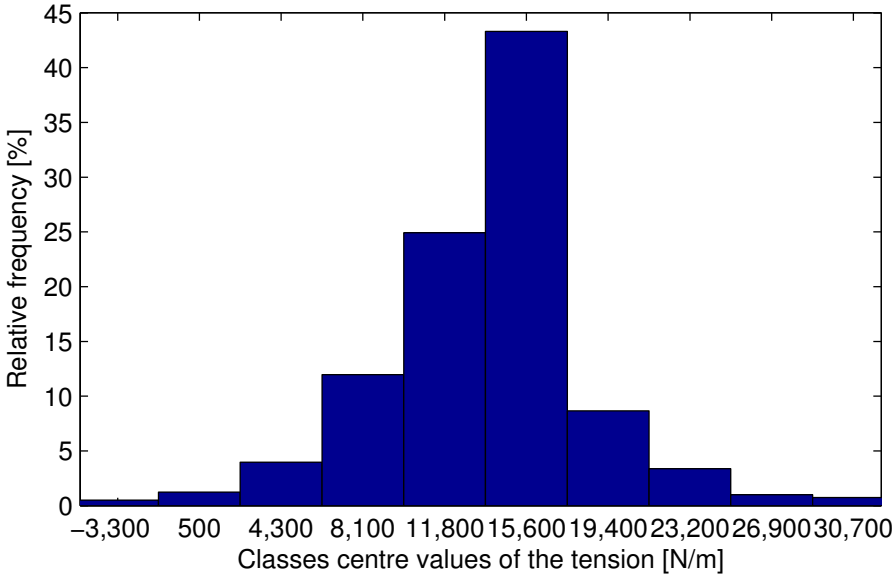

Figure 6.34: Relative frequency distribution of the tension T_1 of the annular membrane.

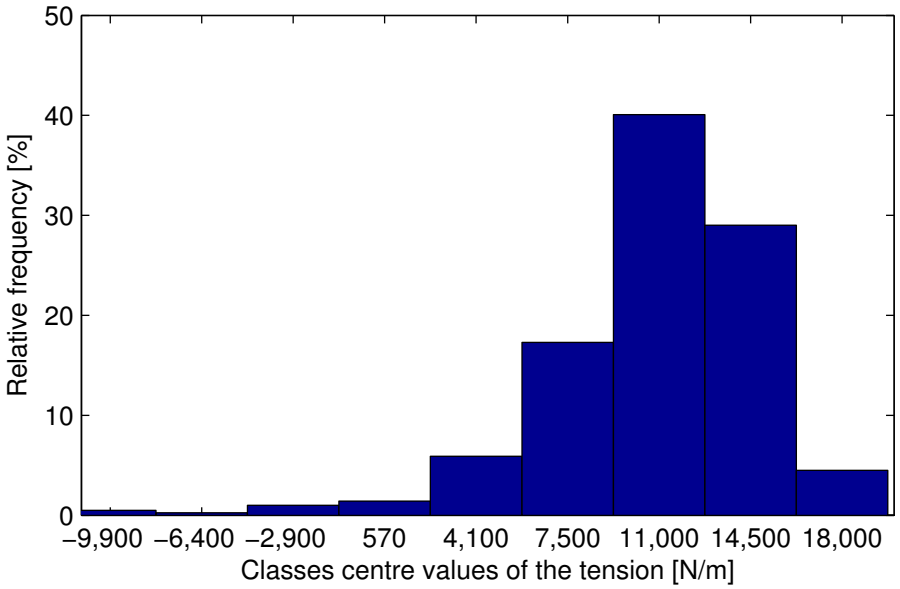

Figure 6.35: Relative frequency distribution of the tension T_2 of the annular membrane.

Data of the tension in the annular membrane have been made available through the DIC experiment. This will enable a comparison of the AMM with the TSR test rig and the AMM can be verified against the TSR test rig. Then, the influence

of the non-uniform tension in the annular membrane of the TSR test rig on the AMM can be assessed.

The target is to adjust the tension in such a way that the first eigenfrequency of the annular membrane matches the first eigenfrequency of the cavity of the TSR test rig, which is approximately 230 Hz. Therefore, the acoustic response of the TSR test rig on white noise excitation is measured at different locations in close proximity to the surface of the annular membrane during the DIC experiment in order to identify the first eigenfrequency of the system. The measured first eigenfrequency changed indeed with an increasing tension. However, after increasing the tension several times and measuring the acoustic response, the first eigenfrequency did not increase any further and, thus, reached a plateau of about 222 Hz. Reaching the end of the thread of the bolts, the experiment had to be stopped.

Potential causes of errors are discussed in the following. The weight of the annular membrane was considerably altered when the black paint was added onto the membrane. The additional weight is approximately 85-100 g, resulting in a total weight of the annular membrane and the paint of 426 g. Further, the paint may not have been uniformly distributed when it was sprayed manually onto the membrane. Thus, local inhomogeneities may arise regarding mass and stiffness of the combination of the paint and the annular membrane material. It is suspected that the additional weight increases the stiffness properties of the combination of the annular membrane and the paint, thus affecting its vibration and sound radiation characteristics.

Polymer materials like the Mylar® polyester film can absorb moisture from the environment, which expands the material. On the other hand, the moisture in the polymer material can evaporate as well, which contracts the material.

The modulus of elasticity is assumed to be constant in this work. With the experimental equipment available it is possible to measure deformation but not stress. Thus, it cannot be checked whether the modulus of elasticity remains constant for each strain state.

It was assumed that the thickness of the annular membrane remains constant in the tensioning process. However, the membrane thickness is likely to alter due to the high stretching of the annular membrane. It was not possible to measure the change in the thickness with the available DIC test equipment.

During the tensioning process, part of the membrane material is pulled over the edge of the outer shell, thus altering the mass of the plane annular membrane. Assuming a constant membrane thickness and a maximum average displacement of 0.85 mm at the outer shell, a weight difference of approximately 0.05 g is estimated for the membrane material without the paint. Due to a minimum weight of the

annular membrane of approximately 300 g, the influence of the weight difference on the vibration characteristics of the annular membrane is deemed negligible.

Distortion of the TSR test rig occurs during the tensioning process due to the elasticity of the parts of the test rig and due to the high forces applied. Fig. 6.2 presents the tensioning mechanism where the force is applied on the outer ring in order to increase the tension in the annular membrane. The reaction force is applied at the lug, which is mounted on the outer shell. Since the claw, bolt and lug are made of metal, they represent the parts with the highest stiffness. Thus, their distortion is small in comparison to the wooden parts like the outer shell or the outer ring. It is assumed that the outer shell and the outer ring are distorted due to the force application via the tensioning mechanism. The thickness of the outer shell is relatively high in comparison to the outer ring, which is significantly distorted whilst the tension is increased. This can be identified in Fig. 6.36, which represents two images of the upper right section of the TSR test rig during the DIC experiment. The distortion of the outer ring, marked by the arrows in the figure, is significantly between the zero strain state on the left and the final strain state on the right. Due to the gap between the tensioning bolt and the outer ring, a torque is created, which twists the outer ring in the radial outward direction. Thus, it appears that the claw pulls the outer ring outwards whilst adjacent parts of the outer ring are pushed inwards. In addition, it is assumed that the force is not evenly applied at the outer ring since the number of the tensioning mechanisms is limited to ten, as can be seen in Fig. 6.1. The force is applied via the claws; however, it is suspected that the force decreases between two claws due to the elasticity of the outer ring. Thus, the annular membrane is not evenly stretched and non-uniformities of the tension develop. Visual distortions at the inner ring could not be identified in Fig. 6.36. Thus, the clamping mechanism at the inner ring is deemed to be sufficiently stiff with negligible distortion.

The speckle pattern is of a distinctive characteristic with different sized speckles, which are distributed across the annular membrane in a non-uniform pattern. Speckles must not be too small since the DIC analyser may not identify them accurately. Medium sized speckles with a diameter between 1-2 mm are recommended. Then, the DIC measurement equipment can be operated with such a large specimen, which is the annular membrane mounted on the TSR test rig. The accurate estimation of the deformation of the annular membrane depends also on the definition of the zero strain state. In the current zero strain state, the membrane surface was smooth without wrinkles, which is required in order to achieve accurate results in the DIC post-processing. Due to the large deformation at the outer circumference of the annular membrane, some speckles are moved across the outer circumference and hence are not suitable to be utilised in the

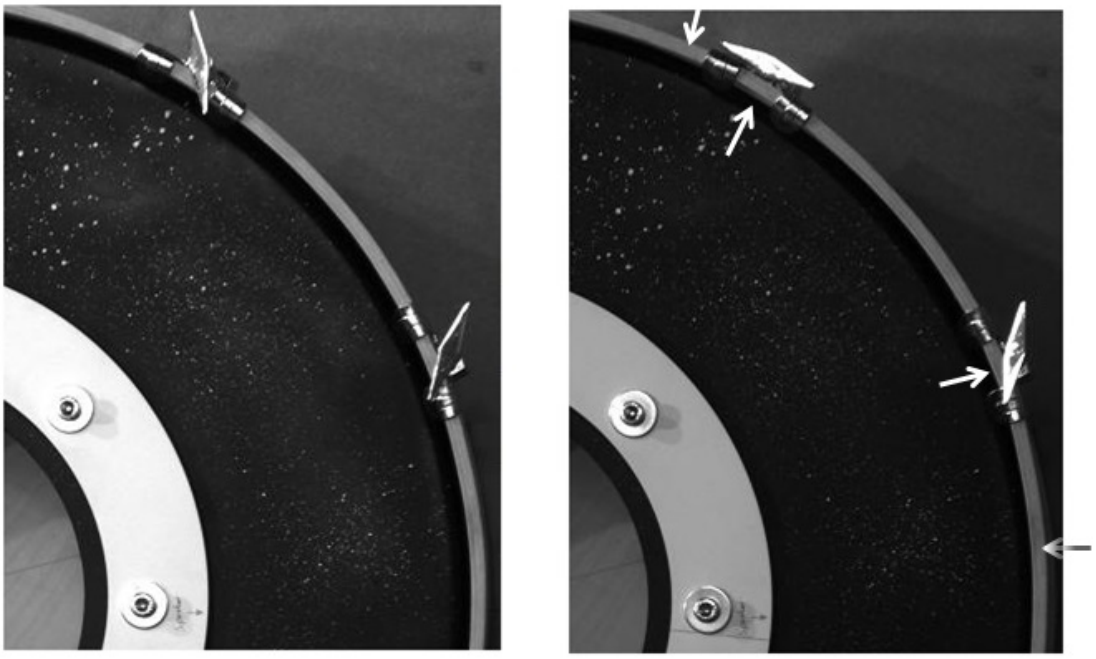

Figure 6.36: Distortion in the TSR test rig. Left: image of the zero strain state. Right: image of the final strain state. The arrows mark the distortion direction of the outer ring.

post-processing of the image. However, the maximum deformation at the outer circumference, which varies between 0.8-1.2 mm, is small in comparison to the length of the evaluation grid pattern, which is 12.5 mm. Thus, the effect on the post-processing result is assumed to be negligible. Overall, the accuracy of the DIC equipment, which comprises the production of the image and the post-processing stage, is deemed to be able to produce accurate measurement results.

6.5 Noise radiation experiments

This section summarises the sound pressure experiments being conducted in order to analyse the sound radiation characteristics of the tyre sidewall replica (TSR) test rig with a tensioned annular membrane. The TSR test rig is a complex noise source. Thus, a thorough analysis of the sound radiation characteristics is required in order to determine whether resonances of the annular membrane are excited by the cavity resonances. First, the experimental procedure for the recording of the sound pressure in close proximity to the annular membrane is presented. The measurement data is analysed and compared to the calculated resonance frequencies of the annular membrane model (AMM) of Section 6.3. Then, the measurement of the directivity sound pressure, in conjunction with Section 3.1, is described, which is required for the pass-by noise prediction method. Eventually,

the directivity sound pressure is analysed at the end of this section.

6.5.1 Measurement procedure in close proximity to the annular membrane

For the analysis of the noise radiation of the annular membrane of the TSR test rig, sound pressure measurements are carried out in the close vicinity of the membrane. Therefore, 24 locations are selected on the annular membrane, which is schematically represented in Fig. 6.37. In circumferential direction, eight measurement locations exist, which are 45° apart. As it is illustrated in Fig. 6.37, the circumferential measurement location closest to the acoustic excitation source is denoted 1. In the counterclockwise direction, the subsequent measurement locations are denoted 2 to 8. At each of those locations, three measurement positions exist in radial direction, which are denoted the inner, middle and outer position. The inner position is 32 mm away from the inner ring of the TSR test rig. Then, an equal spacing between the measurement positions is feasible, which is 31 mm. For the sound pressure recording, microphones are positioned above the measurement positions on the annular membrane at a distance of approximately 5 mm or less. There is no contact between the microphones and the membrane during the experiments. A white noise excitation signal is utilised and radiated from the acoustic excitation source.

The sound pressure measurements were conducted after the annular membrane was tensioned during the DIC experiment. Therefore, the condition of the TSR test rig as well as the environmental conditions like temperature and humidity are assumed to have remained constant throughout the experiments. Since only four microphones are available, the radial outer measurement positions of the circumferential positions 1, 3, 5 and 7 are measured first. Then, the microphones are moved to the middle and the inner measurement positions in sequence. The whole procedure is then repeated for the outer, middle and inner positions of the circumferential positions 2, 4, 6 and 8. For each measurement position, a 20 times averaged PSD spectrum is obtained.

A structural mode shape of the annular membrane has a specific sound radiation characteristic due to the location of the nodal lines and the amplitudes. Almost no or a very small motion of the membrane surface can be identified in areas of nodal lines, which, therefore, can be detected through low sound pressure values being recorded in close proximity to the surface of the annular membrane. On the other hand, the areas with the amplitudes of a mode shape can be identified through high sound pressure values. Therefore, the measured sound pressure data in close proximity to the annular membrane indicate the mode shapes of the

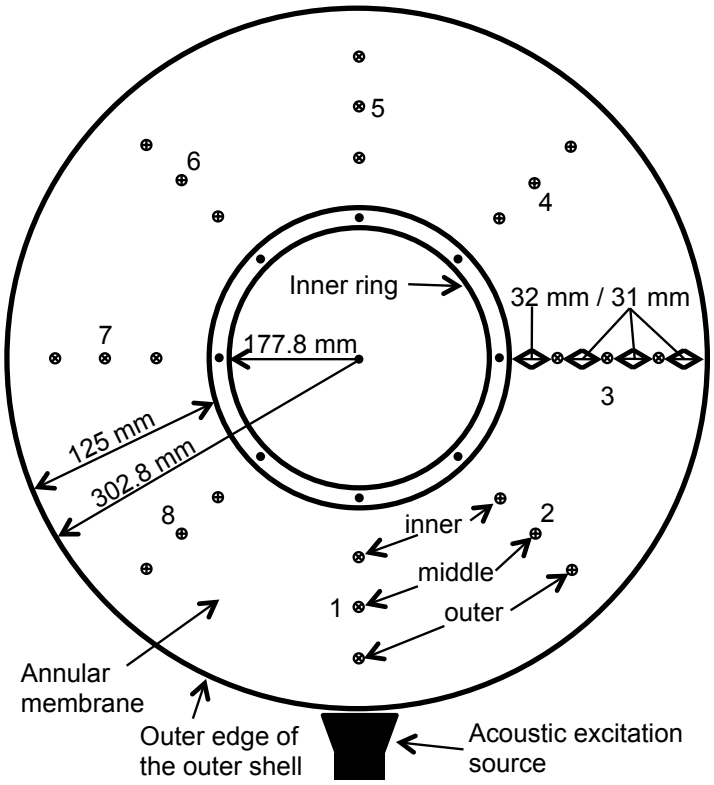

Figure 6.37: Schematic of the sound pressure measurement positions, marked with ⊗, on the annular membrane of the TSR test rig.

annular membrane, if no alternative measurement procedure, as a laser vibrometer for example, is available. For the evaluation of the sound pressure measurement data in the vicinity of the annular membrane of the TSR test rig, a Matlab® code was developed using bilinear interpolation. This is applied in order to represent the interpolated distribution of the measured sound pressure level on the annular membrane in a colour map, which has the shape of an annulus. This shall improve the visualisation of the mode shapes of the annular membrane. Since the number of measurement positions is limited, it is assumed that only low-order mode shapes can be identified accurately.

In a bilinear interpolation, the interpolation procedure is carried out in two different coordinate directions. Therefore, it is assumed that the TSR test rig is a linear system to which linear interpolation can be applied. First, the sound pressure is interpolated in circumferential direction applying Eq. 6.27. Therefore, the measured sound pressure values of two circumferentially adjacent measurement positions on the same radius $p^2(\vartheta_{i-1}, r_j)$ and $p^2(\vartheta_{i+1}, r_j)$ and their corresponding angles relative to the acoustic excitation source ϑ_{i-1} and ϑ_{i+1} are utilised to interpolate the sound pressure $p^2_{interp}(r_j = \text{const.}, \vartheta_i)$ at the angular position ϑ_i, which lies between the two measurement positions. This procedure is repeated in order to interpolate the sound pressure at intervals of 5°. The interpolation is carried

out for the inner, middle and outer radius at which the measurement positions are located.

$$p^2_{interp}(r_j = \text{const.}, \vartheta_i) = \frac{\vartheta_i - \vartheta_{i-1}}{\vartheta_{i+1} - \vartheta_{i-1}}(p^2(\vartheta_{i+1}, r_j) - p^2(\vartheta_{i-1}, r_j)) + p^2(\vartheta_{i-1}, r_j) \tag{6.27}$$

Then, Eq. 6.28 is applied in order to carry out the interpolation in radial direction using the measured sound pressure values as well as the interpolated results from the angular interpolation in Eq. 6.27. Therefore, the measured and interpolated sound pressure values of two radially adjacent measurement or interpolation positions $p^2_{interp}(\vartheta_i, r_{j-1})$ and $p^2_{interp}(\vartheta_i, r_{j+1})$, which are located on the same angle, and their corresponding radial coordinates r_{j-1} and r_{j+1} are utilised to calculate the interpolated sound pressure $p^2_{interp}(\vartheta_i = \text{const.}, r_j)$ at the radial position r_j. This procedure is carried out in order to interpolate once between the inner and middle as well as between the middle and outer radial positions.

$$p^2_{interp}(\vartheta_i = \text{const.}, r_j) = \frac{r_j - r_{j-1}}{r_{j+1} - r_{j-1}}(p^2_{interp}(\vartheta_i, r_{j+1}) - p^2_{interp}(\vartheta_i, r_{j-1})) + p^2_{interp}(\vartheta_i, r_{i-1}) \tag{6.28}$$

6.5.2 Analysis of the sound radiation in close proximity to the annular membrane

The sound pressure recorded in close proximity to the tensioned membrane, as described in Section 6.5.1 is analysed using frequency spectra and colour maps.

The power spectral density (PSD) of the sound pressure which is recorded at the inner, middle and outer positions of the measurement location 5 is illustrated in Fig. 6.38. Measurement location 5 is close to the measurement location of the cavity resonances in the outer shell of the TSR test rig as described in Sec. 6.2. The sound pressure data have been averaged 20 times. An overview of the measurement positions, which are closely positioned to the surface of the annular membrane is given in Fig. 6.37. Using the sound pressure recordings at discrete locations across the annular membrane shall assist in the analysis of low-order modes of the annular membrane. Such mode shapes can be detected with only eight measurement positions in the circumferential direction. Figs. 6.10 and 6.11 illustrate the principal mode shapes of an annular membrane. For example, it should be possible to identify the mode shapes $(0, 1)$, $(1, 1)$ and $(2, 1)$ with reason-

able accuracy. Since three measurement positions exist in the radial direction at each circumferential measurement location, it should be possible to indicate when the mode shapes $(0, 2)$, $(1, 2)$ and $(2, 2)$ occur. For higher-order mode shapes, the number and the arrangement of the measurement positions on the annular membrane are deemed to be not adequate.

The sound pressure data in Figs. 6.38 and 6.39 illustrate representative examples of the recorded data across the annular membrane. The significant resonances are 220 Hz, 546 Hz, 733 Hz and 952 Hz. These are higher than, but fairly close to, the in-cavity measurements of the first to the fourth cavity resonances of the TSR test rig, which are 208 Hz, 531 Hz, 719 Hz and 939 Hz, as presented in Sec. 6.2. The deviations between the two measurement procedures is between 12-15 Hz, which is relatively constant. The cavity resonances are predicted as 230 Hz, 459 Hz, 689 Hz and 919 Hz in Sec. 6.2. Although the first resonance frequency of 220 Hz is closer to the predicted first cavity resonance at 230 Hz, higher deviations occur for the other cavity resonances. In this regard, the close proximity measurement data show similar characteristics to the in-cavity measurement data, discussed in Sec. 6.2.

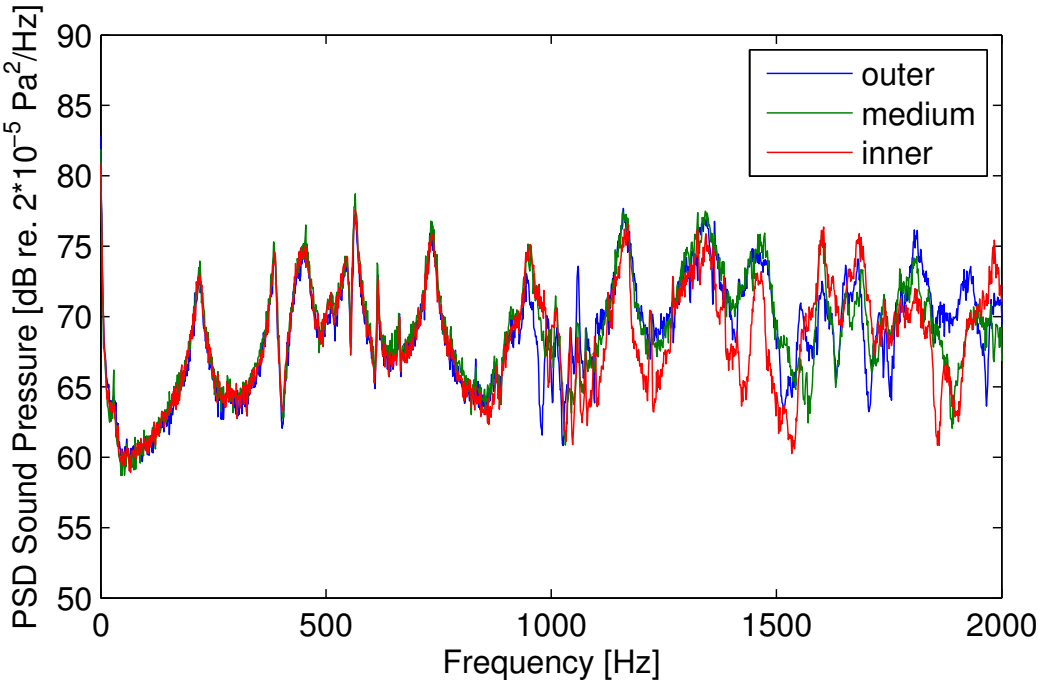

Figure 6.38: The power spectral density of the measured sound pressure for the inner, middle and outer position at measurement location 5.

The corresponding SPLs of the close proximity measurement data are not as high as the in-cavity measured resonances in Sec. 6.2, which may be caused by a change in the strength of the excitation signal or the insulating characteristics of the annular membrane. It is also noticed that the SPLs of the second to fourth

cavity resonances are generally either as high as or higher than the SPL of the first cavity resonance. This is in contrast to the in-cavity SPLs, which are highest for the first cavity resonance and smaller for the other cavity resonances.

It seems that the damping is generally very similar for the cavity resonances measured inside the cavity and the cavity resonances measured in the close vicinity of the annular membrane surface. This contributes to the assumption that these resonances are actually the cavity resonances of the TSR test rig, although the resonance frequencies are slightly apart.

Such deviations in the resonance frequencies of the two measurement procedures may be attributed to the ambient temperatures during the experiments. High temperatures of approximately 28°C occurred during the close proximity measurements. During the in-cavity measurements, the ambient temperature was lower at approximately 12°C. In general, a higher ambient temperature leads to an increase in the resonance frequency whilst a lower temperature leads a decrease. Applying the known temperatures and an effective length of 1.475 m in the formula $f = c/\lambda$, the corresponding resonance frequencies can be estimated, which vary for the two temperatures between 6 Hz, 13 Hz, 21 Hz and 25 Hz for the first to the fourth cavity resonance frequency. This means that the frequency variations increase with increasing frequency, which does not occur in the measurements. In reality, the variations between in-cavity and close proximity measurements are smaller with 12-15 Hz, which is also within a range of just 3 Hz. Overall, the significant resonance peaks are deemed to represent the cavity resonances.

Up to a frequency of 1000 Hz, other significant resonance peaks are at 385 Hz, 474 Hz, 614 Hz and 664 Hz. These peaks may be associated with structural resonances of the annular membrane. The damping of these resonances appears to be smaller than the damping of the peaks which are associated with the cavity resonances. This may be an inherent characteristic of the structural resonances of the annular membrane, which is deemed to exhibit a small amount damping.

The measurement data of the three radial measurement positions, i.e. inner, middle and outer, match well up to a frequency of approximately 1000 Hz. However, beginning from approximately 1000 Hz, discrepancies between the data of the radial measurement positions increase at all of the circumferential measurement locations. For example, resonance peaks of the three radial positions vary in height, or resonance frequencies occur only at one of the radial measurement positions, or the damping of a resonance differs depending upon the radial measurement position. Thus, the unambiguous identification and declaration of resonances and their corresponding mode shapes becomes more difficult. Further, the modal density of the annular membrane increases with increasing frequency, which generally exacerbates the identification of the resonance frequencies and

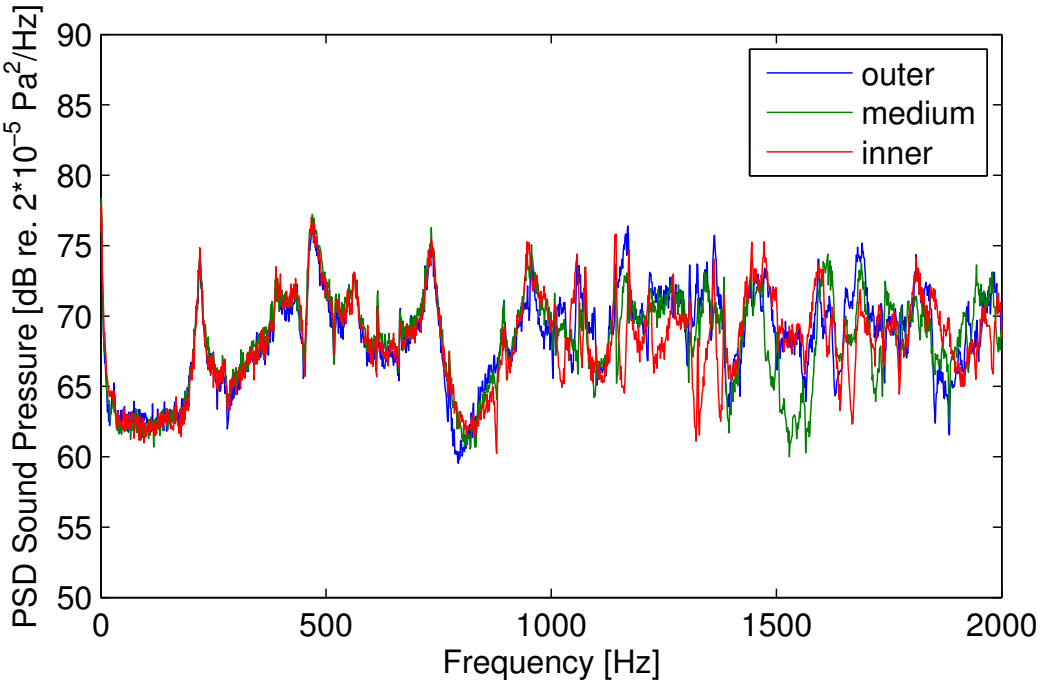

Figure 6.39: The power spectral density of the measured sound pressure for the inner, middle and outer position at measurement location 8.

their corresponding mode shapes because masking of adjacent resonances may occur. Another influence may originate from the modes across the cavity width or radius, which begin to occur at higher frequencies around 1000 Hz.

A distinct cause and effect connection cannot be identified between the resonances in the sound pressure spectra in Figs. 6.38 and 6.39 and the tension in the annular membrane, which is illustrated in Figs. 6.32 and 6.33. At the measurement location 5, the tension gradient rises from the outside towards the inside of the annular membrane. However, it is not possible to identify whether a high tension value leads to a high sound pressure amplitude or a shifted resonance frequency. Even for a relatively constant distribution of the tension at the measurement location 8, an effect on the sound pressure spectrum in Fig. 6.39 cannot be detected. A higher number of measurement locations in conjunction with an optical measurement method, which measures the surface velocity of the annular membrane, may be a possible option in the future in order to investigate the link between the local tension in the membrane and the surface velocity.

In addition to the sound pressure spectra, colour maps in the shape of an annulus are utilised, which represent the surface of the annular membrane. Then, the measured sound pressure of a particular frequency can be plotted at their actual measurement positions on the colour map using distinctive colours according to their levels. Between the measurement positions, a bilinear interpolation is applied in order to approximate a complete visual representation of the sound

pressure levels across the annular membrane. The annular shape in the colour map represents the area between the inner and the outer measurement positions on the surface of the annular membrane. Since measurement values at the inner and outer boundaries of the annular membrane are not available, these positions are excluded from this form of illustration. The measurement positions are marked and numbered. Measurement position 1 is the closest to the location of the acoustic source. Thus, the arrangement of the colour maps corresponds to the arrangement of the diagrams which represent the strain, stress and tension in Sec. 6.4.3.

Sound pressure spectra are helpful in the identification of resonances, but it is difficult to identify any mode shapes. The interpolated colour map spatially illustrates the sound pressure levels (SPL) of all measurement positions at a particular frequency, which supports the identification of mode shapes. However, this form of identification is limited due to the number of measurement locations. It is assumed that the eight measurement locations in the circumferential direction are sufficient in order to detect low-order mode shapes of the sound pressure radiation of the annular membrane. If the number of nodal lines is greater or equal to the number of circumferential measurement locations, it is assumed that the mode shapes cannot be detected properly anymore. Further, the interpolation represents an approximation, which is assumed to be applicable for low-order mode shapes, which consist of a linear characteristic between adjacent measurement locations.

The annular colour map in Fig. 6.40 illustrates the SPLs at 220 Hz. Maximum values are reached between the first and the eighth measurement locations as well as between the fourth and the fifth measurement locations. Due to the proximity to the acoustic excitation source, slightly higher amplitudes may be caused at the first measurement location. Minimum values occur at the third and between the sixth and seventh measurement locations. The difference between maximum and minimum values is between 3-5 dB. If the minimum values are considered to indicate the existence of a nodal line, the plot visualises the mode shape of the first cavity resonance. Thus, the sound radiation of the annular membrane of the TSR test rig increases at the locations of the maximum SPLs due to excitation of the first cavity resonance.

From the sound pressure spectra at every measurement location, it is assumed that the second cavity mode shape occurs between 545-552 Hz. Fig. 6.41 illustrates the SPLs in the annular colour map at 545 Hz at which the maximum SPLs occur at the first, third, fifth and seventh locations. The highest SPLs exist at the mid measurement positions, which indicates a semi-circular or semi-oval shape of the deflected annular membrane in the cross-sectional direction. Minimum SPLs exist at the second, fourth, sixth and eighth measurement locations. The difference between maximum and minimum SPLs is up to 9 dB. Considering the minimum

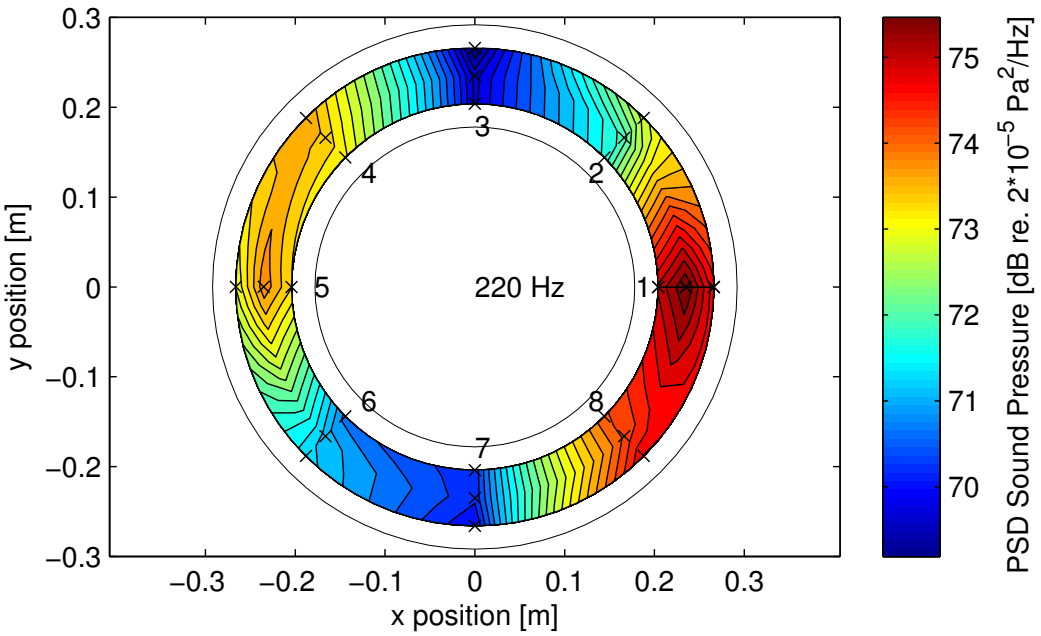

Figure 6.40: The annular colour map of the measured sound pressure levels at 220 Hz.

values as the beginning and end points of two nodal lines, the colour map illustrates the second cavity mode shape.

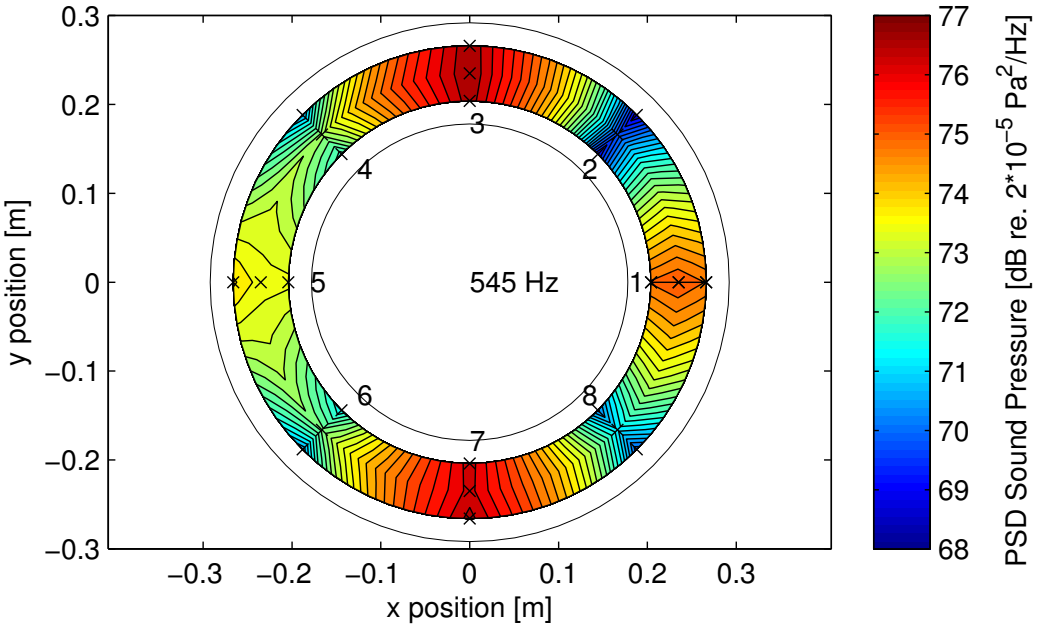

Figure 6.41: The annular colour map of the measured sound pressure levels at 545 Hz.

It is assumed that the third cavity resonance appears between 730-735 Hz according to the sound pressure spectra. Fig. 6.42 illustrates the measured SPLs at 733 Hz. Two distinctive minimum values are found at the third and seventh

measurement locations. In the sound pressure spectrum of location 3 in Fig. 6.43, the resonance peak is not identifiable. Hence, the existence of a nodal line is indicated at these locations. Apart from these two minimum values, the amplitudes are almost constant at the mid measurement positions. Deviations from the maximum SPLs up to 3 dB occur at the inner and outer positions of the second, fourth and sixth measurement locations. Three nodal lines and six maximum values are expected to occur for the third cavity mode shape. However, this characteristic cannot be identified in the annular colour map of Fig. 6.42. This may be caused through the insufficient resolution given by the limited number of the measurement locations in the circumferential direction. These are positioned at a 45° interval and, hence, it is not possible to detect any nodal line which falls between adjacent measurement locations in the circumferential direction. For example, two nodal lines could be located between the measurement locations 1/2 and 5/6 as well as between 4/5 and 8/1. In that case, three nodal lines would exist, which would confirm the mode shape of the third cavity resonance. However, this cannot be proven without additional measurement locations.

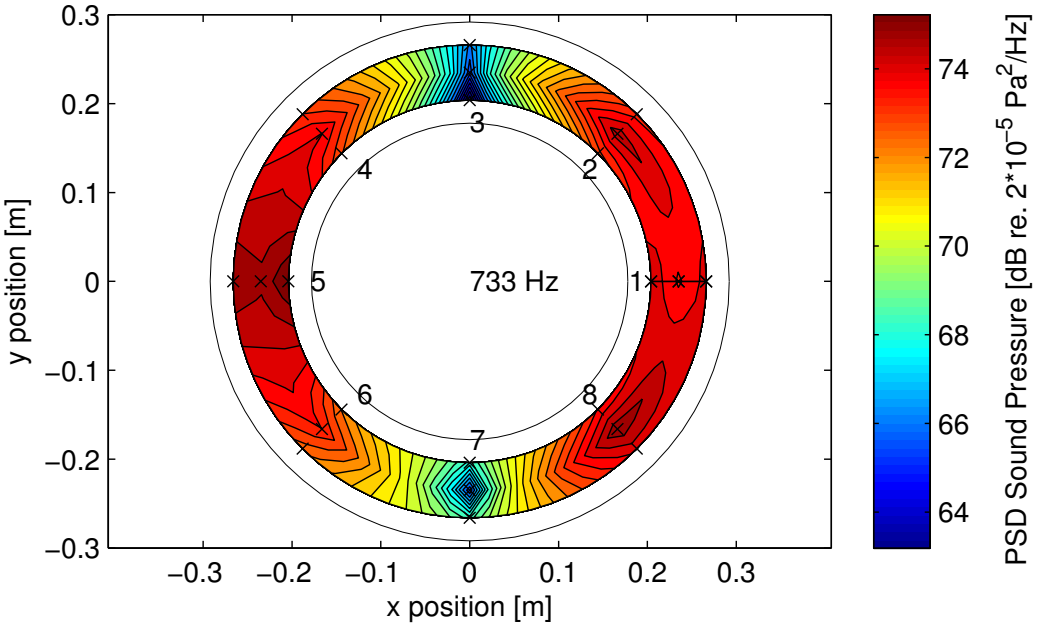

Figure 6.42: The annular colour map of the measured sound pressure levels at 733 Hz.

Fig. 6.44 illustrates the measured SPLs at 950 Hz, which is assumed to be the fourth cavity resonance. The corresponding mode shape of the fourth cavity resonance consists of four nodal lines and eight maximums. However, the annular colour map in Fig. 6.44 does not show any of these characteristics. Due to the coarse resolution of the measurement locations, it may not be possible to detect and identify the fourth cavity mode shape with this measurement setup.

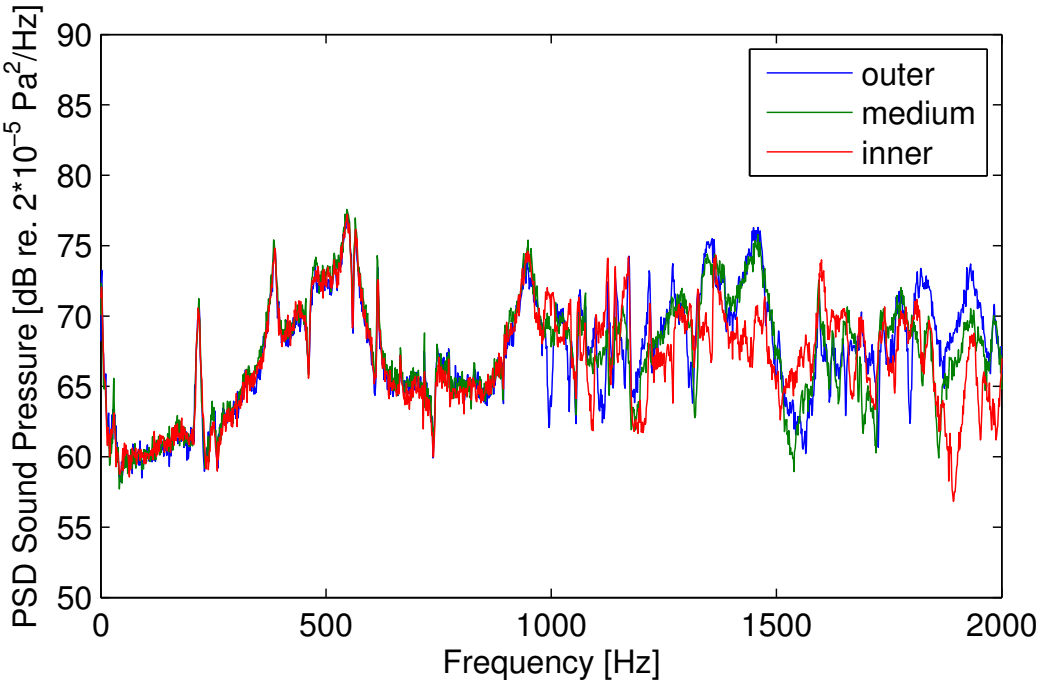

Figure 6.43: The power spectral density of the measured sound pressure for the inner, middle and outer position at measurement location 3.

In addition, the colour map reveals high gradients in the measured sound pressure between the inner and outer measurement points at the locations 2, 3, 5, 7 and 8. Neither a diametrical nor a circumferential nodal line can be clearly identified. The mode shape may be described as a distorted mode shape, since the minimum and maximum values swap their positions from the inner to the outer measurement positions. Whilst the gradient of the measured SPLs is positive towards the outer measurement positions between the gaps of the locations 2/3 and 8/1, the gradient becomes negative between the gaps of the locations 8/1 and 2/3.

In addition to the cavity resonances, other resonances occur in the measured sound pressure spectra, which may be associated with the structural mode shapes of the annular membrane. The second resonance peak occurs in the range of 384-388 Hz. The corresponding colour map of the measured SPLs is illustrated in Fig. 6.45. It is noticeable that the mode shape in Fig. 6.45 is almost identical to the mode shape of the second cavity resonance in Fig. 6.41. The illustrated mode is considered to be a structural mode of the annular membrane. According to the theoretical mode shapes of an annular membrane in Figs. 6.10 and 6.11, it can be identified as the $(2, 1)$ mode with two diametrical nodal lines. Since it is the second resonance peak in the spectra, it is assumed that the number, and the arrangement, of the measurement positions are sufficient in order to identify this mode accurately. In comparison to the second cavity mode, the SPLs occur at the same locations, which are the mid positions at the locations 1, 3, 5 and 7.

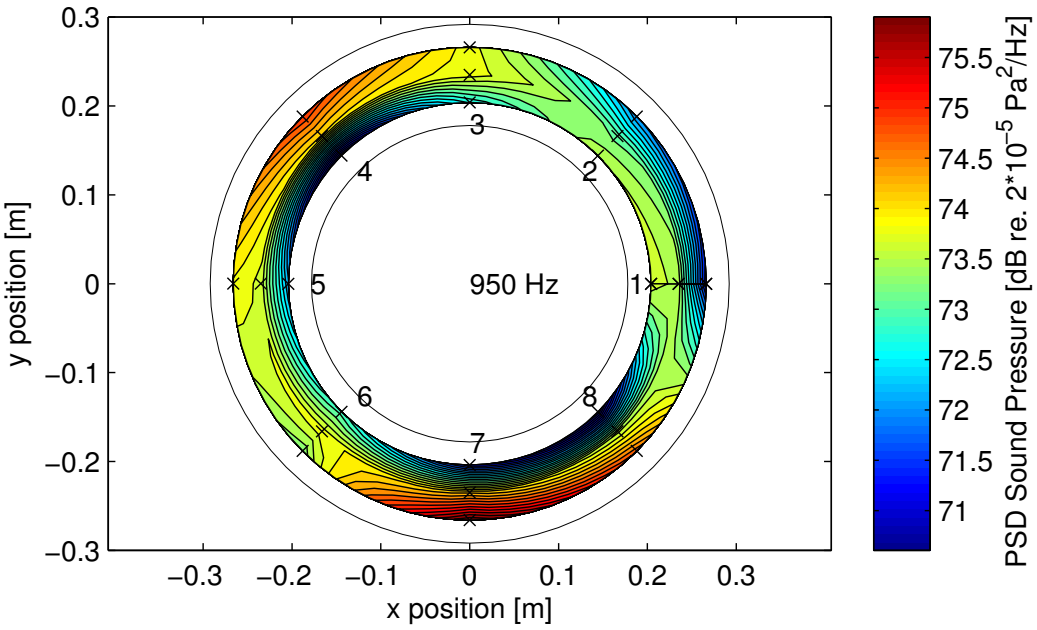

Figure 6.44: The annular colour map of the measured sound pressure levels at 950 Hz.

The SPLs are lower by up to 2 dB at the locations 3, 5 and 7 for the $(2, 1)$ mode than they are for the second cavity mode. However, the SPL at the location 1 is the highest for the structural mode, which may be caused due to the close vicinity to the acoustic excitation source. Therefore, it appears that the second cavity mode produces an even higher sound radiation than the $(2, 1)$ structural annular membrane mode or the first cavity mode.

The identification of particular mode shapes becomes difficult if the resonance peaks of the different measurement locations vary slightly with frequency in the sound pressure spectra of all measurement locations. The true resonance frequency may be actually enclosed within a small frequency band of approximately 5 Hz. In addition, the heights of the SPLs vary, which is expected since the SPLs represent the mode shape including nodes and anti-nodes for the sha. This may be caused through inaccuracies in the data processing of the analyser or the conducting of the measurement procedure in which only four microphones are available. Therefore, they have to be swapped between each of the measurement positions in order to cover all of them. The swap leads to a disruption in the measurement procedure in which the acoustic excitation source is switched off. The microphone swap and the disruption may result in variabilities which cause small shifts of some resonance frequencies. An additional effect may originate from the non-uniform distribution of the (static) tension in the annular membrane. It is imaginable that the local alteration in stiffness results in an alteration of the corresponding eigenfrequencies.

The peak around the frequency of 470 Hz serves as an example for a non-

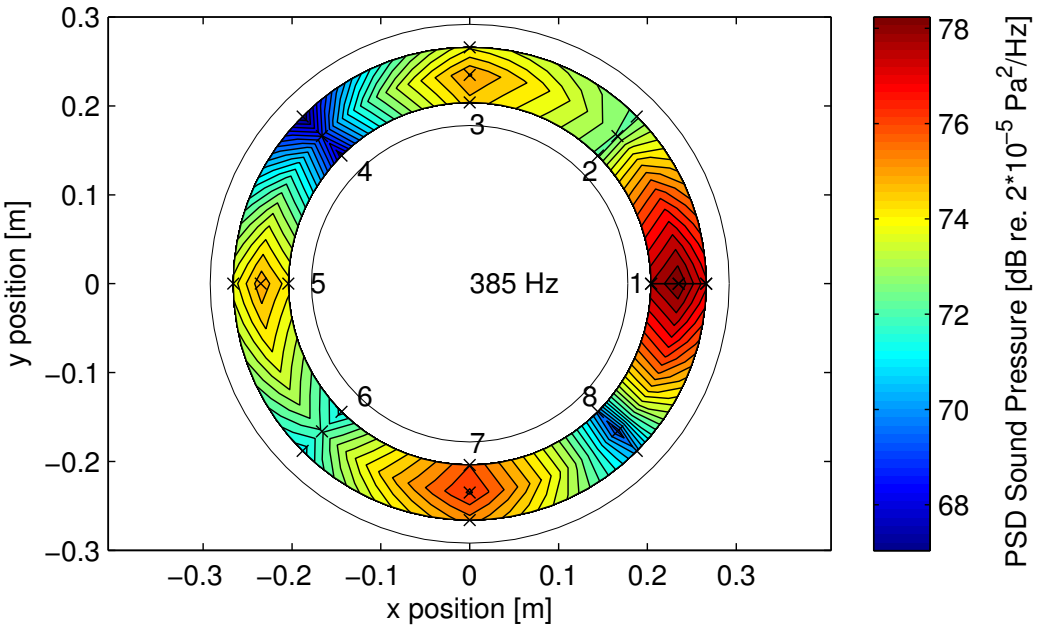

Figure 6.45: The annular colour map of the measured sound pressure levels at 385 Hz.

clear identification of a mode shape. The peak is clearly visible at 470 Hz in the sound pressure spectra of the circumferential measurement locations 4 and 8. For the measurement locations 5 and 7, the peak is not pronounced clearly, which might indicate the existence of a nodal line at these locations. For the other measurement locations, the peak seems to be moved to a frequency between 474-476 Hz. Among the SPLs at these frequencies, a mode shape with four maxima at the circumferential measurement locations 2, 4, 6 and 8 and their corresponding nodal lines in between can be identified best in the colour map, shown in Fig. 6.46, which illustrates the SPLs at 474 Hz. The SPL is highest at the eighth location and lowest at the sixth. The difference of approximately 4 dB between the two SPLs is quite large. It is noticed that the determined tension values in the annular membrane are lowest in the area of the measurement location 6 and they are highest in the area of the measurement locations 8 and 2. This may indicate a connection between the membrane tension and the sound radiation. The mode shape is almost identical to the mode shapes at 385 Hz in Fig. 6.45 and at 220 Hz in Fig. 6.40 except that its nodal lines are shifted by 45°. However, having already identified a $(2, 2)$ mode shape and due to the very low SPLs between locations 5 to 7, it is questionable whether the mode shape has been identified accurately.

Other resonance frequencies, worth mentioning due to their consistent appearance in the sound pressure spectra, occur at 614 Hz and at 664 Hz. Both peaks seem to have little damping and both vary slightly by ±1 Hz. The measured SPLs are illustrated at 614 Hz and 664 Hz in the annular colour maps in Figs. 6.47

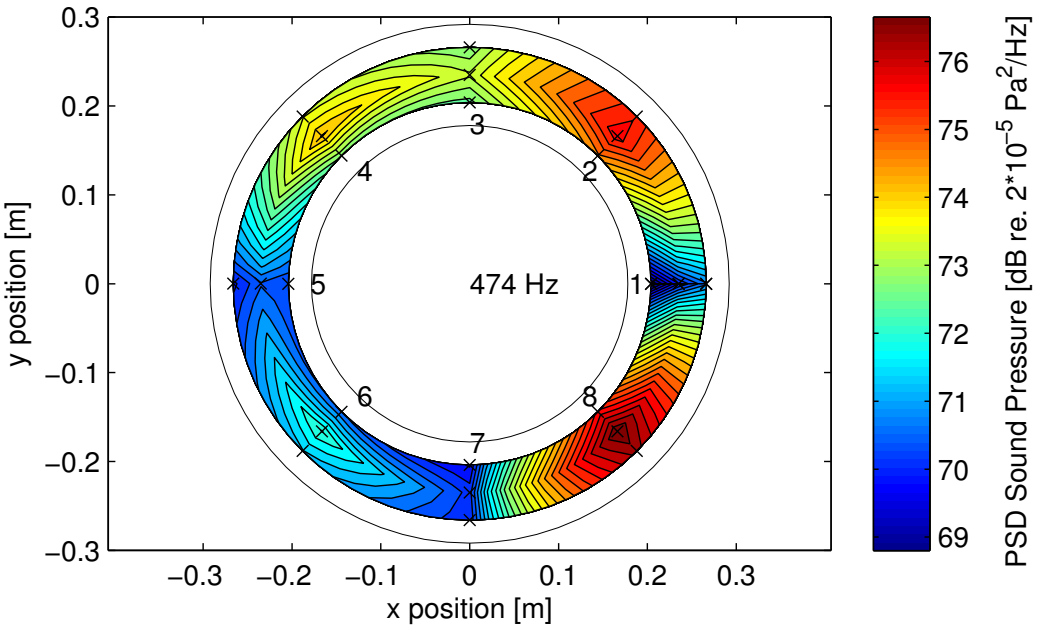

Figure 6.46: The annular colour map of the measured sound pressure levels at 474 Hz.

and 6.48, respectively. It is noticed that the mode shape at 614 Hz appears to be identical to the $(2, 2)$ mode shape in Fig. 6.45. However, the sound pressure gradient in the radial direction is higher at 614 Hz than at 385 Hz. At 614 Hz, the difference between the middle and outer or inner measurement positions are between 2-3.6 dB whilst it is 1.2 dB maximum at 385 Hz. This may indicate that this is actually a mode shape with one or more circumferential nodal lines, which usually occurs in the higher frequency range according to eigenfrequencies of the AMM. Unfortunately, this cannot be clearly determined with the current arrangement of the measurement positions, which consists of just three measurement positions in the radial direction and does not measure the sound pressure at the inner or outer boundaries of the annular membrane. A similar conclusion can be drawn for the mode shape at 664 Hz. However, this mode shape does not seem to have distinctive nodal lines due to the absence of a proper maximum SPL at or around the measurement location 6.

The mode shape at 220 Hz suggests that it is the first cavity mode. In addition, its resonance frequency is close to the theoretical value of the first cavity resonance frequency. However, the same resonance peak varied during the DIC experiment, when it was moved towards higher frequencies whilst the tension in the annular membrane was increased. Its final value became 220 Hz. Hence, the resonance may actually be associated with the structural $(1, 1)$ mode of the annular membrane since the frequency changed with the tension. The coincidence of both the $(1, 1)$ mode and the first cavity mode at around 220 Hz would fulfill the initial objective

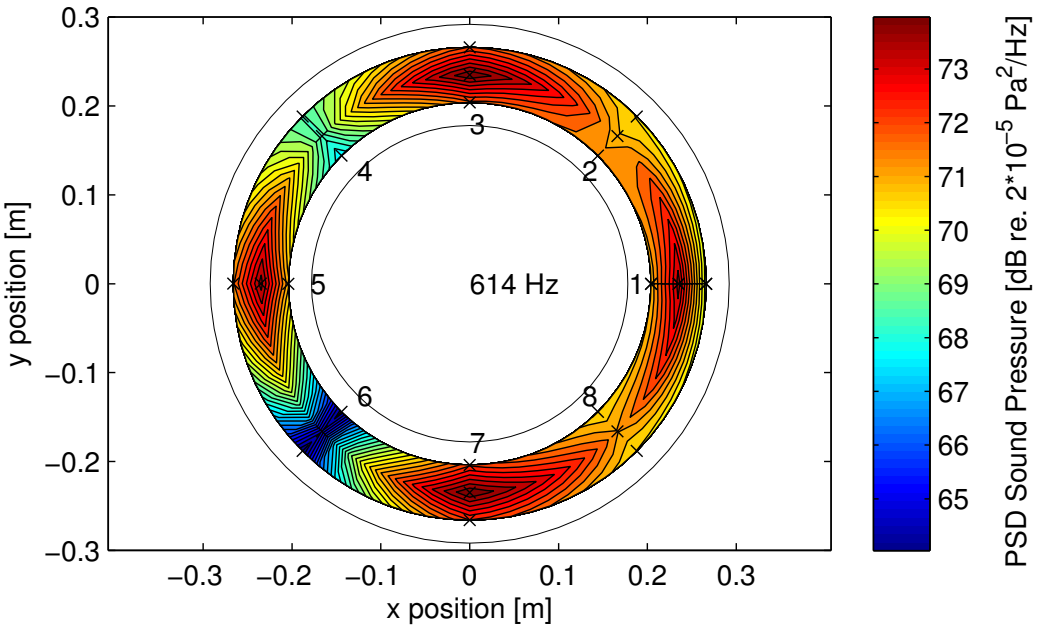

Figure 6.47: The annular colour map of the measured sound pressure levels at 614 Hz.

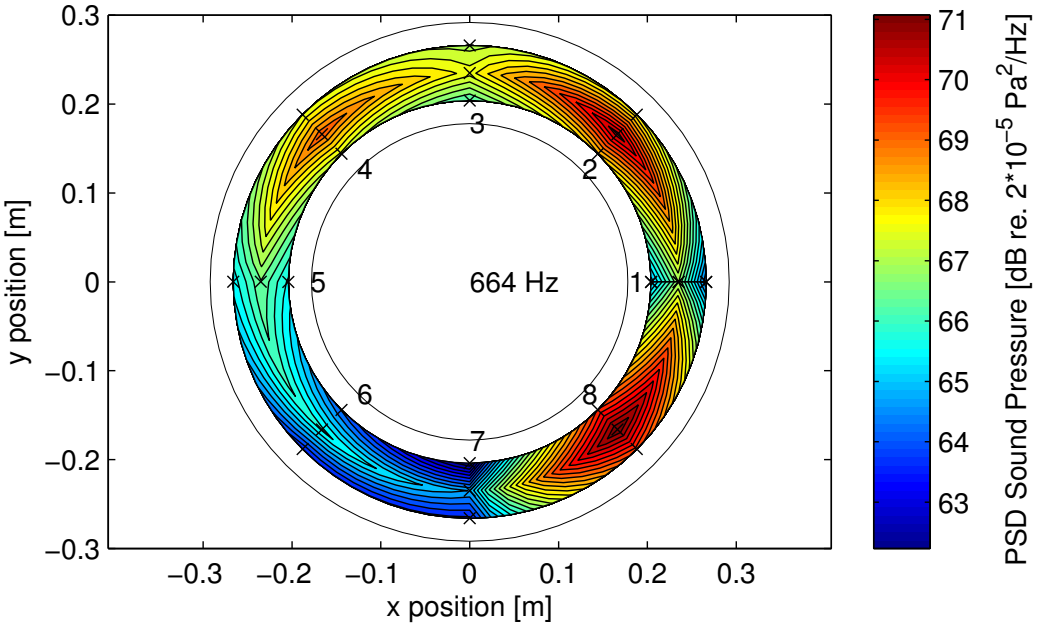

Figure 6.48: The annular colour map of the measured sound pressure levels at 664 Hz.

of the coupling of the cavity and annular membrane modes. However, the distance between the $(1,1)$ and the $(2,1)$ mode is relatively large, and the resonances are approximately 165 Hz apart. The results of the theoretical AMM suggest a maximum distance of 20 Hz between them. The $(0,1)$ mode could not be detected with this experimental setup.

The coherence between the sound pressure and the voltage of the electric cur-

rent sensor, which measures the current into the loudspeaker and, thus, represents the energy input, is shown in Fig. 6.49 for the measurement location 5. The coherence reaches generally values greater than 0.9, which indicates that the sound pressure resonances originate from the excitation signal of the loudspeaker. Below 100 Hz, the coherence values are low. This may be related to the DC component in the signal, since a high peak can be identified at very low frequencies in the sound pressure spectrum in Fig. 6.38. The coherence data of the inner, middle and outer measurement positions match well up to a frequency of approximately 1000 Hz. The dips in the coherence data do not match any of the resonance peaks in the sound pressure spectrum in Fig. 6.38. At frequencies greater than 1000 Hz, discrepancies occur between the data of all three radial measurement positions.

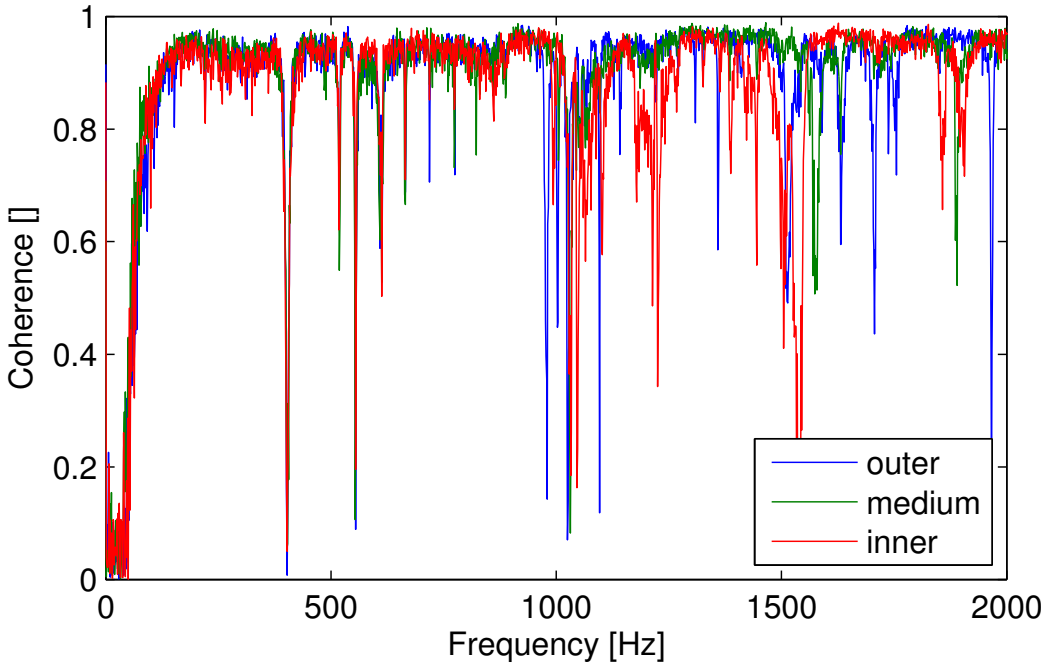

Figure 6.49: The coherence for the inner, middle and outer position at measurement location 5.

6.5.3 Comparison of the measured sound pressure resonances in close proximity and the calculated resonances of the annular membrane model

The resonances of the acoustic measurements in the close proximity of the annular membrane are compared with the structural resonances which are calculated using the annular membrane model (AMM). The physical mechanisms of the experiment and the model, which are acoustics and mechanical vibrations, are different. Therefore, the detection of individual structural resonance frequencies with sound

pressure microphones may depend upon the structural-acoustic coupling between the annular membrane and the ambient air. For a wave speed in the annular membrane, which is close to the wave speed of sound in air, the corresponding mode is supposed to be an efficient sound radiator. Thus, the resonance frequency will be detected by the microphones. A non-contact measurement procedure is crucial in order to not alter the physical properties of the annular membrane, which is already lightweight. Thus, if accelerometers were attached to it, their mass would alter the measurement results significantly .

In the sound pressure measurements in the close proximity of the annular membrane, the structural $(2,1)$ mode occurs at 385 Hz. Since this seems to be the lowest measurable structural resonance frequency of the annular membrane, the $(2,1)$ mode is deemed to be a suitable comparative basis.

The AMM requires a single numerical input value for the representation of the uniformly distributed tension in the annular membrane. However, according to the results of the DIC experiment, the tension is not constant nor uniformly distributed. The areas on the surface of the annular membrane, where a constant tension can be approximately assumed, are limited. Therefore, the mean of the averaged tension values in the principal stress directions $\overline{T}_1$ and $\overline{T}_2$ of the experimentally determined tension values serve as a compromise and provide a single numeric value for the tension parameter in the AMM. The mean becomes $\overline{T} = 12442\,\mathrm{N/m}$. The other input parameter, which is needed in the AMM, is the mass per area. This is $0.353\,\mathrm{kg/m^2}$, which is calculated from the material density according to the specification sheet of the membrane material in Ref. [26] and the membrane thickness, which is 0.254 mm. In the first instance, the value of the mass per area does not consider the mass of the applied paint on the membrane. Using these data in the Eqs. 6.15 and 6.16 of the AMM results in 821 Hz being the frequency for the first mode, which is the $(0,1)$ mode. Subsequent resonance frequencies are 831 Hz and 860 Hz for the $(1,1)$ and the $(2,1)$ mode, respectively. The first resonance frequency of a mode with one circumferential nodal line, which is the $(0,2)$ mode, is 1646 Hz. All of these calculated resonance frequencies are much higher than the experimentally determined resonance frequencies. Applying Eq. 6.9, the wave speed in the annular membrane becomes $c = 188\,\mathrm{m/s}$. This is approximately half of the speed of sound in air at 20°C, thus, the structural modes of the annular membrane are supposed to be non-efficient sound radiators.

Since a substantial amount of spray paint was applied on the annular membrane, consequently, it is reasonable to adjust the mass per area parameter in order to reflect the properties of the combination of the spray paint and the membrane material. Therefore, the amount of paint is estimated to be 0.12 kg, which is based on the mass of paint per spray can. The adjusted value for the mass per

area is obtained via the quotient of the paint mass and the area of the annular membrane, which is $0.12\,\mathrm{kg}/(\pi \times (R_o^2 - R_i^2)) = 1.07\,\mathrm{kg/m^2}$. Applying the same averaged tension value as above, the first resonance frequency is calculated to be 472 Hz, which is the $(0, 1)$ mode. This value is quite close to the measured 470 Hz, which is assumed to represent a structural resonance as discussed in Sec. 6.5.2. However, since diametrical nodal lines seem to exist in the experiment, a comparison is null as no nodal lines exist in the calculated $(0, 1)$ mode. The resonance frequency for the $(2, 1)$ mode is obtained as 494 Hz, which is 109 Hz over the frequency value of 385 Hz from the measurements. In comparison to the previous model parameter values, the wave speed is reduced to 108 m/s, which generally indicates even less efficient sound radiators.

In order to match the measured frequency of 385 Hz of the $(2, 1)$ mode, the wave speed in the membrane has to be lowered in the AMM, which reduces the calculated eigenfrequencies of the annular membrane. Therefore, either the tension is increased or the mass per area is decreased in Eq. 6.9. Reducing the tension value to $T = 7550\,\mathrm{N/m}$ and keeping the value for the mass per area, which is $\hat{\mu} = 1.07\,\mathrm{kg/m^2}$, the wave speed results in $c = 84\,\mathrm{m/s}$. These parameter values enable the measured and calculated frequencies of the $(2, 1)$ mode to be matched, as shown in Table 6.2. The first calculated frequencies are 367 Hz and 372 Hz, which characterise the $(0, 1)$ and the $(1, 1)$ mode, respectively. However, these frequencies do not appear in the measurement spectra. Some of the calculated eigenfrequencies match or are close to some of the measured eigenfrequencies. In Table 6.2, for example, the $(5, 1)$ mode at 466 Hz is close to the measured 470 Hz. At the measured 614 Hz and 664 Hz, the predicted frequencies are more than 10 Hz apart from each of the measured frequency. The predicted frequency at 543 Hz is reasonably close to the second cavity resonance frequency of 546 Hz. Another example is the three eigenfrequencies, which are close to the third cavity resonance frequency. Although, the AMM does not predict the acoustic cavity resonances, an interaction between structural and acoustic modes or a mutual amplification between them is generally possible in reality, if their corresponding eigenfrequencies match or are reasonably close to each other, respectively. If an interaction between the structural and acoustic modes in the TSR test rig occurs, the TSR test rig would replicate the interaction between the tyre cavity and the tyre sidewall realistically. In comparison to the experimentally obtained tension data, the tension value is substantially decreased in order to match the predicted and measured eigenfrequency of 385 Hz. Thus, a general discrepancy exists between the AMM and the experimental data.

The AMM results for the input parameters $T = 2700\,\mathrm{Hz}$ and $\hat{\mu} = 1.07\,\mathrm{kg/m^2}$ are also presented in Table 6.2. In this case, the first frequency of the AMM is

Measurements			AMM			
	In-cavity	Close proximity	$T = 7550\,\mathrm{N/m}$ $\hat{\mu} = 1.07\,\mathrm{kg/m^2}$ $c = 84\,\mathrm{m/s}$		$T = 270\,\mathrm{N/m}$ $\hat{\mu} = 1.07\,\mathrm{kg/m^2}$ $c = 50\,\mathrm{m/s}$	
Mode	f [Hz]	f [Hz]	Mode	f [Hz]	Mode	f [Hz]
1st cavity	208	220			(0,1)	220
					(1,1)	222
					(2,1)	230
⋮	⋮	⋮	⋮	⋮	⋮	⋮
			(0,1)	367		
			(1,1)	371	(9,1)	377
structural (2,1)		385	(2,1)	385		
⋮	⋮	⋮	⋮	⋮	⋮	⋮
structural		470	(5,1)	466	(12,1)	461
					(5,2)	474
⋮	⋮	⋮	⋮	⋮	⋮	⋮
2nd cavity	531	546	(7,1)	543	(9,2)	541
			(8,1)	586	(15,1)	549
structural		614	(9,1)	631	(17,1)	608
					(12,2)	608
structural		664	(10,1)	677	(14,2)	659
					(19,1)	667
3rd cavity	719	733	(11,1)	724	(16,2)	713
			(0,2)	736	(8,3)	718
			(1,2)	739	(21,1)	726
⋮	⋮	⋮	⋮	⋮	⋮	⋮
4th cavity	939	952	(10,2)	940	(28,1)	931
					(19,3)	941
					(24,2)	946
					(29,1)	960

Table 6.2: Comparison of a selection of the measured and calculated resonance frequencies. The measured frequencies originate from the in-cavity and the close proximity experiments whilst the calculated frequencies are obtained using the AMM. (Values are rounded.)

tuned to match the first cavity resonance frequency of 220 Hz, which was obtained in the close proximity measurements. It is noticed that the distance between the frequencies of the $(0, 1)$ and the $(1, 1)$ mode becomes lesser the smaller is the frequency of the $(0, 1)$ mode. In addition, the modal density in the frequency range of interest below 1000 Hz increases since the eigenfrequencies of the modes with circumferential nodal lines decrease. Thus, the frequencies of such modes get closer to the frequencies of less complex modes in the frequency range of up to 1000 Hz. For example, both the $(17, 1)$ and the $(12, 2)$ modes occur at 608 Hz,

which is in the vicinity of the measured structural resonance at 614 Hz. If the mode shape were to be identified experimentally at 608 Hz, a distorted mode shape may be the result due to the superposition of both modes. Thus, the mode shape may not be identifiable clearly in an experiment. In another example, four different predicted eigenfrequencies are within 30 Hz in the range of the fourth cavity resonance. An interaction of their corresponding modes and the fourth cavity resonance could take place in reality. However, this scenario, using such a low tension value in comparison to the measured tension in the experiment, illustrates a rather theoretical case. It would also mean that the experimentally determined $(2, 1)$ mode at 385 Hz cannot be replicated using the AMM.

A possible reason for the discrepancies between the model and the test rig may be the wave speed in the annular membrane. The wave speed had to be decreased in order to converge the eigenfrequencies of the AMM towards the experimentally determined resonances. However, if the wave speed is much smaller in a structure than the speed of sound in the surrounding acoustic medium, the vibro-acoustic coupling may reduce or prevent the radiation of the structural mode into the medium. Hence, a detection of such a resonance may not be possible with the current microphone method. This may also be the reason why not every structural resonance frequency could have been determined experimentally, since the results of the AMM generally suggest that many more eigenfrequencies occur in the frequency range of interest. A non-contact optical measurement method could assist in the identification of the structural resonances by scanning across the surface of the annular membrane in order to provide data of the surface displacement and, thus, information about the structural resonances.

The locally varying tension field in the annular membrane in the experiment cannot be reproduced in the AMM as this only accepts a single tension value. Since the tension is not constant, it is assumed that the wave speed is not constant either. Therefore, discrepancies may evolve between measured and calculated eigenfrequencies, since a single wave speed value is required in the AMM.

The applied amount of paint generally adds mass to the annular membrane. Since the spray paint was applied manually, an uneven distribution of the mass per area across the surface of the annular membrane may have been the result, which is similar to the case of the uneven distribution of the tension. Since the mass per area also affects the wave speed, an uneven distribution of the mass per area results in a locally varying wave speed in the annular membrane. As it is the case for the tension, this cannot be considered in the AMM since a single numerical value is required for the mass per area. In a bonding process between the spray paint and the annular membrane material the liquid spray paint dries and becomes attached to the membrane material. Thus, the stiffness of the annular membrane

may have been altered.

The experimental determination of the tension in the annular membrane could be improved by the avoidance of the spray paint application. Instead, it is suggested to utilise an annular membrane which is originally produced from black polymer film. In that case, only the white speckle pattern has to be added, which is assumed to not raise the weight of the annular membrane significantly. Thus, the effect of the additional mass of the paint is avoided.

6.5.4 Experimental procedure for the determination of the directivity characteristics

In the horizontal directivity measurements of the TSR test rig, five microphones are positioned at different heights in order to measure the sound pressure in front of the TSR test rig in a 180° arc and at a 1 m distance to the reference point. The schematic and a photograph of the experimental setup are presented in Figs. 6.50 and 6.51, respectively. The reference point lies in the geometrical centre of the TSR test rig. The microphones cover the TSR test rig vertically from the centre of the bottom region of the annular membrane to the centre of the top region of the annular membrane, as illustrated in Fig. 6.50. The vertical distance between the measurement positions is 11.5 cm. On the 180° arc, the sound pressure is measured at 5° intervals. Thus, a region of the shape of a half-cylinder covers the TSR test rig.

6.5.5 Analysis of the directivity sound pressure characteristics

The directivity characteristic of the TSR test rig shall be analysed in this section.

From the measured PSD spectra at 5° intervals at five different vertical positions and at a distance of 1 m to the reference point, the overall SPLs are determined at each of the measurement positions and are illustrated in Fig. 6.52, with height 1 representing the top measurement positions in the vertical direction and height 5 the bottom ones. The ±90° marks represent the front and rear positions in the radial direction of the TSR test rig. At the 0° mark, the microphone faced the surface of the annular membrane perpendicularly.

The overall SPLs increase rapidly between ±90° up to approximately 60° and between −70° and − 60°, respectively. Between 60° to 15°, the SPLs are within 0.5 dB and, thus, are taken to be approximately constant. Between −60° and − 30°, the overall SPLs of heights 1 to 3 are relatively constant as well. While the overall SPLs of heights 4 and 5 remain initially constant as well, they increase

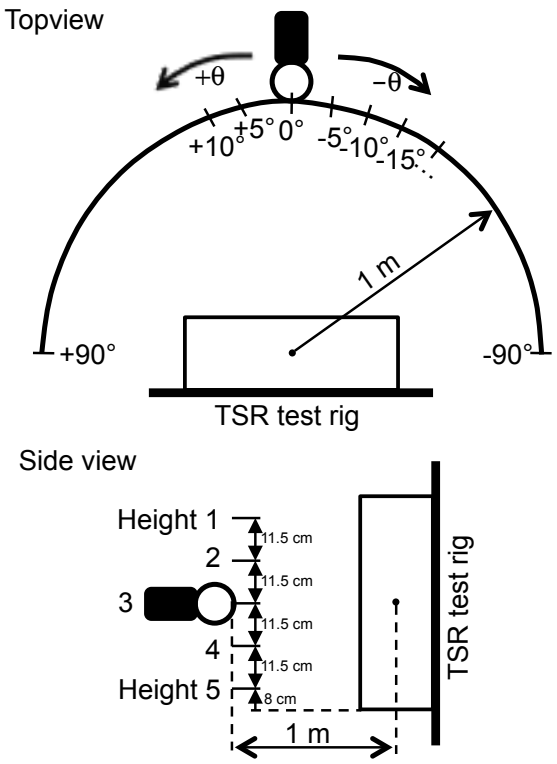

Figure 6.50: Schematic of the horizontal directivity measurements of the TSR test rig. Top: topview of the microphone positions on a 180° arc around the TSR test rig. Bottom: side view of the vertical microphone positions.

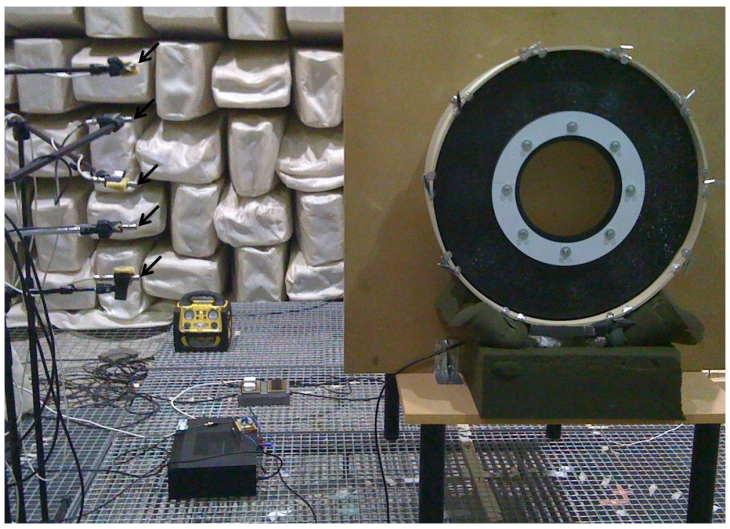

Figure 6.51: Photograph of the TSR test rig in the horizontal directivity measurement. The microphones are in the −90° position.

between the angles −45° to − 30°. The overall SPLs decrease at around 10° as well as between −30° to − 10°. However, they generally increase again towards the 0° mark. The smaller SPLs of heights 3 to 5 at 0° may be related to the hole within the annular shape of the membrane. The measured sound pressure at these positions may be the result of the sound radiation from other regions of the annular

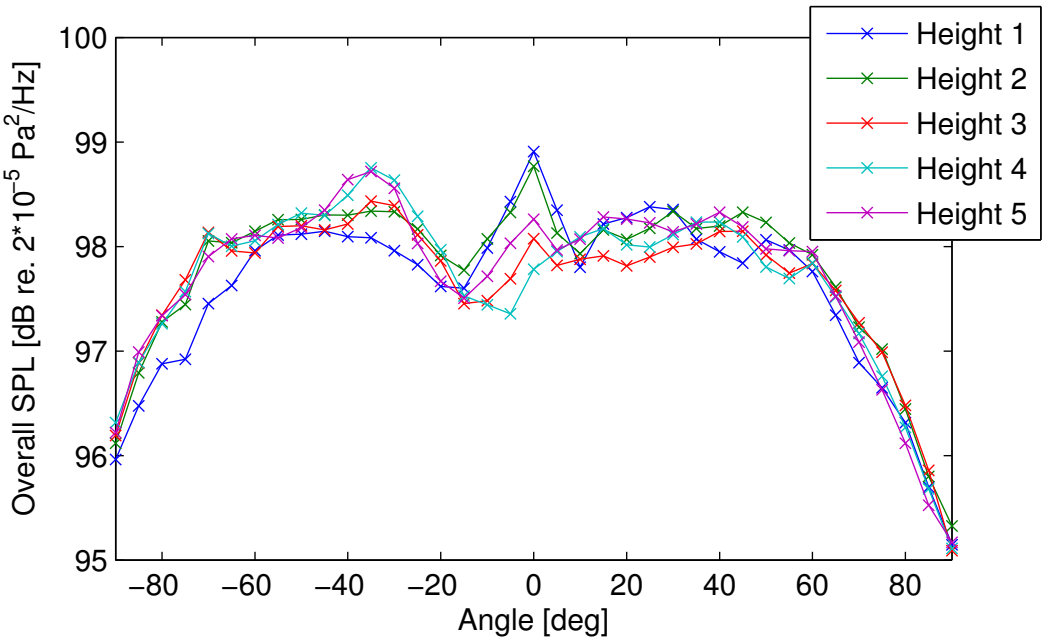

Figure 6.52: The overall SPLs at every measurement position in the directivity experiment. (Height 1 = top, height 5 = bottom.)

membrane. The maximum difference between the SPLs is approximately 4 dB for the 90° and 0° marks. The differences are generally low when the SPLs of the same circumferential positions are compared, with the relative deviations being within 0.5 dB. Hence, differences are hardly identifiable in the sound pressure spectra of the corresponding measurement positions. However, two exceptions occur in the ranges of −40° to − 30° and −10° to 0°, where the deviations rise to 0.7 dB and 1.2 dB, respectively. Here, it seems that the SPLs of heights 3 to 5 show a similar trend. A possible cause could be insufficient insulation of the acoustic excitation source at the bottom of the TSR test rig. Generally, it seems that the overall SPLs of heights 3 to 5 have a similar trend whilst the overall SPLs of heights 1 and 2 share similarities as well. The trend of the overall SPLs is almost symmetrical with regard to the 0° mark. Deviations are within 1 dB and, thus, are small. However, this may indicate that the TSR test rig exhibits a specific sound radiation directivity.

In addition to Fig. 6.52, which shows the SPLs without frequency-weighting, the overall SPLs of the directivity experiment are presented with frequency-weighting in Fig. 6.53. The trend of the SPLs with frequency-weighting is very similar to the SPL without frequency-weighting. Thus, it seems that the effect of the frequency-weighting is small.

The spectrum of the sound pressure in Fig. 6.54 provides an impression of the sound pressure spectra, which are recorded at the various measurement positions. The SPLs vary with the circumferential measurement position. For example, the

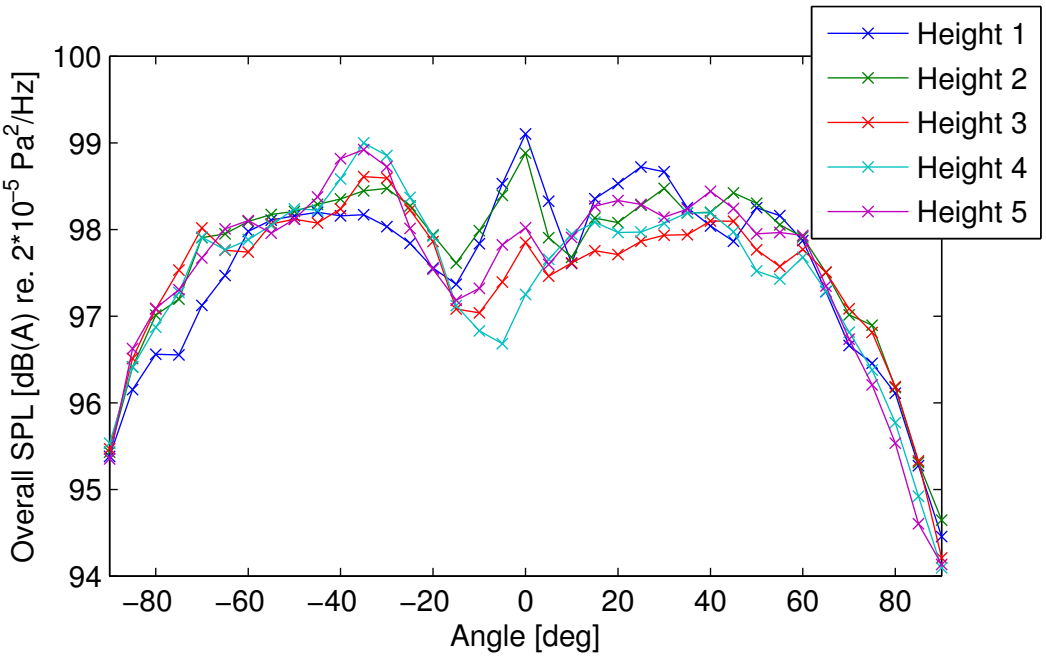

Figure 6.53: The overall SPLs with frequency-weighting at every measurement position in the directivity experiment. (Height 1 = top, height 5 = bottom.)

SPLs at 395 Hz are highest at 0° and decrease at −45°. At −90°, a resonance does not exist. It seems that the resonance at 408 Hz, which occurs at −90°, is shifted up to 426 Hz when the measurement position is altered to 0° via −45°. However, a more rational explanation is that the registration of any resonance frequency varies with the circumferential measurement position, which depends upon the directivity characteristic of the TSR test rig. That means that the resonance at 408 Hz can be detected at −90° but not at 0°. And the resonance at 426 Hz can be detected at 0° but not at −90°. Such characteristics can be repeatedly found over the whole frequency range and may indicate specific directivity properties of the TSR test rig sound radiation along the circumferential direction.

The frequencies associated with the cavity resonances can be identified in the sound pressure spectrum in Fig. 6.54. The resonance frequencies are 208 Hz, 531 Hz, 719 Hz, 939 Hz and 1141 Hz, which are in compliance with the in-cavity sound pressure measurements. The in-cavity and the directivity measurements were conducted close in time and basically in the same environmental conditions, which is not the case for the measurements carried out in the close proximity of the annular membrane, which resulted in different cavity resonance frequencies. Thus, it is assumed that the discrepancies between the measured cavity resonance frequencies are the result of the environmental conditions or changes in the TSR test rig. In the latter case, the membrane material may have been settled, which may result in a change in the tension in the membrane and, thus, the resonance frequencies decrease. Relatively high SPLs are also detected in the higher fre-

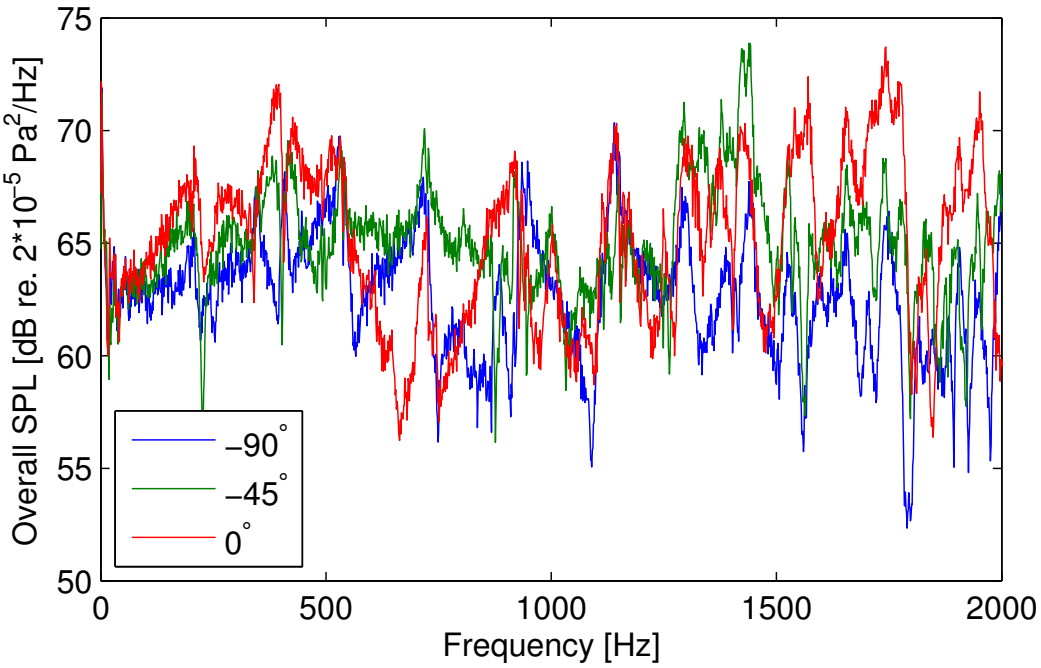

Figure 6.54: The PSD of the sound pressure measured at the top (= height 1) circumferential positions of −90°, −45° and 0°.

quency range like 1570 Hz, 1743 Hz and 1954 Hz, which were also detected in the in-cavity measurement in Fig. 6.3. The corresponding peaks are relatively high. The SPLs in the 0° direction seem to be relatively dominant at the frequencies 208 Hz, 531 Hz, 939 Hz, 1141 Hz, 1570 Hz, 1743 Hz and 1954 Hz. In the −90° direction, the SPLs are dominant at the cavity resonances but are relatively low at other frequencies in comparison to the SPLs in the 0° and −45°. In the −45° direction, the SPLs are highest at 719 Hz and in the frequency range 1290-1450 Hz. Thus, it is concluded that the cavity resonances radiate with different intensities towards the front and rear as well as sidewards of the TSR test rig. Higher frequencies are dominant at −45° and 0°. That means that the pressure fluctuations inside the cavity are transferred via the structure of the TSR test rig, which are mainly the annular membrane and the shells, and, then, are radiated into the environment and, thus, contribute to the pass-by noise under laboratory conditions.

For the analysis of a particular frequency, the template of a colour map has been developed, which enables the coloured two-dimensional illustration of the measured sound pressure for a single frequency at every measurement position in the circumferential and vertical directions. The sound pressure is bi-linearly interpolated between adjacent measurement positions. Such a colour map shall enable a detailed understanding of the directivity characteristics of the cavity and the annular membrane of the TSR test rig.

Fig. 6.55 shows the SPLs in the directivity colour map at 531 Hz. Here, a

distinctive directivity pattern can be recognised with the highest SPLs occuring in the region of the front and rear of the test rig. The SPLs decrease towards smaller angles. The lowest SPLs occur symmetrically around 0° between ±30° and ±5°. Around 0°, the SPLs are relatively increased in comparison to the adjacent SPLs. The SPLs also change in the vertical direction. Around −55° and 50°, the highest variations occur in the vertical direction with increasing SPLs towards the bottom measurement positions. Despite the distinctive directivity pattern in Fig. 6.55, it is doubtful whether the resolution, given through the number and distribution of measurement positions, is sufficient enough in order to clearly identify high frequency patterns. Therefore, this kind of analysis is no longer pursued.

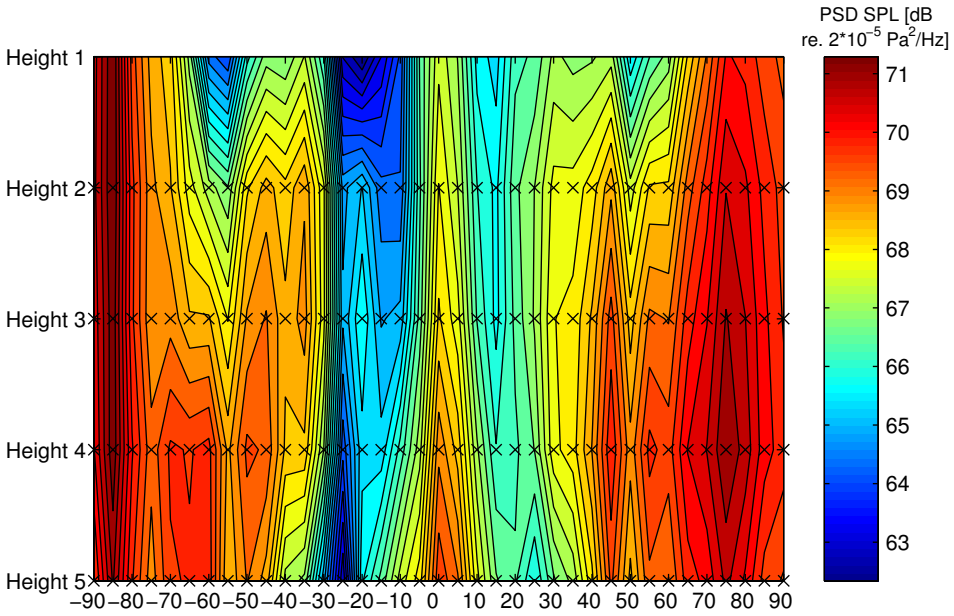

Figure 6.55: The directivity colour map of the measured sound pressure levels at 531 Hz.

The sound radiated from the TSR test rig shows distinctive directivity characteristics. It has been found that the cavity resonances radiate not only towards the front or rear, as reported in Ref. [16], of the TSR test rig but also sidewards. Depending upon the frequency, variations in the SPLs occur in either one direction or both the circumferential and vertical directions. Such directivity pattern may have an effect on the predicted pass-by noise of this noise source and, thus, may have to be considered in the prediction method.

6.6 Prediction of tyre sidewall pass-by noise

In this section, the experimental determination of the pass-by noise validation data of the tyre sidewall replica (TSR) test rig is presented. The measured pass-

by noise is analysed for two positions, at the top and bottom of the TSR test rig. Then, the predicted pass-by noise of the TSR test rig, based on the directivity sound pressure and the instantaneous distance between pass-by microphone and noise source, is presented and compared to the measured pass-by noise.

6.6.1 Measurement of tyre sidewall pass-by noise validation data

The tyre is in a parallel position relative to the direction of motion of the vehicle in the pass-by noise test. This shall be replicated with the TSR test rig and the pass-by noise test rig on a laboratory scale within an anechoic chamber. Due to the size of the TSR test rig, the reciprocal arrangement is preferred for the pass-by noise validation data recording. Fig. 6.56 presents a schematic of the experimental setup. The microphone is mounted on the trolley and the TSR test rig remains stationary off the test track with the plane of the annular membrane facing the pass-by noise test rig. Pass-by noise is measured for two configurations of the TSR test rig. In the first configuration in Fig. 6.57, the pass-by noise microphone is on the same height as the bottom region of the annular membrane. In the second configuration in Fig. 6.58, the pass-by noise microphone is on the same height as the top region of the annular membrane. These locations correspond to 'height 5' (bottom) and 'height 1' (top), respectively, in the directivity experiments.

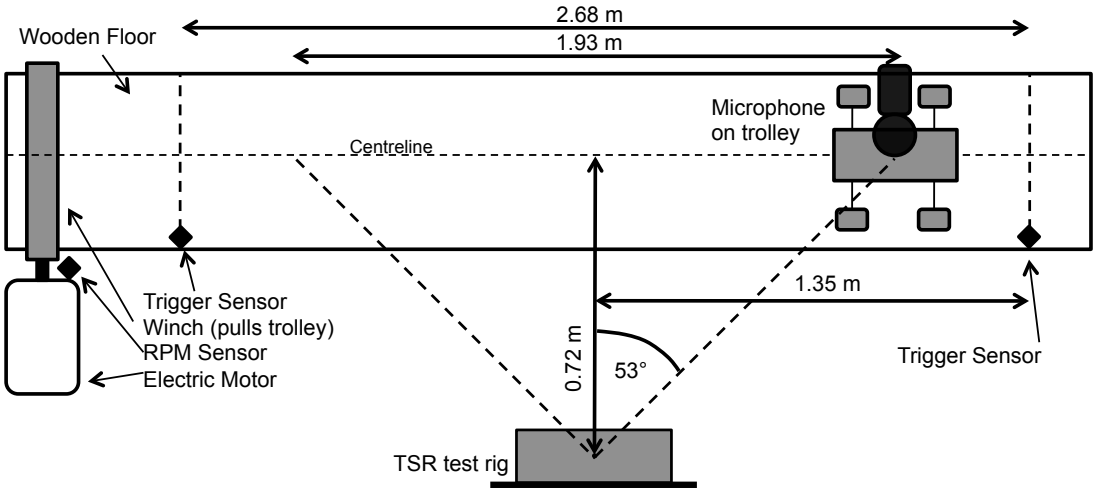

Figure 6.56: Schematic of the pass-by noise validation experiment of the TSR test rig in the reciprocal arrangement.

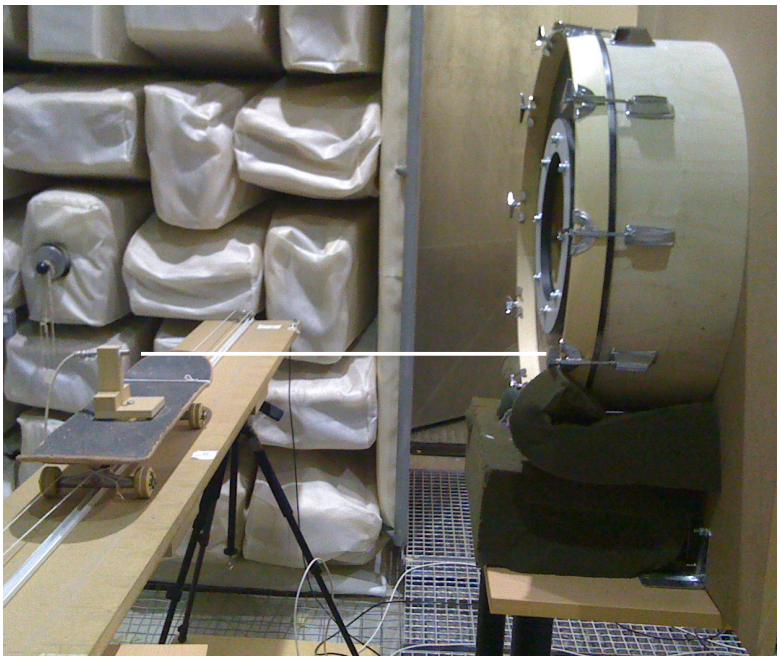

Figure 6.57: Photograph of the TSR test rig in the reciprocal arrangement of the laboratory scale pass-by noise experiment. The pass-by noise microphone and the bottom of the sidewall are on the same height.

Figure 6.58: Photograph of the TSR test rig in the reciprocal arrangement of the laboratory scale pass-by noise experiment. The pass-by noise microphone and the top of the sidewall are on the same height.

6.6.2 Comparison of measured and predicted pass-by noise

Pass-by noise is measured and predicted for two reciprocal arrangements of the TSR test rig. In the first configuration, the pass-by noise microphone is on the

same height as the bottom region of the TSR test rig. In the second configuration, the pass-by noise microphone is on the same height as the top region of the TSR test rig. Thus, two regions of the annular membrane are covered instead of the centre part, which also includes the inner ring section which is not part of the cavity noise generation. A height difference remains in comparison to a real pass-by noise test, in which the microphone height is set to 1.2 m. This is higher than a common tyre of a passenger vehicle. Due to the dimensions of the test equipment, the test configurations are the best solutions available.

The TSR test rig is the largest noise source in this work. The second largest noise source is the shell noise source and the smallest one is the orifice noise source. The distance between the membrane and the centre line of the test track is still 0.72 m. However, the laboratory scale pass-by noise test seems to be even more simplified due to the large dimension of the TSR test rig relative to the length of the test track. However, the scaling seems to be inadequate due to the large dimension of the TSR test rig. On the other hand, a small distance between the microphone and the noise source is considered necessary in order to record a sound pressure signal being dominated by the noise source.

Fig. 6.59 presents the measured and the predicted pass-by noise for the microphone being on the same height as the bottom region of the annular membrane. The frequency-weighted and time-weighted pass-by noise levels comprise the frequency range from 150 Hz to 2000 Hz. The differences between the pass-by noise levels of the three consecutive measurement runs is generally within 1 dB(A). Thus, the repeatability is very good. The offset of 0.1875 m in the pass-by noise graph on the abscissa results from the position of the microphone, which is midway between the front and the rear axle of the trolley. The rear axle of the trolley is the reference of the indirect measurement of the travelled distance. Due to the time-weighting, the measured pass-by noise level increases rapidly after the recording has been started. After approximately 0.15 m, it is assumed that the time-weighted formula produces accurate pass-by noise levels. Up to the 1.05 m mark, the measured pass-by noise level increases by approximately 4 dB(A) to about 82.3 dB(A). It then drops briefly and then rises again to 82 dB(A) at the 1.35 m mark. This characteristic is then repeated with a brief drop and a brief rise until the level decreases again slightly at around the 2 m. This volatility in the pass-by noise level may be due to the inherent directivity characteristics of the TSR test rig.

The pass-by noise prediction of the bottom position is obtained through the application of the horizontal directivity method. The prediction result appears to be generally good. The trend of the predicted levels agrees well with the measured levels. The deviation between prediction and measurement remains

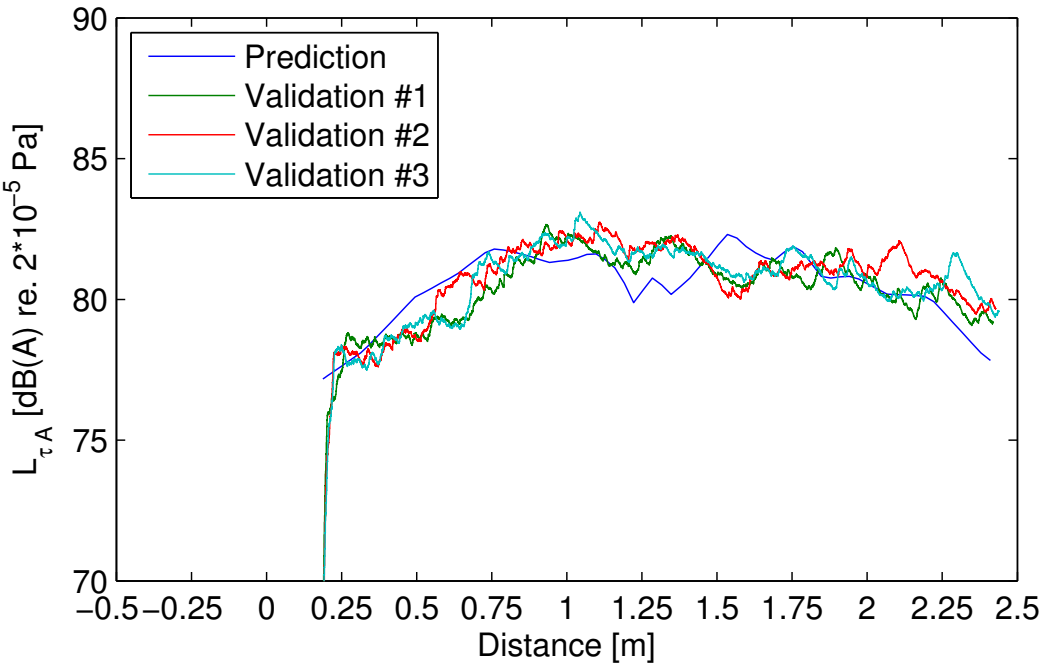

Figure 6.59: Comparison of the measured and the predicted pass-by noise for the TSR test rig. The height of the pass-by noise microphone corresponds the height of the bottom region of the TSR test rig (see also Fig. 6.57).

within 1.5 dB(A) for most of the travelled distance. The initial rise of the predicted pass-by noise level by 5 dB(A) up to the 1 m corresponds the measured pass-by noise levels. The volatility of the measured pass-by noise level in the middle part of the test track is met rudimentarily. In the final part of the test track, the agreement between prediction and measurement is very good. However, whilst the maximum predicted pass-by noise level occurs at the 1.54 m mark, the maximum measured pass-by noise level occurs at around the 1 m mark. Both maximum levels are approximately 82 dB(A).

Fig. 6.60 presents the measured and the predicted pass-by noise levels for the microphone being on the same height as the top region of the annular membrane. The repeatability of the three consecutive runs is considered sufficiently good, with deviations being generally within 2 dB(A) and occasionally rising to 3 dB(A) in the second half of the test track. The progression of the measured pass-by noise levels is steeper and higher noise levels are reached than in the other configuration. The measured pass-by noise pattern, with the slight volatility of the pass-by noise levels in the middle of the test track, is similar for both measurement configurations. In Fig. 6.60, the measured pass-by noise levels rise by approximately 7 dB(A) up to 84.5 dB(A) at around 1.1 m. From here, the levels remain on a generally high level until their tendency is to decrease at around 1.9 m.

The prediction result of this configuration appears to be generally good as

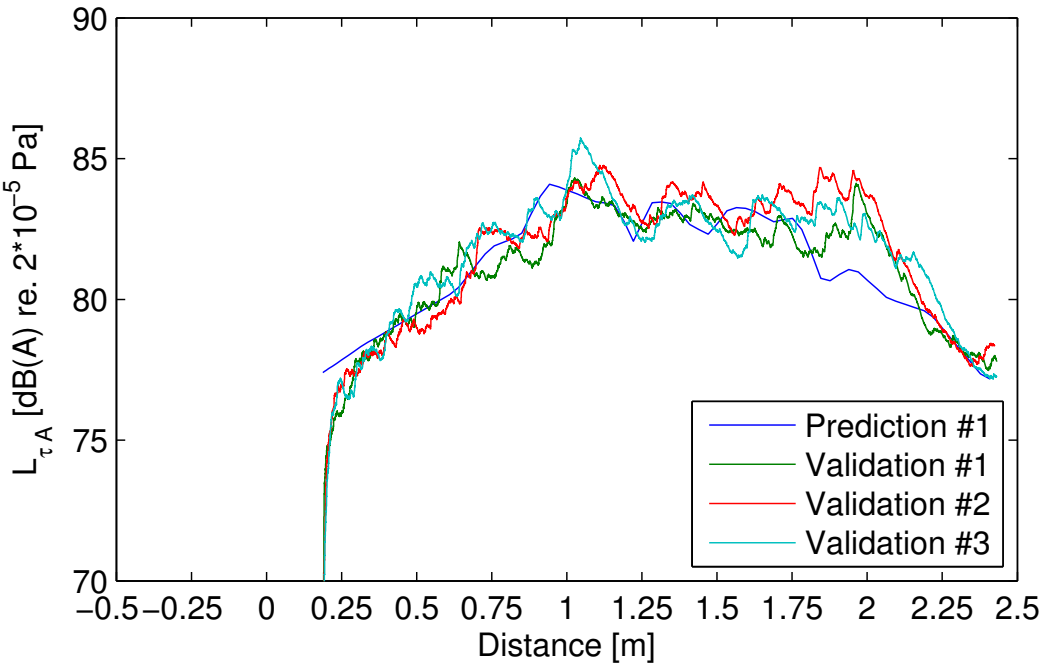

Figure 6.60: Comparison of the measured and the predicted pass-by noise for the TSR test rig. The height of the pass-by noise microphone corresponds the height of the top region of the TSR test rig (see also Fig. 6.58).

well. The trend of the measured levels agree very well with the predicted levels. Deviations are within 1 dB(A) for almost the whole track length. However, the deviation increases up to 3 dB(A) between 1.75-2 m. The maximum predicted pass-by noise level lies within 1 dB(A) of the maximum measured pass-by noise level. However, they are approximately 0.1-0.15 m apart around the 1 m.

6.7 Summary

The design of the tyre sidewall replica (TSR) test rig was presented in this chapter. The TSR test rig consists of a large and a small circular shell which replicate the boundaries of the tyre treadband and the wheel. The shells are mounted on a heavy board, which closes the cavity on one side where the tyre sidewall is located. On the opposite side, the tyre sidewall is replicated by an annular membrane. The tension in the annular membrane can be adjusted through a tensioning mechanism. It is intended to tune the tension in order to match the resonance frequencies of the cavity and the annular membrane. A loudspeaker provides acoustic excitation to the cavity of the TSR test rig. The resulting cavity resonances provide the excitation to the annular membrane, thus, replicating the tyre sidewall excitation mechanism and sound radiation.

The cavity resonances of the TSR test rig are measured with a microphone

inside the cavity. The measured first resonance frequency of the cavity of the TSR test rig is 208 Hz and, thus, close to the estimated resonance frequency using the Cartesian periodic duct theory. However, the multiples of the measured first resonance appear at frequencies of the ratio $(n + 0.5)$ with $n = [2, 3, 4, 5, 6]$. This is an unexpected result, since the Cartesian periodic duct theory produces the multiples of the first cavity resonance at integer ratios $n = [1, 2,]$. However, the measured spectrum shows the typical resonance characteristic of a cavity. The maximum SPLs occur at the first cavity resonance frequency and are between 87 dB(A) and 100 dB(A), depending on the loudspeaker amplification. Modes across the width or the radius of the cavity of the TSR test rig seem to develop at a frequency of 1500 Hz according to the experimental data.

The Digital Image Correlation technology is utilised in order to tune the tension in the membrane and to determine whether the tension is uniformly distributed throughout the annular membrane. Then, the comparison between measurement data and the annular membrane model (AMM) is based on the same assumption that the tension in the membrane is constant. The theoretical formulations of how the membrane tension can be obtained from measured deformation data are presented. The Digital Image Correlation technology is a non-contact, optical experimental method. Through its application, no additional weight or local stiffening is added to the annular membrane. The result is the measured deformation of the annular membrane under tension. The appropriate tension is reached when the measured sound radiation shows a resonance peak at the first cavity resonance. The measured deformation represents a static deformation due to force application at the boundaries of the annular membrane. The measured deformations in the horizontal and the vertical directions appear to be approximately axially symmetric around the vertical and the horizontal axes, indicating a uniformly deformed annular membrane.

Due to the assumption of constant wall-thickness of the membrane, the tension becomes a function of the principal stress. Both tensions T_1 and T_2 point in the same direction as the principal stresses σ_1 and σ_2, which is with $\pm 15°$ approximately in the radial and the tangential direction. The distribution pattern of both tensions T_1 and T_2 appear to be similar. The tension is not quite uniformly distributed in the annular membrane, as it was assumed for the annular membrane model (AMM). The averaged tension and its standard deviation is 13912 ± 5025 N/m for the tension T_1 and 10972 ± 4256 N/m for the tension T_2. Thus, the tension is higher in the radial direction. However, the annular membrane experiences a substantial amount of tension in the tangential direction as well. The standard deviations show the non-uniformity of the tension. High tension occurs in the vicinity of the tensioner bolts on the outer ring. In the

adjacent areas, between the positions of the tensioner bolts, the tension is lower. Thus, it is concluded that the force application is not uniform along the outer ring. On the inner ring, where the annular membrane is clamped via eight bolts, it appears that higher tension values occur between two bolts. However, it has to be noted that the bolts of the outer ring lie radially outwards of these areas. For the tension T_1, 43% of the tension values lie within 13427-17500 N/m, and 68% of the tension values are within 9948-17500 N/m. For the tension T_2, 40% of the tension values lie within 9295-12785 N/m, and 69% of the tension values are within 9295-16275 N/m. Sound pressure measurements during the tensioning procedure showed an increasing resonance frequency which plateaued in the range of the first cavity resonance frequency, thus, confirming that the eigenfrequencies of the annular membrane changed with tension. The application of the spray paint may have led to the non-uniform tension, since it added a considerable amount of weight to the membrane, which may cause local inhomogeneities of the mass and stiffness of the combined paint and membrane material. It was also assumed that the thickness of the membrane does not alter. However, the thickness could have been altered due to the high tension in the membrane. An experimental verification of either one could not be carried out.

Since the TSR test rig is a complex noise source, a thorough analysis of the sound radiation characteristics is envisaged in order to determine whether resonances of the annular membrane are excited by the cavity resonances. Therefore, sound pressure is recorded at overall 24 locations in close proximity, which is less than 5 mm, to the tensioned annular membrane. The measurement locations are 45° apart in circumferential directions; there are three measurement locations in radial direction at each circumferential location. A non-contact measurement method is necessary in order to not alter the physical properties of the annular membrane. Colour maps are utilised in order to spatially illustrate the measured sound pressure at a particular frequency and, then, to identify the mode shapes of the annular membrane. Due to the limited number of measurement locations, it is assumed that this method is limited to the identification of low-order mode shapes. The limiting criteria is the number of nodal lines which should be equal or less than the number of circumferential measurement locations. The low-order modes include for example the $(0,1)$, $(1,1)$, $(2,1)$ as well as the $(0,2)$, $(1,2)$, $(2,2)$ modes. The $(1,1)$ and $(2,1)$ modes correspond to the first and second cavity mode shapes. The measured resonance frequencies of the close proximity test show the distinctive characteristic of the cavity resonances. Other resonance peaks, which occur in the spectra as well, may be associated to structural resonances of the annular membrane. In the frequency range above 1000 Hz, peak amplitudes and resonance frequencies vary among the various measurement locations. Thus, the

occurrence of higher-order modes may be indicated. In addition, the modal density seems to increase with increasing frequency due to a high number of peaks above 1000 Hz. It is indicated that a membrane region with high tension may lead to high sound pressure radiation. However, this could not be detected constantly. The mode shapes of the first and second cavity mode can be identified at the frequencies of the first and second cavity in the colour maps. A higher number of measurement locations would have been necessary in order to clearly identify the other cavity mode shapes.

The derivation of the annular membrane model (AMM) is presented in this section and how it is applied in order to estimate the tension in the membrane in order to result in a specific set of eigenfrequencies. It is assumed that the tension and the wall-thickness are constant throughout the membrane. Bending moments and shear forces in the orthogonal direction of the membrane plane are neglected. The membrane material is assumed to be homogeneous and isotropic. Then, the AMM is given by the solution of hyperbolic linear partial differential equation of second order. The mode shapes of the $(1,1)$, $(2,1)$, $(3,1)$ and $(4,1)$ modes correspond to the first four cavity mode shapes. A direct match of the resonance frequencies should result in an amplified sound radiation of the TSR test rig, which confirms that the replication was successful.

The annular membrane model (AMM) requires the variables tension and mass per area, which are both single values. Since the experimentally derived tension is not evenly distributed in the annular membrane, an averaged tension value is calculated to be substituted into the AMM. The mass per area variable considers both the weight of the membrane and the added weight of the spray paint. However, initial modelling results indicate that the estimated values of the tension and the mass per area do not lead to matching eigenfrequencies between measurement and model. Varying the tension and mass per area values, the first cavity resonance frequency can be matched with the AMM. However, the higher resonance frequencies do not match with the measured frequencies. In addition, the high modal density may make it difficult to clearly identify a particular mode shape, since two modes lie within a few Hertz only. In the AMM, the wave speed in the annular membrane is smaller than the wave speed of sound in air. Thus, individual resonance frequencies may not have been radiated as sound and, hence, were not be detected by the microphones. A laser vibrometer would be an alternative measurement device. A measured non-constant tension may mean that the wave speed is non-constant as well in these areas. The distribution of mass and stiffness may have been altered significantly through the application of the spray paint, which may result in different wave speeds across the annular membrane.

The directivity sound pressure measurements are conducted along a 180° arc

at five different vertical positions around the front of the TSR test rig. The overall SPLs appear to be symmetrical around the lateral axis of the TSR test rig. Within ±65°, the SPLs are within 2 dB(A). The first five cavity resonance frequencies can be identified in the spectra of the directivity measurements. The corresponding SPLs are relatively dominant in the normal direction of the annular membrane. However, they generally vary depending on the measurement position, showing a distinctive directivity pattern. (showing a varying and complex directivity pattern) The cavity resonances radiate not only towards the front and rear but also sidewards, which is in the direction of the microphone in the pass-by noise test.

Two configurations of the TSR test rig are applied in the pass-by noise measurements. First, the bottom region of the annular membrane is positioned on the same height as the reciprocally arranged microphone. Second, the top region of the annular membrane is positioned on the same height as the reciprocally arranged microphone. The measured pass-by noise levels of both configurations show a similar pattern with increasing SPLs at the beginning, which is followed by briefly dropping and rising levels in the middle and decreasing levels at the end of the test track. The predicted pass-by noise levels show a good agreement with the measured levels. Deviations are generally within 1.5 dB(A) for most of the travelled distances. This is even surpassed for the predicted pass-by noise for the top region of the annular membrane. Such results are achieved despite the discrepancies in the tension tuning experiment.

Chapter 7

Summary and future work suggestions

A novel approach for the prediction of the pass-by noise emission of single moving noise sources is presented in this thesis. The validation of the prediction method was carried out utilising an original pass-by noise test rig with three different vehicle noise source replicas.

The prediction method applies the inverse square law. Therefore, horizontal directivity measurements are carried out for each noise source in which the sound pressure is recorded at a constant distance at discrete positions on a horizontal circle with the noise source at its centre. This directivity sound pressure may be considered as the noise source strength and it is substituted into the inverse square law as well as the constant measurement distance in the directivity measurements. The final quantity to be included is the instantaneous distance between microphone and noise source in the pass-by noise test rig. The result of these quantities being substituted in the inverse square law is the predicted pass-by noise for discrete positions of the moving noise source on the test track. This prediction method incorporates the measured directivity sound pressure and the instantaneous distance between microphone and noise source. The latter quantity represents the transfer path in principal. The instantaneous distance can be replaced by an arbitrary data set, if it is desired, which may be based on either an accelerated or a constant-speed pass-by driving manoeuvre. This prediction method is relatively easy to implement in comparison to alternative methods. The indoor simulation of pass-by noise requires a large semi-anechoic chamber with a vehicle chassis dynamometer and at least one microphone line array as well as a complete vehicle prototype. Advanced measurement analysers and equipment and a vehicle prototype, too, are necessary to conduct the transfer path prediction method, which is deemed to be time-consuming. Numerical methods require

specific computation resources and they are not advanced enough currently.

The evaluation of the literature review led to the selection of three vehicle noise sources which were to be replicated in order to test and validate the prediction method in the available test facilities. The three noise source replicas are (i) an orifice noise source (ONS), for the replication of intake or exhaust orifice noise, (ii) a shell noise source (SNS), for the replication of noise from thin-walled structures like an exhaust muffler, and (iii) a tyre cavity and sidewall noise source (tyre sidewall replica (TSR) test rig), for the replication of tyre sidewall noise radiation due to the excitation from the tyre cavity resonances. An extensive analysis of the noise radiation or directivity characteristics, respectively, is carried out for each of the noise sources. It was assumed that each of them replicate their real counter parts sufficiently well.

Validation data was recorded for different arrangements of the noise sources relative to the pass-by microphone, including direct and reciprocal measurements. The velocity profile of the trolley shows an acceleration at the beginning which converts into an approximately constant-speed pass-by manoeuvre. The characteristic of any pass-by noise recording follows a similar trend, which consists of an increasing pass-by noise level when the distance between microphone and the noise source is decreased and of an decreasing pass-by noise level when the distance between microphone and the noise source is increased.

The pass-by noise prediction of the ONS in the normal arrangements and of the tyre sidewall noise source achieved the best results in comparison to the measured pass-by noise. The difference between validation data and prediction is slightly higher for the reciprocal arrangements of the ONS and the SNS. Although, in case of the ONS the trend of the predicted pass-by noise level agrees very well with the validation data. It is assumed that the deviation is caused by the reciprocal recording of the pass-by noise validation data and not by the prediction method. The pass-by noise prediction of the SNS is corrected through the summation of the initially predicted pass-by noise level and the measured rolling noise level of the test rig, since both levels are close in range. Thus, an improvement is achieved for the predicted pass-by noise level. It does not make sense to apply this correction method to levels that are 10 dB(A) or more apart.

The advantage of the prediction method in conjunction with the laboratory scale experimental apparatus are that it is straightforward and relatively easy to operate, the implementation costs are low, the time effort is relatively small, single vehicle noise sources and not a complete vehicle prototype is required, the test facility does not necessarily needs to be certified according to standards related to vehicle pass-by noise [10, 11, 12]. Many of these items are required in the alternative pass-by noise prediction methods. Since the prediction method of

this thesis may be applied in the early development stage, it may provide an instrument to reduce the number of physical prototypes in the later stages of the development process, thus, lowering development costs and the duration of the product development cycle. However, the prediction method of this thesis is limited to the application in anechoic conditions with a constant excitation signal, and it was validated for a scaled pass-by noise test scenario. On the other hand, the environmental influences are minimised which is deemed to ensure a sufficiently good repeatability.

It is envisaged that this pass-by noise prediction method feeds into the requirements of the standard ISO 362 and contributes to the estimation of the pass-by noise contribution of single vehicle noise sources in the early stages of the vehicle development process. Comparison of the directivity sound pressure characteristics as well as the predicted pass-by noise of a particular noise source may enable the identification of the dominant pass-by noise contributors. Alternatively, they provide set of data to which any subsequently modified noise source can be compared to. The application of the prediction method may support the acoustic vehicle development process for current and future pass-by noise test procedures. If the application of the prediction method leads to a vehicle which emits pass-by noise within the legal limits, the method may even contribute to the reduction in road traffic noise.

For future work, it is suggested to use an annular membrane of black colour, which may improve the tuning of the tension of the annular membrane in order to match the cavity eigenfrequencies with the annular membrane eigenfrequencies. Additional spray paint does not need to be applied, thus, the weight and the stiffness of the membrane is not altered. In addition, the experimental procedure of the DIC experiment can be improved by estimating the tension straight after the DIC post-processing, which is typically carried out after an image has been shot, which would involve a data export of the strain field to the Matlab® code. Other vehicle noise source should be included in the prediction method and the overall pass-by noise level of various noise sources can then be estimated. The prediction method seems to work in anechoic conditions. However, it does not consider ground reflections, which should be addressed in the future. The prediction method should be tested with an excitation signal that changes with time, as for example the powertrain noise source in the accelerated pass-by noise test. The advantages of using a laboratory scale model is considered generally advantageous regarding controlled test environment and repeatability, simple operational handling and low costs. However, greater efforts have to be made in order to transfer the application of the prediction method to real vehicle noise sources and the ISO 362 pass-by noise test track.

References

[1] T Abe, K Yoshimori, and A Azuma. Exhaust noise abatement with porous sintered metal silencer. *SAE Technical Paper Series 850326*, 1985.

[2] R Alfredson and P Davies. The radiation of sound from an engine exhaust. *J Sound Vibr*, 13:389–408, 1970.

[3] N Alt, K Wolff, G Eisele, and F Pichot. Fahrzeugaußengeräuschsimulation (vehicle exterior noise simulation). *Automobiltechnische Zeitschrift*, 108:832–36, 2006.

[4] R Arndt, W Fliesser, D Rein, and C Fankhauser. Analysis of pass-by noise using nearfield acoustic holography. In *Proceedings of the joint congress CFA/DAGA '04*, pages 19–20, 2004.

[5] DR Balcombe and PJ Crowther. Practical development problems in achieving 74 db(a) for cars. In *Noise and the automobile: Selected papers from Autotech'93 which took place at the National Exhibition Centre, Birmingham, UK*, pages 109–15, London, 1993. Mechanical Engineering Publications.

[6] JW Biermann. *Geräuschverhalten von Kraftfahrzeugen (Noise characteristics of vehicles)*. Aachen, GER, 2004. Umdruck zur Vorlesung (Lecture Notes).

[7] JW Biermann, T Beckmann, L Wech, and R Meier. Analyse des Reifenabrollgeräuschs mit einem Messfahrzeug (Analysis of rolling tyre noise with a measurement vehicle). *Automobiltechnische Zeitschrift*, 106:562–569, 2004.

[8] W Biermayer, FK Brandl, and M Pflüger. Analyse und Optimierung des Vorbeifahrtgeräuschs von Fahrzeugen (Analysis and optimisation of vehicle pass-by noise). *Automobiltechnische Zeitschrift*, 106:426–32, 2004.

[9] British Standards Institution, London. *Acoustics - Specification of test tracks for the purpose of measuring noise emitted by road vehicles*, 1st edition, 1995. BS ISO 10844:1994.

[10] British Standards Institution, London. *Acoustics - Measurement of noise emitted by accelerating road vehicles - Engineering method*, 3rd edition, 1998. BS ISO 362:1998.

[11] British Standards Institution, London. *Measurement of noise emitted by accelerating road vehicles - Engineering method - Part 1: M and N categories*, 1st edition, 2007. BS ISO 362-1:2007.

[12] British Standards Institution, London. *Acoustics - Specification of test tracks for measuring noise emitted by road vehicles and their tyres*, 2nd edition, 2011. BS ISO 10844:2011.

[13] British Standards Institution, London. *Electroacoustics - Sound level meters - Part 1: Specifications*, 2013. BS EN 61672-1:2013.

[14] British Standards Institution, London. *Measurement of minimum noise emitted by road vehicles*, 2014. Draft BS ISO 16254:2014.

[15] W Choi and JS Bolton. Influence of the cavity mode on tire surface vibration. In *40th International Congress and Exposition on Noise Control Engineering (INTER-NOISE 2011)*, volume 1, pages 600–607, 2011.

[16] WH Choi. Influence of the cavity mode on tire surface vibration. Master's thesis, Purdue University, West Lafayette, IN, USA, 2011.

[17] D Clouth. Characterisation of acoustic sources for the prediction of vehicle pass-by noise (part D final project). Master's thesis, Loughborough University, Loughborough, UK, 2012.

[18] European Commission. Commission Directive 2007/34/EC of 14 June 2007 amending, for the purposes of its adaption to technical progress, Council Directive 70/157/EEC concerning the permissible sound level and the exhaust system of motor vehicles, June 2007.

[19] European Commission. Proposal for a regulation of the European Parliament and of the Council on the sound level of motor vehicles, December 2011. Proposal reference COM(2011)856.

[20] POAL Davies and MF Harrison. Predictive acoustic modelling applied to the control of intake/exhaust noise of internal combustion engines. *J Sound Vibr*, 202:249–74, 1997.

[21] POAL Davies and K Holland. I.C. engine intake and exhaust noise assessment. *J Sound Vibr*, 223:425–44, 1999.

[22] F de Roo, MG Dittrich, PJG van Beek, C Bosschaart, GB Derksen, and M de Kievit. VENOLIVA - Vehicle Noise Limit Values - Comparison of two noise emission test methods - Final Report, 2011.

[23] S Demmerer. *Simulation von Schallfeldern am Kraftfahrzeug (Simulation of sound fields on a vehicle)*. PhD thesis, Technische Universität München, 2002.

[24] W Dreyer, P Hoppe, P Friederich, and H Fuchs. Das neue Volkswagen-Akustikzentrum in Wolfsburg - Teil 1: Prüfstände (The new centre of acoustics of Volkswagen in Wolfsburg - Part 1: Test Facilities). *Automobiltechnische Zeitschrift*, 105:250–60, 2003.

[25] M Endo, Y Futagami, and J Iwamoto. Relation between the flow pattern downstream of duct and the noise. *JSAE Review*, 21:125–32, 2000.

[26] DuPont Teijin Films. Mylar® polyester film - product information [online], 2003. Available at: <http://usa.dupontteijinfilms.com/informationcenter/downloads/Physical_And_Thermal_Properties.pdf> [Accessed 19 August 2013].

[27] H Finsterhölzl, V Caldiero, J Hobelsberger, W Baumann, and F Daiber. Neuer Außengeräuschprüfstand im Entwicklungsprozess bei BMW (New exterior noise test facility in the development process at BMW). *Automobiltechnische Zeitschrift*, 108:256–67, 2006.

[28] AR Fleszar, PJG van der Linden, JR Johnson, and MJ Grimmer. Combining vehicle and test-bed diagnosis information to guide vehicle development for pass-by noise. *SAE Technical Paper Series 2001-01-1565*, 2001.

[29] L Fritschi, AL Brown, R Kim, D Schwela, and S Kephalopoulos. *Burden of disease of environmental noise - Quantification of healthy life years lost in Europe*. World Health Organization Regional Office for Europe, Copenhagen (Denmark), 2011.

[30] J Fry and P Jennings. Using multi-layer perceptrons to predict vehicle pass-by noise. *Neural Computing & Applications*, 11(3):161–7, 2003.

[31] J Fry, P Jennings, N Taylor, and P Jackson. Vehicle drive-by noise prediction: A neural networks approach. *SAE Technical Paper Series 1999-01-1740*, 1999.

[32] H Fuchs, X Zha, G Babuke, and P Friederich. Das neue Volkswagen-Akustikzentrum in Wolfsburg - Teil 2: Reflexionsarme Raumauskleidungen (The new centre of acoustics of Volkswagen in Wolfsburg - Part 1: Low Reflection Room Linings). *Automobiltechnische Zeitschrift*, 105:372–82, 2003.

[33] K Fujita, T Abe, and Y Hori. Simulation of acceleration pass-by noise considering the acoustic radiation characteristics of a vehicle body. *Inter J Veh Des*, 8:514–25, 1987.

[34] S Gade, P Rasmussen, and N Taylor. Passby measurements vs. STSF passby simulations. In *Proceedings InterNoise*, pages 3087–92, 1996.

[35] Gamma Technologies, Inc., Westmon, Il, USA. *GT-Power User's Manual - Version 6.2*, 2006.

[36] K Genuit, S Guidati, and R Sottek. Progresses in pass-by simulation techniques. *SAE Technical Paper Series 2005-01-2262*, 2005.

[37] KB Ginn and G Newton. Contribution analysis in pass-by testing using moving source beamforming. *SAE Technical Paper Series 2011-01-1669*, 2011.

[38] Robert Bosch GmbH, editor. *Bosch - Kraftfahrtechnisches Taschenbuch (Bosch - Automotive Handbook)*. Vieweg + Teubner, Wiesbaden, GER, 25 edition, 2003.

[39] PW Gold, R Schelenz, J Fechler, M Hollenstein, S Pischinger, H-P Lahey, C Steffens, and O Andres. Akustische Untersuchungen im Gesamtsystem Verbrennungsmotor-Getriebe (Acoustic investigations of the system of combustion engine and gearbox). *Automobiltechnische Zeitschrift*, 101(7/8), 1999.

[40] S Guidati, R Sottek, and K Genuit. Simulated pass-by in small rooms using noise synthesis technology. In *Proceedings of the joint congress CFA/DAGA '04*, pages 21–22, 2004.

[41] R Gunda, S Gau, and C Dohrmann. Analytical model of tire cavity resonance and coupled tire/cavity modal model. *Tire Science and Technology*, 28(1):33–49, 2000.

[42] P Hagedorn and A DasGupta. *Vibration and waves in continuous mechanical systems*. John Wiley & Sons Ltd, Chichester, 2007.

[43] M Harrison. *Vehicle Refinement - Controlling noise and vibration in road vehicles*. Elsevier Butterworth-Heinemann, Oxford, 2004.

[44] T Hayashi. Experimental analysis of acoustic coupling vibration of wheel and suspension vibration on tire cavity resonance. *SAE Technical Paper Series 2007-01-2345*, 2007.

[45] M Hueser, K Govindswamy, K Wolff, and R Stienen. Sound quality and engine performance optimization development utilizing air-to-air simulation and interior noise synthesis. *SAE Technical Paper Series 2003-01-1652*, 2003.

[46] J Huijssen, P Fiala, R Hallez, S Donders, and W Desmet. Numerical evaluation of source-receiver transfer functions with the fast multipole boundary element method for predicting pass-by noise levels of automotive vehicles. *J Sound Vibr*, 331, 2012.

[47] K Iwao and I Yamazaki. A study on the mechanism of tire/road noise. *JSAE Review*, 17:139–44, 1996.

[48] K Janssens, P Aarnoutse, P Gajdatsy, L Britte, F Deblauwe, and H van der Auweraer. Time domain source contribution analysis method for in-room pass-by noise. *SAE International 2011-01-1609*, 2011.

[49] AM Jessop and JS Bolton. Tire surface vibration and sound radiation resulting from the tire cavity mode. In *Proceedings of 20th International Congress on Acoustics*, pages 1–5, 2010.

[50] PA Kelly. *Lecture Notes in Solid Mechanics Part II: Engineering Solid Mechanics [online]*. Available at: <http://homepages.engineering.auckland.ac.nz/~pkel015/SolidMechanicsBooks/Part_II/index.html> [Accessed 08 August 2013].

[51] BS Kim, GJ Kim, and TK Lee. The identification of sound generating mechanisms of tyres. *Applied Acoustics*, 68:114–133, 2007.

[52] BS Kim, GJ Kim, and TK Lee. The identification of tyre induced vehicle interior noise. *Applied Acoustics*, 68:133–156, 2007.

[53] GJ Kim, KR Holland, and N Lalor. Identification of the airborne component of tyre-induced vehicle interior noise. *Applied Acoutics*, 51(2):141–156, 1997.

[54] S-R Kim, K-D Sung, D-W Lee, and S-C Huh. Cavity noise analysis of tire contour design factors and application of contour optimization methodology. *J Cent South Univ*, 19:2386–93, 2012.

[55] W Kropp, F-X Bécot, and S Barrelet. On the sound radiation from tyres. *Acta Acustica united with Acustica*, 86:769–79, 2000.

[56] WA Leasure and EK Bender. Tire-road interaction noise. *J Acoust Soc Am*, 58(1):39–50, 1975.

[57] JW Lee and KJ Min. A reduction of vehicle pass-by noise by experimental approach. In *Proceedings of the International Congress on Noise Control Engineering (InterNoise)*, volume 4, page 1973, 1996.

[58] LaVision UK Ltd. Strainmaster - advanced image based tools for optical deformation and strain measurement [online]. Available at: <http://www.lavision.de/en/download.php?id=323> [Accessed 03 September 2013].

[59] JM Mason and FJ Fahy. Application of a reciprocity technique for the determination of the contributions of various regions of a vibrating body to the sound pressure at a receiver point. In *Proceedings of the Institute of Acoustics*, volume 12, pages 469–76, 1990.

[60] L Molisani. *A coupled tire structure-acoustic cavity model*. PhD thesis, Virginia Polytechnic Institute and State University, 2004.

[61] L Molisani, RA Burdisso, and D Tsihlas. A coupled tire structure/acoustic cavity model. *International Journal of Solids and Structures*, 40:5125–38, 2003.

[62] Y Mori, A Fukushima, K Uesaka, and H Ohnishi. Noise directivity of vehicles on actual road. In *Proceedings of Internoise 99*, volume 1, 1999.

[63] ML Munjal. *Acoustics of ducts and mufflers (with application to exhaust and ventilation design)*. John Wiley & Sons, New York, USA, 1987.

[64] L Papula. *Mathematik für Ingenieure und Naturwissenschaftler Band 3 (Mathematics for engineers and scientists, part 3)*. Vieweg, Braunschweig/Wiesbaden, GER, 2001.

[65] S-H Park and Y-H Kim. Visualization of pass-by noise by means of moving frame acoustic holography. *J Acoust Soc Am*, 110:2326–39, 2001.

[66] AV Phillips, A Bruno, M Orchard, DM Rhodes, and N-M Shiau. A process for vehicle drive-by noise analysis. In *IMechE Conference Transactions - European Conference on Vehicle Noise and Vibration*, pages 319–330, 2000.

[67] AV Phillips and M Orchard. Drive-by noise prediction by vehicle system analysis. *SAE Technical Paper Series 2001-01-1562*, 2001.

[68] S Pischinger. *Engine Acoustics (Lecture Notes)*. Aachen, GER, 2006. Lecture Notes.

[69] S Pischinger, H Stoffels, C Steffens, R Aymanns, R Stohr, and M Atzler. Akustische Auslegung von Abgasturboladern (Acoustic design of turbochargers). *Motortechnische Zeitschrift*, 3:238–45, 2008.

[70] AD Polyanin. *Handbook of linear partial differential equations for engineers and scientists*. Chapman & Hall/CRC, 2002.

[71] P Rasmussen. Pass-by noise measurements. *Brüel&Kjær Technical Review*, (1), 1995.

[72] Y Ryu and S Lange. The design and validation of simulated indoor passby noise measurement system. *SAE Paper 2007-26-033*, 2007.

[73] Y Ryu, A Schuhmacher, M Hirayama, and Y Shirahashi. Contribution analysis of exterior noise with indoor pass-by measurment. *SAE International 2011-26-0062*, 2011.

[74] T Sakata, H Morimura, and H Ide. Effects of tire cavity resonance on vehicle road noise. *Tire Science and Technology*, 18(2):68–79, 1990.

[75] U Sandberg. Possibilities to replace outdoor coast-by tyre/road noise measurements with laboratory drum measurements, 2006. Project "Silence", European Commission DG Research, Sixth Framework Programme, Priority 6, Contract No. 516288.

[76] U Sandberg and JA Ejsmont. *Tyre/road noise reference book*. Informex, Kisa, SE, 2002.

[77] RW Scavuzzo, LT Charek, PM Sandy, and GD Shteinhauz. Influence of wheel resonance on tire acoustic cavity noise. *SAE Technical Paper Series 940533*, 1994.

[78] H Steven. *Pkw-Reifen/Fahrbahngeräusche bei unterschiedlichen Fahrbedingungen (Tyre/road noise of passenger vehicles in different driving conditions)*, volume 157 of *FAT Schriftenreihe*. Forschungsvereinigung Automobiltechnik e.V., Frankfurt/Main, GER, 2000.

[79] W Stücklschwaiger. Experimental pass-by noise source analysis - approach based on measured transfer functions, 2006. Project "Silence", European Commission DG Research, Sixth Framework Programme, Priority 6, Contract No. 516288.

[80] N Taylor. Pass-by noise - a brief overview, 2007. Presentation held at Loughborough University.

[81] N Taylor and P Rasmussen. Exterior noise measurements on a Rover 220 GSi, 1995. Brüel&Kjær Application Note.

[82] JK Thompson. Plane wave resonance in the tire air cavity as a vehicle interior noise source. *Tire Science and Technology*, 23(1):2–10, 1995.

[83] PJG van der Linden. Piano - synthesis report for publication: New pass-by noise optimization methods for quiet and economic heavy road vehicles, 1996. Project funded by the European Union under the BRITE EURAM Programme, Project No. 5414 PIANO, Contract No BRE2-CT'-92O210.

[84] PJG van der Linden, H Defay, and JP Le Martret. Truck pass-by noise, detailed sources contribution identification during ISO R 362 pass-by. In *Proceedings of the International Seminar on Modal Analysis 21*, pages 47–54, 1996.

[85] PJG van der Linden, S Goossens, and O Jönnson. Correction of indoor pass-by noise measurements to estimate ISO R 362 outdoor noise using acoustic transfer functions. In *Proceedings of the International Seminar on Modal Analysis 21*, pages 37–46, 1996.

[86] PJG van der Linden and M Mantovani. The validity of reciprocal acoustic transfer function measurements on trucks for pass-by noise. In *Proceedings InterNoise*, pages 2661–6, 1996.

[87] PJG van der Linden and DAC Otte. Diagnosis of pass-by noise of road vehicles. In *Noise and the automobile: Selected papers from Autotech'93 which took place at the National Exhibition Centre, Birmingham, UK*, pages 99–108, London, 1993. Mechanical Engineering Publications.

[88] Verein Deutscher Ingenieure, Düsseldorf. *Geräuschanteile von Straßenfahrzeugen - Meßtechnische Erfassung und Bewertung (Guideline of the Association of German Engineers (VDI): Noise components of vehicles - measurement and assessment)*, 1990. VDI-Richtlinien 2563.

[89] X Wang. *Vehicle noise and vibration refinement*. Woodhead Publishing, Cambridge, 2010.

[90] P Zeller. *Handbuch Fahrzeugakustik (Handbook vehicle acoustics)*. Vieweg + Teubner, Wiesbaden, GER, 2009.

[91] Z Zhang, N Vlahopoulos, T Allen, and KY Zhang. Development and validation of a computational process for pass-by noise simulation. *Int J Veh Des*, 34:12–34, 2004.